

# Study of Magnetic Properties and Exchange Bias in $\text{Co}(\text{Cr}_{1-x}\text{M}_x)_2\text{O}_4$ ( $\text{M} = \text{Fe}, \text{Co} \ \& \ \text{Al}$ )



A thesis submitted to  
Indian Institute of Technology Guwahati  
for the degree of  
Doctor of Philosophy in Physics

by  
Padam Rajender

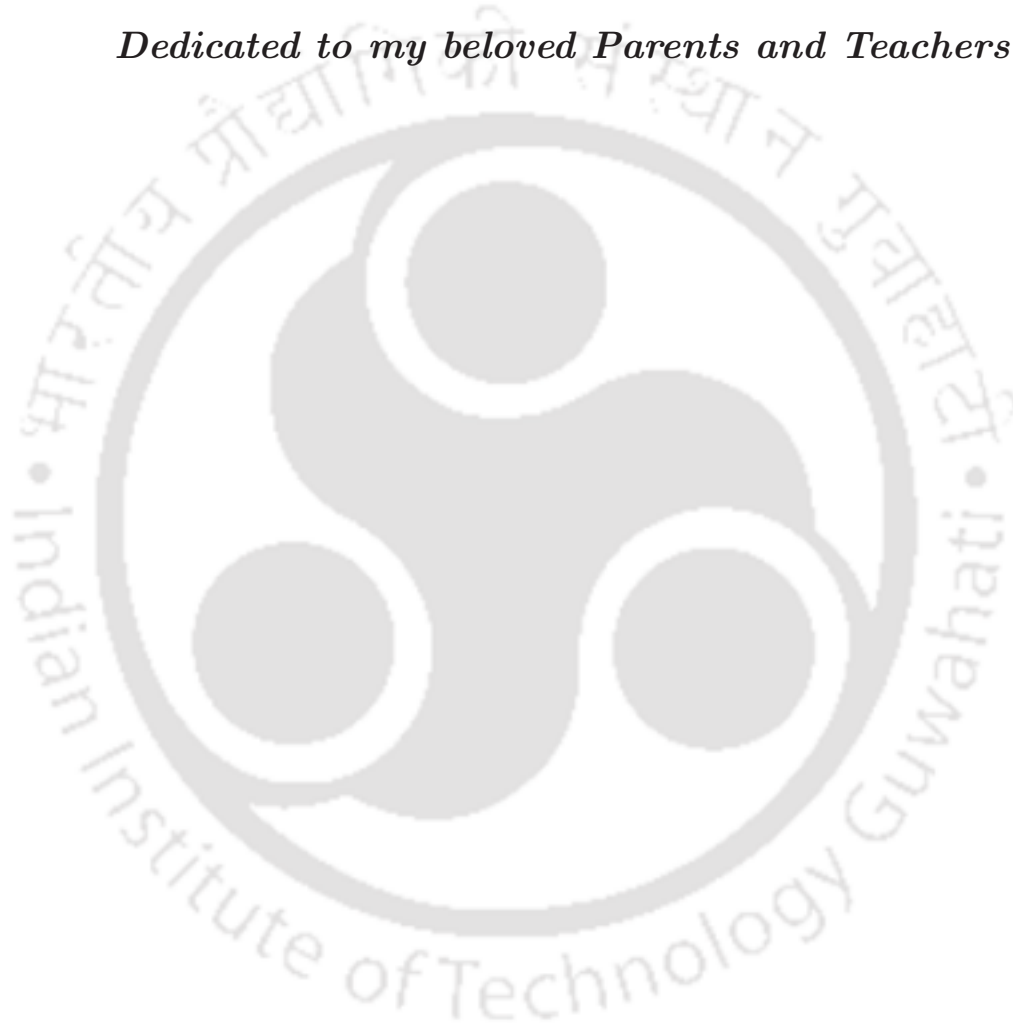
Thesis Supervisors: Dr. Dilip Pal & Prof. S. Ravi

Department of Physics  
Indian Institute of Technology Guwahati, Guwahati-781 039,  
Assam, India.

*August 2014*



*Dedicated to my beloved Parents and Teachers..*





## Declaration

I hereby declare that this thesis entitled “**Study of Magnetic Properties and Exchange Bias in  $\text{Co}(\text{Cr}_{1-x}\text{M}_x)_2\text{O}_4$  (M = Fe, Co & Al)**” is the result of my own doctoral research work. This work was carried out under the supervision of Dr. Dilip Pal and Prof. Seenipandian Ravi at the Department of Physics, Indian Institute of Technology Guwahati. To the best of my knowledge, the work presented in this thesis has not been submitted to any other Institute/University for the award of any degree.

**Padam Rajender**

Research Scholar (Roll No: 09612108)

Department of Physics

Indian Institute of Technology Guwahati

Guwahati-781039, India



## Certificate

It is certified that the work contained in the thesis entitled “**Study of Magnetic Properties and Exchange Bias in  $\text{Co}(\text{Cr}_{1-x}\text{M}_x)_2\text{O}_4$  ( $\text{M} = \text{Fe}, \text{Co} \ \& \ \text{Al}$ )**” by Padam Rajender, a student of Department of Physics, Indian Institute of Technology Guwahati, for the award of the degree of Doctor of Philosophy has been carried out under our supervision. This work has not been submitted elsewhere for any degree.

**Dr. Dilip Pal**

Associate Professor  
Dept. of Physics  
IIT Guwahati  
Guwahati-781039, India

**Prof. Seenipandian Ravi**

Professor  
Dept. of Physics  
IIT Guwahati  
Guwahati-781039, India



# Synopsis

Magnetism and the related phenomena are of interest in the research community for centuries owing to their fundamental as well as technological importance. Recently, exchange bias (EB) effect has conceived a large attention as it is a quintessential aspect of numerous spintronics devices [1–10]. Initially, EB was investigated in numerous composites made of ferromagnetic(FM) and antiferromagnetic(AF) materials [11, 12] and then engineered into FM/AFM multilayers [8, 13].

Even though EB effect is assumed to be an interfacial phenomenon, it has been observed in single phase materials such as spin-glasses, cluster-glasses, magnetically phase separated systems, core-shell nanostructures, and in homogeneous rare earth inter metallic compounds [14–16]. It is anticipated that in these materials also FM and AFM magnetic orderings coexist within the single phase material and gives rise to EB effect.

In the context of rare-earth intermetallic systems a sign change in EB is observed across the magnetic compensation temperature ( $T_{comp}$ ), i.e., the temperature at which magnetization reversal appears [17, 18]. The origin of the EB in these systems is quite different from that of the bilayers, multilayers and composites. It is conjectured that conduction electron polarization plays a significant role on the emergence of EB in these compounds [17, 18].

Later, the sign reversal of both magnetization and EB field have been also observed in core-shell type AFM nanoparticles [19] and few bulk single phase oxide materials [20–22]. But the exact origin of sign change in EB effect is seems to be not very clear. Hence, in this context, it is essential to explore new materials with similar magnetic configurations to observe the wider validity of sign change of magnetization

and EB across  $T_{comp}$ .

$\text{CoCr}_2\text{O}_4$  shows fascinating temperature and magnetic field dependent magneto-electric properties [23–26]. It is one of the rare materials that exhibits saturated magnetization and electric polarization with small magnetic field. The complex local magnetic ordering is believed to be responsible for the magnetoelectric coupling in this compound [23, 24, 27]. It exhibits a collinear ferrimagnetic ordering at  $T_C \sim 94\text{--}97$  K and then the magnetic ordering changes into a complex incommensurate conical spin-spiral structure at  $T_S \sim 24\text{--}27$  K [28, 29]. This incommensurate conical spin-spiral ordering stabilizes down to the lock-in transition temperature ( $T_L \sim 13\text{--}15$  K), at which it crosses over to a commensurate spin-spiral ordering [30]. The commensurate spin-spiral phase is metastable and undergoes unconventional magnetostructural transitions at high magnetic fields [31, 32]. This results in very rich magnetic phase diagram as a function of temperature and field in this material [31, 32]. All these unique features of this compound are the resultant of the weak geometric magnetic frustration (GMF) which is very much sensitive to nearest neighbour superexchange interactions along B–O–B and A–O–B pathways [28, 29, 33].

These interactions can be tuned with substituting different elements in the place of existed elements. However, the systematic study of substitution effect is lacking in this compound [34–36]. This thesis presents detailed study of how the magnetic properties of  $\text{CoCr}_2\text{O}_4$  get affected with substitution of different elements. We have chosen  $\text{Fe}^{+3}$ ,  $\text{Co}^{+3}$  and  $\text{Al}^{+3}$  to substitute for Cr-site in  $\text{CoCr}_2\text{O}_4$ . Here  $\text{Fe}^{+3}(3d^5)$  possess larger magnetic moment and larger ionic size compared to that of the  $\text{Cr}^{+3}(3d^3)$  ion. On the other hand  $\text{Co}^{+3}(3d^6)$  and  $\text{Al}^{+3}(3d^0)$  consist zero moment, but the effect of  $d^6$  cation is different compared to  $d^0$  on the superexchange interactions via B–O–B and A–O–B chains. We attempt to construct the magnetic phase diagram as a function of different substituted elements.

For a few percent of Fe substitution, we have noticed the novel phenomena of magnetization and EB reversals across  $T_{comp}$ . These are bulk insulating samples, so there is no possibility of presence of conduction electrons and as well as there is no

signature of glassy behavior. We attempt to address the plausible underlying origin of sign change of EB across  $T_{comp}$  in these bulk samples. We know that the non-collinear spin compound  $\text{CoCr}_2\text{O}_4$  displays multiple spin-flop transitions in its temperature dependent magnetic phase diagram. Hence,  $\text{CoCr}_2\text{O}_4$ , along with the different elements substituted samples,  $\text{Co}(\text{Cr}_{1-x}\text{M}_x)_2\text{O}_4$  ( $\text{M} = \text{Fe}^{+3}$ ,  $\text{Co}^{+3}$  and  $\text{Al}^{+3}$ ) are model systems to explore the EB effect across the  $T_S$  and  $T_L$ . We observed noticeable EB effect mainly below the lock-in transition  $T_L$ .

**Chapter 1** briefly introduces the basic aspects of magnetism, multiferroicity and exchange bias effect. Crystal structure of spinels is discussed. It also consists the discussion on various superexchange interactions which give rise to the magnetism in the spinel systems. Influence of GMF on the magnetic properties of spinel compounds is discussed. Various multiferroic properties of  $\text{CoCr}_2\text{O}_4$  have been presented to emphasize the importance of this compound. Detailed summary of exchange bias phenomenon and its origin in different magnetic systems ranging from FM/AFM composites and multilayers to single phase materials is provided. Finally, motivations to undertake this work are also given.

**Chapter 2** summarises various experimental tools and their working principles used to carry out the present work. Sample synthesis techniques such as standard solid state reaction method and sol-gel method are discussed. Powder x-ray diffraction (XRD) technique used for the structural characterization of the prepared samples and Retveld refinement method by using FULL PROF utility software for the confirmation the phase purity of the sample have been discussed in a short note. Scanning electron microscope (SEM) and energy dispersive analysis of X-rays (EDAX) used for probing the microstructure and stoichiometry, respectively, are explained. Differential scanning calorimetry (DSC) and thermal gravimetric analysis (TGA) to shortly understand the sample formation mechanism are presented. Various other commercial magnetometers such as Vibrating Sample Magnetometer (VSM) and Superconducting quantum interference device (SQUID) magnetometer utilized to probe magnetic properties of the samples are also described. The working principle of Quantum Design Physical Properties Measurement System (PPMS) used to measure the thermody-

dynamic properties of the samples is portrayed.

**Chapter 3** deals with the preparation, structural, temperature and magnetic field dependent magnetization, EB effect and thermodynamic properties of  $\text{Co}(\text{Cr}_{1-x}\text{Fe}_x)_2\text{O}_4$ . It is observed that the substituted Fe ions mainly occupy the octahedral site upto  $x \sim 0.11-0.125$ , thereafter it is distributed in both tetrahedral and octahedral sites. For  $x = 0.044-0.11$  samples exhibit magnetization reversal below  $T_{comp}$  under low applied fields. Field induced transitions are noticed across  $T_{comp}$  for large applied field. In the compensated stoichiometry the EB field change sign across  $T_{comp}$ . We ascertain the sign reversal of the exchange bias on the premise of the reorientation of the magnetic moments across the  $T_{comp}$ . In addition, the identification of EB effect below  $T_S$  relates to the presence of non-collinear spin spirals, unveils the richness of physics in the  $\text{Co}(\text{Cr}_{1-x}\text{Fe}_x)_2\text{O}_4$  system. Detailed analysis of thermodynamic properties endorse the understanding of the physical origin of the emergence of EB and the switching of its sign across  $T_{comp}$  and  $T_S$ . Magnetic phase diagram at various levels of substituted Fe concentration is constructed. Influence of metastability on the spin reorientation transition across  $T_{comp}$  is discussed in the form of a field-temperature( $H-T$ ) phase diagram.

**Chapter 4** presents the studies obtained from the Co substituted  $\text{CoCr}_2\text{O}_4$ . Structural and magnetic properties of  $\text{Co}(\text{Cr}_{1-x}\text{Co}_x)_2\text{O}_4$  ( $x = 0.0-0.1$ ) are discussed. In contrast to the Fe substitution, the Co substitution enhances the magnetization. The thermal hysteresis has been observed both across magnetostructural transition( $T_S$ ) and lock-in transition( $T_L$ ). We observed the noticeable EB only below the lock-in transition,  $T_L$ . The value of coercivity also shows the dramatical increase below  $T_L$ . Detailed analysis of the magnetization data with the help of simple LKDM (Lyons, Kaplan, Dwight and Menyuk) model showed that the GMF decreases with increasing the Co concentration, resulting in the enhancement of total magnetization. The noticeable EB only below  $T_L$  is may be due to the reduction in the frustration in the commensurate spin-spiral magnetic ordering below  $T_L$ .

**Chapter 5** is dedicated to describe the structural and magnetic properties of  $\text{Co}(\text{Cr}_{1-x}\text{Al}_x)_2\text{O}_4$  ( $x = 0.0-1.0$ ). Compared to previous two works here the substi-

tuted  $\text{Al}^{+3}$  is in  $3d^0$  configuration with smaller ionic size. This series shows that the magnetization increases enormously upto  $x = 0.5$ , shows kind of soft ferromagnetic nature. Beyond  $x = 0.5$ , it decreases and high Al concentration samples exhibit AFM behavior with weak glassy behavior observed from the magnetic relaxation measurement. Further, magnetic phase diagram is constructed as a function of Al concentration. It is found that low Al concentration samples i.e up to  $x \sim 0.2$  exhibit both the long range ferrimagnetic and the spin-spiral phases. With increasing the Al concentration the volume of the ferrimagnetic phase increases upto  $x = 0.5$  and then decreases. Also seen that the while increasing the Al concentration gradually the non-collinear spin-spiral phase becomes narrow and the weak glassy states started emerging due to the diluted magnetic interactions and the ionic disorder in the pyrochlore Cr-lattice.

**Chapter 6** is devoted for comprehensive summary of the over all work undertaken in the present thesis.

## List of Publications/conf. proceedings

- [1] **R. Padam**, S. Ravi, A.K. Grover, S. Ramakrishnan and D. Pal, Exchange Bias Effect in spin-spiral system  $\text{Co}(\text{Cr}_{1-x}\text{Co}_x)_2\text{O}_4$  ( $x = 0.0-0.1$ ); J. Magn. Magn. Mater. **371** 144–148 (2014).
- [2] **R. Padam**, S. Ravi, and D. Pal, Entanglement of Exchange Bias and Lock-in transition in  $\text{Co}(\text{Cr}_{0.9}\text{Co}_{0.1})_2\text{O}_4$ ; Physica B: Condens. matt. **448**, 191–193 (2014).
- [3] **R. Padam**, Swati Pandya, S. Ravi, A. K. Nigam, S. Ramakrishnan, A. K. Grover and D. Pal, Magnetic compensation effect and phase reversal of exchange bias field across compensation temperature in multiferroic  $\text{Co}(\text{Cr}_{0.95}\text{Fe}_{0.05})_2\text{O}_4$ ; Appl. Phys. Lett. **102**, 112412 (2013).
- [4] **R. Padam**, D. Pal, S. Ravi, S. Ramakrishnan and A. K. Grover, Structural and Magnetic Properties of  $\text{Co}(\text{Cr}_{1-y}\text{Al}_y)_2\text{O}_4$  ( $y = 0.0-0.2$ ) Compounds; J. Supercond. Nov. Magn. **26**, 1607–1610 (2013).
- [5] **R. Padam**, Swati Pandya, S. Ravi, A. K. Grover and D. Pal, Exchange Bias Effect In  $\text{Co}(\text{Cr}_{0.925}\text{Fe}_{0.075})_2\text{O}_4$ ; AIP Conf. Proc. **1512**, 1112 (2013)
- [6] **R. Padam**, Swati Pandya, S. Ravi, A. K. Nigam, S. Ramakrishnan, A. K. Grover, and D. Pal, Multiple switching of exchange bias field due to spin flop/reorientation and field induced anomalies in spin compensation multiferroic compound  $\text{Co}(\text{Cr}_{1-x}\text{Fe}_x)_2\text{O}_4$  (Communicated).
- [7] **R. Padam**, S. Ravi, S. Ramakrishnan, A. K. Grover, and D. Pal, Meta-magnetic transitions and phase diagram of  $\text{Co}(\text{Cr}_{1-x}\text{Fe}_x)_2\text{O}_4$  ( $x = 0.0-1.0$ ); (To be communicated).
- [8] **R. Padam**, S. Ravi, S. Ramakrishnan, A. K. Grover, and D. Pal, Evaluation of magnetic phase in  $\text{Co}(\text{Cr}_{1-x}\text{Al}_x)_2\text{O}_4$  ( $x = 0.0-1.0$ ); (Communicated).

## List of Conference/Workshop Presentations

- [1] International Conference on Magnetic materials & Applications ICMagMA-2014, Dept. Of Physics, Pondicherry University, Pondicherry & Magnetism Society of India, September 15–17, 2014 (abstract accepted)
- [2] International Conference on Strongly Correlated Electron Systems, SCES-2014, Campus Saint Martin d'Hères Grenoble, France July 7–11 2014 (abstract accepted)
- [3] Oral presentation in Research Scholars Work Shop at UGC-DAE Consortium for Scientific Research, Indore (Madhya Pradesh), India during Dec 23-24, 2013.
- [4] International conference on Magnetic materials & Applications MagMA- 2013, Dept. Of Physics, IIT Guwahati & Magnetism Society of India, 5-7 Dec 2013.
- [5] 58<sup>th</sup> DAE Solid State Physics Symposium DAE SSPS 2012, Board of Research in Nuclear Sciences Department of Atomic Energy Government of India.
- [6] 3<sup>rd</sup> National Conference on Advanced Materials, NCAM2013, Processing, Characterization and Applications, PSN College of Engineering & Technology, Tirunelveli, Tamilnadu 23-25 January 2013
- [7] 57<sup>th</sup> DAE Solid State Physics Symposium-DAE SSPS 2012, Board of Research in Nuclear Sciences Department of Atomic Energy Government of India.
- [8] 3<sup>rd</sup> International conference on superconductivity and magnetism, ICSM-2012, 29 April–4 May 2012, İstanbul, Turkey.
- [9] 56<sup>th</sup> DAE Solid State Physics Symposium DAE SSPS 2011, Board of Research in Nuclear Sciences Department of Atomic Energy Government of India.
- [10] National conference on Magnetic materials & Applications MagMA-2011, S.N. Bose National Centre for Basic Sciences, Kolkata & Magnetism Society of India.



# Acknowledgements

Numerous people have played important role in the successful completion of the work undertaken in this dissertation and I will try my best to thank all of them.

Fist of all I would like to begin by thanking my thesis supervisors, Dr. Dilip Pal and Prof. S. Ravi for giving me an opportunity to work under their guidance. Right from the very beginning to the submission of this thesis their constant motivation, inspiration, encouragement and support never let me down. Their friendly nature towards me has allowed me even to choose my research topic myself. The freedom they have given allowed me to read many concepts and helped me to understand my research problem deeply. They understood my soft nature and never showed their anger towards me, I am really indebted for them in this regard. During the course of my doctoral research I have not only learned the physics from them but also so many personal things. I am also extremely grateful for their patience and help in revising manuscripts, annual progress reports and my thesis in great detail. I hope they extend their kind support in the upcoming future as well.

I express my sincere thanks to my doctoral committee chairman Dr. Subhradip Ghosh and members Dr. D. Pamu & Prof. Gopal Das for their valuable suggestions and reviewing my doctoral research, that helped me to improve the quality of understanding of the problem. Especially I am grateful to Dr. Subhradip Gosh for accepting our request to perform theoretical calculations to address some of the issues have risen from my experimental study. I am also faithful to Prof. Gopal Das and the other group members for allowing me to carry out my sample preparation in the chemistry laboratory, indeed there only I have started my project. I also acknowledge Dr. D. Pamu for availing the experimental facilities such as LCR meter.

Its my pleasure to thank all the faculty members of Physics Department, IIT Guwahati for their friendly nature in teaching me various physics concepts during the course work time as well as through out my Ph.D time. My special thanks to Dr. Subhash Thota for his valuable suggestions and clearing various solid state physics problems.

I extend my sincere regards to present and former head of the department Prof.

Saurabh Basu and Prof. S. Ravi for their generous support for attending conferences and schools during Ph.D period and providing me various departmental facilities.

I will take this opportunity to express my sincere gratitude from the bottom of my heart to Prof. A. K. Grover (Vice Chancellor of Punjab University) and Prof. Ramakrishnan of Tata Institute of Fundamental Research(TIFR), Mumbai for providing me golden opportunity to visit TIFR, and availing various experimental facilities. Its my pleasure to say that the TIFR visits have changed my attitude and the way of approaching towards the research. Specially I am indebted to Prof. A. K. Grover for considering me as his student and teaching me various physics concepts in magnetism. He is role model of my research career. His dynamic way of thinking about the problem, enthusiasm towards research, dedication at this old age have inspired me a lot. Discussion with him always pumps me up and reinforce my curiosity towards research. I will never forget the wonderful days I worked with him. I am also grateful to Prof. Thamizhavel, Prof. A. K. Nigam & Prof. P. L. Paulose of TIFR for availing me heat capacity measurements, high temperature furnaces and 14 Tesla VSM.

Its my honour to devote special thanks to all my teachers from schooling to post graduate, A. Linga Reddy (M.Sc, M.ed & Rtd. MEO) Sir, Late Nagabushanam Sir, S. Narayana (M.ed) Sir, J. Anjaiah(Telugu pandit) Sir, Rajesham Sir, Ravish Kumar Sir, Rajamouly(M.Sc Physics), Naresh Sir(MFCA), Prof. A. Ramakant and Prof. K. Altaf for motivating and made me realize who am I and what I am capable of doing. Especially, A. Linga Reddy Sir if you didn't inspire me I could have ended up my career in the village of Thatipally. I hope your blessings always guide me in the right direction.

I thank Dr. Sidananda Sarma, Mr. Chandan and all other scientific officers of Central instrumental facilities for their help in performing various experiments.

I want to thank Dr. Samantaray, Dr. Sangeetha, Dr. Sunita, Dr. B. Dutta, Dr. Paoulomy, Dr. V. Meera, Dr. Jaheer, Dr. Vindyavasini Dr. Ramesh & all other seniors friends for their advices and kind help in various aspects.

Its my pleasure to thank all friends, Suresh, P. C, Ram, Santhosh, Tribedi, Munendhar, Enam, Laxman, Ramesh, Kishore, Deepa, Abijit, Partha, Apu, Sathi, Bipul, Ranjan, Mahi, Ranga, Anil, Junmony, Akilesh, Shyni, Vibuthi, Gone, Bagaban, Sanjeev, Deep and all other colleagues and juniors for establishing friendly environment in the department of physics as well as in the campus. Especially my personal thank is devoted to Suresh, P. C, Ram and Santhosh for their help, various discussions and debates on physics concepts, obviously that helped me to strengthen my understanding of Physics.

I am also thankful to Surya, Emorkay, Harish for helping me in various software and computer related problems. Abijit, Partha, Ruhit, Loknath, Pradip thanks guys

for your funny moments in the hostel due to which the course of 5 years just melt like a piece of ice. I will carry this happy moments to the rest of my life.

I deeply admire to express my sincere thanks to Dr. Swati, Anil, Ulhas, Bhanu, Pranab, Ohm, Arvind, Mr. Devendra, Mr. Patade for their help in various experiments and making my TIFR visits successful. Even they postponed their experimental slots to make sure my work is done.

I adore my friends from school to post graduate, Shekhar Anna, Thiru, KRK, Late Srihari, Chiru, Srinu, KLKN, Raju, B. Rajender, B. Srinu, Ravi, Pundra, Lara, B. Venkatesh, Bandari, Nagi, Kish, Jaggu, N. Venky, Anush, Palli, S. Rajender, Anil, GPB, Srikanth, Venktramulu, Raams, Nagaraju, Chari, Puri, Swarna, Kanakam, Sra-vanthi, Bollam, Chanti, Chandu, and all other. You guys are really amazing.

I also acknowledge the well-wishers from my beautiful village, K. Rajanna, N. G. Reddy, A. Kishan, G. Lakshminarayana, R. Ravi, and many others for their encouragement at each and step of my studies.

I extend my acknowledge to various software developers such as FULLPROF program, Rietveld refinement technique, Origin software, Vesta, Mathematica, Matlab and all other research analysis tools. Without all these I know how painful is researcher life is. Thank you very much for your pains in developing them.

I am also grateful to MHRD, India for the financial assistance in the form of JRF and SRF during my doctoral research period. And of course I thank IIT Guwahati for assisting me to peruse my Ph.D degree, I felt this place as my second home.

Last but not least, my parents (Amma-Nanna; Gangaraju-Raja Reddy), brother Anee, Grany(Gauramma) and all other family members for making my personal life lovable, affectionable. Personal emotions from you always remind my responsibilities in studies. It is your love that always balances my personal and professional life. By looking at your patience and hard work I always think that if I work 5–10 % of you I can achieve any thing in my professional life. Amma-Nanna, you are my role model, I feel proud to be son of you!! I am indebted to you for keeping faith in me and allowing me to study what ever I want. If the concept of God is believed to true you are my first God. I am thankful to you Anee for sharing the agricultural burden along with the parents, due to this I am able to put my 100 % effort on studies. Well, finally I started feeling wonderful towards love and the understanding nature of newly joining member of our cute family. I hope you all will continue this momentum in my upcoming future as well !!!!!

Sincerely,  
**Padam Rajender**



# Contents

|   |           |
|---|-----------|
| List of Figures   | xxiii     |
| List of Tables  | xxxii     |
| <b>1 Introduction</b>   | <b>1</b>  |
| 1.1 Basic aspects of magnetism . . . . .  | 2         |
| 1.2 Structural and magnetic properties of $\text{CoCr}_2\text{O}_4$ . . . . .             | 5         |
| 1.2.1 Crystal structure of $\text{CoCr}_2\text{O}_4$ . . . . .                            | 5         |
| 1.2.2 Magnetic frustration due to geometric constrains . . . . .                          | 7         |
| 1.2.3 Magnetic phase diagram of $\text{CoCr}_2\text{O}_4$ . . . . .                       | 13        |
| 1.2.4 Other ferroic properties in $\text{CoCr}_2\text{O}_4$ . . . . .                     | 16        |
| 1.3 Exchange bias effect . . . . .  | 19        |
| 1.3.1 Tunable exchange bias . . . . .   | 23        |
| 1.4 Motivation of the thesis . . . . .  | 28        |
| <b>2 Experimental Techniques</b>  | <b>31</b> |
| 2.1 Sample Preparation . . . . .  | 31        |
| 2.1.1 Solid state reaction . . . . .  | 31        |
| 2.1.2 Sol-gel method . . . . .  | 32        |
| 2.2 Measurement Techniques . . . . .  | 33        |
| 2.2.1 X-ray Diffraction . . . . .   | 33        |
| 2.2.2 Scanning electron microscopy . . . . .  | 35        |
| 2.2.3 Differential scanning calorimetry . . . . .   | 36        |
| 2.2.4 Superconducting Quantum Interference Device (SQUID) mag-<br>netometer . . . . .     | 37        |
| 2.2.5 Physical Property Measurement System . . . . .                                      | 39        |
| <b>3 Studies in <math>\text{Co}(\text{Cr}_{1-x}\text{Fe}_x)_2\text{O}_4</math> series</b> | <b>41</b> |
| 3.1 Introduction . . . . .  | 41        |

## CONTENTS

---

|          |   |            |
|----------|---|------------|
| 3.2      | Experimental details . . . . .  | 42         |
| 3.3      | Results . . . . .   | 43         |
| 3.3.1    | X-ray diffraction studies . . . . .   | 43         |
| 3.3.2    | Temperature and field dependent magnetic properties . . . . .                           | 48         |
| 3.3.3    | Magnetic compensation and field induced transitions . . . . .                           | 51         |
| 3.3.4    | Exchange bias effect . . . . .  | 56         |
| 3.3.5    | Thermodynamic properties . . . . .  | 64         |
| 3.3.6    | Magnetic relaxation properties . . . . .  | 68         |
| 3.4      | Discussion . . . . .  | 70         |
| 3.4.1    | Magnetic phase diagram . . . . .  | 79         |
| 3.5      | Summary . . . . .   | 83         |
| <b>4</b> | <b>Studies in <math>\text{Co}(\text{Cr}_{1-x}\text{Co}_x)_2\text{O}_4</math> series</b> | <b>85</b>  |
| 4.1      | Introduction . . . . .  | 85         |
| 4.2      | Experimental details . . . . .  | 86         |
| 4.3      | Results and Discussions . . . . .   | 87         |
| 4.3.1    | Structural properties . . . . .   | 87         |
| 4.3.2    | Temperature and field dependent magnetic properties . . . . .                           | 90         |
| 4.3.3    | Exchange bias effect . . . . .  | 99         |
| 4.4      | Summary . . . . .   | 102        |
| <b>5</b> | <b>Studies in <math>\text{Co}(\text{Cr}_{1-x}\text{Al}_x)_2\text{O}_4</math> series</b> | <b>105</b> |
| 5.1      | Introduction . . . . .  | 105        |
| 5.2      | Experimental details . . . . .  | 106        |
| 5.3      | Results . . . . .   | 107        |
| 5.3.1    | Structural properties . . . . .   | 107        |
| 5.3.2    | Magnetic properties . . . . .   | 111        |
| 5.3.2.1  | Thermomagnetic and isothermal magnetization curves                                      | 111        |
| 5.3.2.2  | Magnetic relaxation . . . . .   | 120        |
| 5.4      | Discussion . . . . .  | 122        |
| 5.5      | Summary . . . . .   | 126        |
| <b>6</b> | <b>Conclusions</b>  | <b>127</b> |
|          | <b>References</b>   | <b>131</b> |

# List of Figures

|     |   |    |
|-----|---|----|
| 1.1 | Spinel crystal structure of $\text{CoCr}_2\text{O}_4$ showing edge-shared $\text{CrO}_6$ octahedra (reddish pink) and corner shared $\text{CoO}_4$ tetrahedra (light blue) and $\text{CrO}_6$ octahedra in the 3 dimensional space. Balls indicate different ions of $\text{CoCr}_2\text{O}_4$ . Bond angles of $\text{Cr-O-Cr}$ and $\text{Co-O-Cr}$ paths are also shown. . . . . | 6  |
| 1.2 | (a) Antiferromagnetically arranged neighbouring moments residing on the corners of square. (b) Failure of all pairwise AFM interactions for the moments reside on the corners of a triangle. Here the circles indicate magnetic ions. . . . .   | 9  |
| 1.3 | (b1)–(b6) Six possible magnetic configurations for the moments on the corners of a triangle if we consider simple collinear alignment of AFM moments. But in general much more complicated situations can be realized. . . . .  | 9  |
| 1.4 | Geometric frustration in (a) 1D diamond chain, (b) 2D triangular lattice, (c) 2D Kagomé lattice and (d) the 3D pyrochlore lattice (corner shared tetrahedra) [53, 56, 57]. . . . .  | 10 |
| 1.5 | Schematic diagram showing the relation between the magnetic frustration and magnetic configuration in various spinels as a function of LKDM parameter ‘ $u$ ’. . . . .  | 12 |
| 1.6 | Pyrochlore B sub-lattice structure of $\text{CoCr}_2\text{O}_4$ viewed along the conical spin-spiral modulation direction [110] (denoted as the x axis). The circles with slanted arrows indicate the conical spiral plane of the Co, Cr1 and Cr2 moments [23, 28]. . . . .   | 13 |
| 1.7 | (a) $H$ - $T$ phase diagram of $\text{CoCr}_2\text{O}_4$ based on magnetization and specific-heat measurements[31]. (b) Low-temperature( $T \leq T_L$ ) commensurate spin-spiral $H$ - $T$ phase diagram of $\text{CoCr}_2\text{O}_4$ derived from the ultrasound propagation measurements [32]. . . . .  | 15 |

## LIST OF FIGURES

---

|      |   |    |
|------|---|----|
| 1.8  | (a) Temperature dependence of electric polarization $P$ along the $[\bar{1}10]$ direction, and magnetization $M$ along the $[001]$ direction in $\text{CoCr}_2\text{O}_4$ . (b) and (c) are the field dependence of electric polarization, $P$ , along the $[\bar{1}10]$ direction, and magnetization $M$ along the $[001]$ at 20 K and 10 K, respectively. Here, the magnetic field is applied along the $[001]$ [23].   | 17 |
| 1.9  | Schematic sketch of (a) normal, (b) left side shifted and (c) right side shifted $M$ - $H$ loops; (b) and (c) illustrate the presence of exchange bias.   | 19 |
| 1.10 | Schematic block diagram of the magnetic configurations of FM and AFM materials at the FM–AFM interface. (i) In the temperature range $T_N < T < T_C$ when the sample is cooled in a field for which the FM moments order fully. (ii)–(v) are the magnetic configurations of the FM and AFM materials at various stages of an exchange biased $M$ - $H$ loop measured below $T_N$ . Length and direction of the arrow representing $H$ , indicate the magnitude and direction of the the applied magnetic field at different states of the loop. . . . . | 21 |
| 1.11 | $H_{FC}$ dependent EB field of $\text{FeF}_2/\text{Fe}$ multilayeres with $\text{FeF}_2$ grown at $250^\circ\text{C}(\nabla)$ and $300^\circ\text{C}(\circ)$ . Inset: FC $M$ - $H$ loops for $H_{FC} = 2 \text{ kOe}(\circ)$ and $H_{FC} = 70 \text{ kOe}(\bullet)$ [85]. . . . .   | 24 |
| 1.12 | (a) Temperature dependences of (a) the effective coercive field, $H_C^{eff}$ and (b) the EB field $H_{EB}$ in a single crystalline $\text{Nd}_{0.75}\text{Ho}_{0.25}\text{Al}_2$ . Schematic diagram of the orientation of the different sub-components of magnetization with respect to the applied field (c) for the FM–AFM multilayers and (d) for $\text{Nd}_{0.75}\text{Ho}_{0.25}\text{Al}_2$ single crystal at $T > T_{comp}$ and $T < T_{comp}$ [17].   | 27 |
| 2.1  | Illumination of the Bragg's law in case of set of two parallel planes. . .  | 34 |
| 2.2  | Block diagram showing various physical phenomena occur when an accelerated beam of electrons is impinged onto the specimen. . . . .   | 35 |
| 2.3  | Block diagram of magnetic signal detecting hardware system in a Quantum Design SQUID magnetometer. . . . .  | 37 |
| 3.1  | X-ray diffraction patterns of $\text{Co}(\text{Cr}_{1-x}\text{Fe}_x)_2\text{O}_4$ samples for various values of $x$ recorded at room temperature on the powdered samples. . . .   | 44 |
| 3.2  | Observed and fitted powder XRD patterns of $\text{CoCr}_2\text{O}_4$ , $\text{Co}(\text{Cr}_{0.95}\text{Fe}_{0.05})_2\text{O}_4$ , $\text{Co}(\text{Cr}_{0.5}\text{Fe}_{0.5})_2\text{O}_4$ and $\text{CoFe}_2\text{O}_4$ samples. For the better clarity of the Bragg positions, difference curve between observed and fitted profiles is shifted downward. . . . .   | 45 |

|      |  |    |
|------|--|----|
| 3.3  | (a) Variation of lattice parameter ‘ $a$ ’ and the coordinate ( $z, z, z$ ) of oxygen ion with Fe concentration ‘ $a$ ’ in $\text{Co}(\text{Cr}_{1-x}\text{Fe}_x)_2\text{O}_4$ . (b) Variation of A–O–B and B–O–B bond angles. (c) Variation of A–O and B–O bond lengths. Here, vertical bars indicate the error in ‘ $a$ ’ due to instrumental broadening and the fitting of data in case of other parameters it only due to the error in fitting the data. . . . . | 46 |
| 3.4  | SEM images and EDAX spectra of $\text{Co}(\text{Cr}_{1-x}\text{Fe}_x)_2\text{O}_4$ samples. . . . .  | 47 |
| 3.5  | Temperature dependent magnetization of $\text{Co}(\text{Cr}_{1-x}\text{Fe}_x)_2\text{O}_4$ measured in ZFC and FCW modes for the applied field of $H = 1$ kOe. Here $T_C$ , $T_S$ , $T_{comp}$ and $T_R$ , respectively, are long range FIM transition, magnetostructural transition, compensation temperature and the temperature at which the magnetization show dip, respectively. . . . .  | 49 |
| 3.6  | Field dependent magnetization of $\text{Co}(\text{Cr}_{1-x}\text{Fe}_x)_2\text{O}_4$ samples measured at 5 K measured after cooling the sample in zero field. . . . .  | 50 |
| 3.7  | Coercive field and saturation magnetization of $\text{Co}(\text{Cr}_{1-x}\text{Fe}_x)_2\text{O}_4$ at 5 K. . . . .   | 51 |
| 3.8  | Temperature dependent magnetization curves of $\text{Co}(\text{Cr}_{1-x}\text{Fe}_x)_2\text{O}_4$ samples measured in FCC mode for the applied field of (a) nominal zero ( $\sim 10$ Oe) and (b) 70 kOe. Insets (i) and (ii) of (a) are enlarged views of compensation points of $x = 0.044$ and $x = 0.11$ samples, respectively. . . . .   | 52 |
| 3.9  | Temperature dependent $M_{FCC}$ of (a) $\text{Co}(\text{Cr}_{0.95}\text{Fe}_{0.05})_2\text{O}_4$ , (b) $\text{Co}(\text{Cr}_{0.925}\text{Fe}_{0.075})_2\text{O}_4$ and (c) $\text{Co}(\text{Cr}_{0.9}\text{Fe}_{0.1})_2\text{O}_4$ samples under various applied fields ranging from 100 Oe to 70 kOe (140 kOe for $x = 0.075$ ). In all the panels, $T_C$ , $T_{comp}$ , $T_S$ and $T_R$ denote different transition temperatures. . . . .                          | 53 |
| 3.10 | Applied field dependence of $T_{comp}$ and $T_R$ for $\text{Co}(\text{Cr}_{1-x}\text{Fe}_x)_2\text{O}_4$ samples extracted from FCC magnetization while applied field varying from 10 Oe to 70 kOe (140 kOe in case of $x = 0.075$ ). . . . .  | 54 |
| 3.11 | Temperature dependence of $M_R$ (the magnetization obtained after cooling the sample under the field of 50 kOe from 300 K to 2 K, then drooping field the field to $\sim 50$ Oe) measured under the field of 50 Oe, while warming from 2 K along with the field cooled warming magnetization ( $M_{FCW}(T)$ ) measured in the same field ( $\sim 50$ Oe). . . . .  | 55 |
| 3.12 | (a)-(i) 70 kOe field cooled $M-H$ loops of $\text{Co}(\text{Cr}_{0.95}\text{Fe}_{0.05})_2\text{O}_4$ sample at various temperatures. The linear trend of $M-H$ loop in the vicinity of $T_{comp} \approx 43.8$ K indicate the quasi AFM behaviour of the sample. . . . .   | 57 |
| 3.13 | (a)-(f) Enlarged portions of 70 kOe FC $M-H$ loops of $\text{Co}(\text{Cr}_{0.95}\text{Fe}_{0.05})_2\text{O}_4$ sample in the vicinity of $T_{comp} \approx 43.8$ K recorded by implementing the procedure explained in the text. . . . .  | 59 |

## LIST OF FIGURES

---

- 3.14 (a)-(f) Enlarged portions of  $M$ - $H$  loops of  $\text{Co}(\text{Cr}_{0.925}\text{Fe}_{0.75})_2\text{O}_4$  sample in the vicinity of  $T_{comp} \approx 67.8$  K. . . . . 60
- 3.15 Temperature dependence of  $H_c^{eff}$ ,  $H_{EB}$  and  $M_{EB}$  extracted from 70 kOe FC  $M$ - $H$  loops of  $\text{Co}(\text{Cr}_{0.95}\text{Fe}_{0.5})_2\text{O}_4$  sample (panels (a), (b) and (c)),  $\text{Co}(\text{Cr}_{0.925}\text{Fe}_{0.75})_2\text{O}_4$  sample (panels (d), (e) and (f)) and that of  $\text{Co}(\text{Cr}_{0.9}\text{Fe}_{0.1})_2\text{O}_4$  sample (panels (g), (h) and (i)), respectively. The top x-scale of (a), (d) and (g) panels shows the reduced temperature( $t$ ). The collapse in  $H_c^{eff}$  in the vicinity of  $T_{comp}$  can be seen to happen in the window  $-0.1 \leq t \leq 0.1$ . . . . . 61
- 3.16  $H_{FC}$  dependence of  $H_{EB}$  of  $\text{Co}(\text{Cr}_{0.925}\text{Fe}_{0.075})_2\text{O}_4$  sample at (a) 69 K (i.e., well above  $T_{comp}$ ) and (b) 65 K (i.e., well below  $T_{comp}$ ). Inset of (b) is the  $H_{EB}$  versus  $H_{FC}$  at 65 K on log scale. (c) and (d) show an enlarged portion of different FC  $M$ - $H$  loops at 69 K and 65 K, respectively. 62
- 3.17 Temperature dependence of  $M_{rem}$  and  $\chi_{hf}$  computed from 70 kOe FC  $M$ - $H$  loops for  $\text{Co}(\text{Cr}_{0.95}\text{Fe}_{0.5})_2\text{O}_4$  sample(panels (a) and (b)),  $\text{Co}(\text{Cr}_{0.925}\text{Fe}_{0.075})_2\text{O}_4$  sample(panels (c) and (d)) and that of  $\text{Co}(\text{Cr}_{0.9}\text{Fe}_{0.1})_2\text{O}_4$  sample(panels (e) and (f)), respectively. . . . . 63
- 3.18 (a) and (b)  $C_P(T)$  of  $\text{Co}(\text{Cr}_{0.95}\text{Fe}_{0.5})_2\text{O}_4$  and  $\text{Co}(\text{Cr}_{0.925}\text{Fe}_{0.75})_2\text{O}_4$  samples, respectively, in zero magnetic field, under the applied field of 50 kOe & 90 kOe. Insets (i) and (ii) of in both the panels are the enlarged view of  $C_P(T)$  across the  $T_S$  and  $C_P(T)/T$  across  $T_{comp}$ , respectively. . 65
- 3.19 (a) and (b)  $C_m(T)$ (see the text for definition) of  $\text{Co}(\text{Cr}_{0.95}\text{Fe}_{0.5})_2\text{O}_4$  and  $\text{Co}(\text{Cr}_{0.925}\text{Fe}_{0.75})_2\text{O}_4$  samples, respectively, across their corresponding  $T_{comp}$  for various applied fields. (c) and (d) depict the jump in magnetic entropy  $\Delta S_{mag}(T)$  across the  $T_{comp}$  under various applied fields. Inset of (c) is the change in the height of  $\Delta S_{mag}(T)$  across  $T_{comp}$  as function of applied field. Here error is smaller than size of the symbols given in the plots. . . . . 66
- 3.20 (a) and (b) Time dependent magnetization of  $\text{Co}(\text{Cr}_{0.925}\text{Fe}_{0.75})_2\text{O}_4$  sample at 69 K and 65 K, respectively. (c) Magnetization measured in FCC (with two stops at 69 K & 65 K) and FCW mode together with the  $H_{EB}(T)$  across  $T_{comp}$ . . . . . 69
- 3.21 Schematic block diagram of the magnetic configurations with respect to applied field in the two temperature regions  $T_S < T < T_{comp}$  and  $T_{comp} < T < T_C$  for small and large applied fields.  $\mu_{Co}$ ,  $\mu_{Cr1}$ ,  $\mu_{Cr2}$  and  $\mu_{Fe}$  are longitudinal components of magnetic moments of  $\text{Co}^{+2}$ ,  $\text{Cr}^{+3}(1)$ ,  $\text{Cr}^{+3}(2)$  and  $\text{Fe}^{+3}$  ions, respectively, along applied field.  $\mu_A$  and  $\mu_B$  are the resultant moments of A and B-sites, respectively. . . . . 71

|      |  |    |
|------|--|----|
| 3.22 | Schematic block diagram of the magnetic configurations with respect to applied field to explain the EB effect in the two temperature regions $T_S < T < T_{comp}$ and $T_{comp} < T < T_C$ caused by high field cooling. . . .   | 72 |
| 3.23 | $M$ - $H$ loops of $x = 0.05, 0.075$ & $0.1$ samples at their compensation temperature $T \sim T_{comp}$ . Inset depicts the $M$ - $H$ loops in the full scale. . .  | 77 |
| 3.24 | Magnetic phase digram of $\text{Co}(\text{Cr}_{1-x}\text{Fe}_x)_2\text{O}_4$ . For $T \geq T_C$ all the samples exhibit paramagnetic (PM) state. $T_S$ separates the collinear FIM ordering and that of the non-collinear spin-spiral ordering. $T_L$ separates the incommensurate spin-spiral and that of commensurate spin-spiral phase. $T_{comp}$ is the boundary between the B-site and A-site dominated regimes of the series. . . . . | 80 |
| 3.25 | $M(T)$ curves of $\text{Co}(\text{Cr}_{0.9}\text{Fe}_{0.1})_2\text{O}_4$ sample measured in ZFC, FCC and FCW modes for the applied field of 1 kOe. Here, $T_{SR}^{FCC}$ and $T_{SR}^{FCW}$ are spin reorientation transitions in FCC and FCW curve, respectively. . .  | 81 |
| 3.26 | Field-temperature( $H$ - $T$ ) phase digram of $\text{Co}(\text{Cr}_{1-x}\text{Fe}_x)_2\text{O}_4$ for $x = 0.05, 0.075$ and $0.1$ samples. Different transition temperatures as a function of applied field are taken from the temperature dependent magnetization in different modes as shown in the Fig.3.25. . . . .   | 82 |
| 4.1  | Powder XRD patterns of $\text{Co}(\text{Cr}_{1-x}\text{Co}_x)_2\text{O}_4$ samples measured at room temperature. . . . .   | 87 |
| 4.2  | Experimental and fitted powder XRD patterns of $\text{Co}(\text{Cr}_{0.9}\text{Co}_{0.1})_2\text{O}_4$ sample. Inset shows the variation of lattice parameter ' $a$ ' with 'Co' concentration ' $x$ ' in $\text{Co}(\text{Cr}_{1-x}\text{Co}_x)_2\text{O}_4$ . Here, vertical bars indicate the error in ' $a$ ' due to instrumental broadening and fitting the data. Solid line is just guide to the eye. . . . .                           | 88 |
| 4.3  | SEM images(left panel) and EDAX spectra (right panel) of $\text{Co}(\text{Cr}_{1-x}\text{Co}_x)_2\text{O}_4$ samples. . . . .  | 89 |
| 4.4  | DSC and TG plots of (a) $x = 0.0$ and (b) $x = 0.1$ samples measured in the air environment. . . . .   | 90 |
| 4.5  | Temperature dependent magnetization curves of $\text{Co}(\text{Cr}_{1-x}\text{Co}_x)_2\text{O}_4$ samples measured in FCC mode for the applied field of nominal zero ( $\sim 10$ Oe) and ZFC, FC modes under the applied field of $H = 1$ kOe. Inset of (a) shows the the variation of $M_{max}/M_{min}$ and $M_{3K}/M_{min}$ as a function Co concentration(see text for details). . . . .  | 92 |

## LIST OF FIGURES

---

|      |   |     |
|------|---|-----|
| 4.6  | (a), (b) and (c) enlarged views of the FCC & FCW magnetization curves across different low temperature transitions of $x = 0.0$ , $x = 0.05$ and $x = 0.1$ samples, respectively. Whereas (d), (e) & (f) temperature dependent $dM/dT$ curves of $x = 0.0$ , $x = 0.05$ and $x = 0.1$ samples, respectively. . . . .  | 93  |
| 4.7  | (a) and (b) are the isothermal magnetization loops of $\text{Co}(\text{Cr}_{1-x}\text{Co}_x)_2\text{O}_4$ samples at 5 K and 75 K, respectively, measured after zero-field cooling from above $T_C$ . . . . .   | 94  |
| 4.8  | Temperature dependent of ZFC magnetization curve of $x = 0.0$ sample measured after cooling the sample in positive and negative remanent field. . . . .   | 95  |
| 4.9  | Fitting of Néel model to the paramagnetic susceptibility(left scale) and inverse susceptibility(right scale) of $\text{Co}(\text{Cr}_{1-x}\text{Co}_x)_2\text{O}_4$ samples measured in ZFC mode. . . . .   | 96  |
| 4.10 | (a) and (b), respectively, are the enlarged portions 70 kOe FC $M-H$ loops of loops of $x = 0.05$ and $0.1$ samples at 3 K, 5 K & 30 K . . . . .  | 99  |
| 4.11 | Main panels of (a), (b) & (c) are the temperature dependence of EB field (left scale) and vertical shift in the $M-H$ loop(right scale) for $\text{CoCr}_2\text{O}_4$ , $\text{Co}(\text{Cr}_{0.95}\text{Co}_{0.05})_2\text{O}_4$ & $\text{Co}(\text{Cr}_{0.9}\text{Co}_{0.1})_2\text{O}_4$ samples, respectively. Insets in all the panels are the temperature dependent effective coercive field of the respective samples. . . . . | 100 |
| 5.1  | Powder XRD patterns of selected samples of the $\text{Co}(\text{Cr}_{1-x}\text{Al}_x)_2\text{O}_4$ series measured at room temperature. . . . .   | 107 |
| 5.2  | Experimental and fitted powder XRD patterns of (a) $\text{CoCr}_2\text{O}_4$ , (b) $\text{Co}(\text{Cr}_{0.5}\text{Al}_{0.5})_2\text{O}_4$ and (c) $\text{CoAl}_2\text{O}_4$ samples by using Rietveld refinement technique with the help of FULL PROF program. . . . .   | 108 |
| 5.3  | Variation of (a) lattice parameter ' $a$ ' and (b) oxygen ion coordinate as a function of 'Al' concentration ' $x$ '. Here, vertical bars in (a) indicate the error in ' $a$ ' due to instrumental broadening and fitting the data. Solid line is the straight line fit to the data to illustrate the Vegard law. . . . .   | 109 |
| 5.4  | SEM images of (left panels) and EDAX spectra (right panels) of $\text{Co}(\text{Cr}_{1-x}\text{Al}_x)_2\text{O}_4$ samples. . . . .   | 110 |
| 5.5  | DSC and TGA plots of (a) $x = 0.0$ and (b) $x = 0.5$ samples measured in the air environment. . . . .   | 111 |

|      |  |     |
|------|--|-----|
| 5.6  | Temperature dependent magnetization curves of $\text{Co}(\text{Cr}_{1-x}\text{Al}_x)_2\text{O}_4$ samples measured in FCC mode for the applied $\sim 10$ Oe and ZFC, FCW modes under the applied field of $H = 1$ kOe. Inset of (i) shows the enlarged view of the ordering temperature of the $\text{CoAl}_2\text{O}_4$ sample. . . . .   | 112 |
| 5.7  | Temperature dependent ZFC and FCW magnetization curves of $\text{Co}(\text{Cr}_{0.9}\text{Al}_{0.1})_2\text{O}_4$ sample under the various applied fields. . . . .   | 113 |
| 5.8  | (a)–(i) Isothermal magnetization loops of $\text{Co}(\text{Cr}_{1-x}\text{Al}_x)_2\text{O}_4$ samples at 5 K. . . . .  | 115 |
| 5.9  | Enlarged portion of isothermal magnetization loops of $\text{Co}(\text{Cr}_{0.2}\text{Al}_{0.8})_2\text{O}_4$ sample at 5 K and 13 K. . . . .  | 116 |
| 5.10 | (a), (b) and (c), respectively, the coercive field, saturation magnetization and remanent magnetization of $\text{Co}(\text{Cr}_{1-x}\text{Al}_x)_2\text{O}_4$ as a function of ‘Al’ concentration. . . . .  | 117 |
| 5.11 | (a)–(c) Fitted and experimental inverse paramagnetic susceptibility(right scale) and paramagnetic susceptibility(left scale) of $\text{Co}(\text{Cr}_{1-x}\text{Al}_x)_2\text{O}_4$ samples for $x \leq 0.8$ to the Néel two sub-lattice model of FIM materials given in the eq.5.1. (d) Modified Curie-Weiss fit (eq.5.2) to the data of $\text{CoAl}_2\text{O}_4$ sample. . . . .  | 118 |
| 5.12 | (a) Variation of experimental and calculated effective magnetic moment as a function of ‘Al’ concentration. (b) Curie-Weiss temperature as a function of Al concentration. (c) is the variation of frustration index $f \sim  \Theta /T_C$ with Al concentration $x$ . . . . .   | 119 |
| 5.13 | Variation of the magnetization of $\text{Co}(\text{Cr}_{0.4}\text{Al}_{0.6})_2\text{O}_4$ sample as a function of time at 5 K. . . . .   | 121 |
| 5.14 | Calculated and observed value of magnetization of $\text{Co}(\text{Cr}_{1-x}\text{Al}_x)_2\text{O}_4$ as a function of Al concentration. . . . .   | 122 |
| 5.15 | Magnetic phase diagram of $\text{Co}(\text{Cr}_{1-x}\text{Al}_x)_2\text{O}_4$ . $T_C/T_N/T_S/T_L$ represent FIM/AFM/magneto-structural/lock-in transition temperatures. Shading of the orange colour in the combined phase of long range FIM & short range spin-spiral phase indicates that this phase gradually decreases and finally becomes AFM, i.e., $T_C$ becomes $T_N$ as the contribution from B-site vanishes for $\text{CoAl}_2\text{O}_4$ . . . . . | 123 |



# List of Tables

- 4.1 Parameters obtained from the analysis of the paramagnetic susceptibility of  $\text{Co}(\text{Cr}_{1-x}\text{Co}_x)_2\text{O}_4$  samples. Here exchange interactions  $J_{AA}$ ,  $J_{AB}$  and  $J_{BB}$  are average values of NN superexchange interactions. . . . . 98
- 5.1 Parameters obtained from the analysis of the paramagnetic susceptibility of  $\text{Co}(\text{Cr}_{1-x}\text{Al}_x)_2\text{O}_4$  samples. Here exchange interactions  $J_{AA}$ ,  $J_{BB}$  and  $J_{AB}$  are average values of NN superexchange interactions. . . . . 120



## List of abbreviations/symbols

- FM — Ferromagnetic  
AFM — Antiferromagnetic  
FIM — Ferrimagnetic  
 $T_C$  — Curie temperature  
 $T_N$  — Néel temperature  
 $E$  — Magnetic exchange energy  
 $J_{ij}$  — Superexchange integral  
 $S_i$  — Spin moment  
RKKY — Ruderman-Kittel-Kasuya-Yosida  
 $\chi$  — Magnetic susceptibility  
 $T$  — Temperature  
 $C$  — Curie constant  
 $\Theta/\Theta'$  — Curie-Weiss temperatures of sub lattices  
 $N$  — Avagadro number =  $6.023 \times 10^{23}$   
 $\mu_{eff}$  — Effective paramagnetic moment  
 $\mu_B$  — Bohr magneton  
 $k_B$  — Boltzman constant  
 $g$  — Lande g-factor  
 $J$  — Total angular momentum number  
 $L$  — Orbital angular momentum number  
 $S$  — Spin angular momentum number  
 $\xi$  — A free parameter in Néel two sub-lattice model  
A/B-site — Tetrahedral/Octahedral site in spinel compound

## LIST OF ABBREVIATIONS/SYMBOLS

---

- Q — Propagation vector of spin-spiral
- NN — Nearest neighbours
- NNN — Next nearest neighbours
- $T_S$  — Spin-spiral or Magneto-structural transition in  $\text{CoCr}_2\text{O}_4$
- K — Kelvin (SI unit of temperature)
- T — Tesla (SI unit of magnetic field)
- Oe — Oersted (SI unit of magnetic field)
- GMF — Geometrical magnetic frustration
- 1D/2D/3D — 1/2/3 dimensions
- LKDM — Lyons, Kaplan, Dwight and Menyuk(model)
- $u$  — A parameter in LKDM model
- $f$  — Frustration index
- $T_m$  — Magnetic long range ordering temperature
- MF — Mean-field
- $Z_n$  — Number of  $n^{\text{th}}$  neighbours
- $T_L$  — Lock-in transition in  $\text{CoCr}_2\text{O}_4$
- ZFC — Zero field cooled
- FCC — Field cooled cooling
- FCW — Field cooled warming
- $T^*$  — A temperature below which hi-field magnetization and heat capacity show irreversibility between ZFC and FCW in  $\text{CoCr}_2\text{O}_4$
- $T_{kink}$  — A temperature at which magnetization curve show kink in  $\text{CoCr}_2\text{O}_4$
- FE — Ferroelectric
- $T_{FE}$  — Ferroelectric Curie temperature
- $H$  — Magnetic field
- $M$  — Magnetization
- $E$  — Electric field
- $P$  — Electric polarization
- $\vec{e}_{ij}$  — Position vector joining two adjacent moments in spin-spiral
- $H_C$  — Coercive field

*M-T* — Temperature dependent magnetization

*M-H* — Field dependent magnetization

EB — Exchange bias

$H_{EB}$  — EB field

$H_{C+}/H_{C-}$  — Positive/negative coercive fields of *M-H* loop

MRRAM — Magnetoresistive random access memories

$H_{FC}$  — Cooling field

$H_C^{eff}$  — Effective coercive field

$T_{comp}$  — Compensation temperature

CEP — Conduction electron polarization

XRD — X-ray diffraction

*d* — Inter planar spacing

$\theta$  — Diffraction angle of X-rays

$\lambda$  — Wavelength of X-rays

*n* — Order of diffraction

SEM — Scanning electron microscope

EDAX — Energy dispersive analysis of X-rays

TGA — Thermogravimetric analysis

DSC — Differential scanning calorimetry

SQUID — Superconducting Quantum Interference Device

VSM — Vibrating sample magnetometer

PPMS — Physical Property Measurement System

mg — Milligram( $10^{-3}$  kilogram)

*a* — Lattice parameter of the cubic unit-cell

Å — Angstroms (unit of length)

$M_S$  — Saturation magnetization in *M-H* loop

$M_{FCC}$  — FCC magnetization

$M_{FCW}$  — FCW magnetization

$T_R$  — The temperature at which magnetization shows reorientation (dip)

$M_R$  — Remanent magnetization

## LIST OF ABBREVIATIONS/SYMBOLS

---

- FC  $M$ - $H$  — Field cooled  $M$ - $H$  loop
- CG — Center of gravity(of  $M$ - $H$  loop)
- $M_{EB}$  — vertical shift in the  $M$ - $H$  loop
- $M_{rem+}/M_{rem-}$  — Positive/negative remanent magnetization values
- $t'$  — Reduced temperature  $((T - T_{comp})/T_{comp})$
- $M_{rem}$  — Remanent magnetization
- $\chi_{hf}$  — Highfield susceptibility
- $C_P$  — Heat capacity at constant pressure
- $C_m$  — Magnetic field induced enhancement in heat capacity
- $\Delta S_m$  — Change in magnetic entropy
- $t$  — Time
- $\mu_i$  —  $i^{th}$  element magnetic moment
- $\mu_A/\mu_B$  — Net magnetic moment of A/B-sub lattice in spinel compound
- $H_{critical}$  — The field for which magnetization of compensation sample switch back to positive
- $\phi$  — Angle between the easy magnetization axis and applied field  $H$
- PM — Paramagnetic
- LR — Long range
- SR — Spin reorientation
- IC — Incommensurate
- C — Commensurate
- $T_{SR}$  — Spin reorientation transition
- $\chi_0$  — Temperature independent magnetic susceptibility
- $M_0/M_g$  — Intrinsic FM/glassy component in a glassy system
- $t_r$  — Characteristic time component
- $n$  — Stretched exponential exponent
- nm — Nano meter( $10^{-9}$  meter)
- $\mu\text{m}$  — Micro meter( $10^{-6}$  meter)

# Chapter 1

## Introduction

Magnetism and the related phenomena have received considerable interest for centuries owing to their fundamental as well as technological importance [6, 37–43]. Interplay between the magnetism and other electric properties of systems is believed to bring innovation in the future technology. This basic motivation opened up the era of spintronics which take advantage of the electron spin degree of freedom in addition to charge degree of freedom based on which the conventional semiconducting electronic devices work. We know that the response of spin related properties are much faster compared to the charge related properties. The discovery of intriguing phenomena such as Giant magneto-resistance, Colossal magneto-resistance, etc. have already proved to be valuable in constructing read/write heads and magnetic memory devices [7, 44]. Exchange bias (EB) effect also plays very crucial role in the design of spinelectronics or spintronics devices [6–8]. Functionalities of these devices can be further enhanced with materials exhibiting more than one ferroic ordering. In a ferroic material, the order parameter spontaneously appears below a characteristic transition temperature and that can be switched by an external field. In this context, multiferroics, in which magnetic and ferroelectric ordering coexist and in few cases even they are exclusively coupled to each and, they are expected to be useful. The current quest for strong multiferroic materials has triggered a surge of renewed interest

## 1. Introduction

---

in the research community throughout the world. The strong magnetoelectric coupling also finds large number of potential applications like magnetically tunable capacitor, magnetic field sensors, non volatile multi bit data storage devices and transducers. Multiferroic thin film layer can be useful in tunnelling magneoresistive device, and spin valves in which the magneto-resistance can be also controlled by electric field. In order to tailor materials for the technological applications it is essential to understand their fundamental properties.

### 1.1 Basic aspects of magnetism

Magnetism is mostly related to the spin degrees of freedom of a material. Magnetic compounds exhibit an ordered state below a characteristic temperature, known as transition temperature  $T_C$  or Curie temperature. The corresponding order parameter is net magnetization, and is reversibly switchable with external magnetic field of appropriate magnitude depending on the nature of the material. Mostly, the presence of localized electrons in the partially filled d-shell of transition metal or f-shell of rare-earth ions are the fundamental building blocks of magnetism in the solid state materials. The moments of adjacent elements interact via magnetic exchange interaction. Domination of this exchange interaction energy between these localized moments against the thermal energy leads to magnetic ordering at  $T \leq T_C$ . Depending on the type of ordering of the magnetic moments, magnetic materials are classified as (i) Ferromagnetic(FM) (ii) Antiferromagnetic(AFM) and (iii) Ferrimagnetic(FIM). In FM materials, moments align parallel to each other, even in the absence of external field also they can exhibit spontaneous magnetization below the characteristic temperature called as Curie point( $T_C$ ). In AFM compounds, the neighbouring moments align antiparallel to each other, such that the net magnetic moment is zero below the transition temperature called as the Néel temperature,  $T_N$ . FIM materials contain two magnetic sub-lattices with different magnetic moments and they undergo parallel alignment of

intra sub-lattice moments and antiparallel alignment of inter sub-lattice moments such that there is a net magnetization similar to that of FM materials.

According to Weiss theory [45], the magnetic ordering is facilitated by an internal molecular field which tends to align the moments parallel or antiparallel to each other. Due to the strong internal field, magnetic compounds show spontaneous magnetic moment below  $T_C$  even in the absence of external field. According to Heisenberg theory of magnetism [46], the magnetic exchange energy of a magnetic system can be expressed as

$$E = - \sum_{\langle i,j \rangle} J_{ij} \vec{S}_i \cdot \vec{S}_j \quad (1.1)$$

here  $S_i$  &  $S_j$  are the adjacent spins and the summation is over all the possible nearest neighbours.  $J_{ij}$  is exchange integral, the positive sign of  $J_{ij}$  favours parallel or FM arrangement while the negative sign prefers antiparallel or AFM arrangement between the moments. Exchange integrals  $J_{ij}$  are of two types (i) Direct (ii) Indirect. In transition metals, the outermost 3d electrons are delocalized, the strong overlap between the wavefunctions of neighbouring ions (d-electrons) causes the direct exchange interaction between the spins of these overlapping shells. In oxides and rare-earth metals, direct overlap between the neighbouring d/f wavefunctions is not possible, and the moments interact indirectly. Magnetic ions in oxides interact via non-magnetic oxygen ion, such type of interaction is called as superexchange interaction. In rare-earth inter-metallic compounds, the f-shell electrons are more localized to nucleus and are embedded in a conduction electron sea. The spatial extent of 4f-orbital is small compared to that of inter-ionic distance. Here, rare-earth ions interact via conduction electrons known as indirect Ruderman-Kittel-Kasuya-Yosida (RKKY) interaction.

Above the ordering temperature ( $T_C$  or  $T_N$ ) the thermal energy dominates over the magnetic exchange energy, moments lose their local magnetic ordering and transform

## 1. Introduction

---

into a disordered paramagnetic state. Hence most of the FM, AFM and FIM materials exhibit a paramagnetic state above their ordering temperatures. Thus the ordering temperature is dictated by the strength of magnetic exchange energy. The susceptibility  $\chi(T)$  in the paramagnetic region materials can be analysed by Curie-Weiss law,

$$\chi(T) = \frac{C}{(T - \Theta)} \quad (1.2)$$

In this expression,  $C = N\mu_{eff}^2/3k_B$ , Curie constant.  $\Theta$  is the Curie-Weiss temperature. Negative  $\Theta$  indicates the AFM interactions and positive  $\Theta$  indicates the FM interactions between the local magnetic moments in the sample. By fitting the paramagnetic susceptibility to the eq.1.2 one can estimate the experimental value of effective paramagnetic magnetic moment  $\mu_{eff}$  of the free ions. Theoretically effective paramagnetic moment can be calculated in terms of Bohr magnetons using the relation  $\mu_{eff} = g\sqrt{J(J+1)}$ . Presence of strong crystal field in most of 3d transition metal oxide compounds quenches the orbital moments ( $L = 0$ ), results in  $J = S$ . Hence in many compounds having 3d elements the experimentally observed values of  $\mu_{eff}$  are in better agreement with the theoretical values calculated from the spin only contribution of the free magnetic moment. In heavier transition metals ions (4d and 5d series) the situation is unclear as the heavier ions have a larger spin-orbit coupling strength. In these materials, the strength of crystal field and the spin-orbit interaction are comparable. In inter-metallic compounds the spin-orbit coupling is stronger than the crystal field effect, and as a result there is no orbital quenching. Hence, the experimentally observed values of  $\mu_{eff}$  are in good agreement with the total moments due to both spin and orbital contributions in rare-earth inter-metallic systems.

In spinel compounds the magnetic interaction occur among magnetic ions positioned at different crystallographic sites, and in such cases Curie-Weiss law does not hold good. To analyse the temperature dependence of the paramagnetic susceptibility

of these substances, Néel [47, 48] generalized the concept of the Weiss molecular field. In this model an ion of a given sublattice interacts with neighbours in the intra and inter sub-lattices. He also assumed that the interactions within and between sublattices give rise to distinct internal fields. According to Néel the magnetic susceptibility above the magnetic ordering temperature can be written as,

$$\frac{1}{\chi(T)} = \frac{(T - \Theta)}{C} - \frac{\xi}{(T - \Theta')} \quad (1.3)$$

Here first term is again similar to the Curie-Weiss law. Curie constant  $C$  is the sum of the magnetic ions reside on the different sub-lattices. and  $\Theta$ ,  $\xi$  and  $\Theta'$  are proportional to the superexchange integrals of intra and inter sub-lattice elements [47, 48].

## 1.2 Structural and magnetic properties of $\text{CoCr}_2\text{O}_4$

Cobalt chromate,  $\text{CoCr}_2\text{O}_4$  is one of the oldest compounds, initially studied by Menyuk et al. [28]. It exhibits very complicated magnetic structure compared to that of the conventional simple FIM materials [28, 49]. Structural and magnetic properties of  $\text{CoCr}_2\text{O}_4$  are as follows.

### 1.2.1 Crystal structure of $\text{CoCr}_2\text{O}_4$

$\text{CoCr}_2\text{O}_4$  crystallizes in  $\text{AB}_2\text{O}_4$  type spinel structure. Here A and B are transition metal ions. Spinel structure is a close-packed face-centered cubic lattice formed by oxygen anions. As shown in the Fig.1.1, oxygen anions form two interstitial positions namely octahedron and tetrahedron with 6 and 4 coordination, respectively. In general, the unit cell of a spinel compound consists of 8  $\text{AB}_2\text{O}_4$  units, i.e., 24 cations (8 A-type & 16 B-type) and 32 oxygen anions. Among the 24 cations 8 are distributed in the 64 available tetrahedral sites and the remaining 16 are distributed in the 32 available octahedral sites. Depending on the distribution of the cations in the available two sub-lattices, three types of spinel compounds are possible. If all 8 A-type cations

## 1. Introduction

---

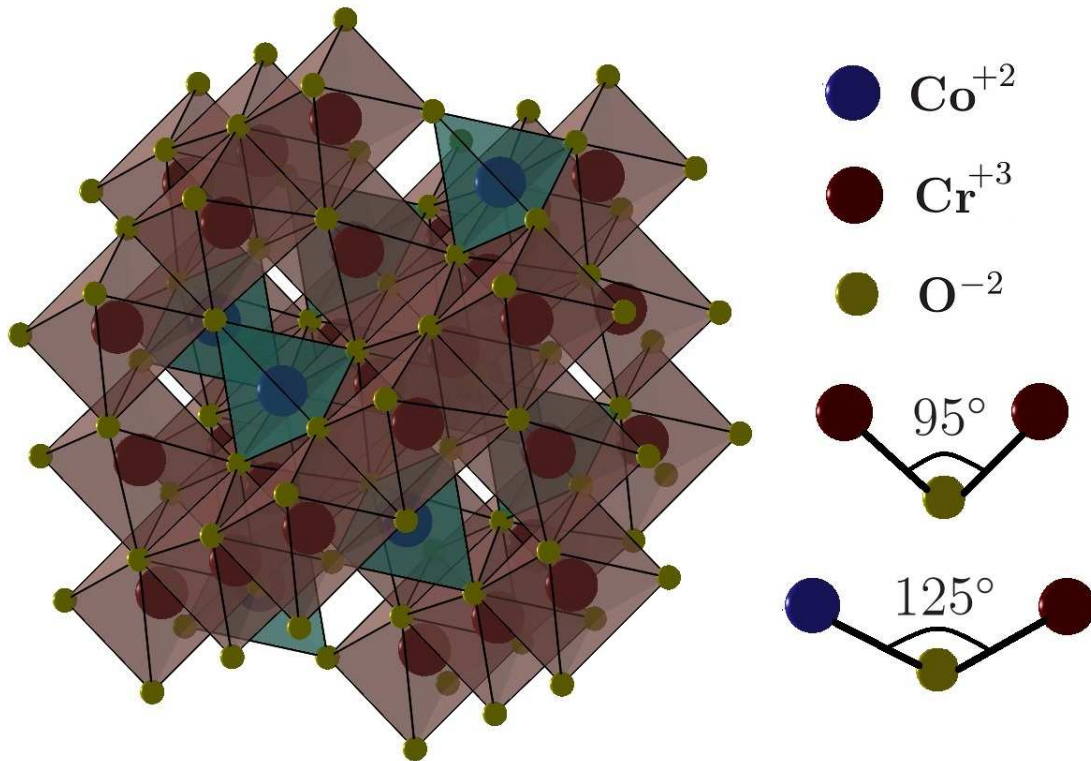


**Figure 1.1:** Spinel crystal structure of  $\text{CoCr}_2\text{O}_4$  showing edge-shared  $\text{CrO}_6$  octahedra (reddish pink) and corner shared  $\text{CoO}_4$  tetrahedra (light blue) and  $\text{CrO}_6$  octahedra in the 3 dimensional space. Balls indicate different ions of  $\text{CoCr}_2\text{O}_4$ . Bond angles of  $\text{Cr}-\text{O}-\text{Cr}$  and  $\text{Co}-\text{O}-\text{Cr}$  paths are also shown.

occupy the tetrahedral site and remaining 16 B-type cations occupy the octahedral site then the resulting spinel is called as normal spinel. The crystal structure of  $\text{CoCr}_2\text{O}_4$  is shown in Fig.1.1, where  $\text{Co}^{+2}$  ions occupy the tetrahedral site and  $\text{Cr}^{+3}$  ions occupy the octahedral site, and forming a normal cubic spinel with lattice parameter around  $8.33\text{\AA}$  [28]. If 8 (50%) of the B-type cations occupy the tetrahedral site and remaining 8(50%) B-type and 8 A-type cations occupy the octahedral site then resultant structure is inverse spinel [50, 51].  $\text{Fe}_3\text{O}_4$  is a complete inverse spinel. But many of spinel compounds are intermediate, i.e., neither complete normal spinel nor inverse spinel. For example,  $\text{CoFe}_2\text{O}_4$  is 70%–85% inverse spinel depending on the preparation conditions [50, 52].

In the cubic spinels, the distribution of near-neighbours (NN) and next-near neighbours (NNN) for A and B site ions is found to be in the following manner. A-site ion consists 4A NN, 12B NN, 12A NNN, and 16B NNN ions, where as the B-site ion consists 6A NN, 6B NN, 8A NNN, and 12B NNN ions. The distance between the ions of B–B neighbor ions is smaller than that of the A–B neighbor and the longest distance exists between A–A neighbors [34]. The octahedron shares with its adjacent octahedra along the edges whereas the tetrahedron and octahedron are linked along the corners. Angle between the Co and Cr, i.e., Co–O–Cr is around  $125^\circ$ , and between the Cr ions, i.e., Cr–O–Cr is around  $95^\circ$  in  $\text{CoCr}_2\text{O}_4$ .

### 1.2.2 Magnetic frustration due to geometric constrains

Spinel compounds exhibit a wide range of magnetic properties depending on the transition elements in its two sub-lattices. In oxide spinels, the magnetism is governed by the AFM superexchange interactions. In  $\text{CoCr}_2\text{O}_4$ , having  $\text{Co}^{+2}$  ( $3d^7$ ) and  $\text{Cr}^{+3}$  ( $3d^3$ ) magnetic ions, the possible NN paths for magnetic super exchange interactions are Cr–O–Cr and Co–O–Cr. It has been found to exhibit a collinear FIM ordering at  $T_C \simeq 94\text{--}97$  K and a magneto-structural transition into a complex conical spin-spiral ordering at  $T_S \simeq 24\text{--}27$  K [28]. Unfortunately, the magnitude of the magnetization in this compound can not be explained by collinear ordering of the moments.

Due to the geometrical constraints and the competition among different interactions in the spinel compounds, magnetism is mainly dictated by the magnetic frustration. Magnetic frustration arises in some of the systems due to the failure of minimization of the energy of all pairwise magnetic interactions simultaneously. This inability of the system gives rise to macroscopic degeneracies, i.e., infinite number of states posses minimum energy, and it leads to exotic new ground states of a magnetic sys-

## 1. Introduction

---

tem [53–57]. The appearance of frustration due to the geometrical constraints is called geometrical magnetic frustration (GMF). Mainly GMF arises in materials containing antiferromagnetically coupled magnetic moments that reside on geometric units such as triangles or tetrahedron. As shown in Fig.1.2(a), for four moments on the corners of square it is easy to satisfy all the NN AFM interactions simultaneously. However, if the strength of NNN interaction  $J'$  is comparable to that of NN interaction  $J$  even spins on the corners of square also gives rise to the magnetic frustration. But in the case of (b) for all NN AFM pairs of moments on the corners of triangle we can see that only two of the three moments can be satisfied at an instant. If first two moments align antiparallel to each other, the third one is frustrated because of its two possible orientations, up and down which possess same energy. The third moment can't simultaneously minimize its interactions with both of the moments on the other two corners of triangle. Since this effect can occur for moments on each corner, the ground state of three moments on the corners of a triangle can possess six equal minimum energy configurations (b1)–(b6) as shown in Fig.1.3. Hence, the system has sixfold degeneracy. In a practical case, the GMF hinders the formation of a collinear magnetically ordered state with a minimum energy, and it rather leads to the emergence of unconventional non-collinear magnetic ground states [56, 58]. This is the case for a single triangle block.

If we consider linked triangles in different dimensions, then it leads to the further complication as shown in Fig.1.4. Corner shared triangles in one dimension (1D) form diamond chain as depicted in Fig.1.4(a). This kind of situation has been observed in  $\text{Cu}_3(\text{CO}_3)_2(\text{OH})_2$  [59, 60]. In the case of two dimension (2D) more complicated magnetic ground states can be found due to the GMF as shown in triangular lattice and Kagomé lattice [Fig.1.4(b) & (c)]. Such states are realized in hexagonal manganites  $\text{RMnO}_3$  ( $R=\text{Y, Lu \& Sc}$ ) [61] and  $\text{KFe}_3(\text{OH})_6(\text{SO}_4)_2$  [62], and other numerous systems [57, 63, 64]. In three dimension (3D), much more exotic behaviour can be

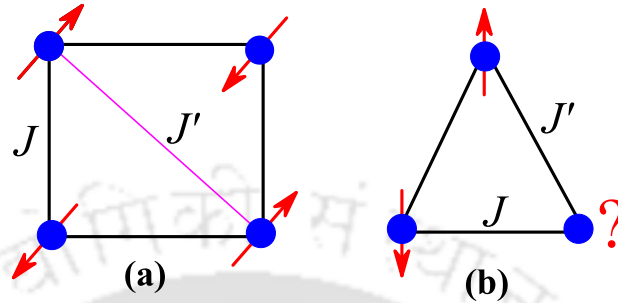


**Figure 1.2:** (a) Antiferromagnetically arranged neighbouring moments residing on the corners of square. (b) Failure of all pairwise AFM interactions for the moments reside on the corners of a triangle. Here the circles indicate magnetic ions.

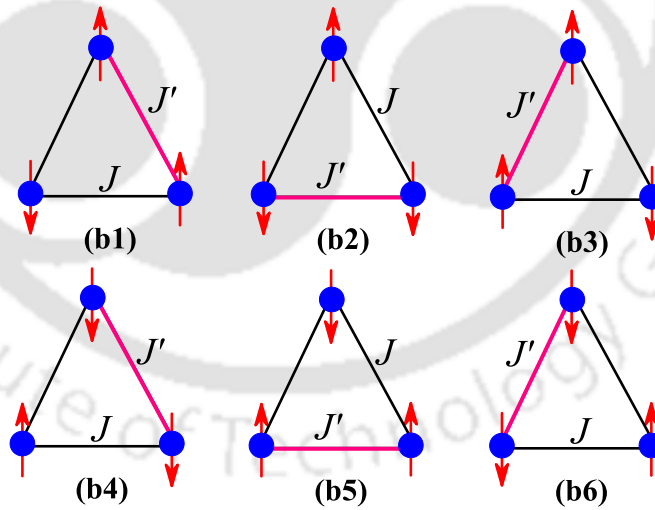


**Figure 1.3:** (b1)–(b6) Six possible magnetic configurations for the moments on the corners of a triangle if we consider simple collinear alignment of AFM moments. But in general much more complicated situations can be realized.

## 1. Introduction

---

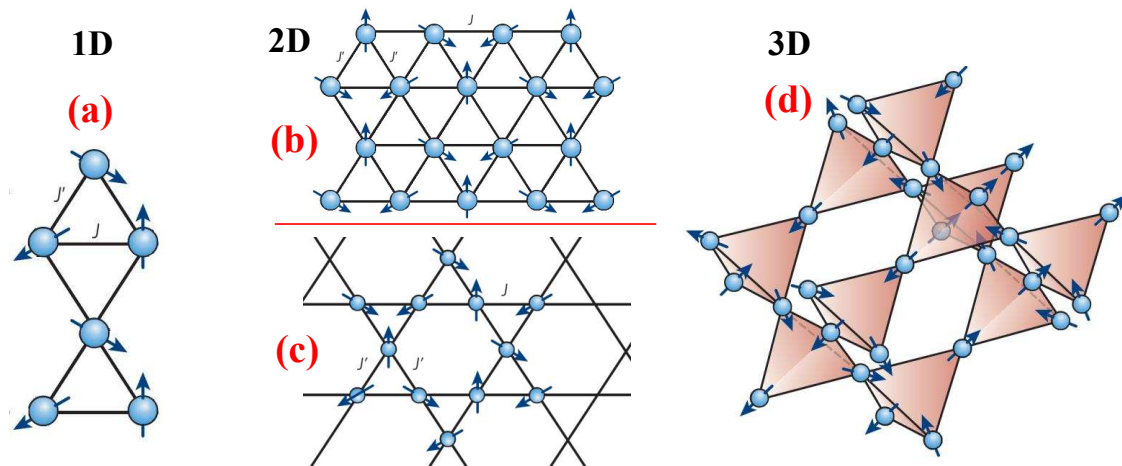


**Figure 1.4:** Geometric frustration in (a) 1D diamond chain, (b) 2D triangular lattice, (c) 2D Kagomé lattice and (d) the 3D pyrochlore lattice (corner shared tetrahedra) [53, 56, 57].

observed as shown in Fig.1.4(d). The magnetic lattice shown in Fig.1.4(d) is called as pyrochlore lattice, realized in systems like  $\text{Ho}_2\text{Ti}_2\text{O}_7$  [65] and  $\text{ACr}_2\text{O}_4$  (A is non magnetic ion). Similar to liquids, where molecules form a highly disordered state, the antiferromagnetically coupled moments which reside in the 1D, 2D and 3D lattices shown in Fig.1.4 also form spin liquid or spin-glass ground states [53, 56].

B-site of the  $\text{AB}_2\text{O}_4$  spinels forms pyrochlore lattice similar to the one shown in Fig.1.4(d) and the A-site forms diamond lattice. If only B-ions are magnetic in nature, the pyrochlore lattice causes unusual GMF, one such example is  $\text{ZnCr}_2\text{O}_4$ , in which emergent excitations of spin states have been observed [66]. If both A and B ions are magnetic in nature, the magnetic interaction between A and B ions provide an alternate way for the frustrated B-site moments to satisfy the different magnetic exchange interactions simultaneously upto some extent. This causes the reduction of the GMF in the B-pyrochlore lattice upto some extent, and results in decrease of degeneracy of the ground state. Hence the characteristics of the configuration is governed by the strength of the interaction between A and B magnetic spins over the

interaction between B and B spins.

To deal this situation Lyons, Kaplan, Dwight and Menyuk(LKDM) proposed LKDM theory for spinel compounds [49] by considering the classical Heisenberg magnetic exchange energy. Solving of the classical Heisenberg exchange energy for many A & B magnetic spinels led to the discovery of a new magnetic ground state configurations, called FIM spin-spirals. According to LKDM theory the strength of the GMF and hence the magnetic ground state of spinel compound can be estimated by utilizing a simple ‘ $u$ ’ parameter.

$$u = \frac{4J_{BB}S_B}{3J_{AB}S_A} \quad (1.4)$$

here,  $J_{BB}$  &  $J_{AB}$  are the NN AFM superexchange integrals along the B–O–B & A–O–B pathways, and  $S_A$  &  $S_B$  are magnitudes of the moments at the A & B-sites, respectively. From this (i) if A-ion is non-magnetic,  $S_A=0$  and  $J_{AB}=0$  then  $u=\infty$  and hence results in the large GMF as noticed in  $\text{ACr}_2\text{O}_4$  [66] and  $\text{AFe}_2\text{O}_4$ . (ii) For the spinels in which A & B ions are magnetic, if ‘ $u$ ’ is finite and  $u > 1.298$  then it has been argued that weak GMF survives and the degeneracy of the spin state decreases upto some extent leaving the spins in the intermediate state and by avoiding the long range ordering with reduced correlation length [28, 29]. This simply results in short range spin-spiral configurations.  $\text{MCr}_2\text{O}_4$  ( $M = \text{Co}, \text{Mn}, \text{Fe} \ \& \ \text{Ni}$ ) with the ‘ $u$ ’ value around 2 showed some kind of spin-spiral configurations evidenced by many experimental studies [24, 28–30, 67]. This short range spiral configuration turnout to be long range one for  $1.298 \geq u \geq 8/9$ . (iii) For the spinels having magnetic ions at A & B sites with  $u < 8/9$  the underlying magnetic configuration become simple Néel-type collinear FIM or AFM ordering. This is noticed in  $\text{MFe}_2\text{O}_4$  ( $M = \text{Fe}, \text{Co} \ \& \ \text{Mn}$ ) due to the domination of  $J_{AB}$  over  $J_{BB}$ . Scaling between the ‘ $u$ ’ and GMF in various cubic spinel/inverse spinels is summarised in the Fig.1.5. In this way LKDM model successfully attempts to explain the non-collinear magnetic orders in spinels.

## 1. Introduction

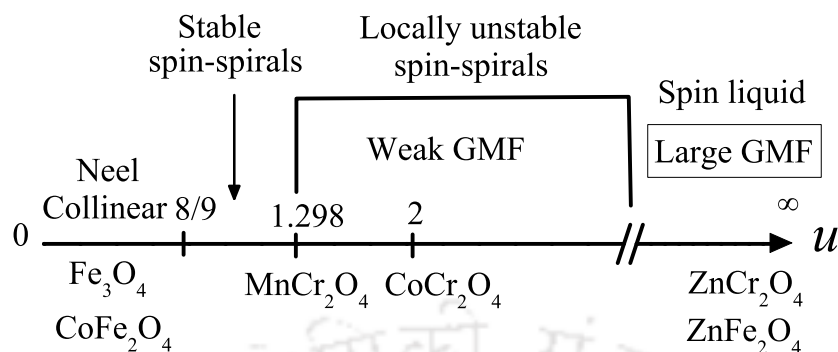


**Figure 1.5:** Schematic diagram showing the relation between the magnetic frustration and magnetic configuration in various spinels as a function of LKDM parameter ‘ $u$ ’.

However, this model failed to explain the presence of GMF in the A magnetic and B non-magnetic spinels. This may be because of the consideration of only NN superexchange interactions. In spinels such as  $MA_2O_4$  ( $M = Co, Mn \& Fe$ ) [68–70] frustration may arise from the diamond A-lattice due to the competition between the NN and NNN superexchange interactions.

To estimate the amount of magnetic frustration experimentally an empirical relation has been formulated, according to its frustration index,

$$f = \frac{|\Theta|}{T_m} \quad (1.5)$$

where  $\Theta$  is the Curie-Weiss temperature and  $T_m$  is the magnetic ordering temperature below which the long range magnetic ordering sets in. Magnitude of  $\Theta$  sets the energy scale for the magnetic interactions, from mean-field theory,  $\Theta = 2S(S + 1)/k_B \sum_n Z_n J_n$ ;  $Z_n$  is number of  $n^{th}$  neighbours and  $J_n$  is corresponding exchange integral. Hence,  $\Theta$  is proportional to the strength of the magnetic interactions in a magnetic system. If magnetic exchange energy is not hindered by other sources, the system should undergo long range magnetic ordering exactly at  $T \simeq |\Theta|$  as demonstrated in bulk FM systems, where  $f \sim 1$ . But this is not the case in AFM materials in which the magnetic ordering temperature  $T_N$  is always smaller compared to  $|\Theta|$ . In

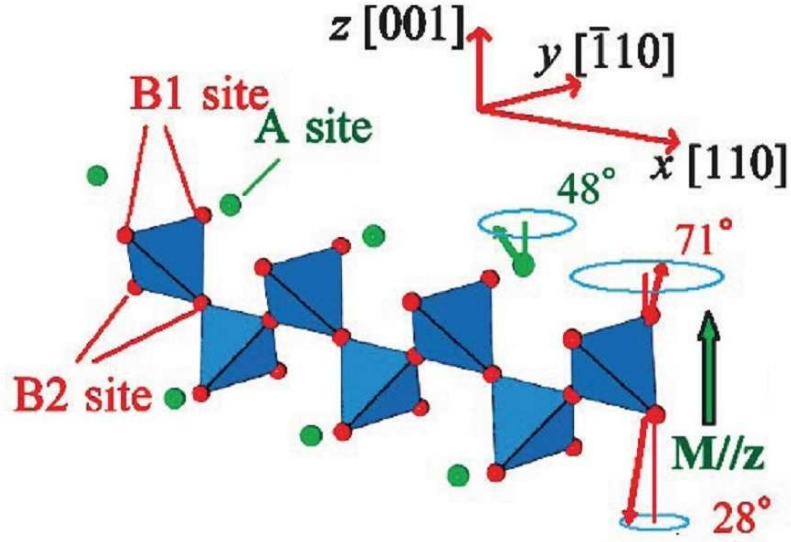


**Figure 1.6:** Pyrochlore B sub-lattice structure of  $\text{CoCr}_2\text{O}_4$  viewed along the conical spin-spiral modulation direction  $[110]$  (denoted as the  $x$  axis). The circles with slanted arrows indicate the conical spiral plane of the Co, Cr1 and Cr2 moments [23, 28].

general weak frustration survives in AFM materials if  $2 \leq f \leq 10$ , and it leads to stable non-collinear spin configurations. For highly frustrated AFM materials, i.e., with  $f > 10$ , it leads to exotic magnetic states such as spin-glass, spin-liquid etc.

### 1.2.3 Magnetic phase diagram of $\text{CoCr}_2\text{O}_4$

As illustrated in the Fig.1.6,  $\text{Co}^{+2}$  in the A-site is coupled to the  $\text{Cr}^{+3}$  in the B-site with the superexchange integral via A–O–B network. Due to the availability of this magnetic cation in the A-site, the superexchange interaction  $J_{AB}$  strength becomes comparable to that of the  $J_{BB}$  in the pyrochlore B-lattice. This causes the reduction in the frustration of the pyrochlore B-lattice, and in turn results in complex non-collinear spin-spirals with three magnetic sub lattices namely Co, Cr1, and Cr2 [28, 67].  $J_{BB}$  &  $J_{AB}$  superexchange integrals estimated from the molecular field calculations [28, 49] and ground state magnetic structure by neutron scattering data [29] endorse the ‘ $u$ ’ value

## 1. Introduction

---

around '2'. According to LKDM model  $u \sim 2$  is favourable condition for the formation of spin-spirals [28, 29, 49]. Experimentally observed FIM  $T_C$  is a result of the ordering of the A-site moments along the [001] easy magnetic axis [28, 71]. Upon lowering the temperature below  $T_C$ , even though the long range order of A-site( $\text{Co}^{+2}$ ) moments persist, due to the weak GMF (which avoids the long range magnetic ordering of the moments in pyrochlore B sub-lattice) the spin components perpendicular to the easy axis and the corresponding moments at Cr-site(Cr1 and Cr2) are still disordered, forming short range spin-spirals in such a way that the resultant magnetic moment is anti-parallel to A-site moment [28, 29, 71]. At  $T_S$  the magnetic structure completely changes into a incommensurate conical spin-spirals. As shown in the Fig.1.6 all the moments are constrained to the surface of the cones. Cone angles for the Co, Cr1 and Cr2 site moments are  $48^\circ$ ,  $71^\circ$  and  $28^\circ$ , respectively. A-site moment is along the [001] direction whereas the resultant moment of B-site (B1 and B2) align along the  $[00\bar{1}]$  direction. Resultant moment of the A-site dominates below  $T_C$  [23, 28, 29].

Further, the detailed neutron scattering studies on  $\text{CoCr}_2\text{O}_4$  revealed that the step-like change observed in the thermomagnetic properties at around 13 K is due to the lock-in transition  $T_L$  [24, 30]. Magnetic order of the conical spin-spiral component with an incommensurate propagation vector of  $(0.63, 0.63, 0)$  observed at  $T_S$ , crosses over into the commensurate conical spin-spiral order with fixed propagation vector of  $(2/3, 2/3, 0)$  across  $T_L$  [30]. The commensurate conical spin-spiral order observed below  $T_L \sim 13$  K is locked to the underlying lattice hence  $T_L$  is named as the lock-in transition [24, 30]. Y. J. Choi et al. [24] reported much more complicated spin-spiral magnetic ordering even above  $T_L$  compared to the earlier neutron scattering studies. They found two incommensurate magnetic modulations  $Q_+$  and  $Q_-$  at a temperature above  $T_L$ . For temperature below  $T_L$ , they observed one commensurate modulation  $Q_C = 2/3[110]$  and two incommensurate modulations,  $Q'_+$  and  $Q'_-$ , with a separation along  $[\bar{1}10]$  much larger than that between  $Q_+$  and  $Q_-$ .

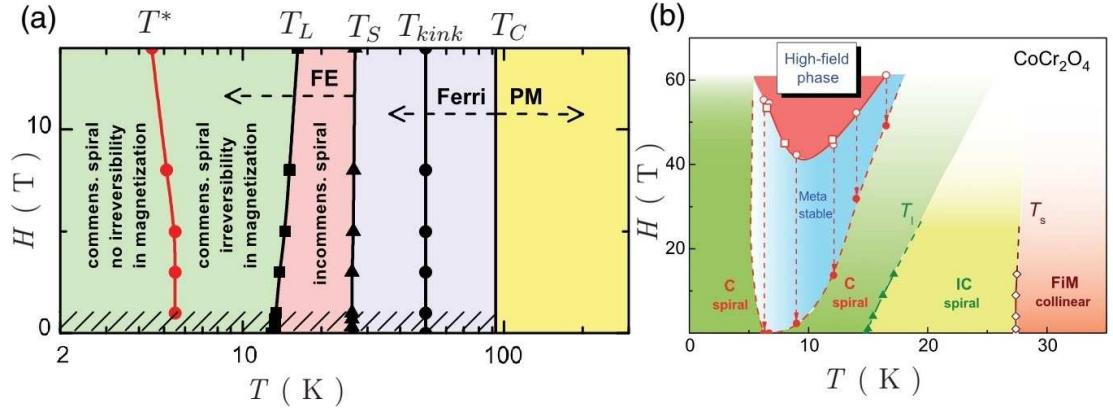


**Figure 1.7:** (a)  $H$ - $T$  phase diagram of  $\text{CoCr}_2\text{O}_4$  based on magnetization and specific-heat measurements [31]. (b) Low-temperature ( $T \leq T_L$ ) commensurate spin-spiral  $H$ - $T$  phase diagram of  $\text{CoCr}_2\text{O}_4$  derived from the ultrasound propagation measurements [32].

The commensurate phase below  $T_L$  is not stable, it undergoes many fluctuations. A. V. Pronin et al. [31] measured the magnetization and specific heat of  $\text{CoCr}_2\text{O}_4$  in magnetic fields up to 14 T. Their high-field magnetization and heat capacity measurements revealed feature of a new phase transition at  $T^* = 5-6$  K. The phase between  $T^*$  and the lock-in transition  $T_L$  is characterized by magnetic irreversibility. Specific-heat measurements confirmed the transition at  $T^*$ , and also show irreversible behavior. Field-temperature ( $H$ - $T$ ) phase diagram of  $\text{CoCr}_2\text{O}_4$  constructed from these high field studies is depicted in the Fig.1.7(a). We can see that the  $\text{CoCr}_2\text{O}_4$  has very complicated magnetic phase diagram as a function of field and temperature. Here the  $T_{kink}$  is derived from the subtle jump in the magnetization at around 50 K. Origin of  $T_{kink}$  is controversial, and not yet clear, initial studies claimed that it is the signature of short range spin-spiral [28, 29] while later studies attributed it to ordering temperature of the B-site [71].

Recent magnetic field and temperature dependent ultrasound propagation and

## 1. Introduction

---

magnetization studies in single-crystalline  $\text{CoCr}_2\text{O}_4$  in static fields (upto 14 T) and pulsed magnetic fields (62 T) discovered much more interesting features in the magnetic phase diagram as shown in Fig.1.7(b) [32]. While the magnetization changes gradually as a function of field upto 62 T, step-like increments in the ultrasound measurements are observed below  $T_L$ . These features clearly signify a transition into a new magneto-structural state between 6.2 and 16.5 K and at high magnetic fields. They argued that the phase below  $T_L$  is a high-symmetry phase with only the longitudinal component of the magnetization being ordered, while the transverse spin-spiral component remains disordered and undergo transitions at high fields. This phase is found to be metastable in the  $H$ - $T$  phase space. Even ultra high fields are not able to induce full net moment of  $3 \mu_B/\text{f.u.}$ , if we assume that the magnetic structure is collinear  $T \leq T_S$  [31, 32]. This indicates how rigid the spin-spirals are there in this system.

### 1.2.4 Other ferroic properties in $\text{CoCr}_2\text{O}_4$

In the current times coexistence of the ferroelectric (FE) and magnetic properties in single phase material is a subject of fundamental as well as technological importance [72–76]. Magnetism and ferroelectricity are related to the spin and the charge degrees of freedom, respectively. Ferroelectricity is the electric analog of FM. A FE material exhibits macroscopic electric polarization below its characteristic temperature,  $T_E$ . Electric dipole moment is the fundamental block of ferroelectricity. Unit cell needs to be non-centrosymmetric for the existence of a dipole moment, i.e., in FE state the centre of the positive ion (cation) of the crystal does not coincide with the centre of the negative charge [77].

Though ferroelectricity and magnetism are two competing physical phenomena, they are found to coexist in some of the materials such as  $\text{BiFeO}_3$  ( $T_{FE} \sim 1100$  K,  $T_N = 643$  K) and  $\text{YMnO}_3$  ( $T_{FE} \sim 914$  K,  $T_N \sim 76$  K). Here also the ferroelectricity

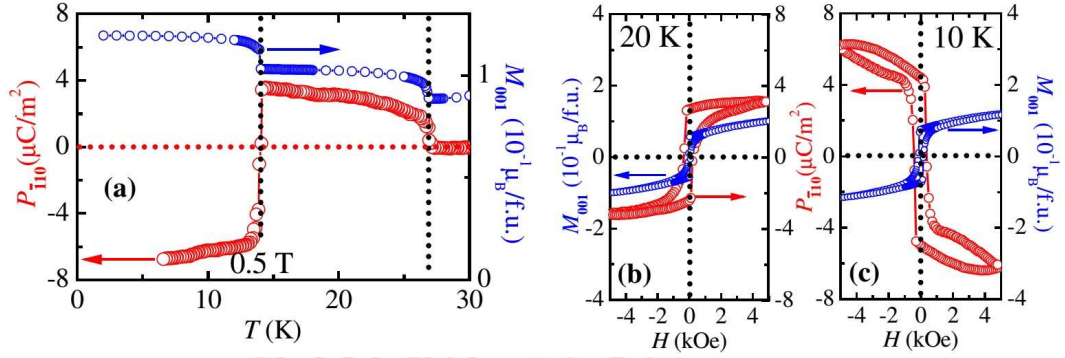


**Figure 1.8:** (a) Temperature dependence of electric polarization  $P$  along the  $[\bar{1}10]$  direction, and magnetization  $M$  along the  $[001]$  direction in  $\text{CoCr}_2\text{O}_4$ . (b) and (c) are the field dependence of electric polarization,  $P$ , along the  $[\bar{1}10]$  direction, and magnetization  $M$  along the  $[001]$  at 20 K and 10 K, respectively. Here, the magnetic field is applied along the  $[001]$  [23].

appears due to the non-centrosymmetric unit cell. Due to different sources of the magnetism and ferroelectricity they are largely independent of each other. In many of them, the critical temperatures of FE transitions are well above room temperature.

Surprisingly, frustrated magnets such as  $\text{CoCr}_2\text{O}_4$ ,  $\text{RMnO}_3$  and  $\text{RMn}_2\text{O}_5$  ( $R = \text{Tb}$ ,  $\text{Dy}$ , and  $\text{Ho}$ ) have been found to exhibit multiferroic properties with a giant magneto-electric coupling [23, 24, 78–80]. In these compounds the electric polarization  $P$  can be reversibly switchable by the external magnetic field [23, 24]. Here the magnetic transition temperature is higher than that of the ferroelectric transition. In this case the electric polarization is believed to be generated from local magnetic ordering.

As shown in the Fig.1.8,  $P$  can be reversed with external magnetic field [23, 24]. Among very few materials  $\text{CoCr}_2\text{O}_4$  exhibits both a saturated magnetization and polarization. The non-collinear conical spin-spirals observed in  $\text{CoCr}_2\text{O}_4$  below magneto-structural transition  $T_S$  are source of magnetically driven  $P$  [23, 24]. Microscopically [27] and phenomenologically [81] magnetically driven ‘ $P$ ’ has been explained by combining spin-current model and the inverse Dzyaloshinskii-Moriya interaction of the

## 1. Introduction

---

form,

$$\vec{P} \propto \sum_{\langle i,j \rangle} \vec{e}_{ij} \times (\vec{S}_i \times \vec{S}_j) \quad (1.6)$$

here,  $\vec{S}_i$  &  $\vec{S}_j$  are the adjacent spin vectors and  $\vec{e}_{ij}$  is the vector joining them. The directions of the spontaneous  $P$ , the spin-spiral plane, and the propagation vector are perpendicular to each other in accord with the spin-current model [27]. The directions of the three vectors  $\vec{S}_i$ ,  $\vec{S}_j$  &  $\vec{e}_{ij}$  and the resultant  $\vec{P}$  for the transverse conical spin-spirals formed in the A and B site of  $\text{CoCr}_2\text{O}_4$  are presented schematically in Fig.1.6, as per the above model. The propagation  $e_{ij}$  of the spin-spirals along the [110] direction leads to spontaneous  $P$  perpendicular to the spiral propagation direction, i.e., along direction of  $[\bar{1}10]$ . Change in the magnetic field direction also causes the change in the direction of spin rotation axis, results in the flipping of  $P$  [23, 24].

Further, it can be also seen in the Fig.1.8 the lock-in transition  $T_L$  [30] in  $\text{CoCr}_2\text{O}_4$  leads to the thermally(a) and magnetically(c) induced reversal of spin induced  $P$  below  $T_L$  [24]. It occurs without change in spiral handedness (i.e., the sign of  $Q$ ) and sign of magnetization. The presence of multiple spiral sublattices are believed to be the reason behind this unusual behaviour. Spin-current model[1.6] failed to explain the this unusual behaviour in  $P$ . Recent reports revealed that the multiferroicity even on the onset of collinear FIM ordering above  $T_S$  and below  $T_C$  [25, 26]. This indicates that the magnetic order in the  $T_S < T_C$  is may not be fully collinear, the short range spin spirals still persists even in the temperature region  $T_S < T_C$  as suggested in the previous neutron scattering diffraction studies [28, 29].

Furthermore, distinctive anomalies in the sound velocity and attenuation have been found at the onset of  $T_S \sim 27$  K and  $T_L \sim 13$  K. As we know that the sound can only interact with the lattice vibrations, but the appearance of anomalies at magnetic transitions evidences a strong spin-lattice coupling in  $\text{CoCr}_2\text{O}_4$  [32]. The magneto-elastic

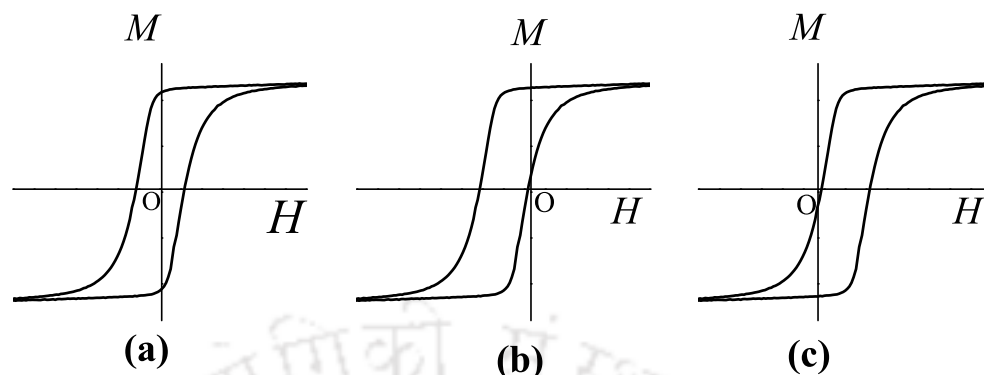


**Figure 1.9:** Schematic sketch of (a) normal, (b) left side shifted and (c) right side shifted  $M$ - $H$  loops; (b) and (c) illustrate the presence of exchange bias.

measurements are also found to exhibit anomalies at the different magnetic transitions in  $\text{CoCr}_2\text{O}_4$  [26]. However, they attributed it to the structural transformations from cubic paramagnetic phase to tetragonal FIM phase across  $T_C$  and again to cubic phase across  $T_S$  [26].

### 1.3 Exchange bias effect

The exchange bias (EB) effect was discovered in the year of 1956 by Meiklejohn and Bean [11]. In general a normal  $M$ - $H$  loop is known to be symmetric about the origin as shown in Fig.1.9(a). But when a system of FM material (Co) in contact with an AFM (CoO) material was cooled in a static applied magnetic field from above the  $T_N$  of the CoO material, and the measured resultant magnetization ( $M$ - $H$ ) loops were found to shift left side on the field axis [11, 12] as shown in the Fig.1.9(b) compared to that of normal  $M$ - $H$  loop depicted in Fig.1.9(b). The loop can also shift right side as shown in the Fig.1.9(c). The amount of shift in the  $M$ - $H$  loop is defined as EB field,

$$H_{EB} = - \frac{(H_{C+} + H_{C-})}{2} \quad (1.7)$$

where  $H_{C+}$  &  $H_{C-}$  are the positive & negative coercive field values of the  $M$ - $H$  loop, respectively. Since its discovery in 1956, EB was investigated in numerous FM–AFM

## 1. Introduction

---

systems but continued to be of fundamental interest. In addition to this, technological interest of EB was triggered in mid 90's when EB effects in FM–AFM multilayers have been revealed to be practically useful in read/write heads of recording devices [6, 41–43]. Thereafter it has found many other technological applications such as magnetoresistive random access memories (MRRAM) [1–5], magnetic field sensors [7, 8] enhanced of the coercivity & energy product of permanent magnets and in overcoming the superparamagnetic limit of memory devices [9, 10]. Over all it can be understood that EB has become a quintessential aspect in the field of spintronics. Due to these practical demands, EB has been studied extensively in numerous combinations of materials like FM, AFM, canted AFM, FIM, spin-glass and disordered magnetic components, etc. [8, 82, 83].

According to Meiklejohn, phenomenologically exchange anisotropy developed at the FM–AFM interface in the cooling process was assumed to be the the origin of the EB [13]. Further it has been found that the exchange anisotropy at the FM–AFM interface is unidirectional in nature [12, 13]. Let us assume that the AFM and FM materials are in contact with each other and their ordering temperatures are  $T_N$  and  $T_C$ , respectively. As shown in Fig.1.10(i) when a field is applied in the temperature range  $T_N < T < T_C$ , the FM moments align in the field direction but the AFM moments remain random as they are in the paramagnetic regime. When  $T \leq T_N$  in the presence of the field the AFM moments also tend to align in the following way. First, the AFM moments next to the FM align parallel (ferromagnetically) to those of the FM moments at the AFM–FM interface. The other moments in the AFM material simply follow the AFM order as illuminated in the Fig.1.10(ii). When the field is decreased and reversed to measure the  $M$ - $H$  loop, the FM moments away from the interface start to rotate along the field direction. But, the AFM spins at the AFM–FM interface do not let the ferromagnetically coupled FM layers at the interface to rotate along the applied field as demonstrated in the Fig1.10(iii). In other sense, the AFM moments at

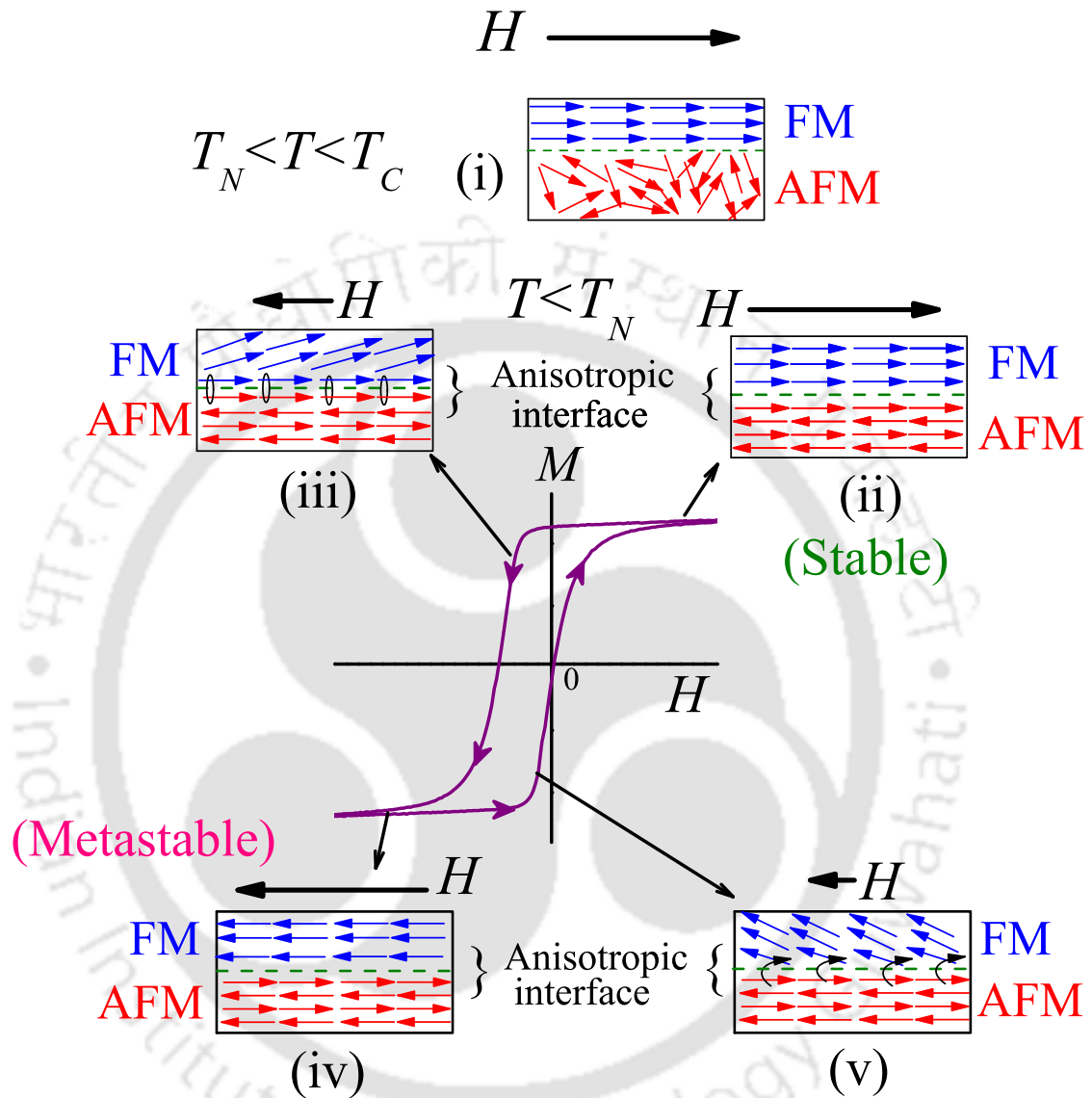


**Figure 1.10:** Schematic block diagram of the magnetic configurations of FM and AFM materials at the FM–AFM interface. (i) In the temperature range  $T_N < T < T_C$  when the sample is cooled in a field for which the FM moments order fully. (ii)–(v) are the magnetic configurations of the FM and AFM materials at various stages of an exchange biased  $M$ - $H$  loop measured below  $T_N$ . Length and direction of the arrow representing  $H$ , indicate the magnitude and direction of the the applied magnetic field at different states of the loop.

## 1. Introduction

---

the interface exert a microscopic torque (pinning) on the FM moments, to keep them in ferromagnetically aligned at the interface. In this way few layers of FM moments at the FM–AFM interface are pinned to the AFM material. So, FM spins at the interface have one fixed and stable configuration, i.e., the magnetic configuration at the FM–AFM interface become anisotropic which is unidirectional. So, more field is required to rotate these pinned moments against this unidirectional anisotropy. However, when the field is large enough to saturate the FM material all the moments in the FM material align to the field as shown in the schematic (iv). But the AFM ordering in the AFM material is unaffected due to the large underlying anisotropy in it. When the field is decreased to complete the loop, the FM moments will start to rotate even at a small negative field, due to the anisotropy at the AFM–FM interface, which now exert a torque in the same direction as the field (Fig.1.10(v)). Hence the magnetic energy required to rotate the FM moments along the positive and negative field directions is unequal, and results in shifting of the  $M$ - $H$  loop, along negative  $H$ -axis. In this way, the FM material experiences an internal biasing field, which oppose (enhance) the rotation of the FM moments along the applied field in the descending (ascending) branches of  $M$ - $H$  loop. This field is caused due to the exchange anisotropy at the interface, hence it is named as the EB field [12, 13]. The depth of pinning in the FM material depends on the strength of the anisotropy in the AFM material, i.e., more the anisotropy in the AFM material pins the more number of layers of FM moments, and thus leading more shifting of the  $M$ - $H$  loop. Further, due to the unidirectional exchange anisotropy developed in the cooling process at the FM–AFM interface, the coercivity of the of FM–AFM multilayers increases compared to that of the individual FM material.

Even though EB effect is assumed to be an interfacial phenomenon, later, it has been observed in structurally homogeneous materials such as core-shell nanostructures, spin-glasses, cluster-glasses and magnetically phase separated systems [14, 15]. Ana-

logues to AFM–FM interfaces in composites and multilayers, in this materials also FM and AFM magnetic configurations coexist within the structurally single phase material and that gives rise to EB effect. The discovery of EB in the single phase materials has renewed attention in this effect in a variety of structurally single phase compounds comprised of various coexisting magnetic phases. If the particle size of an AFM material is reduced to its magnetic domain size, the core can still form bulk AFM ordering but the shell moments behave as a detached part from the core and act a soft FM part with the applied magnetic field. Under field cooling process, AFM core starts exerting pinning force on the FM shell and it gives rise to EB phenomenon. In this way the appearance of EB has been in core-shell nano particles is attributed to the spontaneous interface between the shell(FM) and core(AF).

Another important class of single phase homogeneous materials in which EB is observed due to the coexistence of FM and AFM configurations are the rare-earth inter-metallic compounds. The conduction electrons play important role in the EB effect of rare-earth inter-metallic compounds [16]. In magnetic rare-earth inter-metallic compounds, magnetic moments of the rare-earth elements interact via conduction electrons with the long range indirect RKKY interaction. The sign of magnetic interaction(positive for FM and negative for AFM interactions) varies with distance between the magnetic ions. This gives rise to a coexistence of FM and AFM interactions among different magnetic rare-earth elements in the sea of conduction electrons. Thus, magnetic inter-metallic alloys having coexisting magnetic phases are one class of promising candidates for giving the EB effect.

### 1.3.1 Tunable exchange bias

Most of the materials summarised so far are found to exhibit shift in the FC  $M-H$  loops along the opposite direction to the cooling field( $H_{FC}$ ), i.e., if  $H_{FC}$  is positive, shift in the loop is along the negative field axis and vice versa. It has been claimed that if the

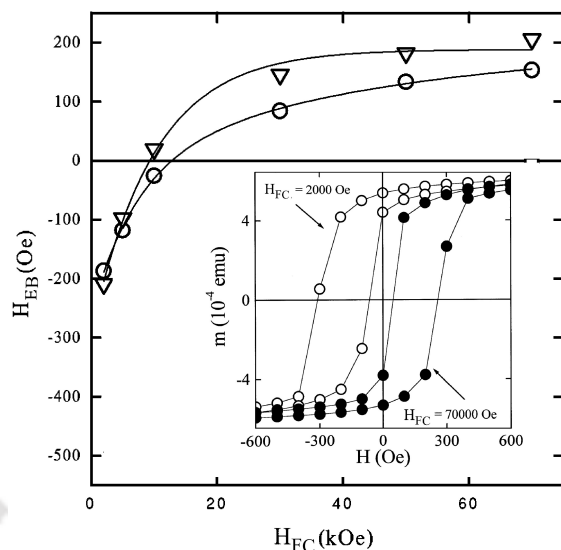


**Figure 1.11:**  $H_{FC}$  dependent EB field of  $\text{FeF}_2/\text{Fe}$  multilayers with  $\text{FeF}_2$  grown at  $250^\circ\text{C}$ ( $\nabla$ ) and  $300^\circ\text{C}$ ( $\circ$ ). Inset: FC  $M$ - $H$  loops for  $H_{FC} = 2$  kOe( $\circ$ ) and  $H_{FC} = 70$  kOe( $\bullet$ ) [85].

AFM material is deposited on top of the FM material in an external magnetic field large enough to saturate the FM moments, the resulting  $M$ - $H$  loop of the bilayer film shows a displacement in the direction of the  $H_{FC}$  [11]. Surprisingly some FM–AFM multilayer systems showed shift along the same direction without applying the field while growing the layers. For example, in  $\text{GdCo}_2$ – $\text{Co}$  multilayers, it is found that the sign of shift in the biased  $M$ - $H$  loops is same as the  $H_{FC}$  sign for the temperatures above the magnetic compensation temperature( $T_{comp}$ ) and below which it is opposite. This indicates that unlike in the EB materials summarised so far the shift in the FC  $M$ - $H$  loops is different at different temperatures in this sample even without changing the  $H_{FC}$  sign. Hence, the EB field in this materials is found to change its sign and diverges at the  $T_{comp}$  [84]. However, the exact underlying microscopic origin of the sign of EB and the divergence of the EB field and the coercive field are not very clear.

Studies in  $\text{FeF}_2$ – $\text{Fe}$  and  $\text{MnF}_2$ – $\text{Fe}$  bilayers revealed unusual behaviour in EB field

when the cooling field magnitude is changed [85]. As shown in the inset of Fig.1.11, for large  $H_{FC}$  the loops instead of shifting towards negative for a positive  $H_{FC}$ , they are shifted towards positive fields, i.e., in the same direction of the  $H_{FC}$ . This is in contradiction to what is observed for small  $H_{FC}$  or what is observed in other systems. This effect is called as the positive EB (according to the definition used by J. Nogues et al. [85] which is opposite to eq.4.2). The magnitude of the  $H_{FC}$  needed to change the sign in the shift of the  $M$ - $H$  loop from negative to positive depends strongly on the microstructure of the sample, and thus the interface coupling at the interface. For strong couplings (i.e., large  $H_{EB}$ ) larger  $H_{FC}$  are needed to obtain positive loop shifts [85]. As depicted in the main panel of Fig.1.11,  $H_{EB}$  is small at the small  $H_{FC}$  values, so the sign change in the  $H_{EB}$  takes place at considerably small values of  $H_{FC}$ . Positive shift has also been observed in  $\text{FeF}_2$  single crystals coated on thin Fe layers for rather small  $H_{FC}$  ( $\sim 2$  kOe) values. This indicates that the interface coupling in this case is rather weak and the  $\text{FeF}_2$  surface moments couple to the external  $H_{FC}$  above  $T_N$ . Different theoretical models have been proposed to explain this effect [85, 86]. All the models are based on the existence of antiparallel coupling between the FM and AFM layers at the interface, quite opposite to the phenomenological model explained in the Fig.1.10 [12, 13]. Thereafter, coexistence of positive and negative EB effect induced by temperature as well as  $H_{FC}$  has become attractive in other FM–AFM multilayers [87–89].

The most stunning feature of the tunable EB effect is the observation of the sign change of EB with changing the temperature across the  $T_{comp}$  even in an ideally homogeneous single crystalline rare-earth inter-metallic system of  $\text{Nd}_{0.75}\text{Ho}_{0.25}\text{Al}_2$  [17]. As shown in Fig.1.12(b), in the close proximity of  $T_{comp}$  the EB field changes sign across  $T_{comp}$ , at which the magnetization of the sample also changes its sign. In this rare-earth inter-metallic compound  $H_{EB}(T)$  reverses its sign at  $T_{comp}$  and exists in the narrow temperature window, where  $H_C^{eff}(T)$  collapses. The occurrence of coexistence of negative and positive  $H_{EB}$  has been discussed in the light of different kinds

## 1. Introduction

---

of exchange coupling between the moments corresponding to conduction electron polarization (CEP) and, two dissimilar rare-earth ions at above and below  $T_{comp}$ . It is anticipated that CEP in this systems is an analogue of a FM material of FM–AFM composites and multilayers [Fig.1.12(c)] [8, 12, 13] and antiferromagnetically coupled local magnetic moments of both the rare-earth ions ( $\mu_{Nd}$  and  $\mu_{Ho}$ ) play the role of AFM material. Two schematics in the Fig.1.12(d) represent the orientations of the local moments of Nd/Ho and that of the CEP with respect to the applied field in two temperature domains i) above  $T_{comp}$  and ii) below  $T_{comp}$ . Point to be noted here is the reversal in the orientation of the different sub-components across  $T_{comp}$  is induced by cooling the sample in a large enough external field. Even though the orientations of different sub-components in the case of  $Nd_{0.75}Ho_{0.25}Al_2$  for  $T < T_{comp}$  in part (d) of Fig.1.12 are apparently equal to part (c), the EB field show negative values contrast to the positive values in the field in the multilayers. Hence the analogy between the CEP in the rare-earth alloys and the FM part in the multilayers & composite materials is opposite [84]. As shown in Fig.1.12(d), for the region  $T > T_{comp}$ ,  $\mu_{CEP}$  is assumed to align antiparallel to the direction of applied field as it is strongly exchange coupled with the rare-earth moments. This kind of situation may not be possible for the FM layer in the multilayers and composites, in which FM component always aligns with the external field as the exchange coupling at the interface is rather weak. Existence of the EB effect in the vicinity of  $T_{comp}$  indicates that the contributions from the local magnetic moments of both the rare-earth ions are nearly compensated (as we see collapse in the  $H_C^{eff}(T)$  of the  $M-H$  loop in Fig.1.12(a)), and the pinning on CEP becomes significant [17]. In this way the soft CEP plays significant role in the existence of the EB effect and its sign change across  $T_{comp}$  in rare-earth inter-metallic compounds. Similar kind of sign change in the EB field across the  $T_{comp}$  has been also observed in the context of other rare-earth inter-metallic compounds of  $Sm_{0.98}Gd_{0.02}Al_2$  [18] and  $Sm_{0.975}Gd_{0.025}Cu_4Pd$  [16]. The difference between the multilayers [84] and single crystalline samples [17] in which the sign change in the EB field is coercive field diverge

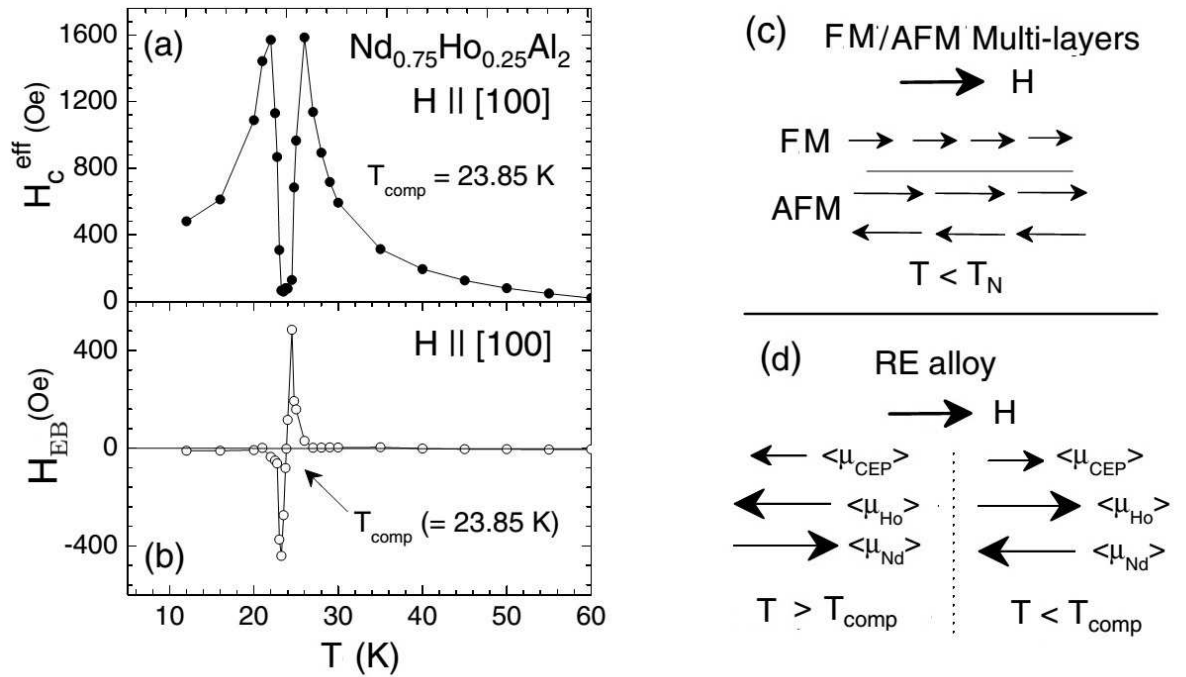


**Figure 1.12:** (a) Temperature dependences of (a) the effective coercive field,  $H_C^{eff}$  and (b) the EB field  $H_{EB}$  in a single crystalline  $Nd_{0.75}Ho_{0.25}Al_2$ . Schematic diagram of the orientation of the different sub-components of magnetization with respect to the applied field (c) for the FM–AFM multilayers and (d) for  $Nd_{0.75}Ho_{0.25}Al_2$  single crystal at  $T > T_{comp}$  and  $T < T_{comp}$  [17].

at the  $T_{comp}$  in the former and collapse in the later.

Later the temperature dependent sign reversal of both magnetization and EB field have been observed in core-shell type AFM  $La_{0.2}Ce_{0.8}CrO_3$  nanoparticles [19]. In this case the negative EB(left shift)/positive EB(right shift) above/below  $T_{comp}$  are explained by considering the antiparallel/parallel coupling between core and shell magnetizations similar to that of  $H_{FC}$  induced tunable EB in multilayers [85]. Core-shell geometry also successfully explained the sign reversal of the magnetization at the  $T_{comp}$ .

Recently even few bulk single phase oxide materials like  $Sr_2YbRuO_6$ ,  $La_{1-x}Pr_xO_3$  and  $NdMnO_3$  also found to exhibit sign reversal of both magnetization and EB across

## 1. Introduction

---

$T_{comp}$  [20–22]. In addition to temperature induced tunable EB,  $H_{FC}$  induced tunable EB is also noticed in these materials. Origin of the EB in these systems is quite different from that of the multilayer and other interface structures and in these materials there is no presence of CEP and core-shell type features. However, various origins have been addressed to explain the tunable EB. One way or other the competing interactions between the magnetic rare-earth ion and the transition metal ion induces the coexistence of FM and AFM orderings within the single phase material, and it results in the EB effect [20–22]. Due to the domination of different orderings above and below the  $T_{comp}$ , and the change of exchange anisotropy between the FM and AFM configurations, the sign change of EB field is seen across  $T_{comp}$ . The exact origin of the tunability of EB effect is not very clear. No common origin is found to explain the tunable EB in these materials. Hence, in this context, it is essential to explore new materials with similar magnetic configurations to observe the wider validity of tunable EB.

### 1.4 Motivation of the thesis

$\text{CoCr}_2\text{O}_4$  possesses very complicated magnetic phase diagram [31, 32]. Non-collinear spin-spirals dictate the magneto-electric coupling in this compound [23–26]. All these unique features of this compound are the result of the weak GMF which is very much sensitive to NN superexchange interactions along A–O–B and B–O–B chains [28, 29, 33]. Substitution of different elements into its different sites may provide ways to vary the strength of superexchange interactions smoothly. Moreover, dependence of particular magnetic sub-lattice on its magnetic and multiferroic properties is seldom studied.

On the other hand, EB effect is a time honoured subject, though a fairly large volume of research has been dedicated to it, the exact underlying origin is still under debate [8, 12, 85, 90, 91]. A new dimension may be added to the technological po-

tentials of the EB effect[12], if it is observed in a multiferroic material [75, 76]. EB effect offers electric control of magnetic properties material [73–76, 92]. Further, the non-collinear magnetic configurations are reported to exhibit EB effect [93–95].

Purpose of this thesis is of two fold. Firstly, it attempts to study the effect of substitution of different elements with different magnetic moments into its Cr-site for the comprehensive understanding of the underlying magnetic properties. We have chosen  $\text{Fe}^{+3}$ ,  $\text{Co}^{+3}$  &  $\text{Al}^{+3}$  to substitute for  $\text{Cr}^{+3}$ , whose magnetic moments and ionic sizes are differ from that of  $\text{Cr}^{+3}$ . We also construct the magnetic phase diagrams as a function of the substituted elements. Secondly, we see the possibility of exploring the tunable EB effect with the substitution of different elements into its Cr-site, while keeping its positive features in the magnetic properties. Non-collinear spin-spiral system  $\text{CoCr}_2\text{O}_4$ , along with the different element substituted samples, are model systems to study EB effect.

## 1. Introduction

---



# Chapter 2

## Experimental Techniques

### 2.1 Sample Preparation

The following sample preparation techniques have been used in this thesis.

#### 2.1.1 Solid state reaction

This is the versatile technique, widely used for synthesising the polycrystalline solid oxide materials [96]. Here, high pure oxides, carbonates, oxalates, acetates, acetonates etc. of metals can be used as the starting materials. The stoichiometric amounts of these starting materials are ground in the organic solvents with the help of agate mortar pestle for several hours to make sure the homogeneity. In general, solids do not react with each other hence these mixtures are heated at high temperatures by using high temperature furnaces. Thermal energy initially decomposes the starting materials and then supplies the energy required for reaction among the constituent elements [96]. Initially the starting materials start to react with each other so the products start forming and for large enough temperatures the reaction completes. The better contact between surfaces of the reactants, gives rise to a fast reaction rate. Hence, a thorough grinding is necessary not only for getting the homogeneity but also to reduce the particle size of the starting materials so that the surface area increases.

## 2. Experimental Techniques

---

Pressing of the samples into pellets with the help of hydraulic press further helps to increase the contact area between the particles of the starting materials. The thermodynamic kinetics of the reaction can also be controlled by the heating/cooling rate of the temperature. This method is well known for the less defective polycrystalline samples. In this method, most of the oxide materials require the temperatures in the range of 1100 °C–1500 °C to form in single phase.

In this thesis Fe and Co substituted  $\text{CoCr}_2\text{O}_4$  samples are prepared by solid state reaction method. Initially required amount of starting materials in the form of oxides/acetates were calculated from the stoichiometric equation and weighed using an electronic balance to an accuracy of 1 mg. These materials ground in the acetone or methanol organic medium using an agate mortar and pestle for several hours such that the homogeneous mixture is obtained. These thoroughly ground mixture of these materials was heated at 600 – 700 °C to evaporate the residual organic solvents. Then the powder was pressed into pellets and sintered at 1100 – 1350 °C for several hours to get single phase polycrystalline samples.

### 2.1.2 Sol-gel method

The drawback of solid state reaction method is that reactants are not mixed on an atomic scale and very high temperature is required to complete the reaction. Hence various liquid reaction methods such as sol-gel methods have been developed to achieve atomic scale mixing of reactants even at considerably low temperatures. Here ‘Sol’ is a stable suspension of colloidal solid particles in a liquid and ‘Gel’ is porous, three dimensional, continuous solid network surrounding a continuous liquid phase. Citrate gel is one of the sol-gel processes. To prepare the sol, initially the starting materials are dissolved in the solvent (distilled water or acid) and then mixed together. The resultant mixture was kept under stirring and then proper ratios of citric acid and ethylene glycol is added. The stirring process is continued for 2–3 hours at 60–80 °C

to ensure the homogeneity. Citric acid is a chelating agent, carboxylate groups in it act as ligands to form complexes with metal cations. The resultant solution is kept at the same temperature for several hours till the water and the acids evaporate. The product obtained after this process is the metal citrate gel. The gel was then fired at high temperatures to remove volatile components trapped in the pores of the gel and organic ligands, and to crystallise the final product. With this process the required particle sizes can be obtained by sintering the samples at different temperatures. Other organic acids like tartaric acid & poly acrylic acid, and polyhydroxy alcohols & poly(ethylene glycol) also can be used as chelating agents. In general metal chlorides and nitrates are widely used as starting materials due to their solubility in water. Typically samples form at the temperatures 500–1200 °C.

Al substituted  $\text{CoCr}_2\text{O}_4$  samples were prepared by using sol-gel method. Here also required amount of nitrates/chlorides along with the citric acid were calculated by using the stiochiometric equation. These materials were dissolved in distilled water/acid, the resultant solutions were mixed together and kept under stirring at 60 °C for several hours to make sure the homogeneous mixing. The black powder obtained after combustion was preheated at 600 °C, then pressed into pellets and sintered at 1100 °C for several hours to get bulk single phase polycrystalline samples.

## 2.2 Measurement Techniques

### 2.2.1 X-ray Diffraction

Phase purity and the crystal structural information of the polycrystalline samples were probed by powder X-ray diffraction measurement at room temperature utilising PANalytical and Rigaku commercial x-ray diffractometer with  $\text{Cu K}\alpha$  ( $\lambda = 1.5406 \text{ \AA}$ ) radiation. In this technique, a thin layer of finely crushed powder of polycrystalline sample is prepared on a glass slide. This layer of powder contains the grains oriented along all the crystallographic directions. As shown in the Fig.2.1 a beam of

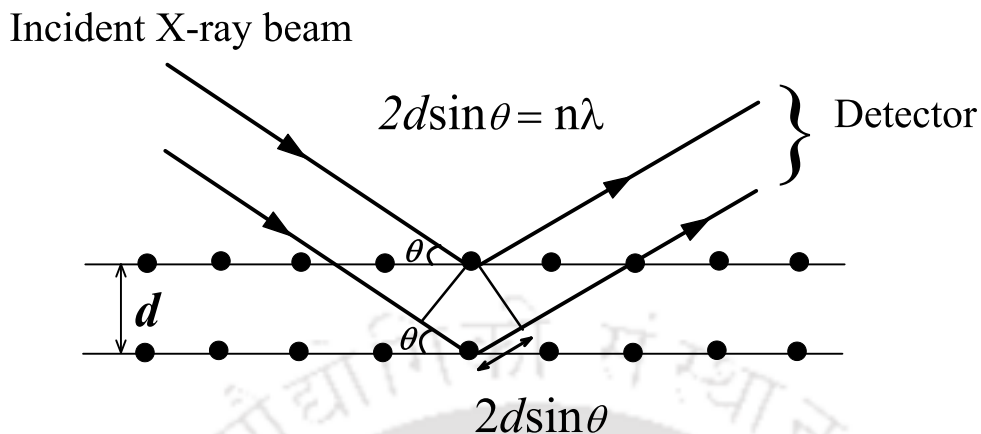


**Figure 2.1:** Illumination of the Bragg's law in case of set of two parallel planes.

monochromatic X-rays such as Cu  $K\alpha$  ( $\lambda = 1.5406 \text{ \AA}$ ) is allowed to incident on to it and then due to the comparable inter-atomic spacing and the wave length, X-rays are diffracted. These diffracted rays are detected by the detector. Diffracted rays undergo constructive interference if Bragg's law is satisfied. Bragg's law can be written as,

$$2d\sin\theta = n\lambda \quad (2.1)$$

where ' $\lambda$ ' is the wavelength of the x-ray beam, ' $d$ ' is the inter planar spacing, ' $n$ ' is the order of diffraction, and ' $\theta$ ' is the angle of incidence/diffraction [37]. When the angle of incidence is changed maximum intensity peaks are observed if different planes are exposed, otherwise no peak is observed. In this way XRD patterns are obtained as a function of  $2\theta$  for all the possible (h,k,l) planes. In order to probe the phase purity of the specimen these patterns are fitted with the theoretical pattern using Rietveld refinement method [97] in a computer program called FULLPROF [98–100]. From this analysis one can extract the crystal structure information such as lattice parameter, different bond lengths, bond angles, atomic positions, occupancies.

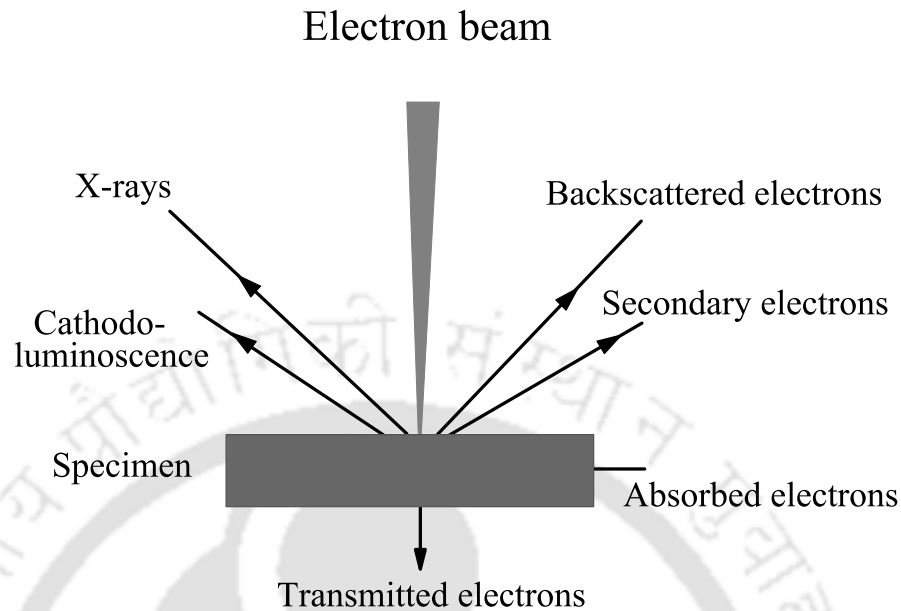


**Figure 2.2:** Block diagram showing various physical phenomena occur when an accelerated beam of electrons is impinged onto the specimen.

### 2.2.2 Scanning electron microscopy

The scanning electron microscope (SEM) is an efficient experimental technique used in both research and industry, to study surface morphology, chemical composition, crystallography and properties on a local scale. In this technique, as shown in the Fig.2.2, the specimen is bombarded by a convergent electron beam from an electron gun. The interaction between the matter and electron beam leads to a number of different types of phenomena such as 1) Backscattered electrons, 2) Secondary electrons, 3) X-rays, 4) Absorbed electrons, 5) Transmitted electrons, 6) Cathodoluminescence. All these generated signals are detected and the intensity of these signals is amplified and converted into image on the computer screen to probe various physical properties of the sample. Backscattered electrons are the electrons of the impinged electron beam that are elastically scattered back from the sample with energies ranging from a few keV to the energy of the incident electrons (typically 15–30 keV). This scattering takes place in a volume extending down to  $0.5 \mu\text{m}$  from the surface and therefore gives information

## 2. Experimental Techniques

---

also about the 'bulk' properties of the material. Secondary electrons are ejected from the inner shells(lower energy) of the atoms of the specimen(mostly within the depth of 5 nm from the surface) in the electron beam impinging process. Secondary electrons and backscattered electrons are used to study the surface morphology related studies. Due to the holes created in the process of secondary electron production, electronic transition from outer shell to lower shell takes place. During this transitions electron emits the X-ray photon. It is known that the energy of these X-rays is different for different atoms. Energy dispersive analysis of X-rays(EDAX) is used to detect what are the elements present in the specimen. Intensity ratio can also give approximate ratio of the elements.

### 2.2.3 Differential scanning calorimetry

Thermal analysis is one of the useful methods to derive both physical and chemical information. Most used technique of thermal analysis is thermogravimetric analysis (TGA). TGA together with thermal analysis techniques such as differential scanning calorimetry (DSC) are used in all types of applications like providing information about the creation/decomposition of chemical bonds between components within the sample, thermal & oxidative stability of a compound, kinematics of the chemical reaction among the reactants, structural transitions in sample, etc. TGA/DSC technique involves the measures of absolute amount and rate of change in weight/heat flow of the sample as either functions of time or temperature in a controlled environment. The basic DSC/TGA setup consists of sample and reference ceramic crucibles mounted on a sensitive simple balance in a closed chamber which has the arrangement for gas inlet and outlet. Both are subjected to identical heat treatments. Initially DSC/TGA curves are measured as function temperature in the required temperature range with the empty sample and reference crucibles for the base line correction. Now sample crucible is filled with the specimen and again the measurement is carried out. TGA

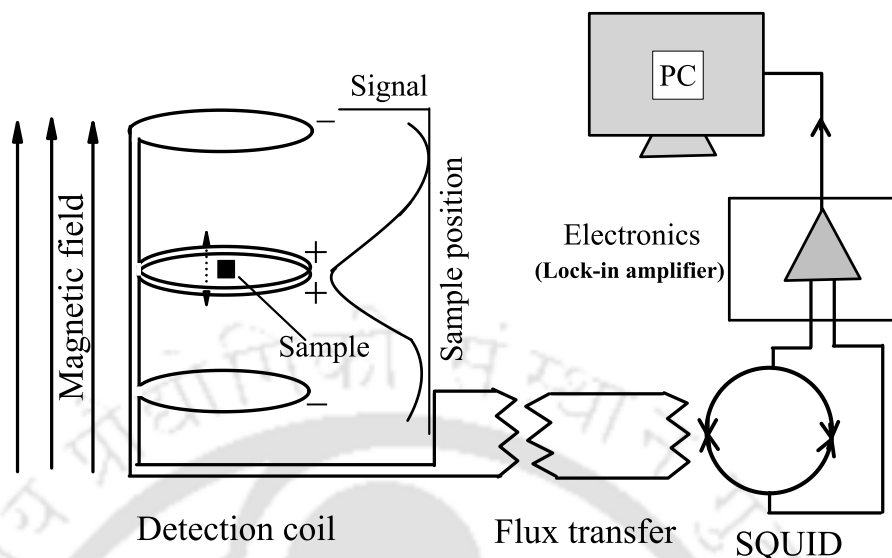


**Figure 2.3:** Block diagram of magnetic signal detecting hardware system in a Quantum Design SQUID magnetometer.

always measures the weight of the sample with respect to that of the reference, whereas the DSC relies on differences in thermal energy required to maintain the sample and reference at an identical temperature. If the reaction/process leads to absorption of heat DSC gives endothermic peak or if deliver the heat then it gives exothermic peak. Temperature at both sample and reference is monitored by the thermocouples fitted along with them.

#### 2.2.4 Superconducting Quantum Interference Device (SQUID) magnetometer

Superconducting Quantum Interference Device (SQUID) magnetometer (S-VSM model 5, Quantum Design, USA) is versatile measurement technique and widely used in the present days for performing precise temperature dependent dc magnetic measurements between 1.8 to 400 K and isothermal magnetization measurements in fields upto 7 Tesla. Magnetization measurements on some of the selected samples under the applied fields upto 14 Tesla were carried out in Vibrating Sample Magnetometer

## 2. Experimental Techniques

---

(VSM) (Oxford instruments, UK). SQUID detection system is the main part of the SQUID magnetometer. Fig.2.3 illustrates the simplified block diagram of the SQUID VSM detection hardware. The superconducting detection coils are configured as a second-order gradiometer, with counterwound outer loops which make the set of coils non-responsive to uniform magnetic fields and linear magnetic field gradients. The detection coils only generate a current in response to local (sample) magnetic field disturbances. So the effect of the magnetic field is only on the sample not on the coil. Sample dimension is much smaller than the dimensions of the detection coils, the current signal in the detection coils is maximum at the centre as shown in the Fig.2.3, hence it is necessary to locate the sample at the center of the coil for the precise measurement. As the sample moves through the detection coils, the magnetic moment of the sample induces an electric current in the coils and is transferred to the SQUID via a transformer. SQUID works as a linear current-to-voltage converter, the variations in the current in the detection coils produce corresponding variations in the SQUID output voltage which is proportional to the magnetic moment of the sample. In this way the flux current generated in the detection coil due to the sample magnetic moment is directly measured in SQUID. But in a conventional VSM the rate of change of flux generated by sample motion gives rise to induced voltages in pick-up coils surrounding the sample and is detected by a lock-in amplifier. If the sample induces a weak signal it is very hard to measure the rate of the flux, VSM fails to measure the weak signal but in SQUID it is not a problem since it measures the flux directly. Hence the sensitivity obtained in SQUID is of the order of  $10^{-7}$  –  $10^{-8}$  emu whereas the sensitivity obtained in the VSM is  $<10^{-6}$  [101]. Error is smaller than size of the symbols given in the plots.

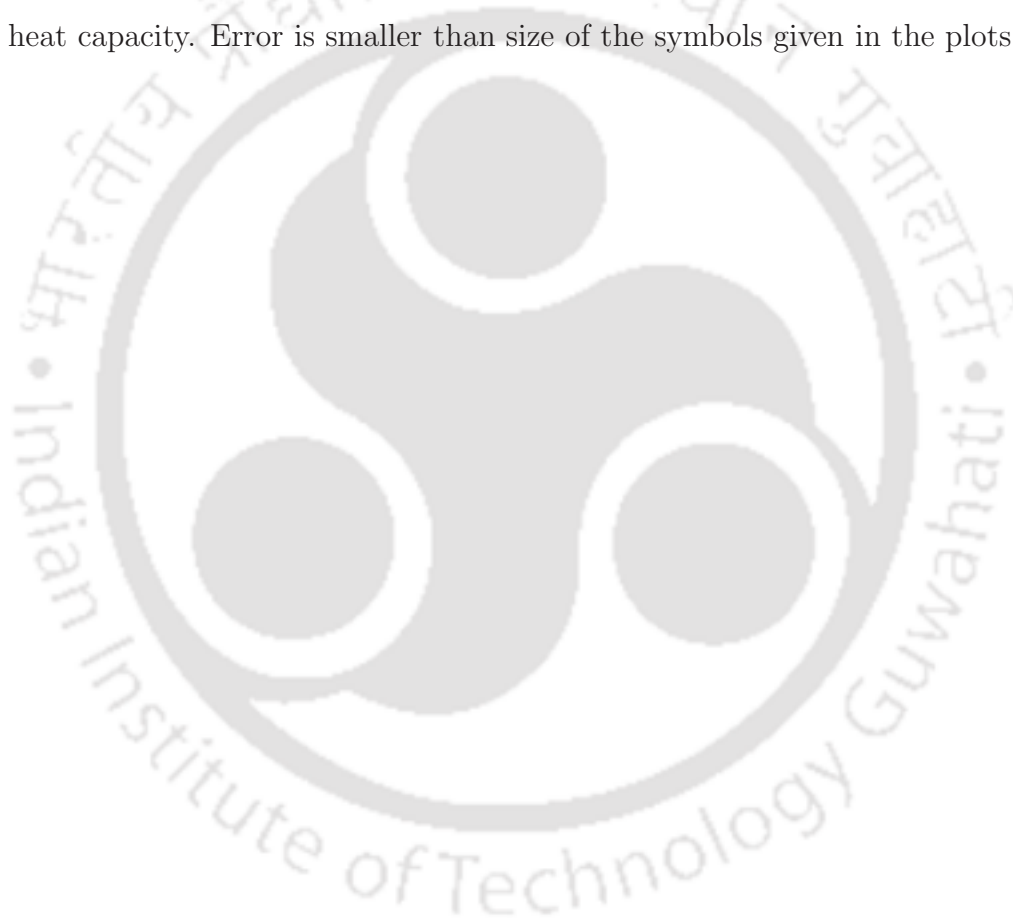
### 2.2.5 Physical Property Measurement System

Physical Property Measurement System (PPMS, Model P 650) is utilised for performing the heat capacity measurements in zero as well as under the applied fields upto 9 Tesla in the temperature range from 1.5 to 300 K. Many different measurement techniques are optimized for different sample sizes and accuracy requirements (high resolution versus accuracy). The Quantum Design heat capacity option in this PPMS uses a relaxation technique that controls the heat added to and removed from a sample while monitoring the resulting change in temperature. Here, a known amount of heat pulse is applied at constant power for a fixed time and then this heating period is followed by a cooling period of the same duration. The heat capacity puck utilizes the standard PPMS 12 pin format for electrical connections, and it provides a small microcalorimeter platform for mounting the sample. Samples are mounted on this platform by a standard cryogenic grease or adhesive such as Apiezon N or H Grease. Typical mass of the sample must be in the order of 10 mg for precise and fast measurement. A single heat capacity measurement consists of several distinct stages. First, the sample platform and puck temperatures are stabilized at some initial temperature. Power is then applied to the sample platform heater for a predetermined length of time, causing the sample platform temperature to rise. When the power is terminated, the temperature of the sample platform relaxes towards the puck temperature. The sample platform temperature is monitored throughout both heating and cooling, providing the raw data of the heat capacity calculation. The sophisticated two-tau model is used to analyse the heat capacity of the sample due to poor thermal attachment of the insulating sample to the platform which produces a temperature difference between the two[102, 103]. The two-tau model simulates the effect of heat flowing between the sample platform and sample, and the effect of heat flowing between the sample platform and puck. The values of the heat capacity and other physical parameters are determined by optimizing the agreement between the

## 2. Experimental Techniques

---

measured data and the two-tau model. In the two-tau model, the first time constant ( $\tau_1$ ) represents the relaxation time between the sample platform and the puck, and the second time constant ( $\tau_2$ ) represents the relaxation time between the sample platform and the sample itself. A second analysis is also performed using a simpler model that assumes perfect thermal coupling between the sample and the sample platform. However, the heat capacity software determines which model fits best to the measured data. The heat capacity of the sample is determined by subtracting the addenda from the total heat capacity. Error is smaller than size of the symbols given in the plots.



# Chapter 3

## Studies in $\text{Co}(\text{Cr}_{1-x}\text{Fe}_x)_2\text{O}_4$ series

### 3.1 Introduction

As described,  $\text{CoCr}_2\text{O}_4$  crystallizes in normal cubic spinel structure, with two magnetic ions  $\text{Co}^{+2}$  ( $3d^7$ ) and  $\text{Cr}^{+3}$  ( $3d^3$ ) in two different sub-lattices namely tetrahedral (A-site) and octahedral (B-Site), respectively. It exhibits very rich magnetic phase diagram [31, 32] and strong magneto-electric coupling [23–26]. It is anticipated that all these interesting properties emerge from the locally unstable conical spin-spirals which depends on the magnetic interactions to  $\text{Cr-O-Cr}$  and  $\text{Co-O-Cr}$ . By studying the magnetic properties of the Fe substituted series one can see how different magnetic transitions are getting affected, while crystal structure remains unchanged. From the point of view of  $\text{CoFe}_2\text{O}_4$ , it is a simple Néel type collinear FIM material with  $T_C$  much above the room temperature. It exhibits almost one order change in the magnitude of the magnetization compared to that of the  $\text{CoCr}_2\text{O}_4$ . Magnetically, the difference between these two compounds is  $\text{Cr}^{+3}$  ( $3d^3$ ) possess the magnetic moment of  $3 \mu_B$ , while that of  $\text{Fe}^{+3}$  ( $3d^5$ ) possess  $5 \mu_B$ . It is also required to see the possibility of enhancing the magnetic transitions of  $\text{CoCr}_2\text{O}_4$ . Further, there is no attempt on the study EB effect in this series.

### 3. Studies in $\text{Co}(\text{Cr}_{1-x}\text{Fe}_x)_2\text{O}_4$ series

---

This chapter deals with the preparation of  $\text{Co}(\text{Cr}_{1-x}\text{Fe}_x)_2\text{O}_4$  for  $x = 0.0-1.0$ , and study of their structural, temperature and magnetic field dependent magnetization, EB effect and thermodynamic properties. To understand the origin of different novel phenomena we propose a temperature and field dependent spin diagram of  $\text{Co}(\text{Cr}_{1-x}\text{Fe}_x)_2\text{O}_4$  and construct Fe concentration dependent magnetic phase diagram.

## 3.2 Experimental details

The phase pure polycrystalline samples of  $\text{Co}(\text{Cr}_{1-x}\text{Fe}_x)_2\text{O}_4$  for  $x = 0.0-1.0$  were prepared by standard solid state reaction method from the starting materials  $\text{Co}_3\text{O}_4$ , (purity 99.9%)  $\text{Cr}_2\text{O}_3$ (purity 99.9%) &  $\text{Fe}_2\text{O}_3$ (purity 99.8%). Thoroughly ground mixer of these materials was first preheated at  $600 - 700^\circ\text{C}$ , then the resultant powders were pressed into pellets and sintered at  $1100^\circ\text{C}$  for 12 hours. Finally, in order to enrich the homogeneity through out the sample, pellets were reground and pelletized and finally sintered at  $1300 - 1350^\circ\text{C}$  for 24 hours. During all heat treatments, the pellets were placed on a bed of powder with the same stoichiometry to minimize the possibility of reaction of the samples with the alumina crucibles. Powder XRD patterns were obtained using  $\text{Cu K}\alpha$  ( $\lambda = 1.5406 \text{ \AA}$ ) radiation in a Panalytical X'pert PRO multi-purpose commercial X-ray diffractometer. Further, the morphology and composition analysis by SEM images and EDAX spectrum, respectively, are used to study the homogeneity and chemical composition of the samples. Magnetization measurements in the temperature range  $2-400 \text{ K}$  and upto the maximum magnetic field of  $140 \text{ kOe}$  were performed using commercial SQUID-VSM (Model S-VSM Quantum design, Inc.). Temperature dependent heat capacity measurements down to  $1.8 \text{ K}$  in the presence of field upto  $90 \text{ kOe}$  were performed using PPMS of Quantum design, Inc. U. S. A. Trapped fields in the superconducting magnet incorporate serious artefacts in the magnetization measurements of FIM materials using SQUID magnetometer. To avoid this artefact, we quenched the superconducting magnet by heating above the super-

conducting state using the reset option available in SQUID-VSM. Trapped field can also be nullified by oscillating the magnet between the positive and negative values. In order to avoid any magnetic field prehistory on the sample magnetic properties, we first performed the thermomagnetic measurements under low applied fields on virgin samples before being exposed to large fields to measure isothermal magnetization etc.

### 3.3 Results

#### 3.3.1 X-ray diffraction studies

Samples are structurally characterized by recording the XRD patterns at room temperature. Fig.3.1 shows the XRD patterns of some of the samples of  $\text{Co}(\text{Cr}_{1-x}\text{Fe}_x)_2\text{O}_4$  series. We can see that all the Fe substituted samples show the XRD patterns similar to the parent  $\text{CoCr}_2\text{O}_4$  compound. To confirm the phase purity of the samples, Rietveld refinement has been performed on the XRD patterns of the all the Fe substituted samples with the help of FULL PROF program. For all the samples the  $\chi^2$  values are found to be in the range of 1 to 1.5, which signify the goodness of the fit to the experimental data. As shown in the Fig.3.2, one can see all the samples adopt cubic spinel structure with  $\text{Fd}\bar{3}\text{m}$  space group. The unit cell parameter  $a \approx 8.332(4)\text{\AA}$  and the coordinates (0.262, 0.262, 0.262) of oxygen ion corresponding to '32e' Wyckoff position of  $\text{CoCr}_2\text{O}_4$  are found to be comparable with the previous reports [31, 104].

Fig.3.3(a) shows the variation in the lattice parameter ' $a$ ' of the cubic unit cell and the coordinate (z, z, z) of oxygen ion corresponding to '32e' Wyckoff position as a function of Fe concentration ' $x$ '. Within the error due to instrumental broadening and fitting, we can see that ' $a$ ' increases non-linearly with Fe concentration ' $x$ '. It is well known that  $\text{Cr}^{+3}$  prefers to occupy the octahedral site due to its very strong crystal field stabilization of  $d^{+3}$  cation ( $t_{2g}^3$ ) in the octahedral crystal field [34, 105]. Hence, tetrahedral (0.25, 0.25, 0.25) as well as octahedral (0.5, 0.5, 0.5) coordinates

### 3. Studies in $\text{Co}(\text{Cr}_{1-x}\text{Fe}_x)_2\text{O}_4$ series

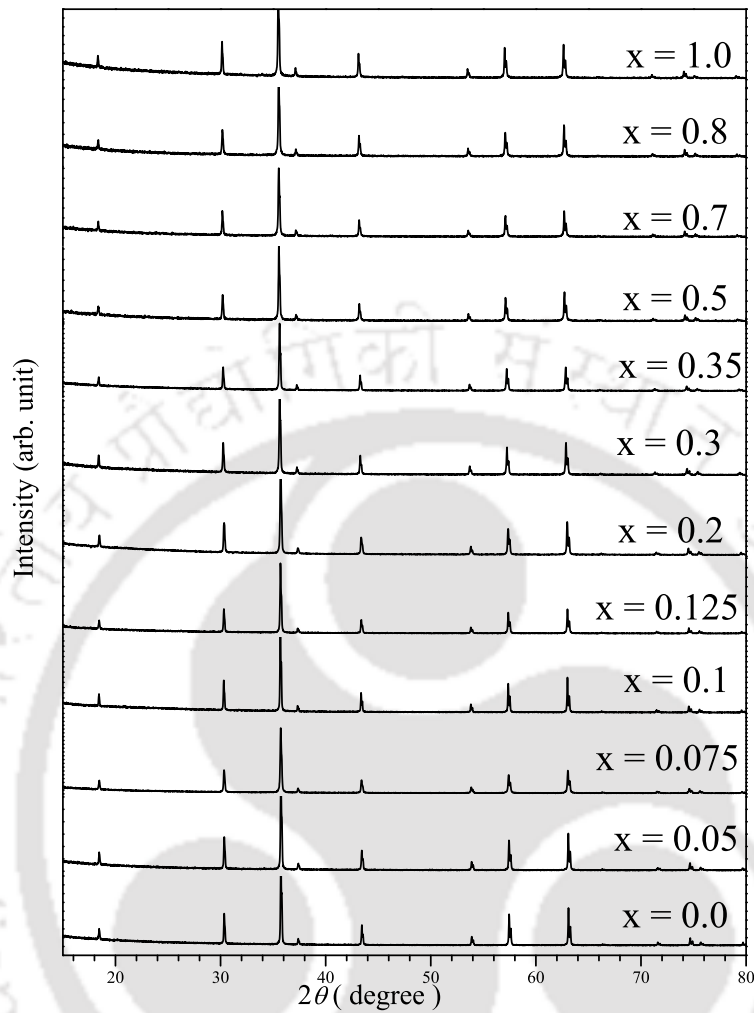


**Figure 3.1:** X-ray diffraction patterns of  $\text{Co}(\text{Cr}_{1-x}\text{Fe}_x)_2\text{O}_4$  samples for various values of  $x$  recorded at room temperature on the powdered samples.

have been provided for Co & Fe ions in the refinement. We know that the ionic sizes of  $\text{Fe}^{+3}$  ( $\sim 0.785 \text{ \AA}$ ) and  $\text{Co}^{+2}$  ( $\sim 0.885 \text{ \AA}$ ) are larger than the ionic size of  $\text{Cr}^{+3}$  ( $\sim 0.755 \text{ \AA}$ ) in the octahedral crystal field. But, in tetrahedral crystal field  $\text{Fe}^{+3}$  has smaller ionic size of  $\sim 0.63 \text{ \AA}$  compared to  $\sim 0.72 \text{ \AA}$  of  $\text{Co}^{+2}$ . If  $\text{Fe}^{+3}$  occupy octahedral site, expansion in unit cell is straight forward. On the other hand, if  $\text{Fe}^{+3}$  occupy tetrahedral site the same amount of  $\text{Co}^{+2}$  occupy octahedral site, expansion in lattice parameter is possible. From this explanation, we can conclude that the Fe substitution for Cr

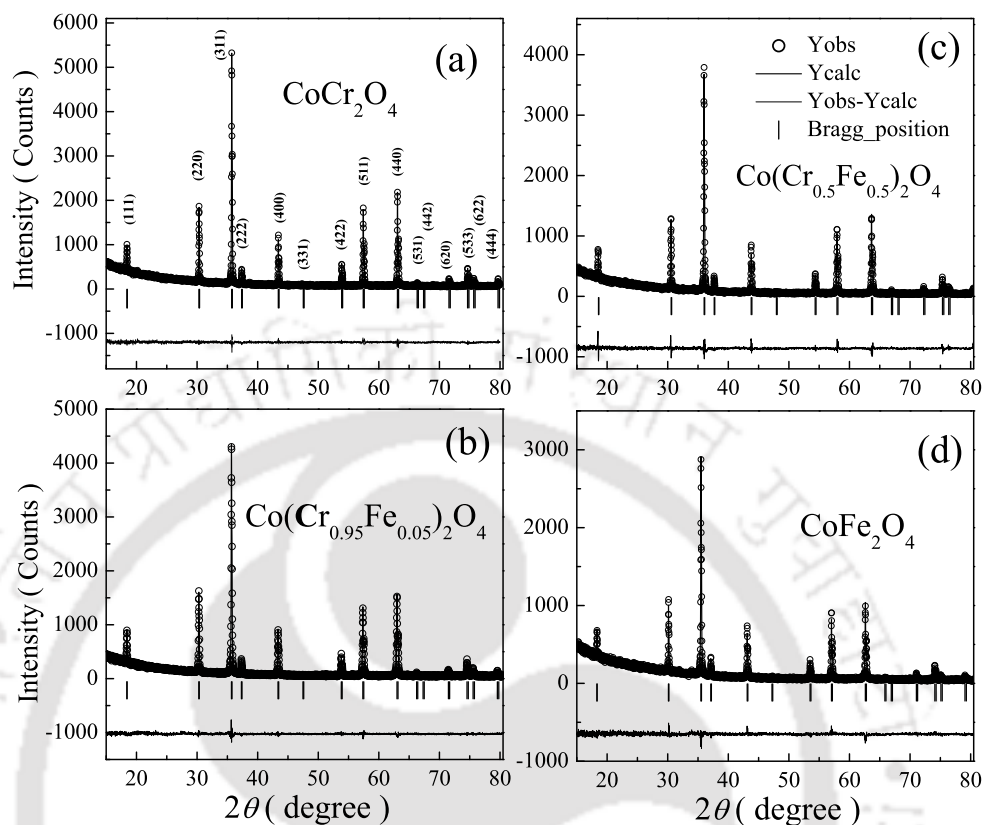


**Figure 3.2:** Observed and fitted powder XRD patterns of  $\text{CoCr}_2\text{O}_4$ ,  $\text{Co}(\text{Cr}_{0.95}\text{Fe}_{0.05})_2\text{O}_4$ ,  $\text{Co}(\text{Cr}_{0.5}\text{Fe}_{0.5})_2\text{O}_4$  and  $\text{CoFe}_2\text{O}_4$  samples. For the better clarity of the Bragg positions, difference curve between observed and fitted profiles is shifted downward.

in  $\text{CoCr}_2\text{O}_4$  induced expansion in the unit cell length may be valid. From the refinement we observed that upto  $x = 0.1$ , Fe ions mainly occupy B-site, beyond which it is distributed in A and B-sites. The rate of increase in  $a$  reduces for  $x \geq 0.5$  and it signifies the substitution of Fe into the octahedral site more preferably. These observations of the ionic distribution at various Fe concentrations are in good agreement with the cation distribution calculated from previous Mössbauer measurements [106–108]. Even the end compound of this series, i.e.,  $\text{CoFe}_2\text{O}_4$  in this study is found to exhibit the saturation magnetization value similar to that Sawatzky et al. [50] in which they observed considerably more presence ( $\sim 24\%$ ) of  $\text{Co}^{+2}$  in tetrahedral site. Decrease in

### 3. Studies in $\text{Co}(\text{Cr}_{1-x}\text{Fe}_x)_2\text{O}_4$ series

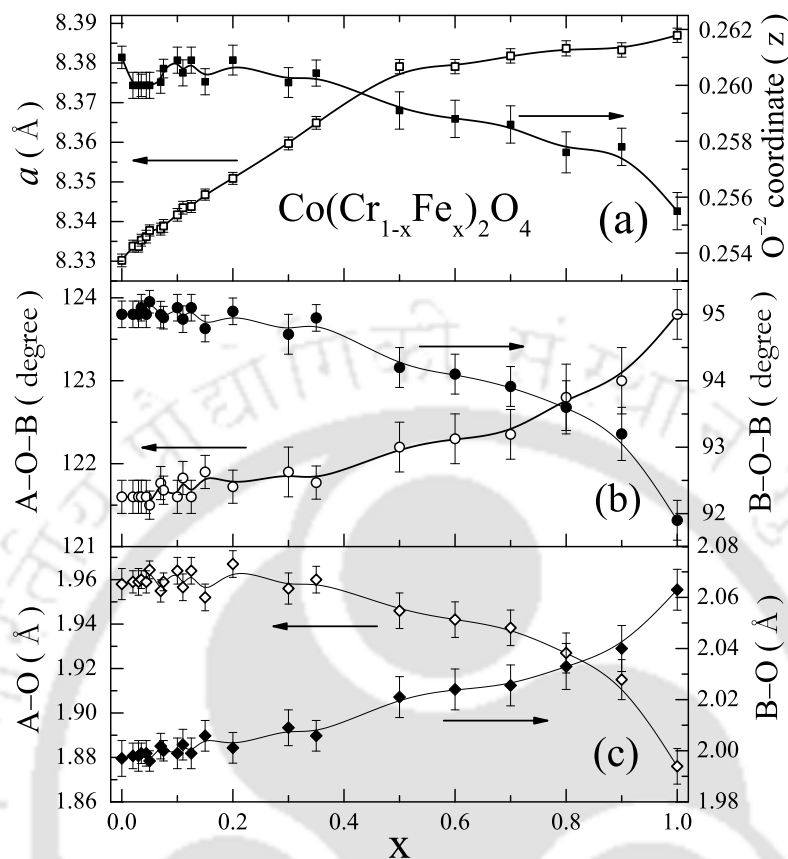


**Figure 3.3:** (a) Variation of lattice parameter ‘ $a$ ’ and the coordinate ( $z, z, z$ ) of oxygen ion with Fe concentration ‘ $x$ ’ in  $\text{Co}(\text{Cr}_{1-x}\text{Fe}_x)_2\text{O}_4$ . (b) Variation of A–O–B and B–O–B bond angles. (c) Variation of A–O and B–O bond lengths. Here, vertical bars indicate the error in ‘ $a$ ’ due to instrumental broadening and the fitting of data in case of other parameters it only due to the error in fitting the data.

the oxygen coordinate towards 0.25 with increase in the Fe concentration may indicate that the spinel structure is becoming less distorted spinel.

Fig.3.3(b) depicts how the bond angles corresponding to the nearest neighbour superexchange networks of A–O–B and B–O–B vary with Fe substitution concentration. Bond angle B–O–B decreases towards  $90^\circ$ , but that of A–O–B increases with increase in Fe concentration. The bond length of A–O decreases and that of B–O increases slightly with Fe concentration [Fig.3.3(c)]. Influence of these struc-

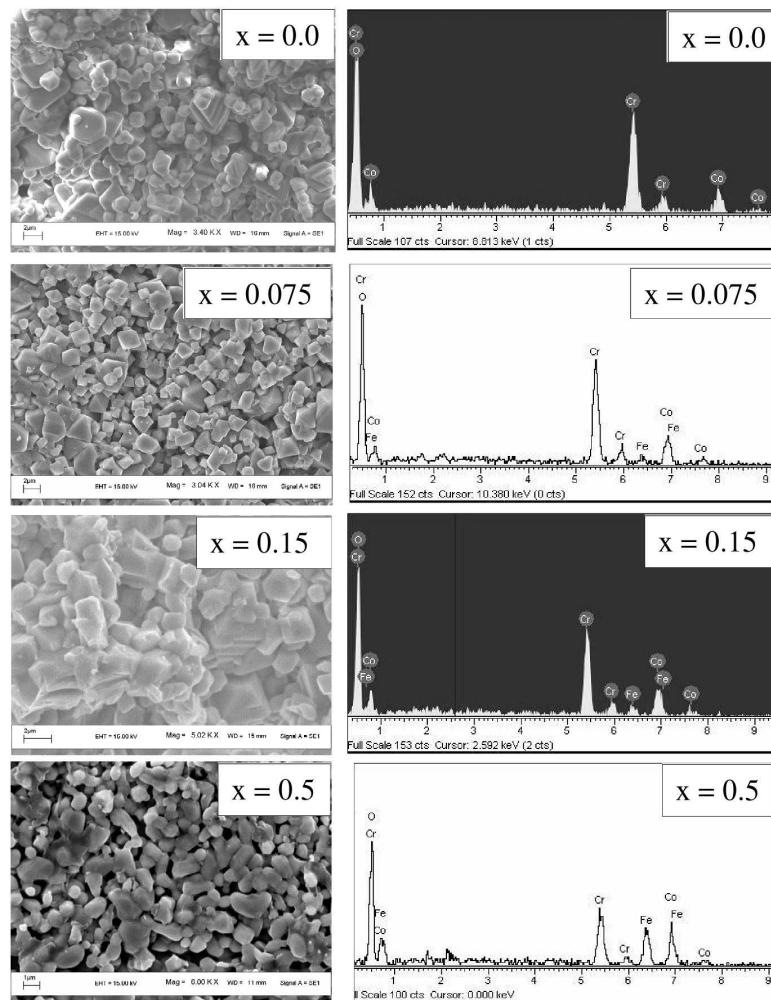


**Figure 3.4:** SEM images and EDAX spectra of  $\text{Co}(\text{Cr}_{1-x}\text{Fe}_x)_2\text{O}_4$  samples.

tural changes on the magnetic properties are discussed in the later sections.

In addition to XRD studies, as shown in the left panels of Fig.3.4 microstructure from the SEM images also confirm the phase purity of the samples. Typical particle of the samples is found to be in the range of 1-2  $\mu\text{m}$ . Chemical compositions obtained from EDAX[right panels of Fig.3.4] analysis are found to be comparable to starting compositions of the samples.

#### 3.3.2 Temperature and field dependent magnetic properties

Fig.3.5(a)-(l) demonstrate the temperature dependent magnetization of  $\text{Co}(\text{Cr}_{1-x}\text{Fe}_x)_2\text{O}_4$  samples measured in zero field cooled (ZFC) and field cooled warming (FCW) mode for the applied field of 1 kOe. In ZFC mode, initially the parent sample is cooled in zero field from 300 K to 3 K and the field is applied at 3 K and then the data is measured while warming up. In FCW mode, sample is cooled to 3 K in a static field from 300 K and the magnetization is measured again while warming the sample by keeping the same field is on. The parent compound  $\text{CoCr}_2\text{O}_4$  exhibits FIM transition at around  $T_C = 94$  K, and it can be seen from the plots that the  $T_C$  increases systematically with increase in the Fe concentration. The  $T_C$  shifts above the room temperature, for the Fe concentration above  $x = 0.5$ . It signifies that substituted Fe ions are strengthening the superexchange interactions of the system. The magneto-structural transition at  $T_S \sim 26$  K and the lock-in transition,  $T_L \sim 13$  K, initially do not get affected by substituted Fe ions upto  $x = 0.1$ , but for  $x > 0.1$  it moves towards low temperature and vanishes for further higher concentrations.

In addition to all these features, the magnitude of the magnetization below  $T_C$  decreases with Fe concentration and for  $x = 0.05$  it exhibits reversal in the magnetization below  $T_{comp}$  in the FCW mode. But surprisingly, the ZFC magnetization data do not show any sign change. The temperature at which the temperature dependent magnetization passing through zero ( $M = 0$  axis) and going towards negative value called compensation temperature,  $T_{comp}$ .  $T_{comp}$  can be seen to increase with Fe concentration upto  $x = 0.1$  and there after the samples do not show any magnetization reversal but show a dip just below  $T_C$  for  $x = 0.125$ . For higher Fe concentrations ( $\geq 0.5$ ) we can see a clear dip marked as  $T_R$ . The ZFC and FCW curves show clear bifurcation below  $T_R$ . Another important feature more feature of ZFC curve with Fe concentration is the sharpened transition at  $T_S$ .

Nine panels (a)-(i) of Fig.3.6 display the field dependent magnetization ( $M-H$ )

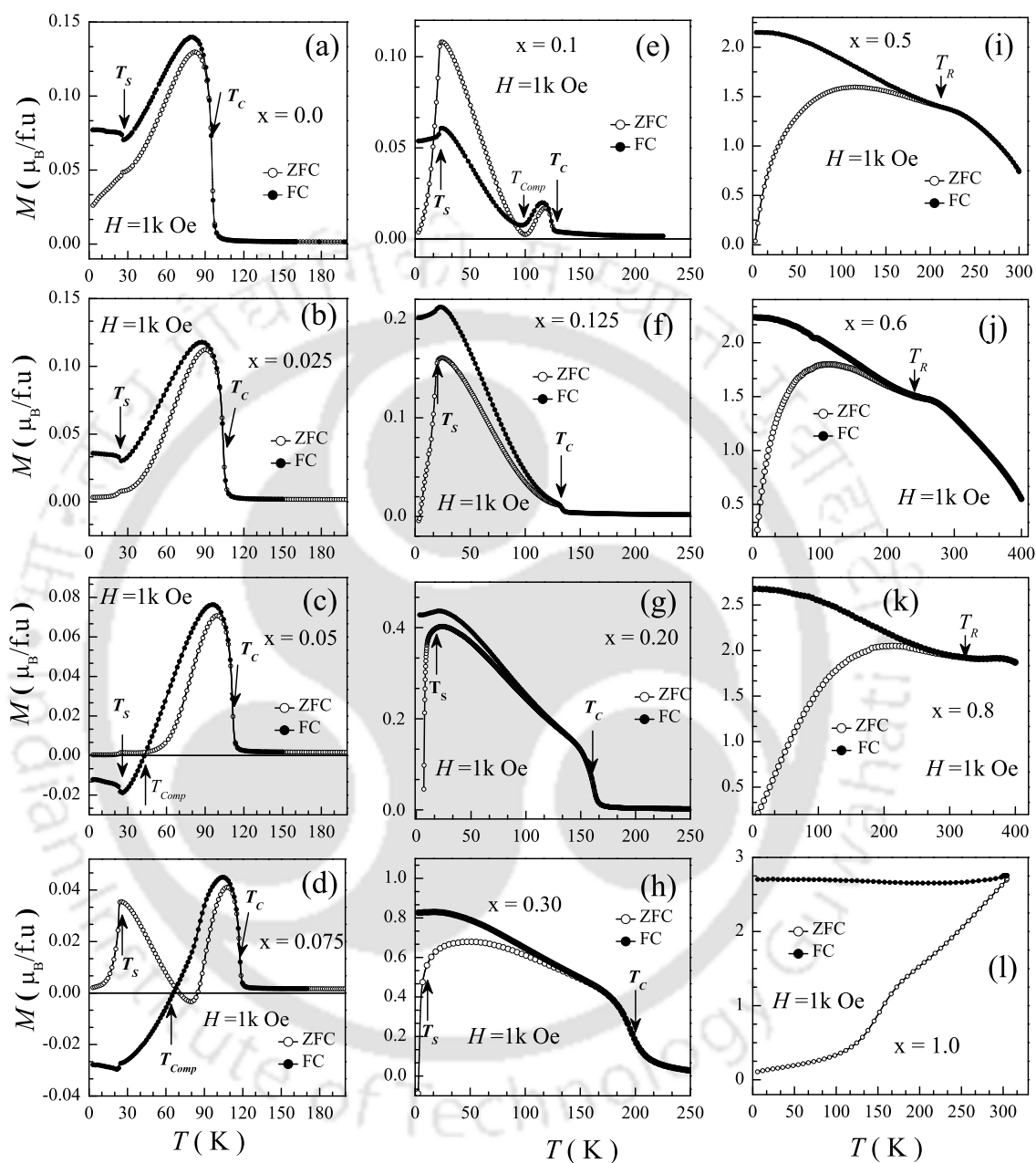


**Figure 3.5:** Temperature dependent magnetization of  $\text{Co}(\text{Cr}_{1-x}\text{Fe}_x)_2\text{O}_4$  measured in ZFC and FCW modes for the applied field of  $H = 1$  kOe. Here  $T_C$ ,  $T_S$ ,  $T_{comp}$  and  $T_R$ , respectively, are long range FIM transition, magneto-structural transition, compensation temperature and the temperature at which the magnetization show dip, respectively.

### 3. Studies in $\text{Co}(\text{Cr}_{1-x}\text{Fe}_x)_2\text{O}_4$ series

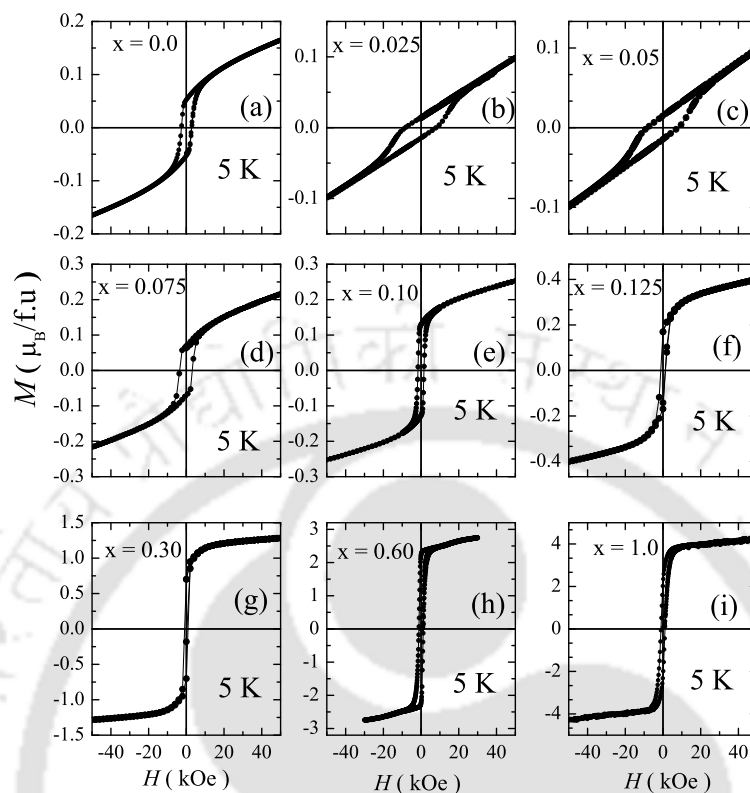


**Figure 3.6:** Field dependent magnetization of  $\text{Co}(\text{Cr}_{1-x}\text{Fe}_x)_2\text{O}_4$  samples measured at 5 K measured after cooling the sample in zero field.

loops of  $\text{Co}(\text{Cr}_{1-x}\text{Fe}_x)_2\text{O}_4$  samples at 5 K measured after cooling the sample in zero field. With Fe concentration the magnitude of the magnetization at the field of 50 kOe decreases upto the  $x = 0.05$ , thereafter it increases systematically. From the shape of the  $M$ - $H$  loop we can see that the magnetization do not show any signature of saturation upto  $x = 0.05$ , this may signify ordering becomes AFM in nature. Above this concentration samples exhibit again FIM behaviour. Fig.3.7 shows the coercive field,  $H_C$  and the saturation magnetization of all the samples at 5 K.  $M_S$  is calculated by fitting the high field part of  $M$ - $H$  data to  $M(H) = \chi_{AFM}H + M_S$ , here  $\chi_{AFM}H$  is the AFM contribution to the magnetization. These two parameters show completely opposite trend as a function of Fe concentration.  $H_C$  increases upto  $x = 0.05$  and decreases while  $M_s$  decreases upto  $x = 0.05$  and then increases. All these features

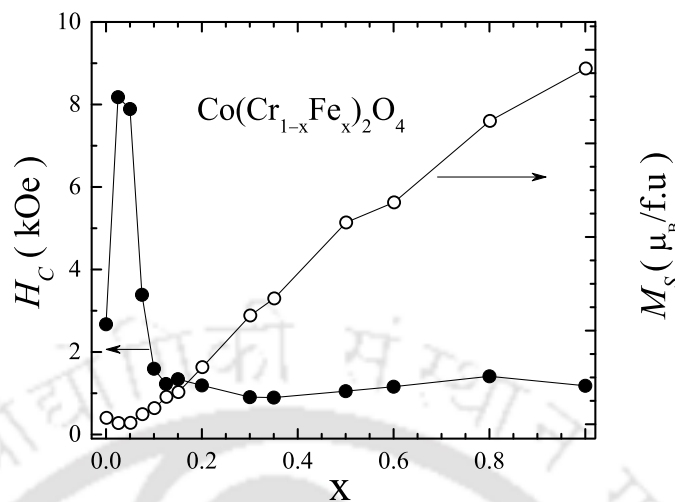


**Figure 3.7:** Coercive field and saturation magnetization of  $\text{Co}(\text{Cr}_{1-x}\text{Fe}_x)_2\text{O}_4$  at 5 K.

employs that the substituted Fe ions are affecting the magnetic structure of the system.

From the Fig.3.5, we can see that the samples upto  $x = 0.125$  exhibit multiple magnetic transitions. For the deeper understanding of the magnetic behaviour of the samples in this range we carried out detailed magnetization studies on the samples with very closed Fe concentrations between  $x = 0.0$  and  $0.125$ .

### 3.3.3 Magnetic compensation and field induced transitions

Main panel of Fig.3.8(a) shows the temperature dependent magnetization measured in field cooled cooling (FCC) mode (i.e., magnetization is measured while cooling the temperature from above  $T_C$  to 2 K with field on) of  $\text{Co}(\text{Cr}_{1-x}\text{Fe}_x)_2\text{O}_4$  under the applied field of nominal zero ( $\sim 10$  Oe) to understand the absolute behaviour of magnetization and hence different transitions. It is clear that  $M_{FCC}(T)$  of  $x = 0.044$  sample is drawn to zero and shows negative magnetization below  $T = 28.7$  K [inset (i) of Fig.3.8(a)]. But it shows up turn as the magneto-structural transition evolves at around 24.9 K. In case of  $x = 0.05$ ,  $0.075$  and  $0.1$  samples the  $M_{FCC}(T)$  crosses  $M = 0$  axis at  $T_{comp} \approx 43.8$  K,  $67.8$  K and  $90$  K, respectively. Below  $T_{comp}$ ,  $M_{FCC}(T)$  continues to be negative,

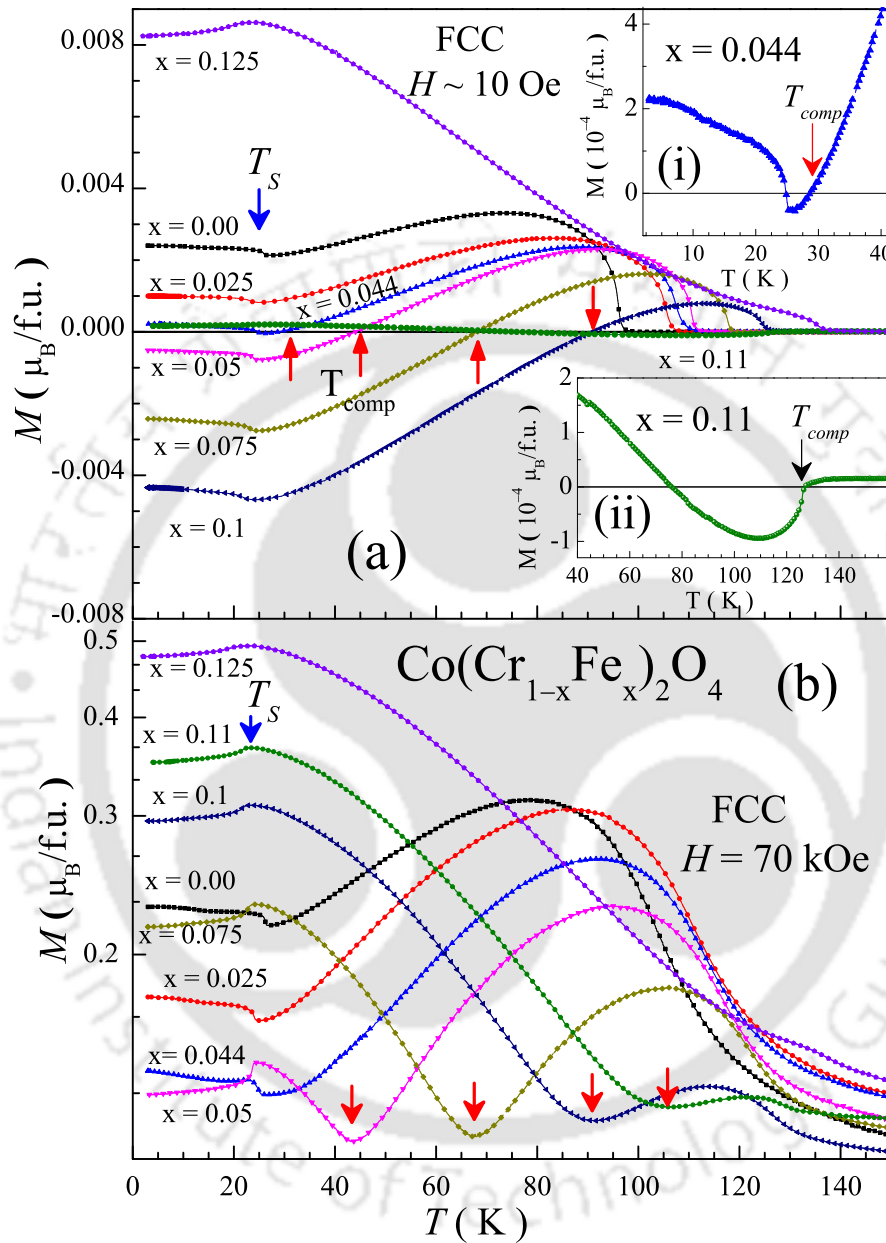


**Figure 3.8:** Temperature dependent magnetization curves of  $\text{Co}(\text{Cr}_{1-x}\text{Fe}_x)_2\text{O}_4$  samples measured in FCC mode for the applied field of (a) nominal zero ( $\sim 10$  Oe) and (b) 70 kOe. Insets (i) and (ii) of (a) are enlarged views of compensation points of  $x = 0.044$  and  $x = 0.11$  samples, respectively.

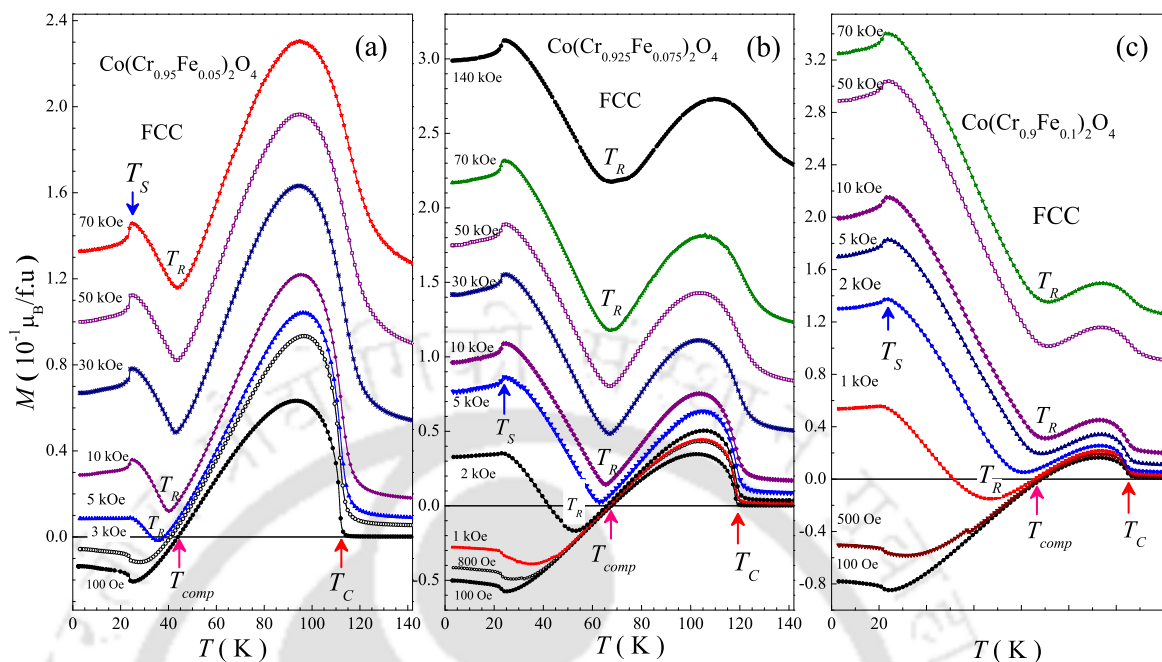


**Figure 3.9:** Temperature dependent  $M_{FCC}$  of (a)  $\text{Co}(\text{Cr}_{0.95}\text{Fe}_{0.05})_2\text{O}_4$ , (b)  $\text{Co}(\text{Cr}_{0.925}\text{Fe}_{0.075})_2\text{O}_4$  and (c)  $\text{Co}(\text{Cr}_{0.9}\text{Fe}_{0.1})_2\text{O}_4$  samples under various applied fields ranging from 100 Oe to 70 kOe (140 kOe for  $x = 0.075$ ). In all the panels,  $T_C$ ,  $T_{comp}$ ,  $T_S$  and  $T_R$  denote different transition temperatures.

and the magnitude of negative magnetization increases. Whereas,  $x = 0.11$  sample shows a peculiar behaviour, we can see the magnetic moments are fully compensated compared to other Fe concentration in the series, due to which it exhibits compensation at a temperature just below  $T_C$  [inset (ii) of Fig.3.8] and the magnetization switches to positive value easily with small applied field. As the Fe concentration increases to a level of  $x = 0.125$  all these features vanish and magnetization remains positive throughout, without crossing  $M = 0$  axis at any temperature, over the full temperature range below  $T_C$ . The magneto-structural transition,  $T_S$  [23, 28, 29] is also clearly seen to exist with Fe substitution but move slightly towards lower temperature with Fe concentration. Fig.3.8(b) dictates the behaviour of  $M_{FCC}(T)$  in  $\text{Co}(\text{Cr}_{1-x}\text{Fe}_x)_2\text{O}_4$  under a large field of 70 kOe, where all the anisotropic effects vanish. The monotonic decreasing trend of  $M_{FCC}$  up to  $x = 0.11$  below the  $T_C$  is much more clear in this panel

### 3. Studies in $\text{Co}(\text{Cr}_{1-x}\text{Fe}_x)_2\text{O}_4$ series

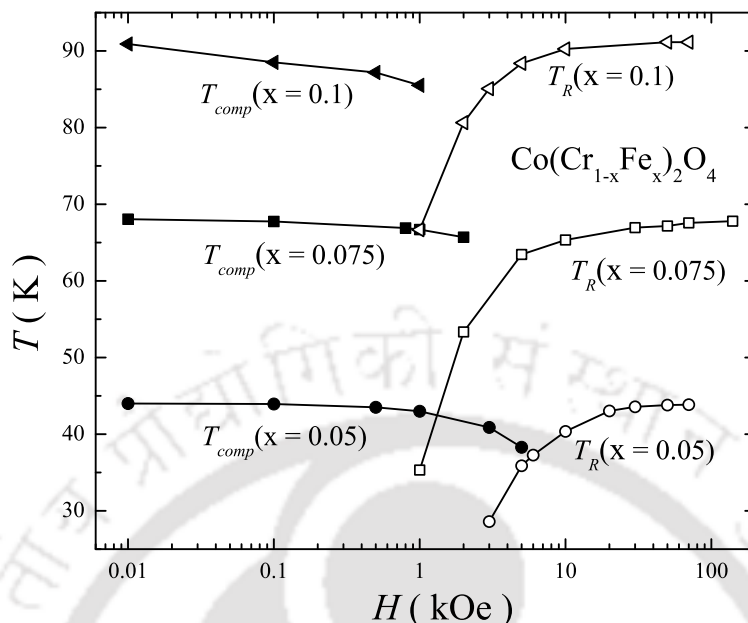


**Figure 3.10:** Applied field dependence of  $T_{comp}$  and  $T_R$  for  $\text{Co}(\text{Cr}_{1-x}\text{Fe}_x)_2\text{O}_4$  samples extracted from FCC magnetization while applied field varying from 10 Oe to 70 kOe (140 kOe in case of  $x = 0.075$ ).

and the  $M_{FCC}(T)$  at a temperature at which we noticed the  $T_{comp}$  in the  $M_{FCC}(T)$  curve in the applied field of  $H \sim 10$  Oe. Below  $T_{comp}$ , the situation reverses compared to that observed in low field,  $M_{FCC}(T)$  is found to increase monotonically with Fe concentration. We can understand that the field induced transitions commenced with the application of large applied field.

Three panels of Fig.3.9, namely (a), (b) and (c), respectively, draw the attention onto how gradually the field induced transitions start appearing in  $M_{FCC}(T)$  of  $\text{Co}(\text{Cr}_{0.95}\text{Fe}_{0.05})_2\text{O}_4$ ,  $\text{Co}(\text{Cr}_{0.925}\text{Fe}_{0.075})_2\text{O}_4$  and  $\text{Co}(\text{Cr}_{0.9}\text{Fe}_{0.1})_2\text{O}_4$  samples with increasing applied field from 100 Oe to 70 kOe (140 kOe in case of  $x = 0.075$  sample). In all the panels, it is prominent that under small applied fields  $M_{FCC}(T)$  exhibits reversal below the respective  $T_{comp}$ . When the field is increased to critical value,  $M_{FCC}(T)$  exhibits field induced transition at  $T_R$ . With increasing the Fe concentration, the

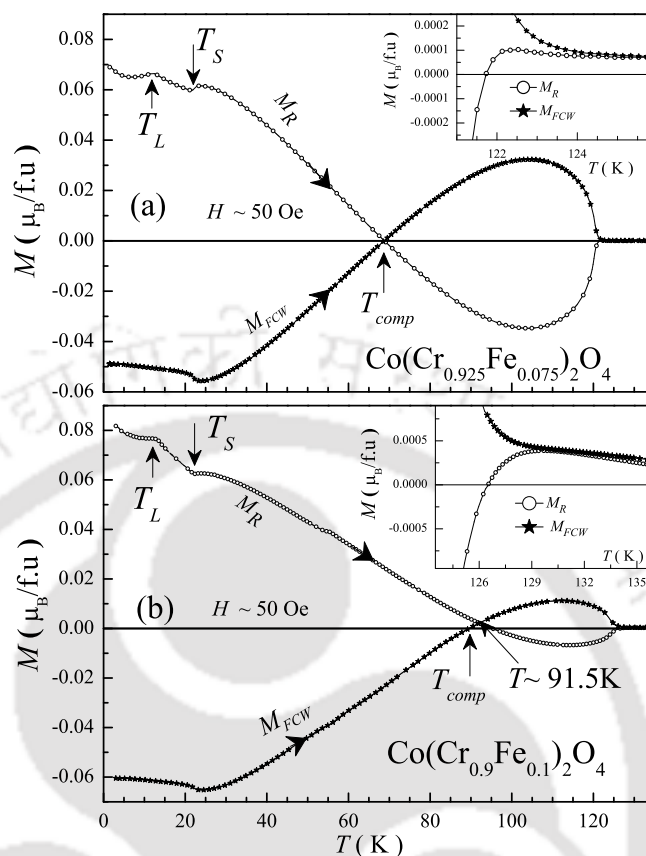


**Figure 3.11:** Temperature dependence of  $M_R$  (the magnetization obtained after cooling the sample under the field of 50 kOe from 300 K to 2 K, then drooping field the field to  $\sim 50$  Oe) measured under the field of 50 Oe, while warming from 2 K along with the field cooled warming magnetization ( $M_{FCW}(T)$ ) measured in the same field ( $\sim 50$  Oe).

critical field required for surfacing of turnover at  $T_R$  decreases. In order to see how much robust is the AFM ordering at  $T_{comp}$ , derived from superexchange interactions in these system, we carried out  $M_{FCC}(T)$  measurement of  $x = 0.075$  sample under a large field of 140 kOe, from this, it is evident that the dip at  $T_R$  is broadened up but the complete rotation of the moments is not possible even at this large field. While increasing the field  $T_C$  is broadened, as expected for a FIM/AFM ordering, whereas transition at  $T_S$ , doesn't get effected too much but becomes sharp. Fig.3.10 depicts how  $T_{comp}$  and  $T_R$  vary as a function of the applied field. It can be seen that the  $T_{comp}$  of each sample decreases with increasing field, thereby  $T_R$  commences. With increase

### 3. Studies in $\text{Co}(\text{Cr}_{1-x}\text{Fe}_x)_2\text{O}_4$ series

---

in field  $T_R$  move toward high temperature, and reaches  $T_{comp}$  under sufficiently high fields but never exceeds the  $T_{comp}$ .

To further elucidate the reversal in the magnetization at  $T_{comp}$ , the temperature dependent  $M_R(T)$  of  $\text{Co}(\text{Cr}_{0.925}\text{Fe}_{0.075})_2\text{O}_4$  and  $\text{Co}(\text{Cr}_{0.9}\text{Fe}_{0.1})_2\text{O}_4$  samples is presented in Fig.3.11(a) and (b), respectively. To obtain  $M_R$  at 2 K, first sample is cooled in the applied field of 50 kOe then the field is decreased to 50 Oe and  $M_R(T)$  is measured while warming. For the comparison  $M_{FCW}(T)$  under same field is also plotted. We can see that these two are mirror image of another in the temperature range  $T \geq T_S$ . One can understand that, these two measurements started with quite opposite magnetic configurations, and hence, with different anisotropies at 2 K.  $M_R(T)$  doesn't follow the path of  $M_{FCC}(T)$  under 50 kOe, as shown in the Fig.3.9, in which the moments are forced to align antiparallel to field across  $T^*(\approx T_{comp})$  as a result, the total magnetization is positive through out temperature, leaving a deep kink in  $M_{FCC}(T)$  at  $T_R$ . Whereas in  $M_R(T)$ , since the small field (less than anisotropic field) the opposite counterpart can't rotate along the field at  $T_{comp}$ , the magnetization changes sign across  $T_{comp}$  and merge with  $M_{FCW}(T)$  at  $T_C$  as shown in the insets of Fig.3.11. The magneto-structural transition observed in  $M_{FCC}(T)$  at  $T_S$  is also clearly seen in the  $M_R(T)$  at the same temperature  $T_S$ . Another interesting feature is the lock-in transition (transformation of incommensurate to commensurate spin-spiral [30, 31]) which is hard to capture in  $M_{FCC}(T)$  is also very prominent in  $M_R(T)$  at  $T_L$ . Hence,  $M_R(T)$  is very efficient tool to resolve sensitive small fluctuations in the magnetic configuration.

#### 3.3.4 Exchange bias effect

From the reports on the rare-earth inter-metallic systems [16–18, 20] and in core-shell type magnetic nano particles [19], it has been found that the materials in which the magnetization reversal appears are prone to exhibit the sign change in the EB across the  $T_{comp}$ . The study of EB effect in the compensated samples may reveal new features

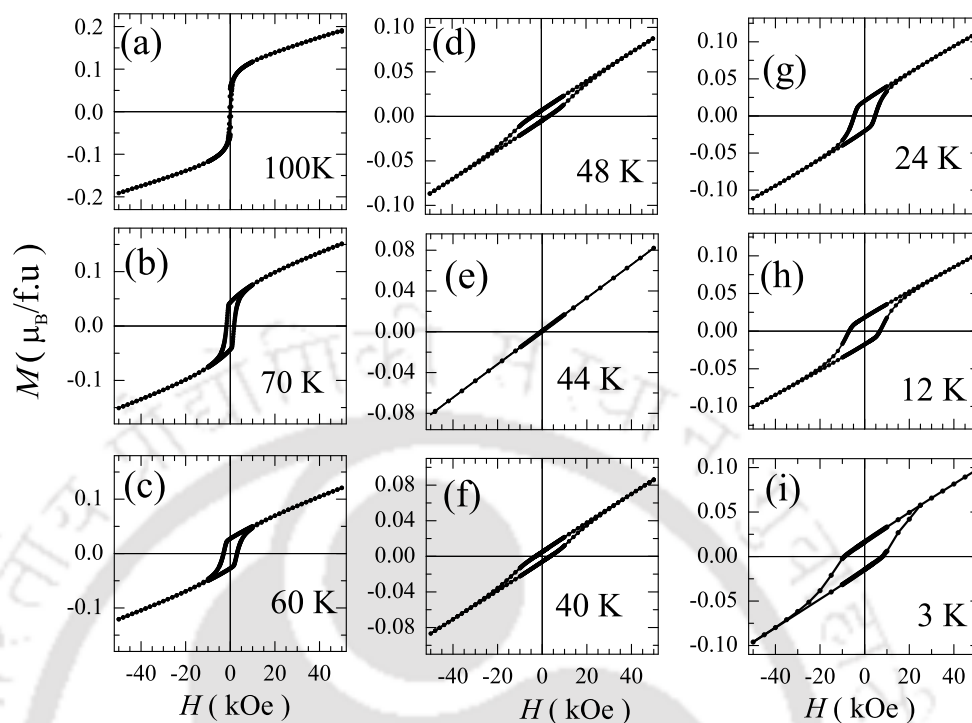


**Figure 3.12:** (a)-(i) 70 kOe field cooled  $M$ - $H$  loops of  $\text{Co}(\text{Cr}_{0.95}\text{Fe}_{0.05})_2\text{O}_4$  sample at various temperatures. The linear trend of  $M$ - $H$  loop in the vicinity of  $T_{\text{comp}} \approx 43.8$  K indicate the quasi AFM behaviour of the sample.

in  $\text{Co}(\text{Cr}_{1-x}\text{Fe}_x)_2\text{O}_4$  series.

To study the temperature dependence of EB effect, the field cooled (FC)  $M$ - $H$  loops are recorded by implementing the following procedure. Here, the specimen was cooled in 70 kOe from 300 K to the target temperature at which we interested in recording  $M$ - $H$  loop, and thereafter the field was cycled between  $\pm 50$  kOe to complete the  $M$ - $H$  loop. In order to avoid the possibility of the sample history on the  $M$ - $H$  loop measurements, this entire process was repeated to obtain the  $M$ - $H$  loop at each and every temperature. Fig.3.12(a)–(i) show the 70 kOe FC  $M$ - $H$  loops of  $\text{Co}(\text{Cr}_{0.95}\text{Fe}_{0.05})_2\text{O}_4$  sample in the magnetically ordered state below  $T_C (\approx 110$  K). We can see just below the  $T_C$  at 100 K the sample exhibits soft FIM behaviour without any opening in the loop. While decreasing the temperature it shows opening in the loop and also reduction in the magnitude of magnetization. This may indicate that

### 3. Studies in $\text{Co}(\text{Cr}_{1-x}\text{Fe}_x)_2\text{O}_4$ series

---

the contribution to the total magnetization is coming from two oppositely aligned sub-lattices. Further lowering in the temperature towards  $T_{comp}(\approx 43.8 \text{ K})$ , we can see that the behaviour of the loop seems to be AFM in nature with the collapsing of the loop width. We observe the linear behaviour of  $M-H$  loop near  $T_{comp}$  which depicts the fact that the moments of the two sub-lattices are nearly compensated at  $T_{comp}$ . Again for the temperatures below  $T_{comp}$  the behaviour becomes FIM with increasing the loop width upto 3 K. Overall, the considerable opening observed in the  $M-H$  loop at little far away from  $T_{comp}$  signify a large contribution coming from the uncompensated moments and in the vicinity of  $T_{comp}$  it becomes AFM because of compensated moments.

A set of six panels in Fig.3.13 show the enlarged portions of 70 kOe FC  $M-H$  loops of  $\text{Co}(\text{Cr}_{0.95}\text{Fe}_{0.05})_2\text{O}_4$  sample around the  $T_{comp} \approx 43.8 \text{ K}$ . The small left shift of center of gravity (CG) of  $M-H$  loop at  $50 \text{ K} > T_{comp}(\approx 43.8 \text{ K})$  [Fig3.13(a)] signify the appearance of positive EB[explained in the following section], which gets enhanced as the temperature is decreased towards the  $T_{comp}$ . For  $44.5 \text{ K}$  it can be observed that the  $M-H$  loop is shifted as a whole to the left side [Fig3.13(b)]. With further decreasing the temperature,  $M-H$  loop shift towards the origin[see Fig.3.13(c)] and becomes symmetric about origin at  $T_{comp}(\approx 43.8 \text{ K})$ . For the temperature, below  $T_{comp}$ , the CG of  $M-H$  loop shifts towards right side and then bounce back to zero via  $38 \text{ K}$  as shown in Fig3.13(f). Thereafter the shift in the loop vanishes upto  $T_S$ , below which again it switches to left. Change in the sign of the shift along with the collapse of the  $M-H$  loop, which otherwise could not observed in the pristine compound of  $\text{CoCr}_2\text{O}_4$ , signify the pronounced temperature dependent changes in the spin configurations of Fe substituted samples. As depicted in the Fig.3.14, we can also see the similar trend of the sign change in the shift of the loop in case of the  $\text{Co}(\text{Cr}_{0.925}\text{Fe}_{0.075})_2\text{O}_4$  sample across  $T_{comp} \approx 67.8 \text{ K}$ .

Nine panels (a)–(i) of Fig.3.15 demonstrate the highlights of 70 kOe FC  $M-H$  loops

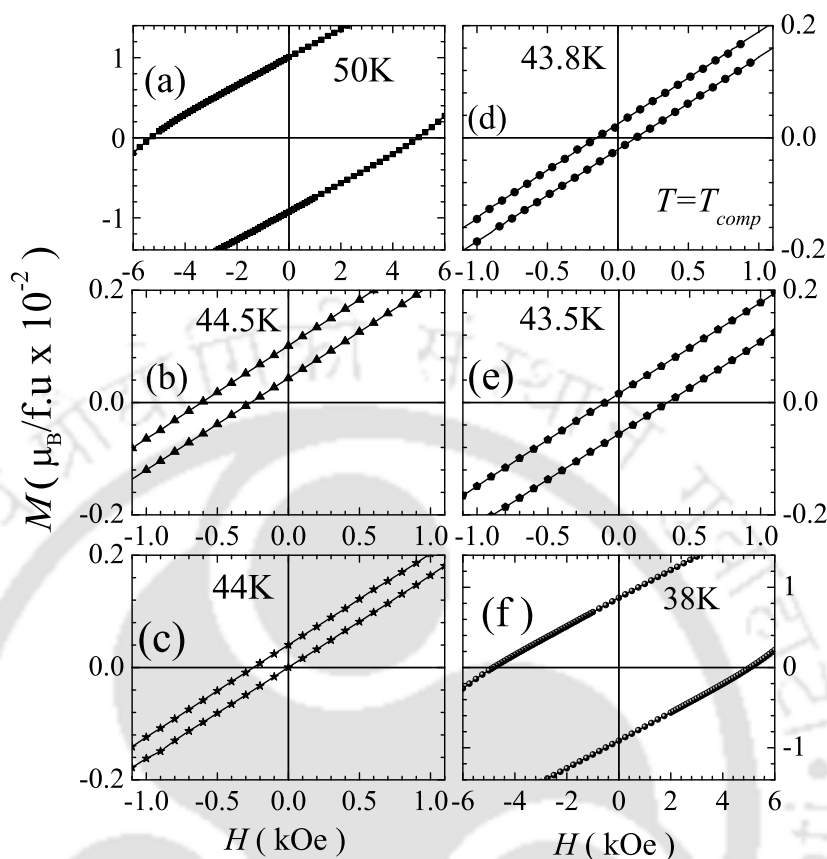


**Figure 3.13:** (a)-(f) Enlarged portions of 70 kOe FC  $M$ - $H$  loops of  $\text{Co}(\text{Cr}_{0.95}\text{Fe}_{0.05})_2\text{O}_4$  sample in the vicinity of  $T_{comp} \approx 43.8$  K recorded by implementing the procedure explained in the text.

measured at various temperatures in the magnetically ordered state for 5%, 7.5% and 10% Fe substituted samples. We define  $EB$  field, i.e., the measure of the amount of shift in the  $M$ - $H$  loop along the field axis and the effective coercive field, i.e., the effective half width of  $M$ - $H$  loop and the vertical shift in the loop in the following manner,

$$H_C^{eff} = \frac{(H_{C+} - H_{C-})}{2} \quad (3.1)$$

$$H_{EB} = - \frac{(H_{C+} + H_{C-})}{2} \quad (3.2)$$

$$M_{EB} = \frac{(M_{rem+} + M_{rem-})}{2} \quad (3.3)$$

### 3. Studies in $\text{Co}(\text{Cr}_{1-x}\text{Fe}_x)_2\text{O}_4$ series

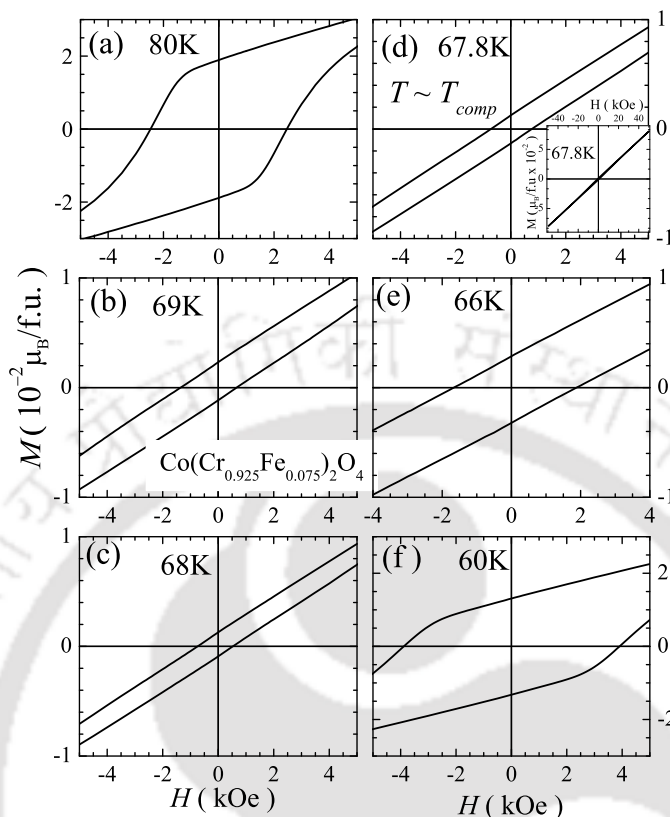


**Figure 3.14:** (a)-(f) Enlarged portions of  $M$ - $H$  loops of  $\text{Co}(\text{Cr}_{0.925}\text{Fe}_{0.075})_2\text{O}_4$  sample in the vicinity of  $T_{comp} \approx 67.8$  K.

Here  $H_{C+}$  and  $H_{C-}$  represents the right and left field values of  $M$ - $H$  loop where the net magnetization crosses the  $M = 0$  axis. Whereas  $M_{rem+}$  and  $M_{rem-}$  are the remanent magnetization values while varying the field from  $+50$  kOe and  $-50$  kOe to zero, respectively. As shown in Fig.3.15(a), 3.15(d) & 3.15(g),  $H_C^{eff}(T)$  of three samples display complicated behaviour. As the temperature approaches  $T_{comp}$  from both, below as well as above,  $H_C^{eff}(T)$  exhibits diverging trend, but dramatically sharply falls to a local minima at their respective  $T_{comp}$ . The local minima value drops to zero for 5 at% Fe sample as expected for the case of zero-magnetization system; however with increasing Fe concentration minima value increases. We can also see that  $H_C^{eff}(T)$  exhibits anomalies across  $T_S$  and  $T_L$ . Now let us focus on to the striking key features in the temperature dependence of  $H_{EB}(T)$  and vertical

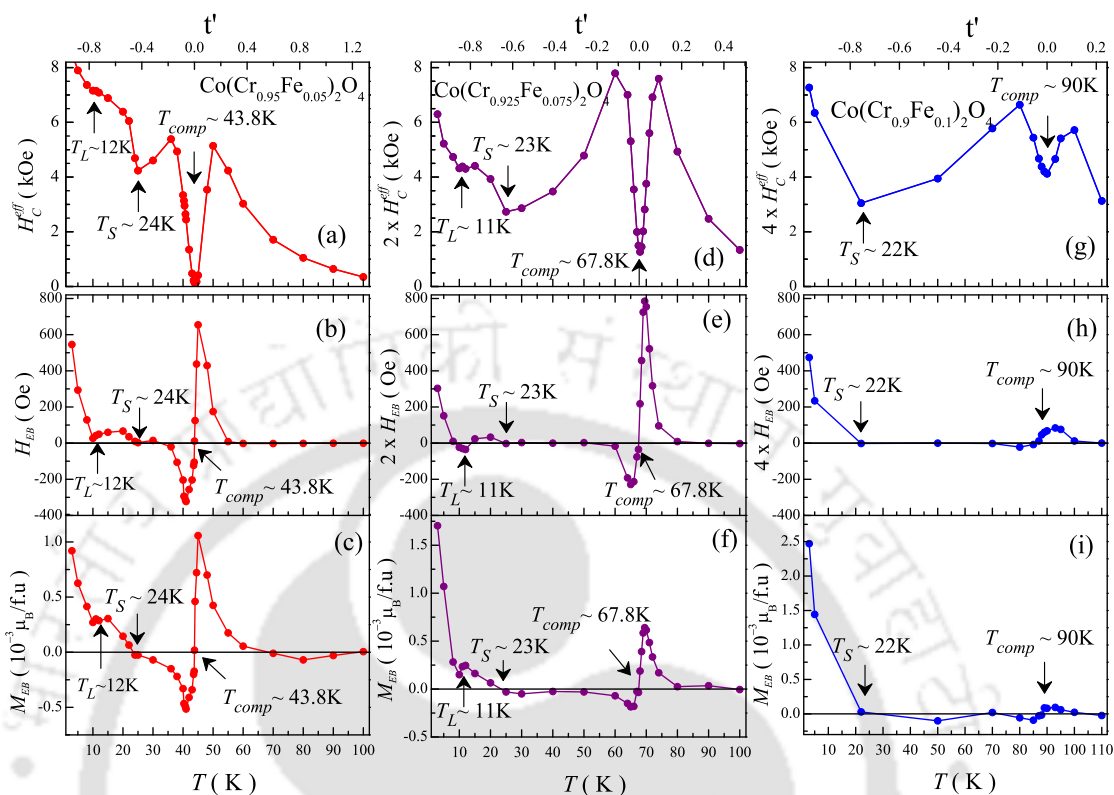


**Figure 3.15:** Temperature dependence of  $H_C^{eff}$ ,  $H_{EB}$  and  $M_{EB}$  extracted from 70 kOe FC  $M$ - $H$  loops of  $\text{Co}(\text{Cr}_{0.95}\text{Fe}_{0.05})_2\text{O}_4$  sample (panels (a), (b) and (c)),  $\text{Co}(\text{Cr}_{0.925}\text{Fe}_{0.075})_2\text{O}_4$  sample (panels (d), (e) and (f)) and that of  $\text{Co}(\text{Cr}_{0.9}\text{Fe}_{0.1})_2\text{O}_4$  sample (panels (g), (h) and (i)), respectively. The top x-scale of (a), (d) and (g) panels shows the reduced temperature ( $t$ ). The collapse in  $H_C^{eff}$  in the vicinity of  $T_{comp}$  can be seen to happen in the window  $-0.1 \leq t \leq 0.1$ .

shift  $M_{EB}(T)$ . Initially,  $H_{EB}$  is immune to temperature upon lowering below  $T_C$ , but suddenly rises to a positive maximum value, then falls sharply to change sign across  $T_{comp}$ , below which it increases to a negative maximum value and becomes zero again. We can see that in the temperature range  $T_S \leq T \leq T_C$ ,  $H_{EB}(T)$  appears only in a temperature window located in the close proximity of  $T_{comp}$ , in which  $H_C^{eff}(T)$  exhibits sharp fall [Fig. 3.15(a), (d) & (g)]. It can be seen that the samples exhibit positive  $H_{EB}(T)$  value below  $T_S$ , thereafter  $H_{EB}(T)$  also show an anomaly at around  $T = T_L$ , designated as the lock-in transition. Upon lowering the temperature below  $T_L$ ,  $H_{EB}$

### 3. Studies in $\text{Co}(\text{Cr}_{1-x}\text{Fe}_x)_2\text{O}_4$ series

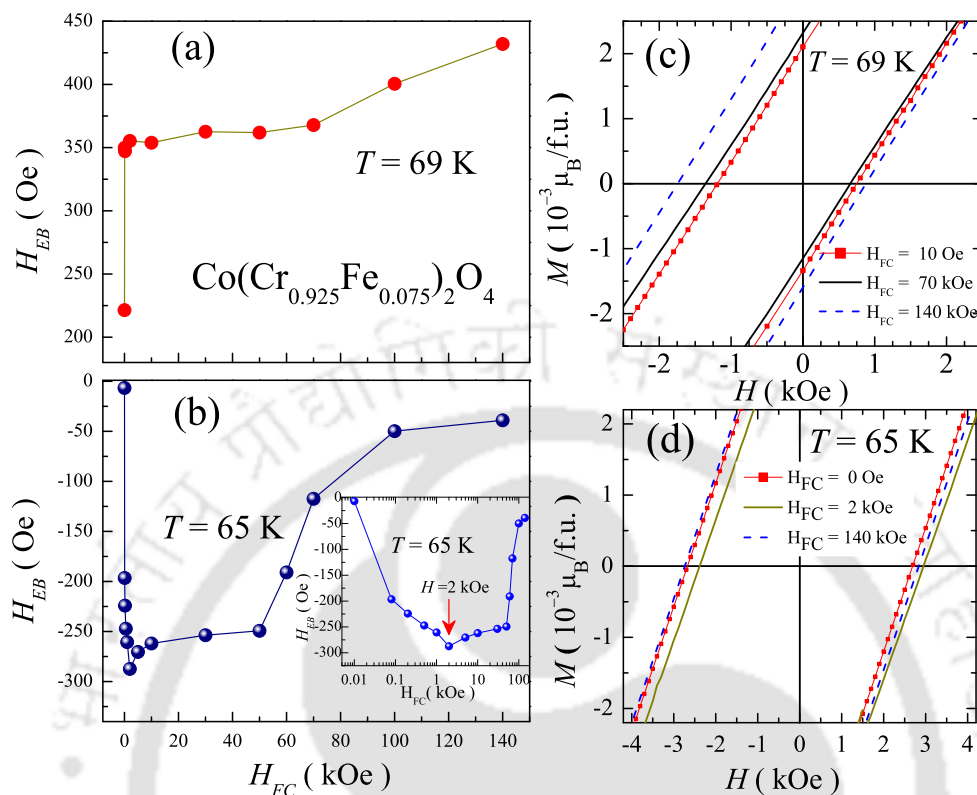


**Figure 3.16:**  $H_{FC}$  dependence of  $H_{EB}$  of  $\text{Co}(\text{Cr}_{0.925}\text{Fe}_{0.075})_2\text{O}_4$  sample at (a) 69 K (i.e., well above  $T_{comp}$ ) and (b) 65 K (i.e., well below  $T_{comp}$ ). Inset of (b) is the  $H_{EB}$  versus  $H_{FC}$  at 65 K on log scale. (c) and (d) show an enlarged portion of different FC  $M$ - $H$  loops at 69 K and 65 K, respectively.

sharply increases. We can see that all the samples exhibit the similar temperature dependent vertical shift  $M_{EB}$ . Magnitude of the  $H_{EB}$  and  $M_{EB}(T)$  decrease with increasing the Fe concentration.

For the deeper understanding of EB, we also measured cooling field ( $H_{FC}$ ) dependence of the  $H_{EB}$ . Fig.3.16(a) & (b), respectively, show the  $H_{FC}$  dependence of the  $H_{EB}$  of  $\text{Co}(\text{Cr}_{0.925}\text{Fe}_{0.075})_2\text{O}_4$  sample at 69 K and 65 K, i.e., well above and below  $T_{comp} \approx 67.8$  K (exactly where we obtained the maximum EB as shown in Fig.3.15(e)), upto a large enough field of 140 kOe. At 69 K, as it is evidenced from the enhancing the left shift of  $M$ - $H$  loop [Fig.3.16(c)], with increasing the  $H_{FC}$  from zero to few Oe, the magnitude of positive  $H_{EB}$  sharply rises. Beyond this  $H_{FC}$ ,  $H_{EB}$  slowly increases

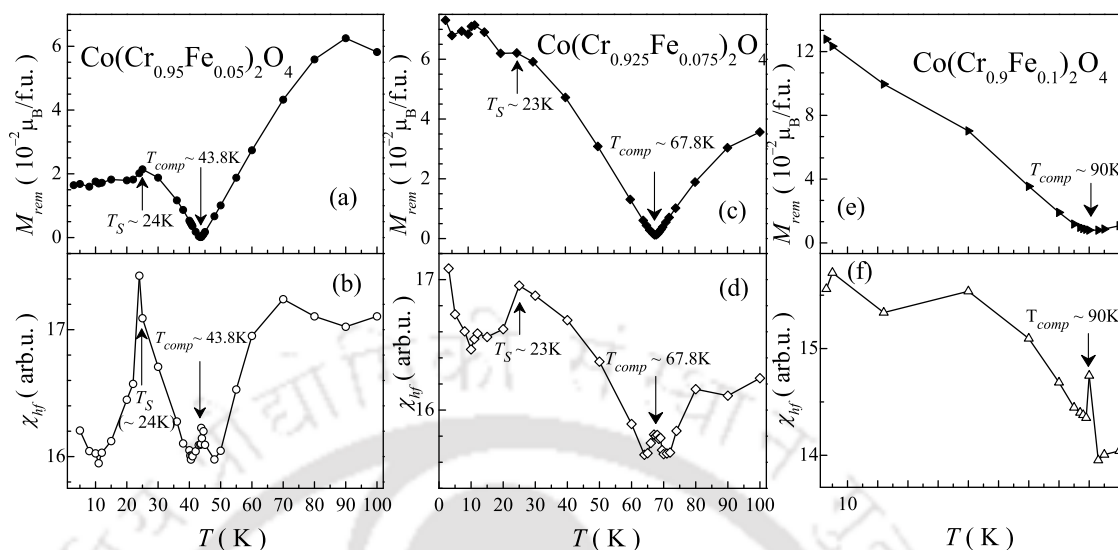


**Figure 3.17:** Temperature dependence of  $M_{rem}$  and  $\chi_{hf}$  computed from 70 kOe FC M-H loops for  $\text{Co}(\text{Cr}_{0.95}\text{Fe}_{0.05})_2\text{O}_4$  sample(panels (a) and (b)),  $\text{Co}(\text{Cr}_{0.925}\text{Fe}_{0.075})_2\text{O}_4$  sample(panels (c) and (d)) and that of  $\text{Co}(\text{Cr}_{0.9}\text{Fe}_{0.1})_2\text{O}_4$  sample(panels (e) and (f)), respectively.

upto  $H_{FC} = 140$  kOe. Compared to the trend observed at 69 K,  $H_{FC}$  dependence of  $H_{EB}$  at 65 K exhibits exotic behaviour. As shown in the Fig.3.16(b) as the  $H_{FC}$  increases from zero, magnitude of the negative  $H_{EB}$  sharply increases upto  $H_{FC} \sim 2$  kOe. Beyond  $H_{FC} \sim 2$  kOe,  $H_{EB}$  decreases non-monotonically upto  $H_{FC} \sim 140$  kOe. Surprisingly,  $H_{FC} \sim 2$  kOe matches with field for which  $M_{FCC}$  switches to positive sign below  $T_{comp}$  (in case of  $x = 0.075$  sample it is  $\sim 2$  kOe as shown in Fig.3.9(b)). All these features can be seen in Fig.3.16(d) in the form of right shift in M-H loop as well. Quick rise of  $H_{EB}$  with  $H_{FC}$  below 2 kOe, where  $M_{FCC}$  switches to positive for the first time below  $T_{comp}$ [Fig.3.9(b)] is reminiscent of the influence of the field induced transition(Fig.3.9(b)) on the  $H_{EB}$ .

The additional interesting information that can be derived from the 70 kOe FC M-H loops are remanent magnetization ( $M_{rem}$ ) measured while dropping the field from 70 kOe to zero and high field susceptibility ( $\chi_{hf}$ ), extracted from the slope of the M-H loop at high fields( $\geq 20$  kOe). Here,  $M_{rem}$  is from zero field and the other hand

### 3. Studies in $\text{Co}(\text{Cr}_{1-x}\text{Fe}_x)_2\text{O}_4$ series

---

$\chi_{hf}$  is from high field regime, at which all the anisotropic effects vanish. Temperature dependence of these two parameters for different samples are demonstrated in the six panels of Fig.3.17. The importance of these plots is that though  $M_{rem}$  and  $\chi_{hf}$  are related to two different regimes of field, as the  $T \rightarrow T_{comp}$  from above and below, both exhibit same trend, we can see they drop to a minima and show near zero values. Within the local minima,  $\chi_{hf}(T)$  exhibits a tiny peak between the temperature values where  $H_{EB}(T)/M_{EB}(T)$ [see Fig.3.15] exhibit maxima just below and above the  $T_{comp}$  but  $M_{rem}(T)$  do not show any peak. In addition to this, it can be seen anomalies surfaced in  $M_{rem}(T)$  on the onset of  $T_S$  and  $T_L$  get enhanced in  $\chi_{hf}(T)$ . All these features may suggest the field induced changes in the magnetic structure of the samples as noticed in the thermomagnetic response[Fig.3.9].

#### 3.3.5 Thermodynamic properties

Thermodynamic properties are efficient tools to probe various magnetic transitions. We explored the thermodynamic properties in the presence and absence of external applied magnetic field to understand the intricate magnetic properties observed in the temperature and field dependent magnetization  $M_{FCC}(T)$ ,  $H_{EB}(T)$ ,  $\chi_{hf}(T)$ . Main panels of Fig.3.18(a) and (b), respectively, show the temperature dependent heat capacity ( $C_P(T)$ ) of  $\text{Co}(\text{Cr}_{0.95}\text{Fe}_{0.05})_2\text{O}_4$  and  $\text{Co}(\text{Cr}_{0.925}\text{Fe}_{0.075})_2\text{O}_4$  samples under the applied magnetic fields of  $H = 0$ ,  $H = 50$  kOe &  $H = 90$  kOe.  $\lambda$ -type jump observed at around  $T = 110$  K and 117 K, respectively, represent their FIM transition as we noticed in thermomagnetic properties[Fig.3.9]. The sharp and large peak, reminiscent of first order nature, observed at around  $T = 24$  K and 23 K for the  $\text{Co}(\text{Cr}_{0.95}\text{Fe}_{0.05})_2\text{O}_4$  and  $\text{Co}(\text{Cr}_{0.925}\text{Fe}_{0.075})_2\text{O}_4$  samples, respectively, is due to the magneto-structural transition. This unusual jump in  $C_P(T)$  at  $T_S$  may represent the transition from one magnetic configurations to another across  $T_S$ . With increasing the Fe concentration, the transition at  $T_S$  seems to become less intensive, as witnessed from the decreasing

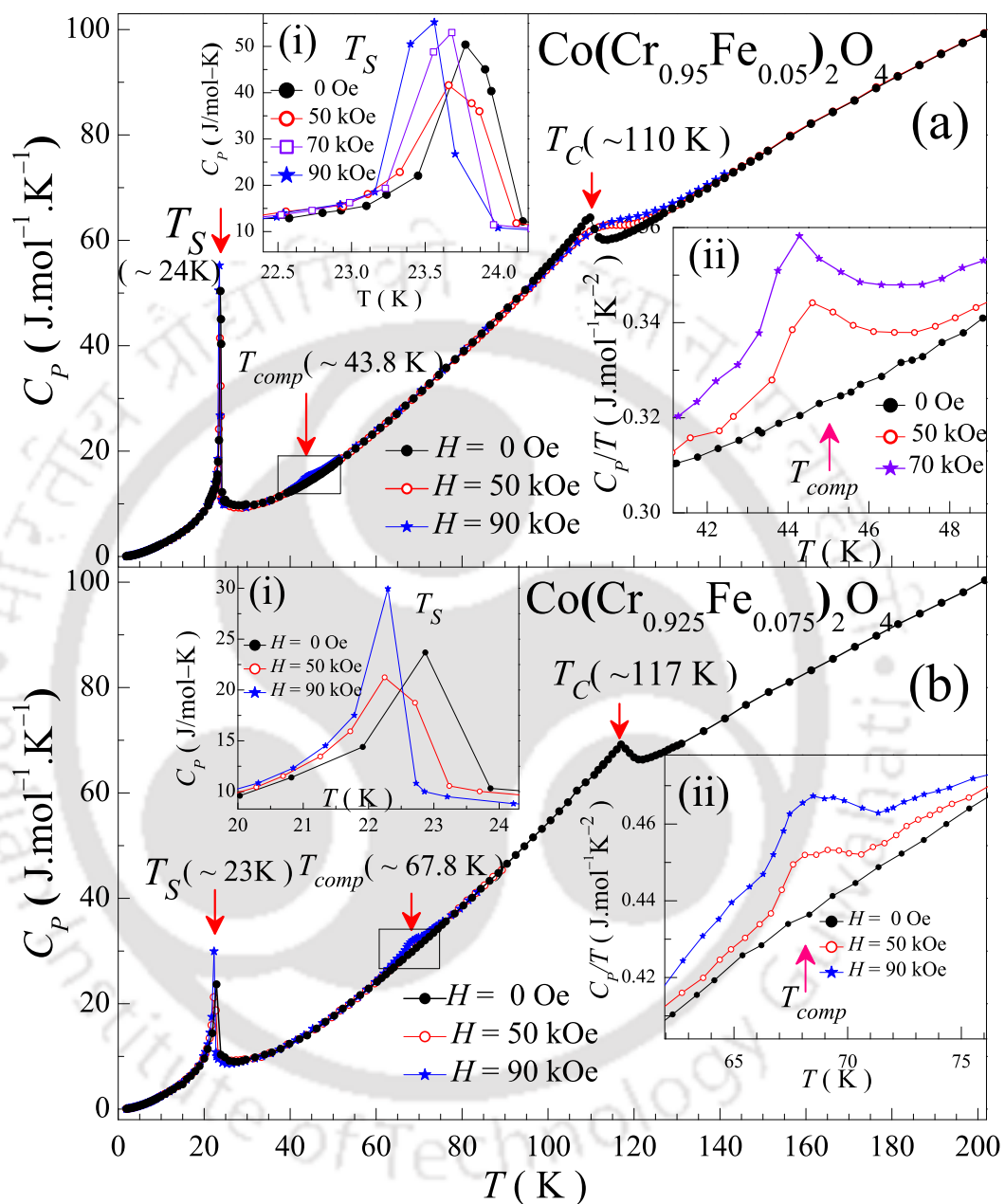


**Figure 3.18:** (a) and (b)  $C_p(T)$  of  $\text{Co}(\text{Cr}_{0.95}\text{Fe}_{0.05})_2\text{O}_4$  and  $\text{Co}(\text{Cr}_{0.925}\text{Fe}_{0.075})_2\text{O}_4$  samples, respectively, in zero magnetic field, under the applied field of 50 kOe & 90 kOe. Insets (i) and (ii) of in both the panels are the enlarged view of  $C_p(T)$  across the  $T_S$  and  $C_p(T)/T$  across  $T_{comp}$ , respectively.

### 3. Studies in $\text{Co}(\text{Cr}_{1-x}\text{Fe}_x)_2\text{O}_4$ series

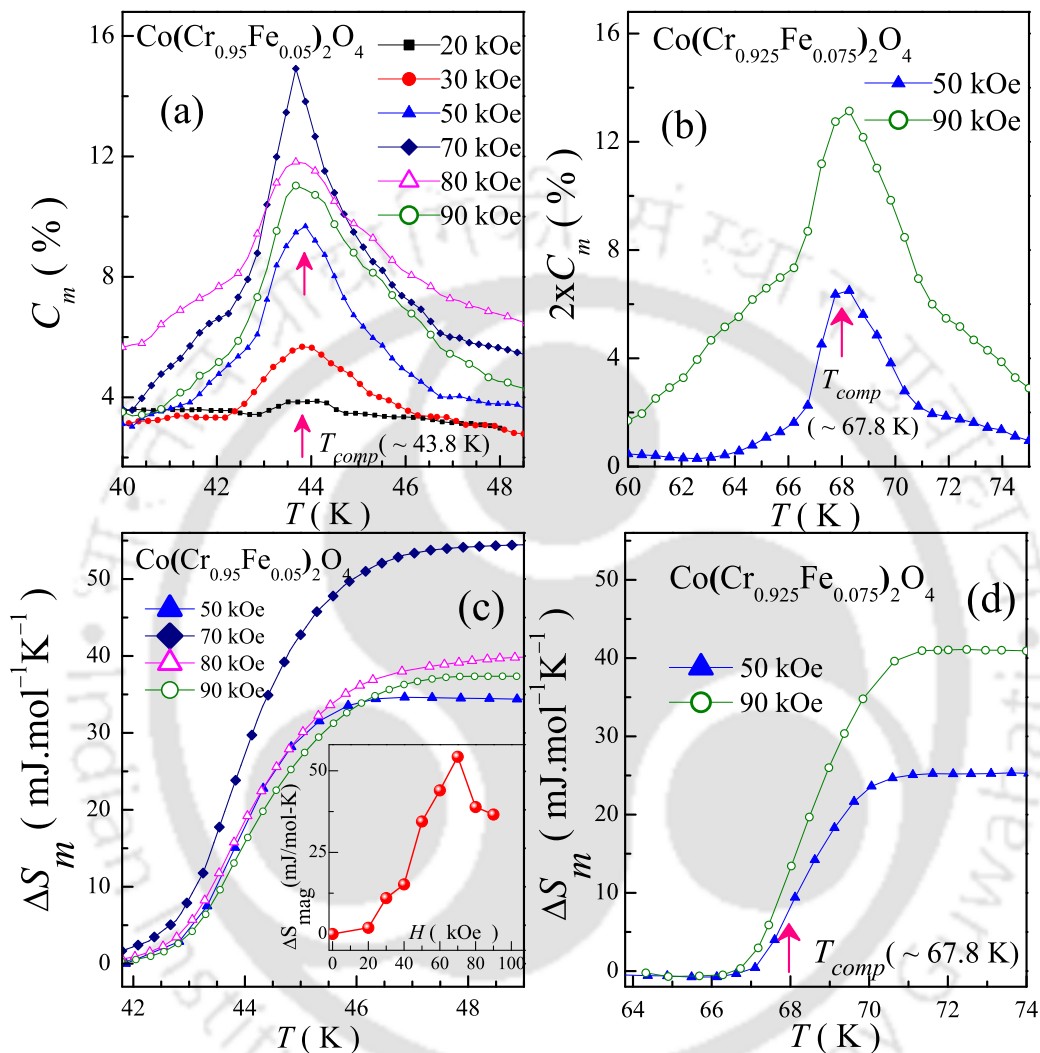


**Figure 3.19:** (a) and (b)  $C_m(T)$  (see the text for definition) of  $\text{Co}(\text{Cr}_{0.95}\text{Fe}_{0.05})_2\text{O}_4$  and  $\text{Co}(\text{Cr}_{0.925}\text{Fe}_{0.075})_2\text{O}_4$  samples, respectively, across their corresponding  $T_{comp}$  for various applied fields. (c) and (d) depict the jump in magnetic entropy  $\Delta S_{mag}(T)$  across the  $T_{comp}$  under various applied fields. Inset of (c) is the change in the height of  $\Delta S_{mag}(T)$  across  $T_{comp}$  as function of applied field. Here error is smaller than size of the symbols given in the plots.

trend of height of  $C_P(T)$  peak. Hence, it can be pointed out that the Fe ions get substituted for Cr and strongly manipulate different superexchange interactions of the system by sitting in lattice, rather than forming their own clusters in the host lattice. Further, applying the large field of 50 kOe and 90 kOe smears the  $T_C$ , as expected for usual FIM/AFM/FM ordering. On the other hand, if the magnetic ordering near  $T_S$  has FIM/AFM/FM like character, then the peaks would have broadened out upon increasing the applied field instead of shifting toward the lower temperature [inset (i) of Fig.3.18(a) & (b)]. It can be understood that in the case of Fe substituted samples, the transition at  $T_L$  seems to be hard to detect in heat capacity measurements. This may dictate that the transformation of spin-spirals from high temperature incommensurate phase to low temperature commensurate phase across  $T_L$  is becoming weak in terms of the energy difference between these two phases compared to the pristine  $\text{CoCr}_2\text{O}_4$  compound. However it can be noted that in case of  $\text{CoCr}_2\text{O}_4$  also transition across  $T_L$  is not feasible in zero-field specific heat but only in 14 T, a small peak appears [31]. In addition to all these existing transitions, shown in the inset (ii) in both Fig.3.18(a) and (b) another  $C_P(T)$  anomaly surfaces at around  $T_{comp}$  or  $T_R$  ( $\sim 43.8$  K and 67.8 K) which is absent in zero field are indicative of the fingerprints of a field-induced transition, as observed in the high field  $M_{FCC}(T)$  data [Fig.3.9(a)].

Magnetic field induced enhancement in heat capacity,  $C_m$  across  $T_{comp}$  is calculated by

$$C_m = \frac{[C_P(T, H) - C_P(T, 0)]}{C_P(T, 0)} \quad (3.4)$$

here  $C_P(T, 0)$  and  $C_P(T, H)$  are  $C_P(T)$  under zero field and under applied field ( $H$ ), respectively. Fig.3.19(a) and (b) demonstrate the temperature dependence of such  $C_m$  under different applied fields across  $T_{comp}$  for  $\text{Co}(\text{Cr}_{0.95}\text{Fe}_{0.05})_2\text{O}_4$  and  $\text{Co}(\text{Cr}_{0.925}\text{Fe}_{0.075})_2\text{O}_4$  samples, respectively. From the Fig.3.19(a), it is prominent that as the applied field increases, anomaly in  $C_m$  of  $\text{Co}(\text{Cr}_{0.95}\text{Fe}_{0.05})_2\text{O}_4$  at  $T_{comp}$  increases sharply up to  $H = 70$  kOe, beyond which it is broadened out. Compared to the  $\text{Co}(\text{Cr}_{0.95}\text{Fe}_{0.05})_2\text{O}_4$

### 3. Studies in $\text{Co}(\text{Cr}_{1-x}\text{Fe}_x)_2\text{O}_4$ series

---

sample,  $C_m$  of the  $\text{Co}(\text{Cr}_{0.925}\text{Fe}_{0.075})_2\text{O}_4$  becomes weak almost decreases by a factor of 2 (see left scale is multiplied by 2). In both the samples, the broadening of anomaly in  $C_m$  with increasing field is again indicate that the moments are in AFM ordering across  $T_{comp}$ .

Change in magnetic entropy involved in the field-induced transition across  $T_{comp}$  (mostly in the temperature window where we noticed seizable magnitude of  $H_{EB}$ ) is estimated by

$$\Delta S_{mag}(T)|_H = \int \frac{C_P(T)}{T} dT \quad (3.5)$$

It can be seen the height of  $\Delta S_{mag}(T)$  jump in  $\text{Co}(\text{Cr}_{0.95}\text{Fe}_{0.05})_2\text{O}_4$  [Fig.3.19(c) & (d)] rises upto  $H=70$  kOe and falls down afterwards [inset of Fig.3.19(c)] in corroboration with  $C_m$ .  $\text{Co}(\text{Cr}_{0.925}\text{Fe}_{0.075})_2\text{O}_4$  sample exhibits comparatively less height in  $\Delta S_{mag}(T)$ . But in  $\text{Co}(\text{Cr}_{0.925}\text{Fe}_{0.075})_2\text{O}_4$ ,  $\Delta S_{mag}(T)$  increases upto the field of  $H=90$  kOe. However, we can not compare as the  $T_{comp}$  of two samples is different and the contribution to  $\Delta S_{mag}(T)$  is also different. One can see that the  $\Delta S_{mag}(T)$  become less effective with increasing Fe concentration in corroboration with the magnitude of  $H_{EB}(T)$  across  $T_{comp}$  [Fig.3.15(b), (e) & (d)]. Anomaly in  $C_m$  might have started at critical value of  $H$ , at which  $M_{FCC}(T)$  shows turnover at  $T_R$ , but with tiny difference of energetics of the system that cannot be accounted to  $C_m$ .

#### 3.3.6 Magnetic relaxation properties

It is well known that the magnetization relaxes as the time elapses if the magnetic system consists of glassy behaviour [109]. Hence, the time dependent magnetization measurement is useful to probe the the glassy behaviour of a magnetic system. Here the sample is cooled down in the applied field of zero to the required temperature at we were interested to carry out the time dependent magnetization. Fig.3.20(a) and (b) show the time dependent magnetization of  $\text{Co}(\text{Cr}_{0.925}\text{Fe}_{0.75})_2\text{O}_4$  sample measured

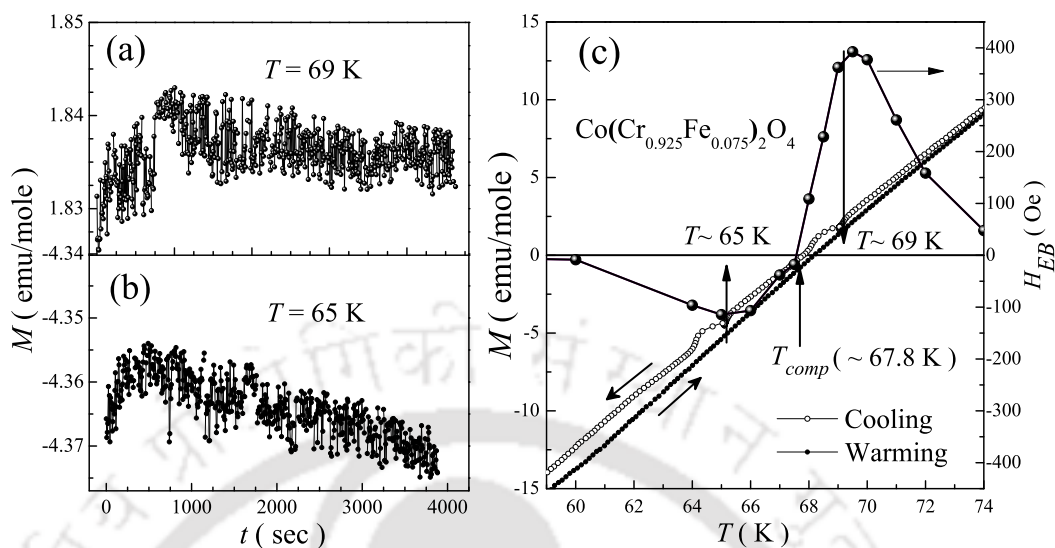


**Figure 3.20:** (a) and (b) Time dependent magnetization of  $\text{Co}(\text{Cr}_{0.925}\text{Fe}_{0.75})_2\text{O}_4$  sample at 69 K and 65 K, respectively. (c) Magnetization measured in FCC (with two stops at 69 K & 65 K) and FCW mode together with the  $H_{EB}(T)$  across  $T_{comp}$ .

at 69 K and 65 K (the temperatures above and below  $T_{comp} \sim 67.8$  K, at which the temperature dependent EB exhibits maximum), respectively. We can see that the magnetization does not exhibit any significant relaxation as a function of time at both 69 K and 65 K. One more characteristic of glassy system is the memory effect. If a glassy system is allowed to relax at different temperatures in the magnetically ordering regime while cooling the sample, it remembers its former relaxed states while warming the sample [109]. Fig. 3.20(c) demonstrates the magnetization measured while cooling with two stops at temperatures 69 K and 65 K for  $\text{Co}(\text{Cr}_{0.925}\text{Fe}_{0.75})_2\text{O}_4$  sample. We can see that the sample does not show any significant amount of change in magnetization at 69 K and 65 K as it is allowed to relax. The warming curve also does not exhibit any memory effect. Absence of relaxation and memory effect may dictate that the samples are not possessing any glassy behaviour.

## 3.4 Discussion

As per the literature available on parent compound  $\text{CoCr}_2\text{O}_4$ , no compensation effect was observed except in the ZFC curve [104] that was attributed to the experimental artifact incorporated due to negative trapped field in the superconducting magnet of the magnetometer [110]. Due to weak GMF in the pyrochlore(B) lattice  $\text{CoCr}_2\text{O}_4$  forms non-collinear spin-spirals with three magnetic sub-lattices namely Co, Cr1, and Cr2 [23, 28, 29, 67]. Due to the said geometrical frustration, even though long range order of A-site( $\text{Co}^{+2}$ ) persists above  $T_S$  and below  $T_C$ , the magnetic moments corresponds to B-site(Cr1 and Cr2) are still in disordered state and form short range spin-spirals [28, 29, 31, 71]. Hence, even the ultra high fields are not able to induce full net moment of  $3 \mu_B/\text{f.u.}$ , if we assume that the magnetic structure is collinear in temperature range  $T_S \leq T \leq T_C$  [31, 32].

Prima facie, thermomagnetic response under nominal zero field[ Fig.3.8(a)], it can be realized that the Fe substitution results in the reduction of the total magnetization and causes the magnetic compensation in  $x = 0.044-0.11$  samples. From this striking feature, combining with XRD analysis, it can be understood that the substituted Fe ions mainly occupy B-site, otherwise we could not observe this trend according to the ground state magnetic configuration of  $\text{CoCr}_2\text{O}_4$  as explained above. Fig.3.21 show the schematic block diagram of the magnetic configuration to unveil the underlying reason behind the magnetization reversal and the field induced transitions across  $T_{comp}$ . In order to avoid the complexity in understanding we consider only the ‘**longitudinal components**’ (along the field) of the moments of different sub-lattices in the compound. As shown in the Fig.3.21(a), below  $T_C$ , for the small applied fields, Cr1, Cr2 and Fe moments in the B-site start aligning in such a way the resultant moment of B-site anti-parallel to A-site moment(which is already aligned along the field direction). This makes sure that the  $\mu_A > \mu_B$  for  $T > T_{comp}$ . At  $T_{comp}$ , B-site moment compensates the A-site moment, results in the zero net moment. Thereafter,



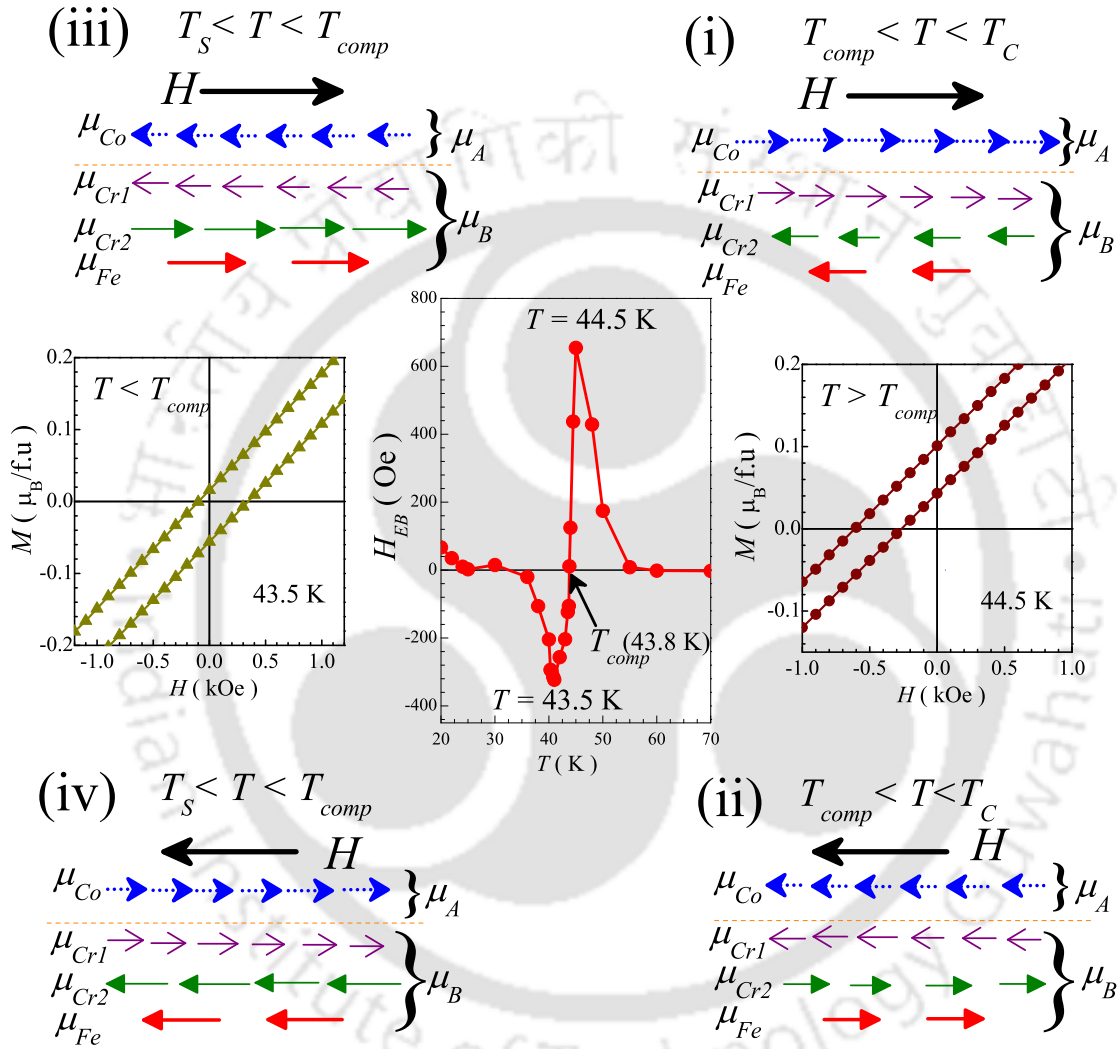


**Figure 3.22:** Schematic block diagram of the magnetic configurations with respect to applied field to explain the EB effect in the two temperature regions  $T_S < T < T_{comp}$  and  $T_{comp} < T < T_C$  caused by high field cooling.

the resultant moment of B-site dominates that of the A-site moment along  $H$ , i.e.,  $\mu_B > \mu_A$  for  $T < T_{comp}$ , reversal in magnetization is observed below  $T_{comp}$  as indicated in Fig.3.21(b). Reversal in magnetization continues to appear for the field  $H < H_{critical}$  ( $H_{critical}$  is the field at which the net magnetization switch back to positive as shown in Fig.3.21). This may be because of the directional anisotropy (which aligns moments in a particular direction, makes that particular direction favourable with minimum energy) dominates the small applied field. This means the internal field developed due to anisotropy is in the order of  $H_{critical}$  but aligned anti-parallel to the applied field. With large enough field,  $H > H_{critical}$  this anisotropic effect vanishes and then all the domains align to the field, the magnetization behaviour of compensated samples across  $T_{comp}$  can be explained by the (c) and (d) configurations of schematic(3.21). For the applied fields  $H > H_{critical}$ , in the region  $T_{comp} < T < T_C$  magnitude of the A-site moment enhances and the net magnetization increases. But below  $T_{comp}$  the field is now able to rotate the moments which were aligned opposite (trying to dominate the field) to it in the B-site. This results in the spin reorientation (SR) compared to that of the configurations (b) and (c). Hence, below  $T_{comp}$  the  $M_{FCC}(T)$  under  $H > H_{critical}$  is mirror image of the trend observed if  $H < H_{critical}$  [Fig.3.21]. Similar SR was observed in case of compensated admixed alloys of (Sm, Gd)Al<sub>2</sub> [18, 111, 112], Nd<sub>0.75</sub>Ho<sub>0.25</sub>Al<sub>2</sub> [17].

Now, let us explain the possible origin for the  $H_{EB}(T)$  (and  $M_{EB}(T)$ ), its sign change at  $T_{comp}$ . From the relaxation and memory effect measurements it can be claimed that the samples are certainly not of glassy in nature. Further, it has been anticipated that the conduction electrons and core-shell geometry play vital role in the appearance of EB [16–20]. It is known that the present oxides are insulators, do not possess any conduction electrons. From the SEM images [see Fig.3.4] it is found that the present samples have 2-3 micron size grains, it can be understood that there is no possibility of core-shell geometry. So the existing models do not explain the EB in this system in which the conduction electron polarization and the shell magnetic

### 3. Studies in $\text{Co}(\text{Cr}_{1-x}\text{Fe}_x)_2\text{O}_4$ series

---

components are replaced by rigid magnetic moments.

While field cooling the sample from  $T_C$  under the large applied field (70 kOe) initially A-site moments undergo ordering then that of the B-site moments [28, 71], for  $T > T_{comp}$  system ends up in the configuration shown in the Fig.3.22(i). Here we can see A-site moments align along the field direction and the B-site has antiferromagnetically aligned moments within it. Configuration (i) in Fig.3.22 resembles the model explained in the introduction chapter [see Fig.1.9]. Due to field cooling A-site moments get pinned to the B-site moments. Because of this pinning the A-site moments do not rotate easily along the field direction when the field is reversed to record the  $M-H$  loop. Hence, during the descending branch of the  $M-H$  loop more field is required to rotate the moments against the pinning force. However, for large enough measuring field the A-site moments are forced to rotate along field as shown in the schematic (ii) of Fig.3.22. But, during the ascending branch of the loop they readily respond to the field as the pinning due to the B-site moments exerts the torque in the same direction of field. So less magnetic field is required to attain the configuration (i) from (ii). Hence, resultant loops shift towards negative side on the field axis and upward on the magnetization axis. Hence gives rise to positive  $H_{EB}$  for  $T > T_{comp}$ . Difference between the model described for FM–AFM interface [Fig.1.9] and the present homogeneous sample is, in former the AFM configuration do not get changed but in the later rotations of all the moments takes place due to the strong internal molecular fields among different sub-lattices.

Field cooling of the sample across  $T_{comp}$  causes SR, resulting in the configuration (iii) for  $T_S < T < T_{comp}$ . It can be seen that below  $T_{comp}$  Cr2 and Fe moments are forced to align along the field direction and other moments also follow them owing to the strong internal molecular fields among different sub-lattices as shown in schematic (iii) of Fig.3.22. We can see that the configuration (iii) is exactly opposite to that of

(i), hence the shifting in the loop for  $T < T_{comp}$  is opposite compared to the case observed for  $T > T_{comp}$ . In detail, we can understand it in the following manner. As the moments are forced to align along the field direction in the configuration (iii), during the descending branch of  $M$ - $H$  loop moments readily respond to the field to attain configuration (iv)(which is energetically unfavourable). Whereas, during the ascending branch of  $M$ - $H$  loop, moments do not rotate easily when the field is rotated from negative to positive. From this it is easy to understand that the resultant  $M$ - $H$  loops below  $T_{comp}$  shift towards positive field on field axis and downward on the magnetization axis, resulting in the negative  $H_{EB}$  for  $T < T_{comp}$ . If the moments are fully compensated the pinning on the FM part is more, and gives rise to more EB. The collapse of the hysteresis loop (Fig.3.12, Fig.3.14 & top panels of Fig.3.15) is reminiscent of the strongly coupled AFM ordering or fully compensated moments in the vicinity of  $T_{comp}$ . Away from  $T_{comp}$  magnetic ordering becomes FIM (Fig.3.12 and Fig.3.14), and as a result moment along field dominates and its counter part can't compete with it. While cycling the field in  $M$ - $H$  loop, dominated one respond to field readily and the counter part follow it. Hence, no shifting in  $M$ - $H$  loop can be observed. Further, it can be also noted that the magnitude of  $H_{EB}$  is more if the sample is close to the zero-magnetization proximity( $H = 0, M = 0$  at  $T \rightarrow T_{comp}$ ). From the Fig.3.23, the collapsed  $M$ - $H$  loop of the sample with composition  $x = 0.05$ , shows that the moments are fully compensated at  $T \sim T_{comp}$ . But, with increasing Fe concentration, rigidity of the AFM ordering decreases and exhibits considerable opening in the  $M$ - $H$  loop, as a result, sample is driven away from zero-magnetization proximity( $H_C^{eff}$  and  $M_{rem}$  do not drop to zero at  $T \rightarrow T_{comp}$ ). Due to this, the effective pinning on the FM component decreases and hence the magnitude of  $H_{EB}$  decreases.

Very useful information can be derived from the non-monotonic behaviour of  $H_{FC}$  dependent  $H_{EB}$  of  $x = 0.075$  sample on both sides of  $T_{comp}$ (specially at  $65 \text{ K} < T_{comp}$ ), exactly where maxima are noticed in  $H_{EB}(T)$ . This non-monotonic behaviour probe influence of the field induced SR on the EB.  $H_{EB}$  exhibits maximum at  $H_{FC} \sim 2 \text{ kOe}$

### 3. Studies in $\text{Co}(\text{Cr}_{1-x}\text{Fe}_x)_2\text{O}_4$ series

---

at which the SR takes place as shown in Fig.3.9(b). Decrease in  $H_{EB}$  with the further increase in  $H_{FC}$  above  $\sim 2$  kOe signifies that the configuration obtained after SR is stabilized with large applied field. Sign change of  $H_{EB}$  with  $H_{FC}$ , that was observed in other compounds [20, 21, 113] is not possible in the present compound within the large field of 140 kOe because the strong AFM ordering in the vicinity of  $T_{comp}$  can't be broken even at the field of 140 kOe as shown in Fig.3.9(b). From this characteristic, concomitantly with the survival of  $H_{EB}$  it could be understood that the origin of  $H_{EB}$  is different from other systems.

By considering molecular level exchange interactions for a homogeneous FIM system Webb et al. [114] predicted that the collapse in  $H_C^{eff}(T)$  to commence when  $T \rightarrow T_{comp}$  for a normalized temperature,

$$t' = \frac{(T - T_{comp})}{T_{comp}} < 0.01 \quad (3.6)$$

However, even in case of ideally homogeneous single crystalline sample of  $\text{Nd}_{0.75}\text{Ho}_{0.25}\text{Al}_2$  the collapse in  $H_C^{eff}(T)$  is found to happen in  $\Delta t' \leq 0.1$  [17]. The collapse of  $H_C^{eff}(t')$  in the plot of  $H_C^{eff}(t')$  vs.  $t'$  (see top panels of Fig.3.15 in view of top x-scale) in the window,  $\Delta t' \sim 0.1$  is comparable to that observed in case of ideally homogeneous single crystal of  $\text{Nd}_{0.75}\text{Ho}_{0.25}\text{Al}_2$  [17]. This, including with the rigid transition at  $T_R$  even at 140 kOe indicate the molecular level FIM ordering and hence the intrinsic origin of the EB effect in these compounds.

Switching of the sign of  $H_{EB}(M_{EB})$  again at around the magneto-structural transition  $T_S$  in the positive direction, and their anomaly around lock-in transition  $T_L$  are surprising. We know that in  $\text{CoCr}_2\text{O}_4$  [23, 24], there is spin-flop transition across  $T_S$ , as the magnetic configuration changes from collinear to conical spin-spiral. Substituted  $\text{Fe}^{+3}$  has larger moment compared to  $\text{Cr}^{+3}$  ion and the conical spin-spirals get disturbed. Observation of  $EB$  below  $T_S$  indicates interconnection between  $H_{EB}$  and spin-spirals below  $T_S$ . The step rise in  $H_{EB}(M_{EB})$  below  $T_L$  could be due to

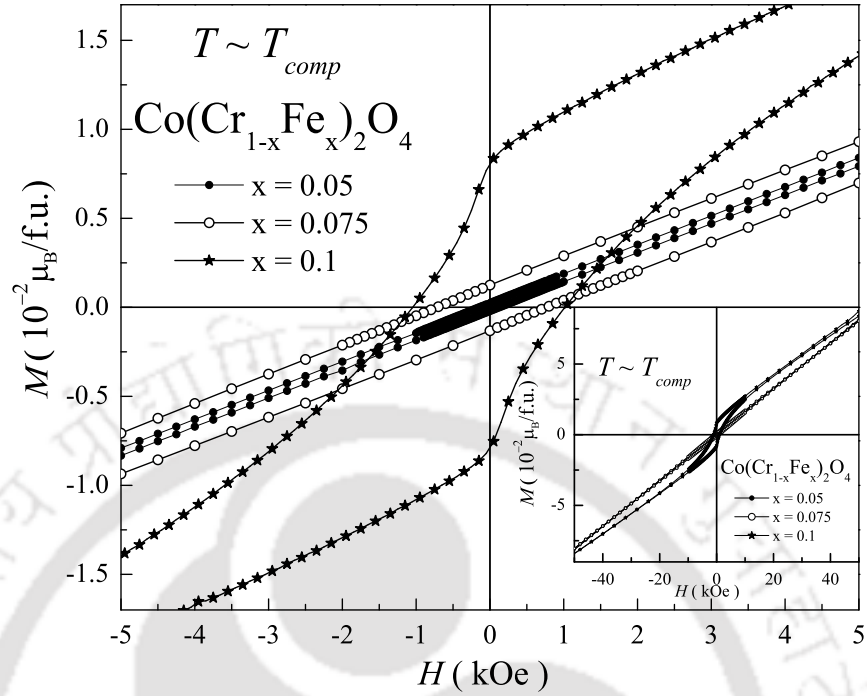


**Figure 3.23:**  $M$ - $H$  loops of  $x = 0.05$ ,  $0.075$  &  $0.1$  samples at their compensation temperature  $T \sim T_{comp}$ . Inset depicts the  $M$ - $H$  loops in the full scale.

the freezing of moments at low temperatures in its commensurate conical spin-spiral phase. This could be the possible origin for the EB in below  $T_S$ . The decrease of magnitude of  $EB$  in the conical phase with Fe substitution above  $x = 0.05$  could be due to the migration of little bit amount of  $Fe^{+3}$  in to the A-site, due to which the conical spin-spiral is expected to become less effective [115]. Similar kind of double switching of sign of the temperature dependent  $H_{EB}(M_{EB})$  is recently observed in rare-earth intermetallic system  $Sm_{0.975}Gd_{0.025}Cu_4Pd$  [16].

Finally, the outcome of field induced anomaly in  $\chi_{hf}(T)$ ,  $C_m(T)$  and the sharp jump in  $\Delta S_{mag}(T)$ , across  $T_{comp}$  when the field exceeds a critical level, manifest the signature of change in the energetics of the system presumably due to the underlying SR. Moreover, the curious perception of  $\chi_{hf}(T)$  and  $C_m(T)$  data reveals that the anomaly start growing towards  $T_{comp}$ , where  $H_{EB}(T)$  exhibits maxima and  $H_C^{eff}(T)$  start col-

### 3. Studies in $\text{Co}(\text{Cr}_{1-x}\text{Fe}_x)_2\text{O}_4$ series

---

lapsing down on both sides of  $T_{comp}$ . In addition,  $H_{EB}(T)$  appears again at around  $T_S$  at which we noticed huge peak in  $\chi_{hf}(T)$  &  $C_P(T)$  and small localized minima in  $H_C^{eff}(T)$ . These features *witnesses* the strong correlation between SR/spin-flip and the EB across  $T_{comp}/T_S$ . Previously, these unexpected field induced transitions were noticed by Chen et al.[111] in the context of zero-magnetization alloy of  $(\text{Sm}, \text{Gd})\text{Al}_2$  across  $T_{comp}$ , and attributed to the lowering of the magnetic symmetry due to the reorientation of fully compensated moments corresponds to orbital, spin and that of unequally coupled soft polarized conduction electrons to them. This makes sure that there is a change in the energetics of the system across  $T_{comp}$ . In the present compound, conduction electrons are not available, but it is known that, the competition among the superexchange interactions along the chains Co–O–Co, Co–O–Cr, Co–O–Fe, Cr–O–Cr, Cr–O–Fe and Fe–O–Fe in the spinel structure leads to the domination of magnetic moments of A and B-sublattices at different temperatures. Hence, the SR demonstrated in Fig.3.21 may respond to field in complicated manner across  $T_{comp}$ .

In order to have the rough estimation of the amount of rotations of the spins across  $T_{comp}$ , we have calculated the  $\Delta S_{mag}(T)$  related to the possible changes in the spin configuration for  $x = 0.05$  sample across  $T_{comp}$ . According to simple classical Heisenberg model [116, 117], energy of spinel compound can be written as

$$E = - \sum_{i,j} J_{ij} S_i \cdot S_j - \frac{\mu_B H}{2\pi} \int_0^\pi \left( g_i \sum_i S_i^z + g_j \sum_j S_j^z \right) \times \sin \phi d\phi \quad (3.7)$$

In eq.3.7, first term is the magnetic exchange energy of the system over all the possible intra and inter NN moments of sub lattices A and B. Second term is the magnetic energy due to the external magnetic field,  $H$  and here the integration factor is to account for all the randomly oriented grains in the polycrystalline sample [118]. These calculations conclude,

i) Change in the entropy calculated by assuming the change in any of the super exchange interaction from AFM to FM across  $T_{comp}$  by considering the superexchange interactions calculated from first principles [116] and spin only moments of all the magnetic ions leads to the large  $\Delta S_{mag}(T)$  value by a few orders of magnitude compared to the observed experimental value. Hence, the sign change of the exchange interaction is not possible with the field up to 140 kOe, only the reorientation in spin configuration and the associated magnetic energy is changing.

ii) Now we calculated the amount of  $\Delta S_{mag}(T)$  required to change their configuration across  $T_{comp}$  for various possible reorientations. Among all the possible reorientations in the configuration we attempted, the one shown between (c) and (d) of schematic of Fig.3.21 posses the calculated  $\Delta S_{mag}(T)$  comparable to the experimental value. For the experimental value of  $\Delta S_{mag}(T)$  under 50 kOe spins in B2-site & A-site rotate fully  $180^\circ$  where as the disordered B1-site rotate only by  $20-30^\circ$ . This looks feasible in the point of view of our magnetization data. Decrease in the  $\Delta S_{mag}(T)$  involved in SR/spin-flop across  $T_{comp}/T_S$  with Fe concentration well supports the reduction of the magnitude of the  $H_{EB}(T)$  as we predicted before.

### 3.4.1 Magnetic phase diagram

By combining all the magnetic and thermodynamic properties we constructed the magnetic phase diagram of  $\text{Co}(\text{Cr}_{1-x}\text{Fe}_x)_2\text{O}_4$  as the Fe concentration  $x$  varies from 0.0 to 1.0. The evolution of the magnetic states in  $\text{Co}(\text{Cr}_{1-x}\text{Fe}_x)_2\text{O}_4$  depending on the Fe concentration and temperature that follows from our studies can be interpreted within the phase diagram shown in Fig.3.24. We can see that  $\text{Co}(\text{Cr}_{1-x}\text{Fe}_x)_2\text{O}_4$  series consists of very rich magnetic phase diagram. The FIM transition temperature  $T_C$  is the boundary between the the paramagnetic(PM) phase and that of the long range FIM ordering in  $\text{Co}(\text{Cr}_{1-x}\text{Fe}_x)_2\text{O}_4$ . The parent  $\text{CoCr}_2\text{O}_4(x=0.0)$  exhibits four magnetic phases as a function of temperature, i.e., paramagnetic(PM) above  $T_C$ , mixed

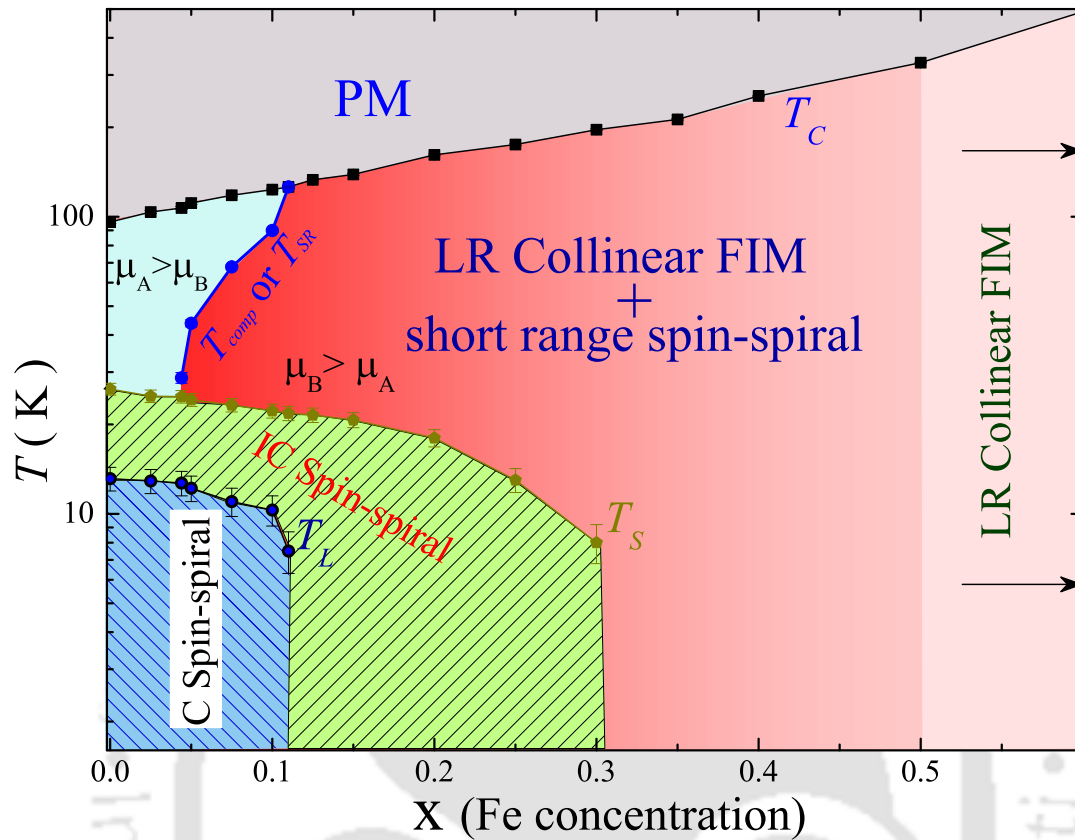


**Figure 3.24:** Magnetic phase diagram of  $\text{Co}(\text{Cr}_{1-x}\text{Fe}_x)_2\text{O}_4$ . For  $T \geq T_C$  all the samples exhibit paramagnetic (PM) state.  $T_S$  separates the collinear FIM ordering and that of the non-collinear spin-spiral ordering.  $T_L$  separates the incommensurate spin-spiral and that of commensurate spin-spiral phase.  $T_{comp}$  is the boundary between the B-site and A-site dominated regimes of the series.

phase of long range collinear plus short range spin-spiral in the temperature range  $T_C \geq T \geq T_S$ , which turnout to be full incommensurate spin-spirals for  $T_S \geq T \geq T_L$  and below  $T_L$  it crosses over to commensurate spin-spiral. In addition to all these phase transitions, with increasing the Fe concentration to 0.044 another phase transition, i.e., magnetic compensation (which turnout to be field induced spin reorientation in high fields) arises. Further, it can be also noted that compensated regime also offers the exchange bias across the phase transitions. For the lower concentrations of Fe the phase boundary between the coexisted long range collinear & short range spin-spirals



### 3. Studies in $\text{Co}(\text{Cr}_{1-x}\text{Fe}_x)_2\text{O}_4$ series

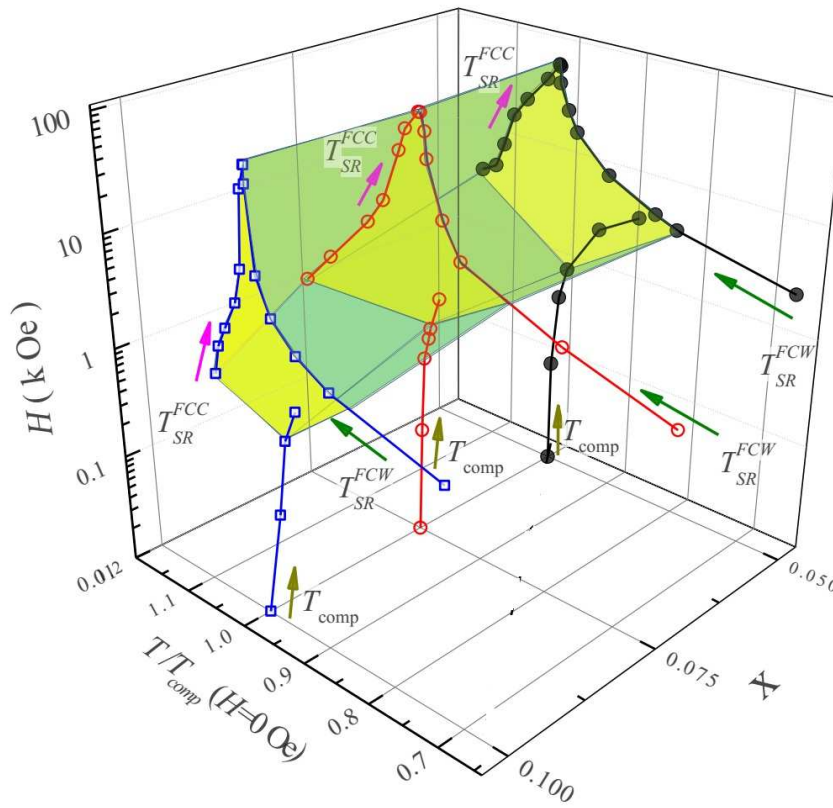


**Figure 3.26:** Field-temperature( $H$ - $T$ ) phase diagram of  $\text{Co}(\text{Cr}_{1-x}\text{Fe}_x)_2\text{O}_4$  for  $x = 0.05$ ,  $0.075$  and  $0.1$  samples. Different transition temperatures as a function of applied field are taken from the temperature dependent magnetization in different modes as shown in the Fig.3.25.

distribution noticed from the XRD analysis. Area of the long range collinear phase increases as a function of Fe concentration and gradually effect of short range spinspirals also decreases, finally for rich Fe concentrated samples magnetic order become fully collinear. In addition to the partially inverted spinel structure the reduction in the bond angles of B–O–B path may also helps to enhance the FM contribution to the total magnetization in the Fe rich concentrated samples.

Fig3.25 shows the temperature dependent magnetization  $\text{Co}(\text{Cr}_{0.9}\text{Fe}_{0.1})_2\text{O}_4$  measured in ZFC, FCC FCW modes. One can see that the FCC curve while cooling from  $T_C$ , initially it exhibits the reversal in magnetization and then a spin reorientation(SR)

transition at  $T_{SR}^{FCC}$  as explained. The FCW curve absolutely follows the FCC curve below the magneto-structural transition,  $T_S$ . But above  $T_S$  it completely deviates, show huge irreversibility with the FCC curve and also exhibits the SR transition at temperature  $T_{SR}^{FCW}$  much higher compared to  $T_{SR}^{FCC}$  and  $T_{comp}$ . From this we can understand that the SR transitions in compensated samples are metastable in nature.

In order to estimate how strong metastable is this SR transition, we carried out the ZFC, FCC and FCW magnetization under various fields ranging from few 10 Oe to 140 kOe for three samples with  $x = 0.05, 0.075$  and  $0.1$  samples. The  $T_{comp}$ ,  $T_{SR}^{FCC}$  &  $T_{SR}^{FCW}$  of all the samples for all applied field are extracted and constructed a field( $H$ ), temperature( $T$ ) and Fe concentration( $x$ ) phase diagram as shown in the Fig.3.26. It is interesting to see that for the low  $H$  values there is no metastability and all the samples exhibit only  $T_{comp}$ , as  $H$  increases the metastability arises. Here the shaded region indicates the amount of the metastability in the SR transition. Width of the metastability first increases and for the higher  $H$  values again decreases and finally for large enough fields it vanishes. It can be also seen that the amount of field to kill the metastability decreases as the Fe concentration and also the width of metastability also decreases. Further it may be also understood that the magnitude of exchange bias also proportional to the amount metastability in the SR.

### 3.5 Summary

To conclude this chapter, we have investigated the detailed structural, thermo-magnetic, isothermal-magnetization, EB effect, and thermodynamic properties of  $\text{Co}(\text{Cr}_{1-x}\text{Fe}_x)_2\text{O}_4$  series under up to large field of 140 kOe. As the function of Fe concentration the FIM transition systematically enhances, for the lower Fe concentrations the magneto-electric transitions prevails but decreases sharply and disappears. It is also observed that few percent of Fe substitution for Cr in  $\text{CoCr}_2\text{O}_4$  drive the system to zero-magnetization limit, results in the magnetization reversal below  $T_{comp}$  under low ap-

### 3. Studies in $\text{Co}(\text{Cr}_{1-x}\text{Fe}_x)_2\text{O}_4$ series

---

plied fields, which turnout to be field induced SR across  $T_{comp}$ . In the compensated stoichiometry, the EB field, evaluated from unusual hysteric behaviour, is elucidated to change sign across  $T_{comp}$ , for the first time in a multiferroic compound and is replica to the recent findings [17, 18] in the context of rare-earth intermetallics. In addition, the search and identification of EB effect in the conical phase below  $T_S$  unveils the richness of physics in the  $\text{Co}(\text{Cr}_{1-x}\text{Fe}_x)_2\text{O}_4$  system. Later, the excellent platform we established from the thorough analysis of thermodynamic properties endeavour the understanding of the physical origin of the emergence of EB and the switching of its sign across  $T_{comp}$  and  $T_S$ . Different anisotropy formed at different temperatures due to the field induced SR and spin-flop, caught from in field & out of field thermodynamic properties and the high field susceptibility, could be the possible underlying origin. We constructed the Fe concentration dependent magnetic phase diagram for the  $\text{Co}(\text{Cr}_{1-x}\text{Fe}_x)_2\text{O}_4$  series. It exhibits very rich magnetic phase diagram, it offers various magnetic phases emerges at different levels of Fe substitution. In case of compensation regime of this series the metastability plays a main role on the field-temperature magnetic phase diagram.

# Chapter 4

## Studies in $\text{Co}(\text{Cr}_{1-x}\text{Co}_x)_2\text{O}_4$ series

### 4.1 Introduction

We noticed that the substitution of ‘Fe’ for Cr-site in  $\text{CoCr}_2\text{O}_4$  influences its magnetic properties and the underlying magnetic phase diagram in a significant manner. ‘Fe’ substitution also leads to the emanation of novel phenomena of magnetization and EB field reversal across the  $T_{comp}$ . Another unique characteristic feature is the observation of the EB effect in the non-collinear spin-spiral phase below  $T_S$  and more significantly below  $T_L$ , at which the complex incommensurate conical spin-spiral magnetic order with propagation vector of (0.63, 0.63, 0) observed at  $T_S$  [28, 29] crosses over to a commensurate spin-spiral order with propagation vector of (2/3, 2/3, 0) [30]. Below  $T_L$ , the spin configuration locks to the lattice [24]. It seems that the ‘Fe’ substitution disturbs the spin-spiral phase, resulting in the observation of the EB below  $T_S$ .

Kim et al. [36] demonstrated enhanced electric polarization of  $\text{CoCr}_2\text{O}_4$  with the modification of magnetic configuration by mixing its Cr-site with  $\text{Co}^{+3}$  ions. This result has been explained by a broken balance between two electric polarization contributions with  $\text{Co}^{+3}(3d^6)$  ions in Cr-site, which consists of zero magnetic moment in its low spin state. It is appreciable to see the influence of  $\text{Co}^{+3}$  substitution for ‘Cr’ on

## 4. Studies in $\text{Co}(\text{Cr}_{1-x}\text{Co}_x)_2\text{O}_4$ series

---

the magnetic properties of  $\text{CoCr}_2\text{O}_4$ . It is also useful to probe the origin of negative magnetization observed in  $\text{Co}(\text{Cr}_{1-x}\text{Co}_x)_2\text{O}_4$  [36].

Anomalous temperature dependent EB effect is reported in multilayers of non-collinear spin AFM and collinear spin FM materials[93, 94]. Even in a bulk single phase material, it has been claimed that the non-collinear spin configurations can give rise to EB effect [21, 95]. Hence, study of EB is important in non-collinear spin-spiral  $\text{Co}(\text{Cr}_{1-x}\text{Co}_x)_2\text{O}_4$  multiferroic compounds.

This chapter deals with the preparation, structural, temperature and magnetic field dependent magnetization and EB effects of  $\text{Co}(\text{Cr}_{1-x}\text{Co}_x)_2\text{O}_4$ .

### 4.2 Experimental details

The polycrystalline samples of  $\text{Co}(\text{Cr}_{1-x}\text{Co}_x)_2\text{O}_4$  ( $x = 0.0-0.1$ ) are prepared by standard solid state reaction method. Stoichiometric amounts of high purity( $\geq 99.9$ )  $\text{Co}_3\text{O}_4$ ,  $\text{Cr}_2\text{O}_3$  & Cobalt(III) acetylacetonate are used as starting materials. The powders obtained after the calcination at  $600^\circ\text{C}$  are pressed into pellets and then sintered at  $1100^\circ\text{C}$  for 12 hours for two times followed by regrinding and palletizing. During all heat treatments, the pellets were placed on a bed of powder with the same stoichiometry to minimize the possibility of reaction of the samples with the crucible. Powder XRD patterns were obtained using  $\text{Cu-K}\alpha$  ( $\lambda = 1.5406 \text{ \AA}$ ) radiation in a Rigaku commercial X-ray diffractometer. The morphology and composition analysis are investigated by SEM images and EDAX spectrum, respectively. DSC/TGA analysis have been carried by using commercial Netzsch DSC/TG machine (Model: STA449F3A00). Magnetization measurements between 2 K and 320 K, and upto the maximum magnetic field of 70 kOe are performed using SQUID-VSM (Model 5 Quantum design.).

## 4.3 Results and Discussions

### 4.3.1 Structural properties

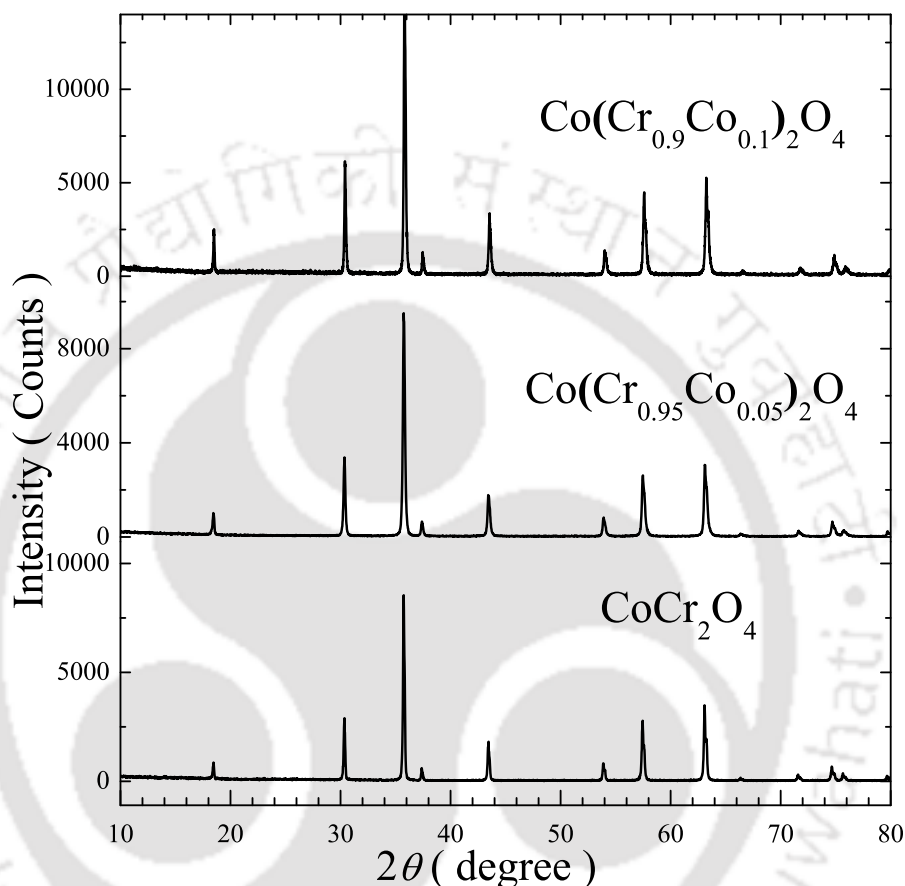


**Figure 4.1:** Powder XRD patterns of  $\text{Co}(\text{Cr}_{1-x}\text{Co}_x)_2\text{O}_4$  samples measured at room temperature.

Fig.4.1 shows the XRD patterns of  $\text{Co}(\text{Cr}_{1-x}\text{Co}_x)_2\text{O}_4$  samples recorded at the room temperature. We can see that all ‘Co’ substituted samples show the XRD patterns similar to the parent  $\text{CoCr}_2\text{O}_4$  compound. We noticed that beyond the 10% of Co substitution the samples are not found to be in single phase.

Phase purity of the  $\text{Co}(\text{Cr}_{1-x}\text{Co}_x)_2\text{O}_4$  samples is analysed by Rietveld refinement technique with the help of FULL PROF utility software. From Fig.4.2 it can be seen that all the peaks are well fitted to the cubic spinel structure ( $\text{Fd}\bar{3}\text{m}$  space group)

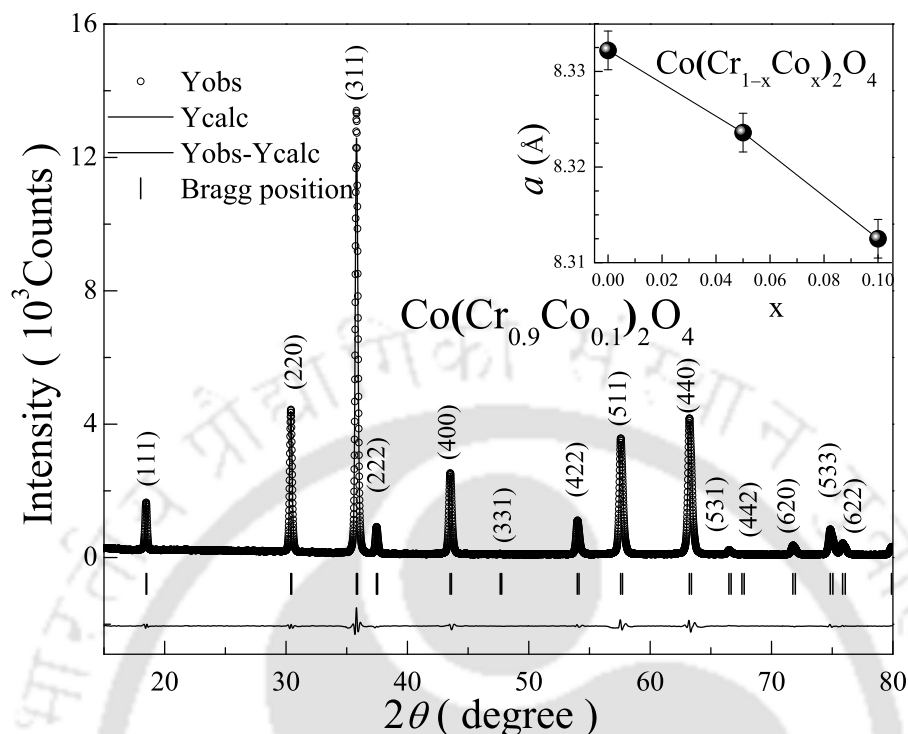


**Figure 4.2:** Experimental and fitted powder XRD patterns of  $\text{Co}(\text{Cr}_{0.9}\text{Co}_{0.1})_2\text{O}_4$  sample. Inset shows the variation of lattice parameter ‘ $a$ ’ with ‘Co’ concentration ‘ $x$ ’ in  $\text{Co}(\text{Cr}_{1-x}\text{Co}_x)_2\text{O}_4$ . Here, vertical bars indicate the error in ‘ $a$ ’ due to instrumental broadening and fitting the data. Solid line is just guide to the eye.

up to  $x = 0.1$ . However, from the refinement it is found that beyond  $x = 0.1$ , extra phase of the  $\text{CoO}$  is formed. Inset of Fig.4.2 depicts the variation in the unit cell parameter, ‘ $a$ ’ as a function of ‘Co’ concentration ‘ $x$ ’ in  $\text{Co}(\text{Cr}_{1-x}\text{Co}_x)_2\text{O}_4$  obtained from the fitting. It is evident that the lattice parameter ‘ $a$ ’ decreases with increase in the ‘Co’ the concentration. Contraction in the unit cell parameter is due to the smaller ionic size of  $\text{Co}^{+3}$  ( $3d^6$ ) compared to that of  $\text{Cr}^{+3}$  ( $3d^3$ ) in the octahedral crystallographic environment. Moreover, the contraction in ‘ $a$ ’ also demonstrates that the Co ion is in the  $+3$  ( $3d^6$ ) state, otherwise, we would have noticed the expansion in ‘ $a$ ’, since the ionic size of  $\text{Co}^{+2}$  ( $3d^7$ ) is larger than  $\text{Cr}^{+3}$  ( $3d^3$ ).

Left panels of Fig.4.3 depict the SEM images of  $x = 0.05$  and  $x = 0.1$  samples. Uniform contrast in the images indicates the phase purity of the samples. In addition

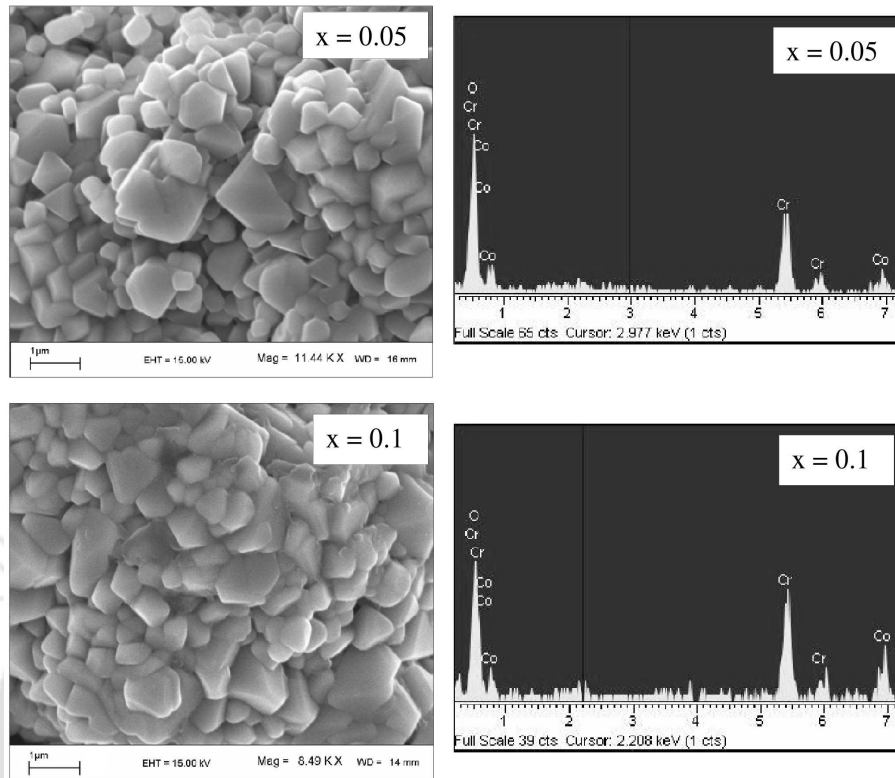


**Figure 4.3:** SEM images(left panel) and EDAX spectra (right panel) of  $\text{Co}(\text{Cr}_{1-x}\text{Co}_x)_2\text{O}_4$  samples.

to this we can see the sharp edged pyramids and polyhedral grains in both the images. This type of self-organized and ordered pattern of pyramid clusters have been observed in spinel  $\text{CoCr}_2\text{O}_4$  thin films [119]. The facets of these pyramids are found to be the minimum surface energy crystal planes of the cubic spinel  $\text{CoCr}_2\text{O}_4$  [119, 120]. Observation of the similar structures with sharp edges in our samples may indicate the ordered growth of the micro crystals of the spinel  $\text{Co}(\text{Cr}_{1-x}\text{Co}_x)_2\text{O}_4$ . The average grain size is found to be around 1-2 micrometer. Composition analysis using EDAX spectra as shown in the right panels of Fig.4.3 confirmed that the atomic ratio of the elements is comparable to the nominal starting stoichiometric ratios.

To understand the formation mechanism of the samples from the starting materials,

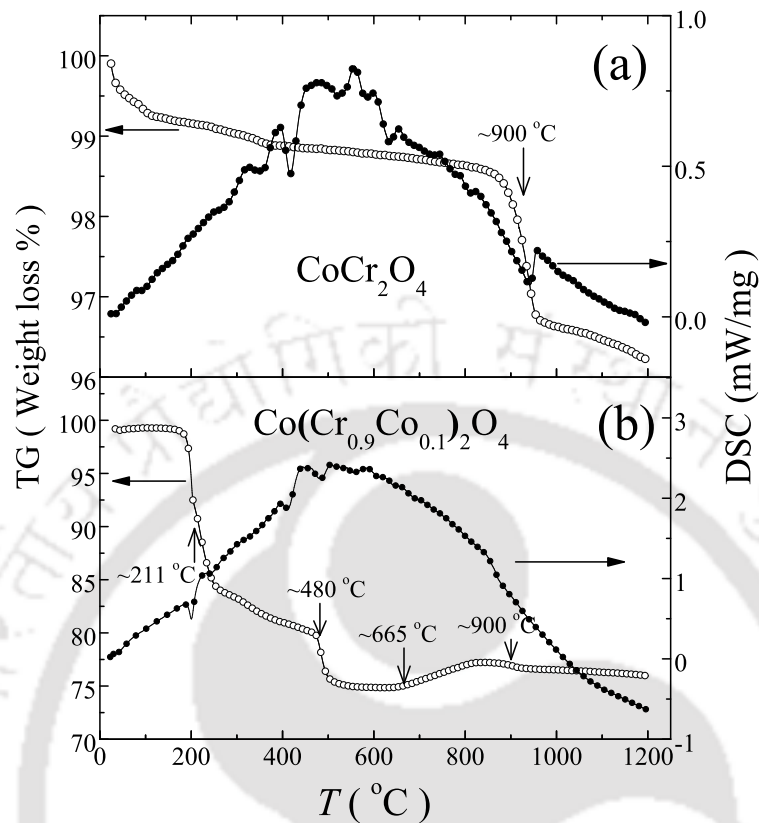


**Figure 4.4:** DSC and TG plots of (a)  $x = 0.0$  and (b)  $x = 0.1$  samples measured in the air environment.

we carried out the differential scanning calorimetry (DSC) and Thermal gravimetric analysis (TGA) measurements in air environment. Fig.4.4(a) and (b) describe the temperature dependent DSC & TG curves of the  $x = 0.0$  and  $x = 0.1$  samples, respectively. From this analysis we can see that the  $x = 0.0$  sample shows major weight loss at around  $900^{\circ}\text{C}$  and that could be attributed to the decomposition process of  $\text{Co}_3\text{O}_4$  into  $\text{CoO}$ . But the  $x = 0.1$  sample shows the complicated behaviour. Upon increasing the temperature, the first and the major weight loss in the temperature range  $200\text{--}250^{\circ}\text{C}$  with a sharp fall at around  $211^{\circ}\text{C}$  is due to the decomposition of the Cobalt(III) acetylacetonate. The second weight loss around  $480^{\circ}\text{C}$  could be ascribed to the evaporation of the decomposed organic ligands. This type of multiple weight loss mechanism is comparable to the previous reports [121, 122]. The gain

in the weight of the  $x = 0.1$  sample which starts around  $665^\circ\text{C}$  and continues to increase till the temperature reaches the decomposing temperature of  $\text{Co}_3\text{O}_4$  (as noticed in  $x = 0.0$  sample) may be due to the absorption of the oxygen by the decomposed Cobalt(III) acetylacetonate. Due to the decomposing temperature of  $\text{Co}_3\text{O}_4$  around  $900^\circ\text{C}$ , sample again show weight loss. From the DSC curve it can be seen that the both the decompositions are exothermic processes.

### 4.3.2 Temperature and field dependent magnetic properties

In order to explore the influence of ‘Co’ substitution on the different magnetic transitions of  $\text{CoCr}_2\text{O}_4$ , temperature dependent magnetization measurements have been performed in different modes. Three panels of Fig.4.5 namely (a), (b) & (c) show the detailed thermomagnetic response in the FCC mode under the applied field of  $H \sim 10$  Oe and ZFC & FCW modes under the applied field of  $H = 1$  kOe for  $x = 0.0$ ,  $x = 0.05$  &  $x = 0.1$  samples, respectively. The collinear FIM transition temperature  $T_C$  decreases slightly with increasing the Co concentration. Unlike, the temperature dependent magnetic behaviour observed in the Fe substituted samples[123], ‘Co’ substitution for ‘Cr’ enhances the magnetization and do not show any compensation effect. We can see the clear increase in the magnitude of the magnetization as ‘Co’ concentration increases.

In case of parent compound  $\text{CoCr}_2\text{O}_4$ , the reduction in the resultant magnetization after reaching the  $M_{max}$  below  $T_C$  is attributed to the ordering of the B-site (combination of antiferromagnetically arranged B1 and B2 moments) ions in such a way that the resultant moment is antiparallel to the A-site moment which is aligned along the field. Due to the underlying geometrical frustration short range order of B-sub lattice moments continues till  $T_S$ , below which it turns out to be fully spin-spiral [23, 24, 28, 29]. This results in the sharp transition at  $T_S$ . Hence, one can understand the substituted ‘Co’ ions decreases the resultant moment of the

#### 4. Studies in $\text{Co}(\text{Cr}_{1-x}\text{Co}_x)_2\text{O}_4$ series

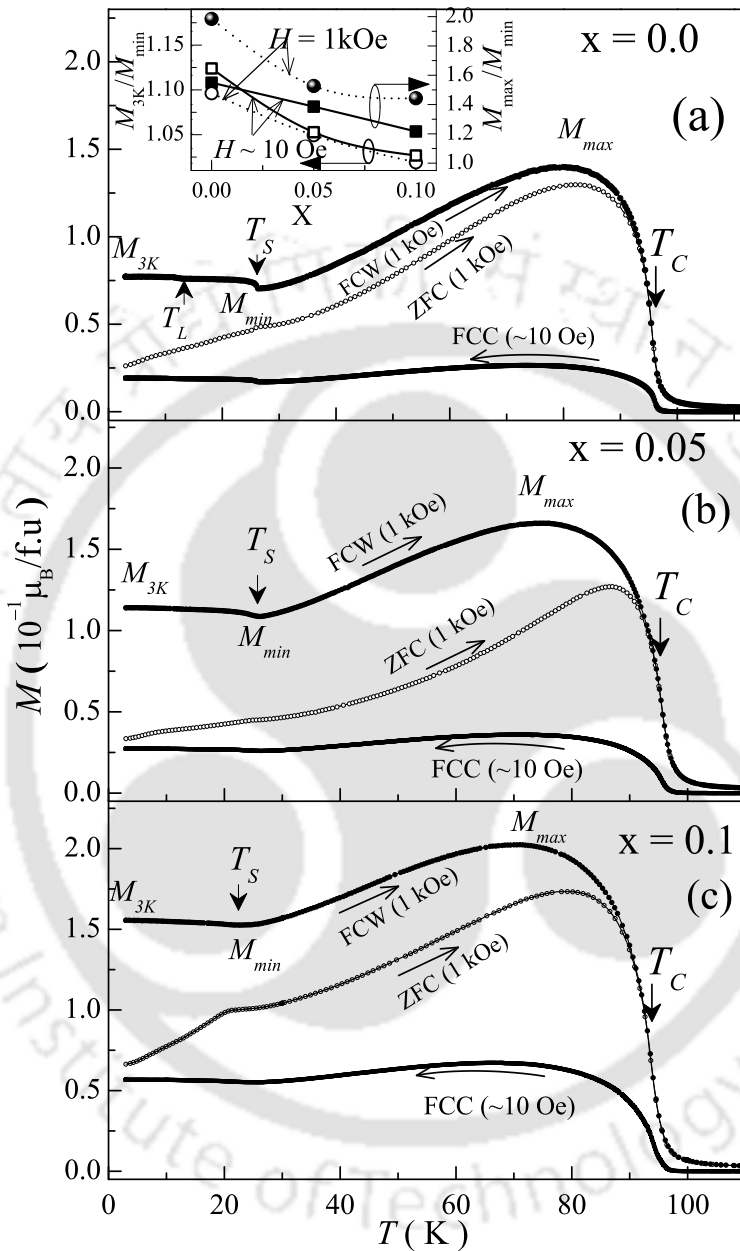


**Figure 4.5:** Temperature dependent magnetization curves of  $\text{Co}(\text{Cr}_{1-x}\text{Co}_x)_2\text{O}_4$  samples measured in FCC mode for the applied field of nominal zero ( $\sim 10$  Oe) and ZFC, FC modes under the applied field of  $H = 1$  kOe. Inset of (a) shows the variation of  $M_{max}/M_{min}$  and  $M_{3K}/M_{min}$  as a function Co concentration (see text for details).

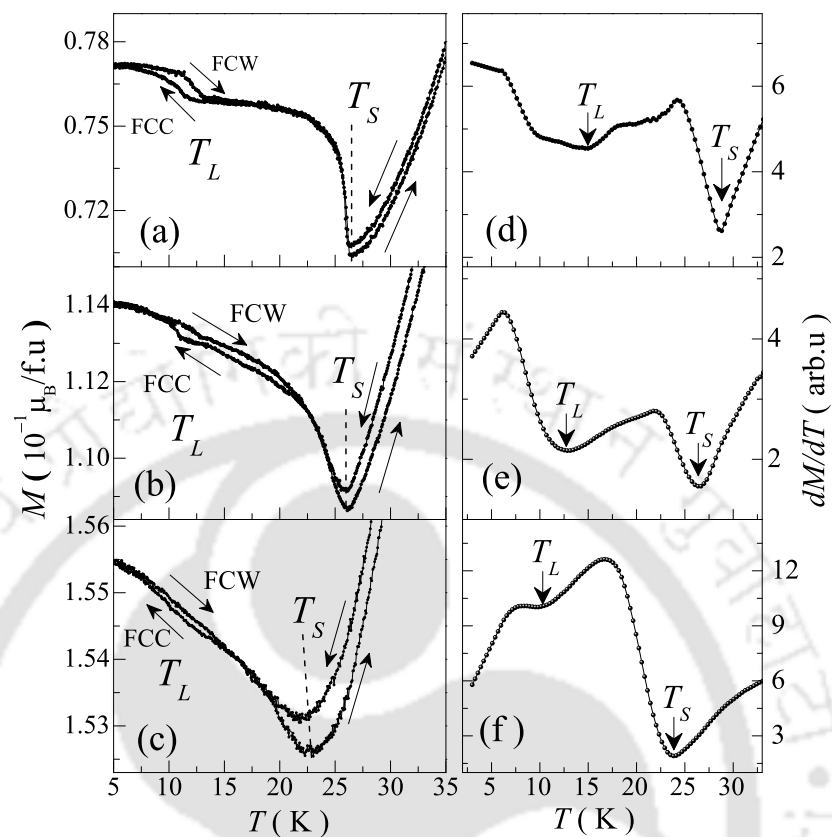


**Figure 4.6:** (a), (b) and (c) enlarged views of the FCC & FCW magnetization curves across different low temperature transitions of  $x = 0.0$ ,  $x = 0.05$  and  $x = 0.1$  samples, respectively. Whereas (d), (e) & (f) temperature dependent  $dM/dT$  curves of  $x = 0.0$ ,  $x = 0.05$  and  $x = 0.1$  samples, respectively.

B-site. In addition, as depicted in the inset of Fig.4.5(a) the ratio of the maximum magnetization ( $M_{max}$ ) on the onset of  $T_C$  & magnetization at 3 K ( $M_{3K}$ ) to the minimum magnetization ( $M_{min}$ ) at  $T_S$ , viz.  $M_{max}/M_{min}$  &  $M_{3K}/M_{min}$  decrease as a function of ‘Co’ concentration. Decreasing trend of  $M_{max}/M_{min}$  &  $M_{3K}/M_{min}$  with ‘Co’ concentration signifies that the magnitude of the temperature dependent magnetization below  $T_C$  is not uniformly changed with ‘Co’ concentration and this may suggest the significant change in the underlying magnetic frustration.

We can see that with increasing the Co concentration the magneto-structural transition at  $T_S$  shifts towards low temperature compared to that of  $\text{CoCr}_2\text{O}_4$ . Enhance-

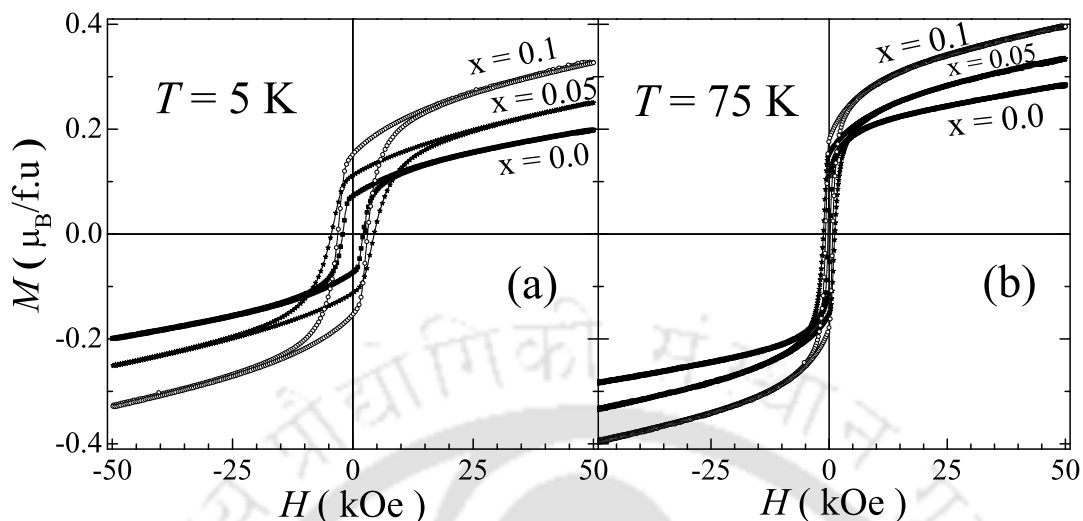


**Figure 4.7:** (a) and (b) are the isothermal magnetization loops of  $\text{Co}(\text{Cr}_{1-x}\text{Co}_x)_2\text{O}_4$  samples at 5 K and 75 K, respectively, measured after zero-field cooling from above  $T_C$ .

ment in the magnetization and slight lowering of the  $T_C$  &  $T_S$  with ‘Co’ substitution are in well agreement with the previous report [36], in which the ‘Co’ ions in Cr-site are found to be in +3 state and non-magnetic in nature.

Fig.4.6 describes the low temperature behaviour of magnetization of all the samples. Left panel of Fig.4.6((a), (b) & (c)) depict the enlarged view of  $M$ - $T$  curve measured in FCC and FCW mode across the  $T_S$  and  $T_L$ . We can see that the  $T_S$  &  $T_L$  are shifted towards lower temperature. It can be also seen that the magneto-structural transition at  $T_S$  gets broadened out with Co concentration. Further, we can see that the FCC and FCW curves exhibit a thermal hysteresis across  $T_L$  and  $T_S$ . While cooling the sample in field, below  $T_L$ , the spin state becomes anisotropic due to locking of the commensurate spin-spirals to that of lattice. Upon warming from 3 K, more thermal energy is required to overcome the anisotropy, which results in the shifting of transition point at  $T_L$  in the FCW curve to higher temperature compared to FCC curve. But the transition point(indicated by vertical dashed lines) across  $T_S$  do not show any significant shift in FCC and FCW curves. This may be due to the fact that the incommensurate spin-spiral below  $T_S$  is not locked to the lattice. However, the hysteresis

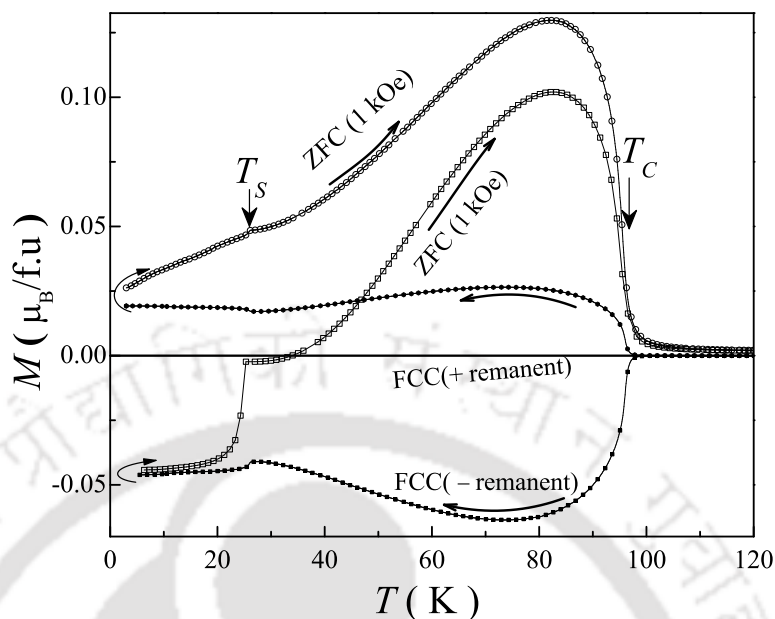


**Figure 4.8:** Temperature dependent of ZFC magnetization curve of  $x = 0.0$  sample measured after cooling the sample in positive and negative remanent field.

across  $T_S$  may be due to the change in the magnetic structure from the collinear FIM observed in  $T_S \leq T \leq T_C$  to that of non-collinear incommensurate spin-spirals below  $T_S$ . The thermal hysteresis in FCC and FCW curves across  $T_L$  also indicates a first order nature of lock-in transition.

From the enlarged portions of  $dM(T)/dT$  versus  $T$  plots as shown in the right column ((a), (b) & (c)), it is much more evident that the  $T_S$  move towards lower temperatures. The sharpness of the magneto-structural transition also becomes less effective. Furthermore, the designated lock-in transition observed at around  $T_L = 13$  K in  $\text{CoCr}_2\text{O}_4$  due the conversion of spin-spiral component with an incommensurate propagation vector of  $(0.63, 0.63, 0)$  observed at 27 K to the conical spin order with commensurate propagation vector of  $(2/3, 2/3, 0)$  [30] is also shifts to lower temperature with increase in ‘Co’ concentration. All these features signify that the substituted ‘Co’ ions successfully replace the Cr ions and influence the spin-spirals below  $T_S$ .

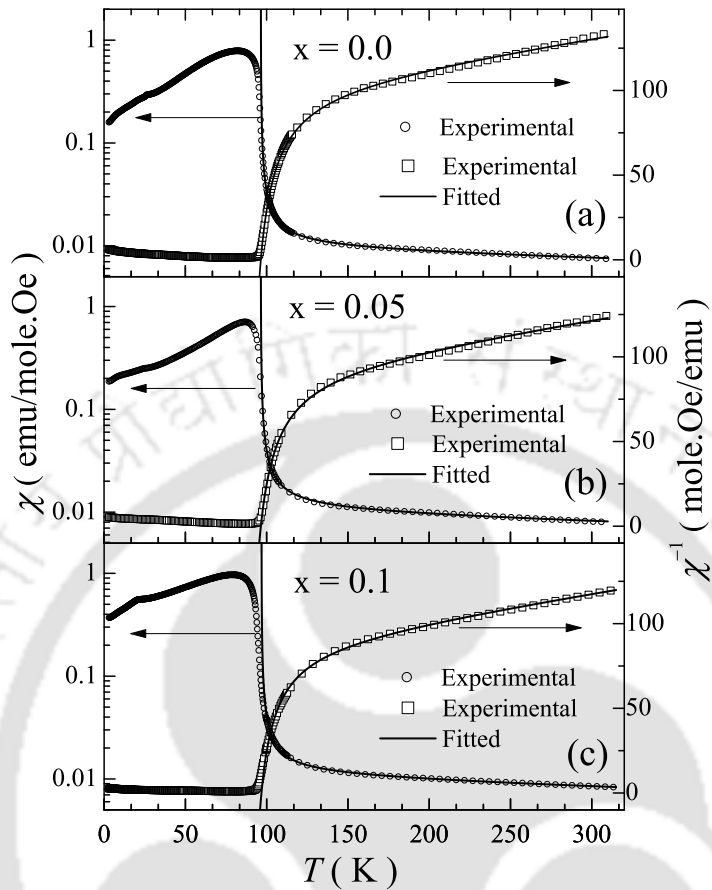


**Figure 4.9:** Fitting of Néel model to the paramagnetic susceptibility(left scale) and inverse susceptibility(right scale) of  $\text{Co}(\text{Cr}_{1-x}\text{Co}_x)_2\text{O}_4$  samples measured in ZFC mode.

Fig.4.7 (a) and (b) show the ZFC  $M$ - $H$  loops of  $\text{Co}(\text{Cr}_{1-x}\text{Co}_x)_2\text{O}_4$  samples at 5 K and just below the  $T_C$  at which the samples exhibit maximum value of magnetization in the temperature dependent magnetization curve, i.e., in spin-spiral and collinear magnetic phases, respectively. Here also we can observe the clear enhancement in total magnetization with Co substitution even at high fields where all the magnetic domains align to the field and all the anisotropic effects vanish. Loops at 5 K show reduction in the magnetization at 50 kOe field compared to the loops at below  $T_C$ , similar to that of the thermomagnetic behaviour of the samples. In the view of ground state magnetic configuration of  $\text{CoCr}_2\text{O}_4$  [23, 28, 29], reduction of  $S_B$  due to the occupation

of non-magnetic Co in B-site causes the enhancement in resultant magnetization with increase in Co concentration.

Fig.4.8 depicts the impact of the consideration of remanent magnetic field on the temperature dependent magnetic properties of ferrimagnets using SQUID magnetometer. Here we can see the ZFC measurement carried out in the positive low applied field after cooling the sample in the positive minimum remanent field ( $\sim 10$  Oe) do not show any negative magnetization. But it can be seen that the ZFC curve measured in positive field after cooling the sample in considerable negative remanent field shows negative magnetization. If the remanent field is more (in the range of 100–300 Oe) the ZFC curve show more negative magnetization even upto FIM transition. This is the possible origin for the observed negative magnetization in ZFC curve in various reports on simple FIM systems [36, 104]. Hence, to get the reliable ZFC data, it is necessary to reduce the remanent field in the SQUID magnetometer to the possible minimum value and then secondly the sign of the applied field should be similar to the sign of the remanent field.

Paramagnetic susceptibility  $\chi(T)$  (above  $T_C$ ) of  $\text{Co}(\text{Cr}_{1-x}\text{Co}_x)_2\text{O}_4$  samples is analysed by the Néel two sub-lattice model of the form [47],

$$\frac{1}{\chi(T)} = \frac{(T - \Theta)}{C} - \frac{\xi}{(T - \Theta')} \quad (4.1)$$

The best fits to the experimental paramagnetic  $1/\chi(T)$  and  $\chi(T)$  data [as shown in the Fig.4.9] of  $\text{Co}(\text{Cr}_{1-x}\text{Co}_x)_2\text{O}_4$  samples can be obtained by the parameters  $\Theta$ ,  $C$ ,  $\xi$  and  $\Theta'$  listed in the Table.4.1. Curie-Weiss constant  $C = N\mu_{eff}^2/3k_B$  allows to estimate the effective paramagnetic magnetic moment ( $\mu_{eff}$ ) of the sample.  $\mu_{eff}$  of the samples are comparable to the theoretically calculated effective moment of orbital quenched (spin only) and unquenched (orbital + spin) free  $\text{Cr}^{+3}$  and  $\text{Co}^{+2}$  ions, respectively. Magnitude of the asymptotic Curie temperature  $\Theta$  represents the strength of the anti-ferromagnetic exchange coupling between the spins on the A-and B-sites in the spinel

#### 4. Studies in $\text{Co}(\text{Cr}_{1-x}\text{Co}_x)_2\text{O}_4$ series

structure. Negative sign of  $\Theta$  signify the magnetism in this materials is governed by the negative superexchange interactions. Lotgering [124] developed a mean-field approach to estimate the approximate values of nearest neighbor exchange interactions in spinel compounds from the paramagnetic susceptibility. AFM superexchange constants  $J_{ij}$  have been obtained in case of  $\text{MnCr}_2\text{O}_4$  [125]. We used the fitted values of  $\Theta$ ,  $C$ ,  $\xi$  and  $\Theta'$  to estimate the  $J_{ij}$  in case of  $\text{Co}(\text{Cr}_{1-x}\text{Co}_x)_2\text{O}_4$  samples using this approach. Average values of  $J_{AA}$ ,  $J_{AB}$  and  $J_{BB}$  are presented in the Table.4.1. We can see  $J_{AB}$  and  $J_{BB}$  decrease with increasing the Co concentration. The values of  $J_{ij}$  are in good agreement with the reported isostructural spinel compounds  $\text{MnCr}_2\text{O}_4$  [125] and  $\text{ZnCr}_2\text{O}_4$  [126].

**Table 4.1:** Parameters obtained from the analysis of the paramagnetic susceptibility of  $\text{Co}(\text{Cr}_{1-x}\text{Co}_x)_2\text{O}_4$  samples. Here exchange interactions  $J_{AA}$ ,  $J_{AB}$  and  $J_{BB}$  are average values of NN superexchange interactions.

| x    | C      |      | $\Theta$<br>( K ) | $\xi$<br>( $\frac{\text{mole.Oe}}{\text{K}}$ ) | $\Theta'$<br>( K ) | $J_{AA}$<br>( K ) | $J_{BB}$<br>( K ) | $J_{AB}$<br>( K ) | u           |
|------|--------|------|-------------------|--|--------------------|-------------------|-------------------|-------------------|-------------|
|      | Exp    | Cal  |                   |  |                    |                   |                   |                   |             |
| 0.0  | 6.9(1) | 7.13 | -634(12)          | 1006(13)                                       | 86.9(1)            | -9.24             | -24.34            | -12.14            | $\sim 2$    |
| 0.05 | 6.7(1) | 6.94 | -553(10)          | 995(13)  | 86.1(1)            | -7.12             | -23.35            | -11.26            | $\sim 1.96$ |
| 0.1  | 6.6(1) | 6.76 | -508(2)           | 933(10)  | 85.7(1)            | -6.04             | -23.31            | -10.94            | $\sim 1.9$  |

The magnetic ordering of spinel compounds is mainly decided by the underlying magnetic geometrical frustration(MGF) in pyrochlore B-sublattice, that makes the inability of the system to satisfy the competing magnetic interactions. Due to MGF, magnetic ordering become unpredictable, and have large degenerate magnetic configurations [66, 126]. As described in the chapter 1, according to the LKDM model, strength of the MGF and hence, the magnetic ground state of spinels can be esti-

ated by utilizing  $u = (4J_{BB}S_B/3J_{AB}S_A)$ . The ratio of  $J_{BB}/J_{AB}$  estimated in case of  $\text{CoCr}_2\text{O}_4$  from the paramagnetic susceptibility also gives rise to the ‘ $u$ ’ value approximately ‘2’ as listed in the Table.4.1. This value is a favourable condition for the formation of spin-spirals [28, 29]. Remarkably, in  $\text{CoCr}_2\text{O}_4$   $J_{BB}$  &  $J_{AB}$  integrals estimated from the molecular field calculations [28] and ground state magnetic structure by neutron scattering data [29] also found to give similar value of ‘ $u$ ’. But, the  $\text{Co}^{+3}$  ( $3d^6$ ) substituted for  $\text{Cr}^{+3}$  ( $3d^3$ ), becomes non-magnetic in its low spin state[36] due to the large crystal splitting energy in octahedral crystallographic environment. This results in the reduction of resultant magnitude of  $S_B$  and also causes the interruption of the superexchange interaction as we noticed the reduction in  $J_{BB}$  and  $J_{AB}$ . Further, the corresponding ‘ $u$ ’ parameter also decreases slightly compared to  $\text{CoCr}_2\text{O}_4$ .

This may cause the decrease in the magnetic frustration of the pyrochlore B-sublattice, as a result the spin-spirals may become stable compared to the parent compound. In support to this conclusion the frustration index  $f \sim |\Theta|/T_C$ , which is assumed to be the experimental estimate of the frustration, also decreases from  $\sim 6.5$  to  $\sim 5.4$  with increasing the ‘Co’ concentration from 0 to 0.1.

### 4.3.3 Exchange bias effect

We noticed complicated temperature dependent EB effect in ‘Fe’ substituted samples. Let us see the EB effect in ‘Co’ substituted samples along with parent compound of  $\text{CoCr}_2\text{O}_4$ . Fig.4.10(a) and (b) depict the 70 kOe FC  $M$ - $H$  loops of  $x = 0.05$  and  $0.1$  samples, respectively. 70 kOe FC  $M$ - $H$  loops are performed by using the procedure explained in the previous chapter. One can see the  $M$ - $H$  loops at 30 K are symmetric with respect to the origin. But the loops at 5 K and 3 K are clearly off centered viz. shifted left on the field axis as well as up side on the magnetization axis with respect to the origin. Whereas, the pristine  $\text{CoCr}_2\text{O}_4$  compound does not exhibit any

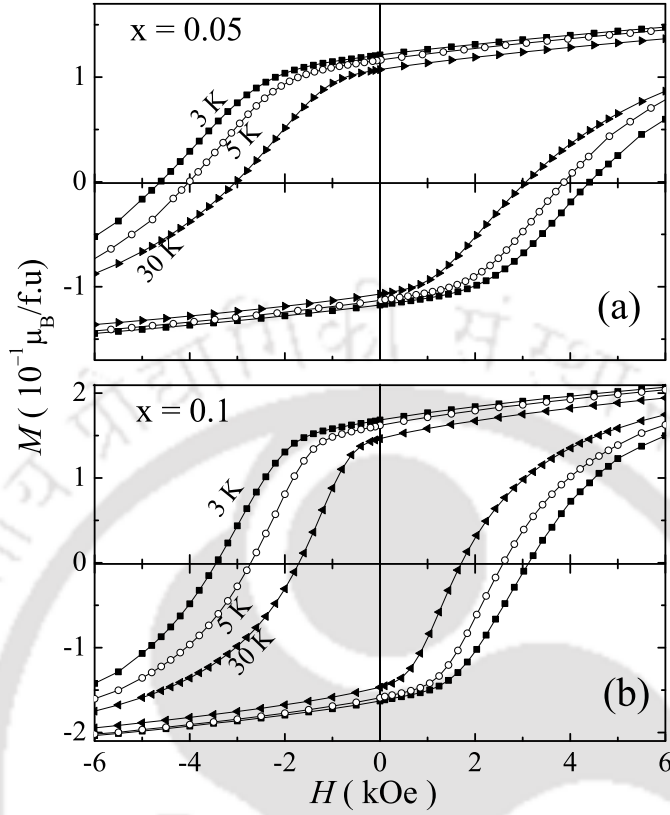


**Figure 4.10:** (a) and (b), respectively, are the enlarged portions 70 kOe FC  $M$ - $H$  loops of loops of  $x = 0.05$  and  $0.1$  samples at 3 K, 5 K & 30 K

unusual shifting in FC  $M$ - $H$  loops. This denote that unlike in Fe substituted samples, ‘Co’ substituted compounds show the asymmetric characteristics only at lowest temperature, i.e., in the conical spin-spiral phase below  $T_S$ .

Main panels of Fig.4.11(a), (b) and (c) describe the temperature dependence of EB(amount of shift along field axis) field  $H_{EB}$  & the vertical shift  $M_{EB}$  obtained from the 70 kOe FC  $M$ - $H$  loops of  $x = 0.0, 0.05$  and  $0.1$  samples, respectively. Here,  $H_{EB}$  and  $M_{EB}$  are defined as

$$H_{EB} = - \frac{(H_{C+} + H_{C-})}{2} \quad (4.2)$$

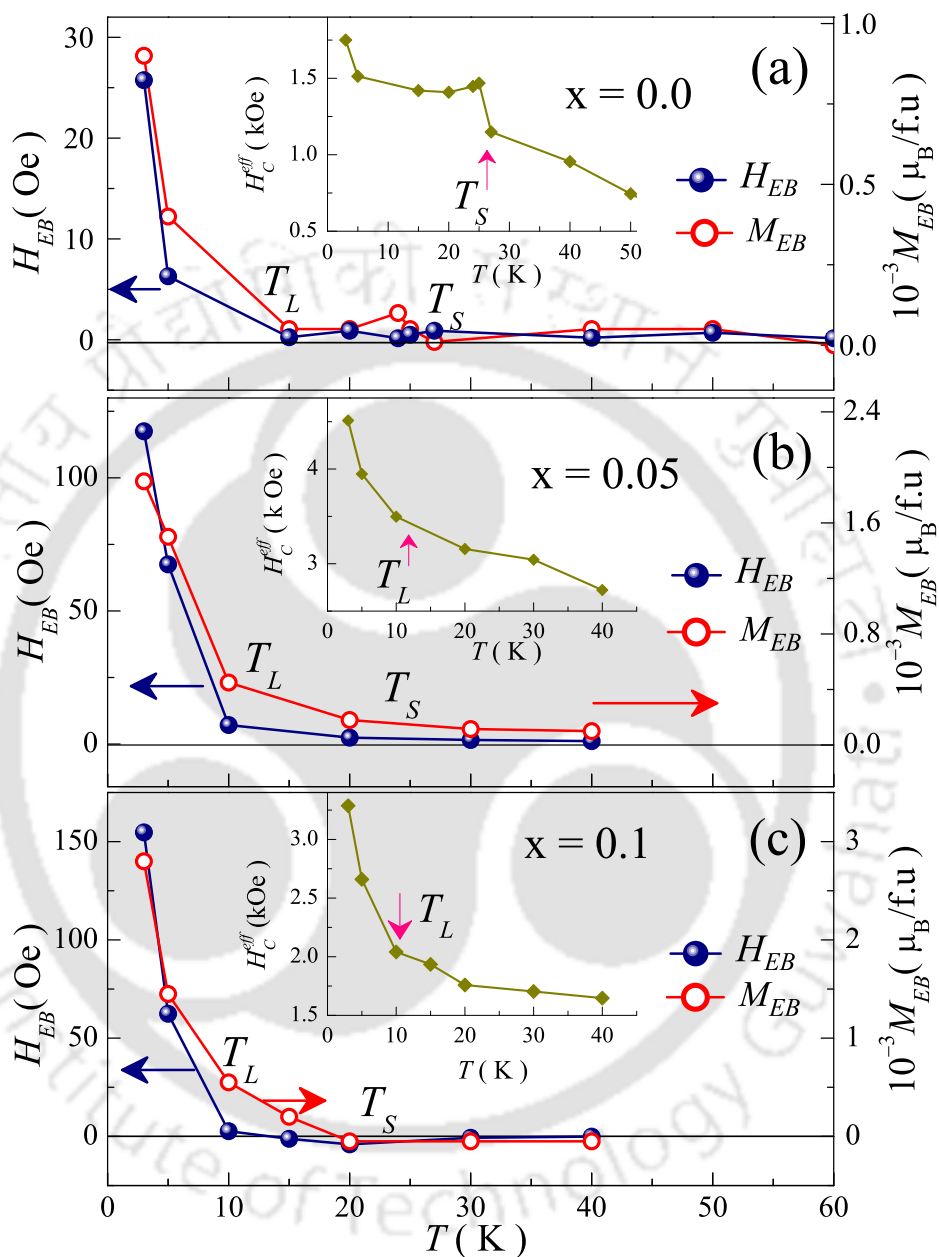


**Figure 4.11:** Main panels of (a), (b) & (c) are the temperature dependence of EB field (left scale) and vertical shift in the  $M$ - $H$  loop (right scale) for CoCr<sub>2</sub>O<sub>4</sub>, Co(Cr<sub>0.95</sub>Co<sub>0.05</sub>)<sub>2</sub>O<sub>4</sub> & Co(Cr<sub>0.9</sub>Co<sub>0.1</sub>)<sub>2</sub>O<sub>4</sub> samples, respectively. Insets in all the panels are the temperature dependent effective coercive field of the respective samples.

#### 4. Studies in $\text{Co}(\text{Cr}_{1-x}\text{Co}_x)_2\text{O}_4$ series

---

$$M_{EB} = \frac{(M_{rem+} + M_{rem-})}{2} \quad (4.3)$$

where  $H_{C+}$  &  $H_{C-}$  are the positive & negative coercive field values and  $M_{rem+}$  &  $M_{rem-}$  are the positive & negative remanent magnetization values of FC M-H loops, respectively.

One can see  $x = 0.0$  exhibits very small  $H_{EB}$  and  $M_{EB}$  values at all the temperatures in its magnetically ordered state below  $T_C$ . The fluctuations marked at around  $T_S$  feasibly due to the spin-flip transitions. However, magnitude of  $H_{EB}$  is not considerable. But upon increasing the Co concentration,  $H_{EB}$  start increasing below the lock-in transition  $T_L$ , whereas the vertical shift,  $M_{EB}$  show rising tendency below  $T_S$ . The magnitude of the  $H_{EB}(T)$  and  $M_{EB}(T)$  also can be seen to strengthen with 'Co' concentration. This indicates the entanglement of the lock-in transition with that of the EB effect, in this non-collinear spin-spiral system.

The substituted non-magnetic  $\text{Co}^{+3}$  for some of magnetic Cr ions causes the release of magnetic frustration of that particular triangular blocks of the pyrochlore B-sublattice and hence become the soft FIM. But the remaining blocks do not get affected, they can still form the rigid conical spin-spirals. Hence there is provision to form different kind of soft and hard magnetic configurations within the crystallographically homogeneous material. While cooling the sample across the spin-flop transitions the non-collinear spin-spiral magnetic ordering develops uni-axial anisotropy and hence exert pinning force on the soft magnetic blocks [127]. This may be the possible underlying origin for the observation of the  $H_{EB}(M_{EB})$  in non-collinear spin-spirals. Moreover, it is more effective in the commensurate spin-spiral phase below  $T_L$  as the spin-spirals are locked to the underlying lattice sites. Due to this locked spin-spirals the magnetic configuration get frozen with lowering temperature below  $T_L$ , so an extra field is required to overcome the microscopic torque in the descending branch of the  $M$ - $H$  loop,

results in the shift along negative field. But in the long range collinear phase above  $T_S$ , system as a whole becomes softer then all these effects vanish. This is analogous to that anomalous EB observed in the non-collinear and collinear interfaces [75, 93]. Enhancement in the coercive field ( $H_C^{eff} = (H_{C+} - H_{C-})/2$ ) as shown in the insets of Fig.4.11 below  $T_S$  is the indicative of the development of unidirectional anisotropy in non-collinear spin configuration [93]. The coexistence of different spin configurations in the magnetic phase separated single phase samples also found to induce unidirectional anisotropy [95]. Further, the inhomogeneity in the magnetic interactions in the system due to the non-magnetic ‘Co<sup>+3</sup>’ ions may also causes to the EB effect.

## 4.4 Summary

In summary, we studied the structural, magnetic and EB properties of  $\text{Co}(\text{Cr}_{1-x}\text{Co}_x)_2\text{O}_4$  ( $x = 0.0-0.1$ ). It has been found that the substituted Co ions occupy the B-site in the spinel structure of  $\text{CoCr}_2\text{O}_4$  and become non-magnetic. Due to the non-magnetic nature of substituted Co ions, the magnitude of magnetic moment of B-sublattice decreases and as a result the net moment of the compound increases. Further, it also leads to slight reduction in geometric magnetic frustration, and hence the stability of the conical spin-spirals. In addition we observed the asymmetric characteristics of the field cooled isothermal magnetization loops viz. EB effect only in the non-collinear spin-spiral magnetic phase below  $T_S$ , more significantly below  $T_L$ , indicating the entanglement of the lock-in transition and that of the EB effect in this non-collinear spin-spiral system. We attempted to explain the EB below  $T_L$  in the light of presence of commensurate spin-spiral and the unidirectional magnetic anisotropy driven by the non-collinear spin-spirals. However, more detailed study is needed to get microscopical origin of the EB in these compounds.



# Chapter 5

## Studies in $\text{Co}(\text{Cr}_{1-x}\text{Al}_x)_2\text{O}_4$ series

### 5.1 Introduction

In the previous chapters we attempted to understand the influence of non- $d^0$  ion substitution on the magnetic properties of  $\text{CoCr}_2\text{O}_4$ . In this work let us see the influence of the  $d^0$  ion substitution effect. For this purpose  $\text{Al}^{+3}$  ion has been chosen to substitute for  $\text{Cr}^{+3}$  in  $\text{CoCr}_2\text{O}_4$ . We can also use  $\text{Ga}^{+3}$  for this purpose but the problem is Ga has the tendency of occupying the tetrahedral site [128], but our primary interest is mainly to see the influence of substitution effect in the Cr-site. Unlike  $\text{CoFe}_2\text{O}_4$ , here the end compound of  $\text{Co}(\text{Cr}_{1-x}\text{Al}_x)_2\text{O}_4$  series, i.e.,  $\text{CoAl}_2\text{O}_4$  is also normal cubic spinel [68, 129] similar to  $\text{CoCr}_2\text{O}_4$ . This series provides appreciable way to look into the impact of the Cr-site on the magnetic properties  $\text{CoCr}_2\text{O}_4$  while the crystal structure remains same. On the other hand,  $\text{CoAl}_2\text{O}_4$  is also very interesting system. The magnetic frustration originating from the A-site of the spinel, even though the pyrochlore B-lattice is fully occupied with the non-magnetic  $\text{Al}^{+3}$  ions is an open question [68, 70, 128, 129]. Hence it is worth to study the magnetic properties of the samples by varying the  $\text{Al}^{+3}$  concentration between  $0.0 \leq x \leq 1.0$ . It has been claimed that even though the net magnetic moment of the  $\text{Co}^{+3}(3d^6)$  is zero similar to the  $\text{Al}^{+3}$ , their impact on the magnetic properties are quite different [129]. This

difference can be also seen from the variation of the ordering temperatures of  $\text{CoAl}_2\text{O}_4$  and  $\text{Co}_3\text{O}_4$  [68, 129].

This chapter focuses on the preparation, structural and temperature, magnetic field and time dependent magnetic properties of  $\text{Co}(\text{Cr}_{1-x}\text{Al}_x)_2\text{O}_4$ . Detailed analysis of the data is presented for the comprehensive understanding of the magnetic properties.

### 5.2 Experimental details

The polycrystalline samples of  $\text{Co}(\text{Cr}_{1-x}\text{Al}_x)_2\text{O}_4$  ( $x = 0.0-1.0$ ) are prepared by sol-gel technique from  $\text{CoCl}_2 \cdot 6\text{H}_2\text{O}$ ,  $\text{Cr}(\text{NO}_3)_3 \cdot 9\text{H}_2\text{O}$  and  $\text{Al}(\text{NO}_3)_3 \cdot 6\text{H}_2\text{O}$  (purity >99%) precursor materials. The black powders obtained from the self combustion in the sol-gel process are preheated at  $600^\circ\text{C}$  then pressed into pellets. The resultant pellets are sintered at  $1100^\circ\text{C}$  for 12 hours for two times. In order to enrich the homogeneity throughout the sample pellets were reground and pelletized at each step of process. During all heat treatments, the pellets were placed on a bed of powder with the same stoichiometry to minimize the possibility of reaction of the samples with the crucible. Powder XRD patterns were obtained using  $\text{Cu-K}\alpha$  ( $\lambda = 1.5406 \text{ \AA}$ ) radiation in a Rigaku multipurpose commercial X-ray diffractometer. The morphology and composition analysis are investigated by SEM images and EDAX spectrum, respectively. Differential DSC/TGA measurements have been carried by using commercial Netzsch DSC/TG machine (Model: STA449F3A00). Magnetization measurements between 2 K and 320 K, and upto the maximum magnetic field of 70 kOe are performed using commercial SQUID-VSM (Model 5 Quantum design.).

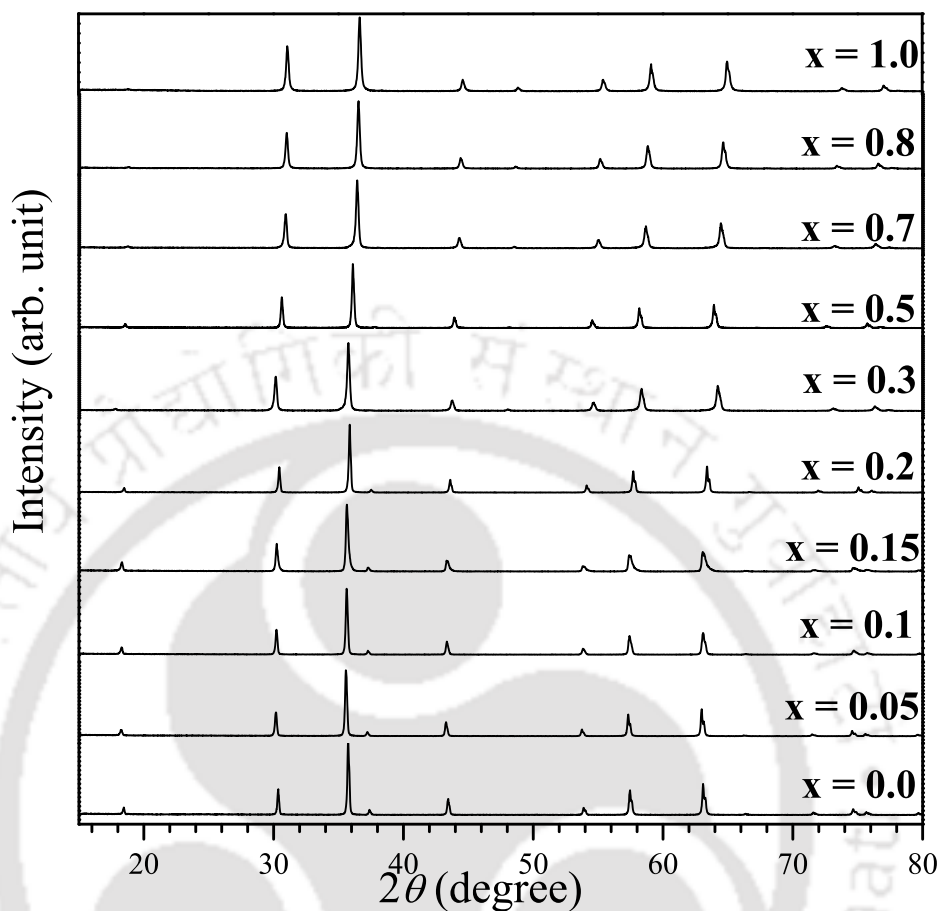


**Figure 5.1:** Powder XRD patterns of selected samples of the  $\text{Co}(\text{Cr}_{1-x}\text{Al}_x)_2\text{O}_4$  series measured at room temperature.

## 5.3 Results

### 5.3.1 Structural properties

Fig.5.1 presents the XRD patterns of  $\text{Co}(\text{Cr}_{1-x}\text{Al}_x)_2\text{O}_4$  samples. It can be seen that all the Al substituted samples possess peaks similar to that of the parent compound  $\text{CoCr}_2\text{O}_4$ . With increasing the Al concentration, peaks are found to shift towards the higher diffraction angles compared to  $\text{CoCr}_2\text{O}_4$ .

Phase purity of  $\text{Co}(\text{Cr}_{1-x}\text{Al}_x)_2\text{O}_4$  samples (for  $x = 0.0-1.0$ ) is analysed by Rietveld refinement technique with the help of FULL PROF utility software. As demonstrated

## 5. Studies in $\text{Co}(\text{Cr}_{1-x}\text{Al}_x)_2\text{O}_4$ series

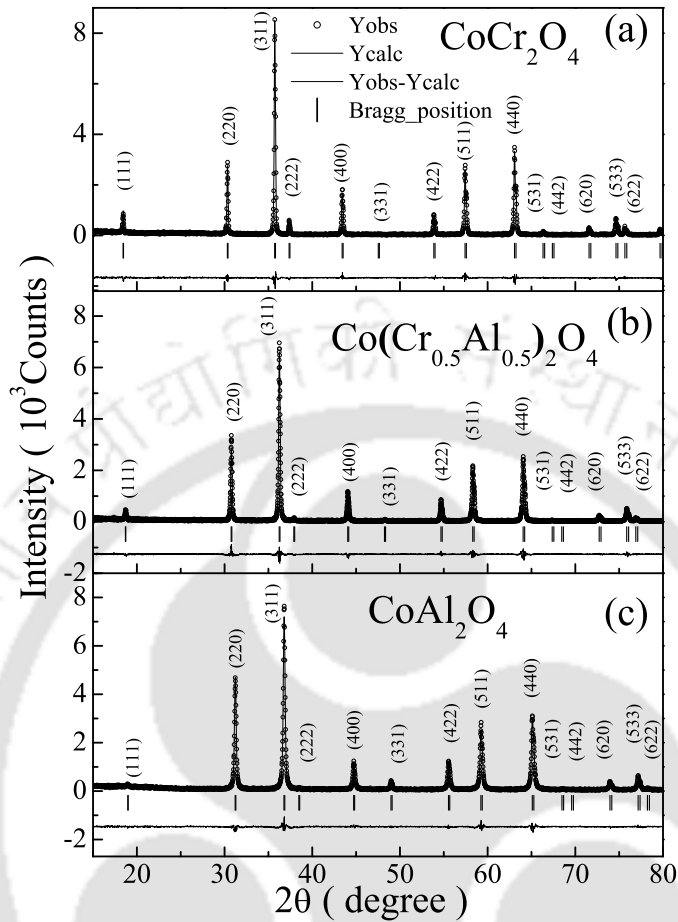


**Figure 5.2:** Experimental and fitted powder XRD patterns of (a)  $\text{CoCr}_2\text{O}_4$ , (b)  $\text{Co}(\text{Cr}_{0.5}\text{Al}_{0.5})_2\text{O}_4$  and (c)  $\text{CoAl}_2\text{O}_4$  samples by using Rietveld refinement technique with the help of FULL PROF program.

in Fig.5.2 XRD patterns of all the samples can be well fitted to spinel structure ( $\text{Fd}\bar{3}\text{m}$  space group). Lattice parameters of the end compounds of the series, i.e.,  $\text{CoCr}_2\text{O}_4$  and  $\text{CoAl}_2\text{O}_4$ , extracted from the refinement, are in close agreement with the previous reports [31, 68, 104, 129]. Fig.5.2(a) depicts the variation in the unit cell parameter ‘ $a$ ’ as a function of ‘Al’ concentration ‘ $x$ ’ in  $\text{Co}(\text{Cr}_{1-x}\text{Al}_x)_2\text{O}_4$ . The lattice parameter ‘ $a$ ’ decreases linearly and follows the Végard law as a function of ‘Al’ concentration. Decrease in the unit cell parameter may be due to the smaller ionic size of  $\text{Al}^{3+}$  ( $3\text{d}^0$ ) compared to that of  $\text{Cr}^{3+}$  ( $3\text{d}^3$ ). Moreover, from the Fig.5.3(b), it can be seen that the

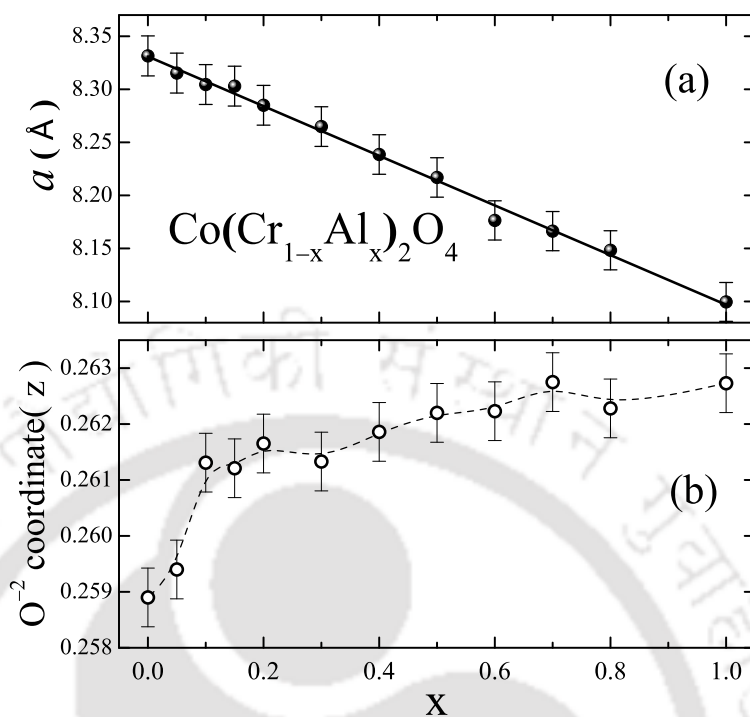


**Figure 5.3:** Variation of (a) lattice parameter ‘ $a$ ’ and (b) oxygen ion coordinate as a function of ‘Al’ concentration ‘ $x$ ’. Here, vertical bars in (a) indicate the error in ‘ $a$ ’ due to instrumental broadening and fitting the data. Solid line is the straight line fit to the data to illustrate the Vegard law.

oxygen coordinate( $z$  position) increases with increase in the ‘Al’ concentration. This may indicate the spinel structure is becoming more distorted with smaller cation size of the ‘ $\text{Al}^{+3}$ ’ ion. Further the SEM images and EDAX spectra shown in the left and right panels of Fig.5.4, also confirmed the phase purity and the stoichiometric ratios of elements of the samples, respectively.

Fig.5.5 (a) and (b) show the temperature dependent DSC & TG curves of  $x = 0.0$  and  $x = 0.5$  samples, respectively. The weight loss around  $100\text{ }^\circ\text{C}$  in both the samples resulted from the evaporation of moisture and residual solvent in the xerogel. Weight loss at around  $360\text{--}390\text{ }^\circ\text{C}$  may be due to the decomposition of organic compounds

## 5. Studies in $\text{Co}(\text{Cr}_{1-x}\text{Al}_x)_2\text{O}_4$ series

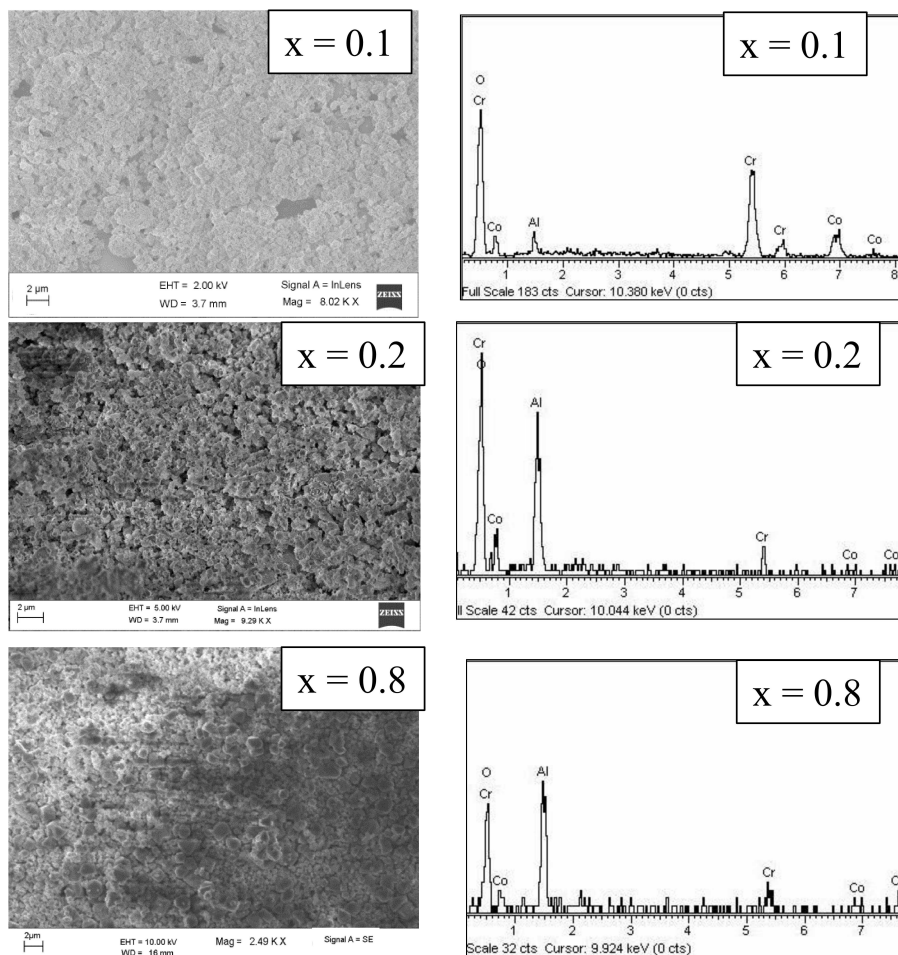


**Figure 5.4:** SEM images of (left panels) and EDAX spectra (right panels) of  $\text{Co}(\text{Cr}_{1-x}\text{Al}_x)_2\text{O}_4$  samples.

such as citrates covalently bonded to the  $\text{Co}^{2+}$ ,  $\text{Cr}^{3+}$  and  $\text{Al}^{3+}$  ions. We can see that above  $600\text{ }^\circ\text{C}$  the structure of the samples is stabilized. From the DSC curve it can be seen that the evaporation of moisture and the organic solvents is exothermic in nature. But after the decomposition of the citrates samples undergo endothermic process that may be due to the formation of new bonds.

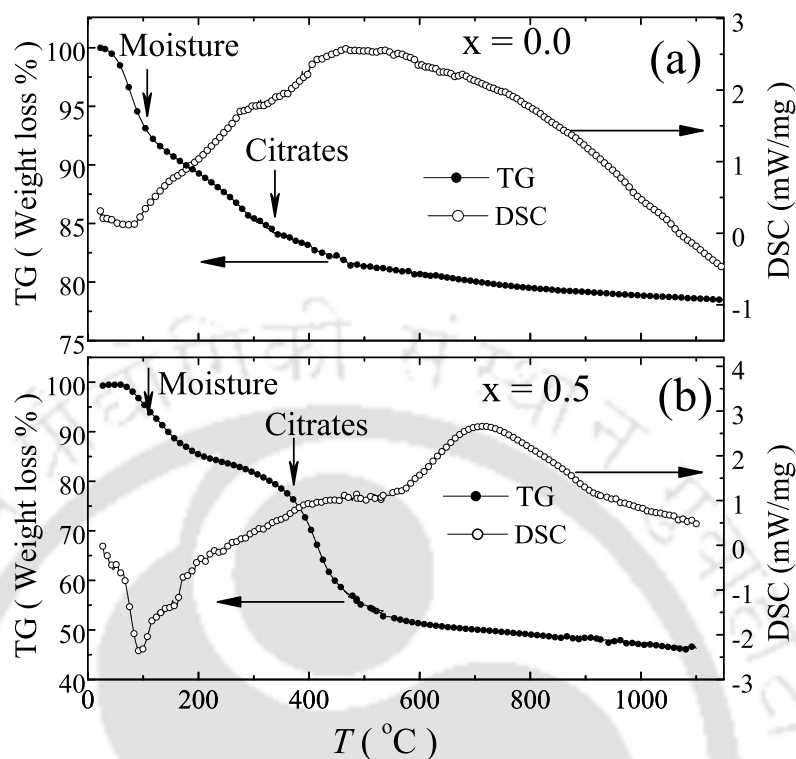


**Figure 5.5:** DSC and TGA plots of (a)  $x = 0.0$  and (b)  $x = 0.5$  samples measured in the air environment.

### 5.3.2 Magnetic properties

#### 5.3.2.1 Thermomagnetic and isothermal magnetization curves

Fig.5.6(a)–(i) demonstrate the temperature dependent magnetization curves of the  $\text{Co}(\text{Cr}_{1-x}\text{Al}_x)_2\text{O}_4$  samples measured in FCC mode for the applied field of nominal zero ( $\sim 10$  Oe) and ZFC, FCW modes under the applied field of  $H = 1$  kOe. It can be seen from the FCC curve under applied field of  $H \sim 10$  Oe that all the ‘Al’ substituted samples do not exhibit any magnetic compensation effect. It is evident that compared to the substitution of previous two elements, ‘Al’ substitution for Cr-site causes to decrease in the FIM transition temperature  $T_C$ . It can be also seen that  $T_C$  becomes broad as the ‘Al’ concentration increases. For  $x \geq 0.6$ , behaviour of the transition changes unusually compared to that of the samples for  $x \leq 0.5$ , and the  $0.6 \leq x \leq 0.8$

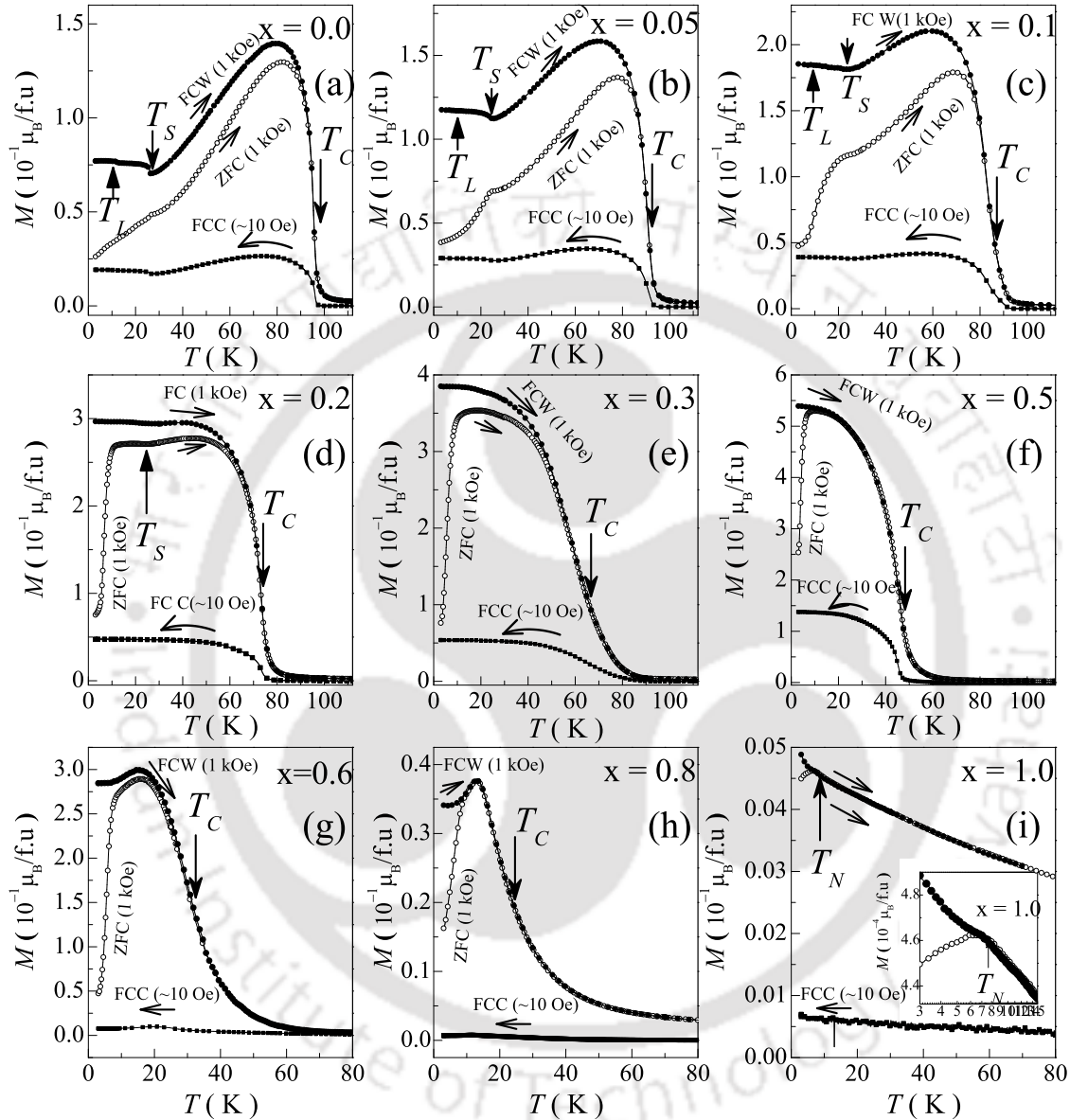


**Figure 5.6:** Temperature dependent magnetization curves of  $\text{Co}(\text{Cr}_{1-x}\text{Al}_x)_2\text{O}_4$  samples measured in FCC mode for the applied  $\sim 10$  Oe and ZFC, FCW modes under the applied field of  $H = 1$  kOe. Inset of (i) shows the enlarged view of the ordering temperature of the  $\text{CoAl}_2\text{O}_4$  sample.

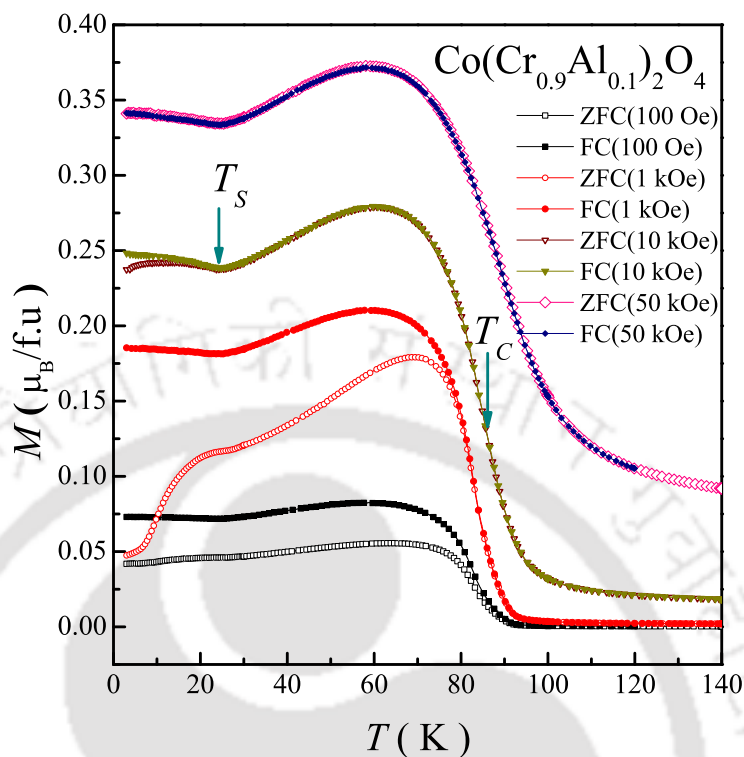


**Figure 5.7:** Temperature dependent ZFC and FCW magnetization curves of  $\text{Co}(\text{Cr}_{0.9}\text{Al}_{0.1})_2\text{O}_4$  sample under the various applied fields.

samples exhibit typical glassy type transition. The end compound  $\text{CoAl}_2\text{O}_4$  exhibits the magnetic ordering at very low temperature at around 8 K, in better agreement with the previous reports [68, 129]. The typical AFM behaviour of ordering temperature in  $\text{CoAl}_2\text{O}_4$  may signify that the magnetic contribution from the B-site vanishes. Further, one can see that the magneto-structural transition  $T_S$  and the lock-in transition  $T_L$  both become weak and also move towards low temperature with increasing ‘Al’ concentration. We know that the decrease in the magnetization in FCW curve with lowering the temperature below  $T_C$  in case of the parent compound  $\text{CoCr}_2\text{O}_4$  is due to the ordering of the B-site moments ferrimagnetically with that of the A-site moments. With increase in the ‘Al’ concentration one can see that this trend in FCW curve vanishes and for samples with ‘Al’ concentration in the range of  $0.2 \leq x \leq 0.5$  magnetization rather increases with lowering the temperature below  $T_C$ . This may

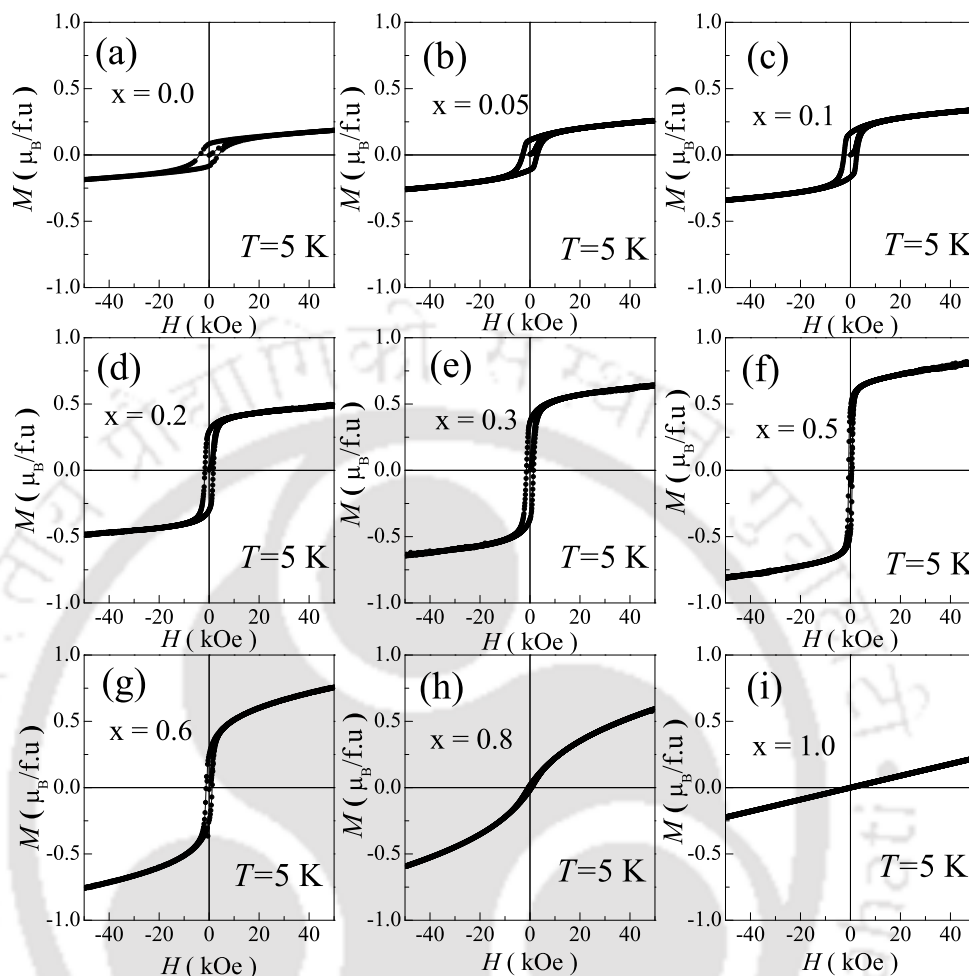
## 5. Studies in $\text{Co}(\text{Cr}_{1-x}\text{Al}_x)_2\text{O}_4$ series

---

indicate ‘Al’ substitution influences the ordering of the B-site and hence the stiffness of the conical spin-spirals due to the  $d^0$  configuration of  $\text{Al}^{+3}$  ion.

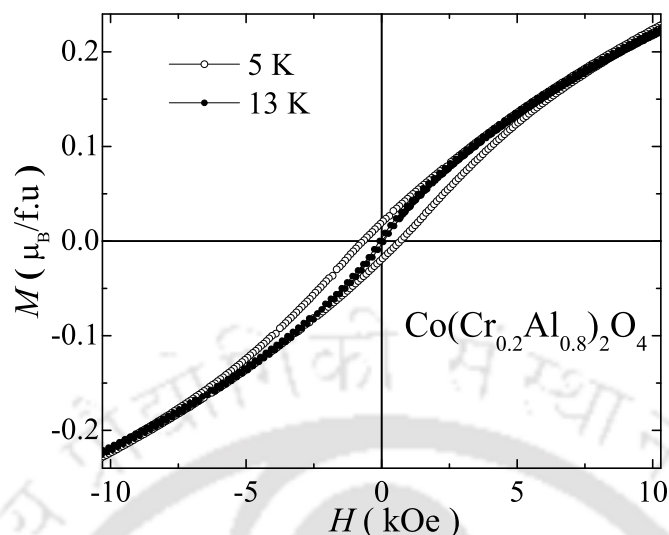
Fig.5.7 depicts the temperature dependent ZFC and FCW magnetization curves of  $\text{Co}(\text{Cr}_{0.9}\text{Al}_{0.1})_2\text{O}_4$  sample under the various applied fields from 100 Oe to 50 kOe. Under the small applied field the ZFC and FCW curves display huge bifurcation below the  $T_C$ . Upon increasing the field, initially both the curves start merging below  $T_C$ , but still show the bifurcation below  $T_S$ . However, for large enough fields they merge together completely. This may signify the spin-spirals become less effective with the ‘Al’ substitution compared to the parent  $\text{CoCr}_2\text{O}_4$ , in which even large enough field of 140 kOe unable to diminish the bifurcation[31]. In addition, the transition gets broadened out with increase in the field as expected for the FIM transition but the the magneto-structural transition at  $T_S$  becomes sharp.

Fig.5.8(a)–(i) show the  $M$ - $H$  loops of the various ‘Al’ substituted samples at 5 K measured after cooling in zero field. It is prominent that with increasing the ‘Al’ concentration magnitude of the magnetization increases enormously upto  $x = 0.5$ , then decreases sharply. The coercive field of the loop decreases with increasing the ‘Al’ concentration. We can see that with increasing the Al concentration the behaviour of the loop changes from typical FIM to AFM. End compound of the series,  $\text{CoAl}_2\text{O}_4$  exhibits no tendency of saturation even upto 50 kOe, indicating strong AFM ordering in line with the previous reports[68, 129]. It can be seen that  $x \geq 0.6$  samples do not show any considerable opening in the loop. Fig.5.9 shows the enlarged portions of the  $M$ - $H$  loops of  $\text{Co}(\text{Cr}_{0.2}\text{Al}_{0.8})_2\text{O}_4$  sample at 5 K and 13 K, i.e., well below and above the blocking temperature(below which the ZFC and FCW curves exhibit bifurcation). We can see that the small opening observed below the blocking temperature vanishes for the loop above this temperature. So this blocking temperature is may be due to the glassy behaviour.



**Figure 5.8:** (a)–(i) Isothermal magnetization loops of  $\text{Co}(\text{Cr}_{1-x}\text{Al}_x)_2\text{O}_4$  samples at 5 K.

Fig.5.10 shows the variation of characteristic parameters as a function of Al concentration in  $\text{Co}(\text{Cr}_{1-x}\text{Al}_x)_2\text{O}_4$ , extracted from the  $M$ - $H$  loops at 5 K. From Fig.5.10(a) it can be seen that the coercive field  $H_C$  decreases systematically with increase in the Al concentration. The linear part of  $M(H)$  curve at high field can be fitted to  $M(H) = \chi_{AFM}H + M_S$ , here  $\chi_{AFM}H$  is the AFM contribution to the magnetization and  $M_S$  is the saturation magnetization, the FM contribution to the total magnetization. As shown in the Fig.5.10(b)  $M_S$  increases upto  $x = 0.5$  then decreases, indicating that the FM contribution comes from the uncompensated moments of the A and B-site



**Figure 5.9:** Enlarged portion of isothermal magnetization loops of  $\text{Co}(\text{Cr}_{0.2}\text{Al}_{0.8})_2\text{O}_4$  sample at 5 K and 13 K.

ions, and its value increases upto  $x = 0.5$ , and then decreases. The remanent magnetization  $M_{rem}$  extracted while decreasing the field to zero from 50 kOe also shows the similar behaviour as a function of ‘Al’ concentration.

As described in the Fig.5.11(a)–(c), paramagnetic susceptibility  $\chi(T)$  above  $T_C$  of  $\text{Co}(\text{Cr}_{1-x}\text{Al}_x)_2\text{O}_4$  samples for  $x \leq 0.8$  can be well analysed by the Néel two sub-lattice model of the form[47],

$$\frac{1}{\chi(T)} = \frac{(T - \Theta)}{C} - \frac{\xi}{(T - \Theta')} \quad (5.1)$$

But in case of the end compound  $\text{CoAl}_2\text{O}_4$ , the paramagnetic susceptibility failed to follow this two sub-lattice model. This may be due to the contribution from the B-sub-lattice vanishes as the B-site is fully occupied by the non-magnetic ‘ $\text{Al}^{+3}$ ’. In this case as shown in the Fig.5.11(d) best fit to the experimental  $1/\chi(T)$  and  $\chi(T)$  data of  $\text{CoAl}_2\text{O}_4$  sample can be obtained by the modified Curie-Weiss law of the form,

$$\chi(T) = \chi_0 + \frac{C}{(T - \Theta)} \quad (5.2)$$

here  $\chi_0$  is the temperature independent magnetic susceptibility. Effective paramagnetic magnetic moment  $\mu_{eff}$  of the samples can be calculated from the Curie constant

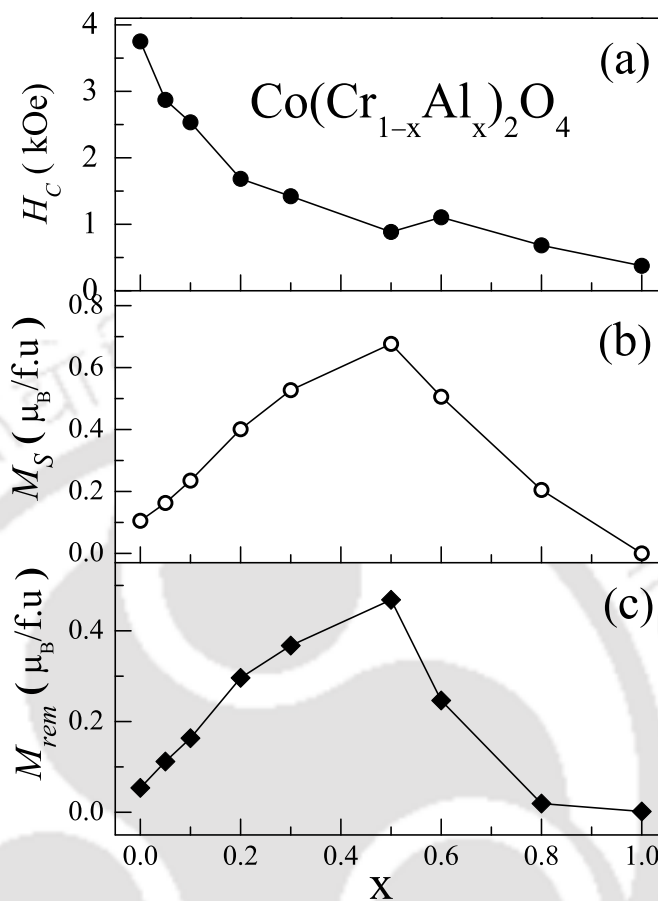


**Figure 5.10:** (a), (b) and (c), respectively, the coercive field, saturation magnetization and remanent magnetization of  $\text{Co}(\text{Cr}_{1-x}\text{Al}_x)_2\text{O}_4$  as a function of ‘Al’ concentration.

$C = N\mu_{eff}^2/3k_B$ . By using  $\mu_{eff} = \sqrt{\mu_{Co}^2 + 2(1-x)\mu_{Cr}^2}$  relation we can also calculate the theoretical values of  $\mu_{eff}$ , here,  $\mu_{Co}$  and  $\mu_{Cr}$  are the magnetic moments of the  $\text{Co}^{+2}$  and  $\text{Cr}^{+3}$  ions, respectively. The values of  $\Theta$ ,  $C$ ,  $\xi$  and  $\Theta'$  obtained from the best fit of the experimental data are listed in the Table.5.1. As depicted in the Fig.5.12(a) experimentally calculated values of  $\mu_{eff}$  are found to be comparable to that of theoretically calculated values of  $\mu_{eff}$  by considering the spin-only moment of  $\text{Cr}^{+3}$  ( $\mu_{Cr} = 2\sqrt{S(S+1)} \mu_B$ ,  $S$  is the spin angular momentum number) and unquenched orbital moment of  $\text{Co}^{+2}$  ( $\mu_{Co} = g\sqrt{J(J+1)} \mu_B$ ,  $L$  is the orbital angular momentum number). Negative sign of the Curie-Weiss temperature  $\Theta$  for all the samples indicates

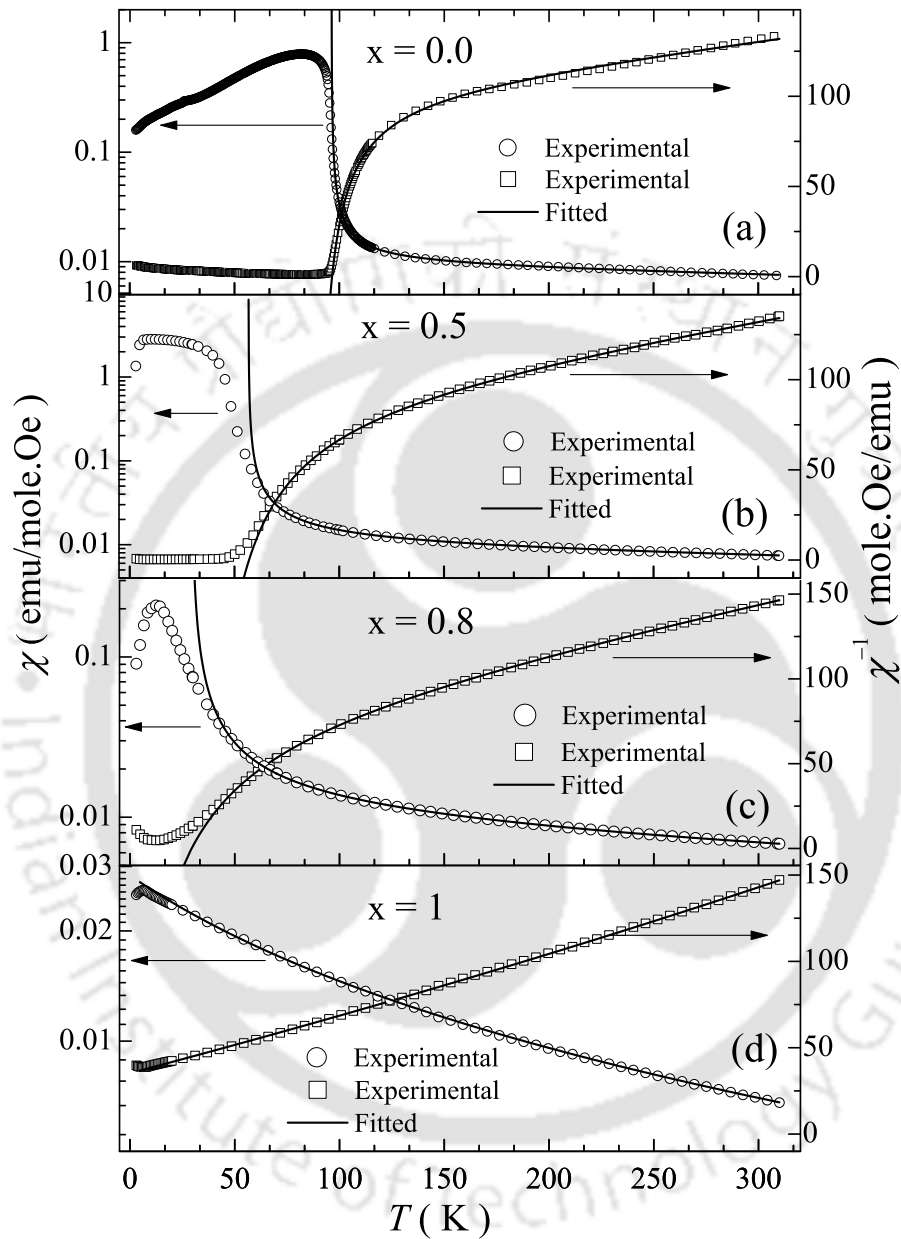


**Figure 5.11:** (a)–(c) Fitted and experimental inverse paramagnetic susceptibility(right scale) and paramagnetic susceptibility(left scale) of  $\text{Co}(\text{Cr}_{1-x}\text{Al}_x)_2\text{O}_4$  samples for  $x \leq 0.8$  to the Néel two sub-lattice model of FIM materials given in the eq.5.1. (d) Modified Curie-Weiss fit (eq.5.2) to the data of  $\text{CoAl}_2\text{O}_4$  sample.

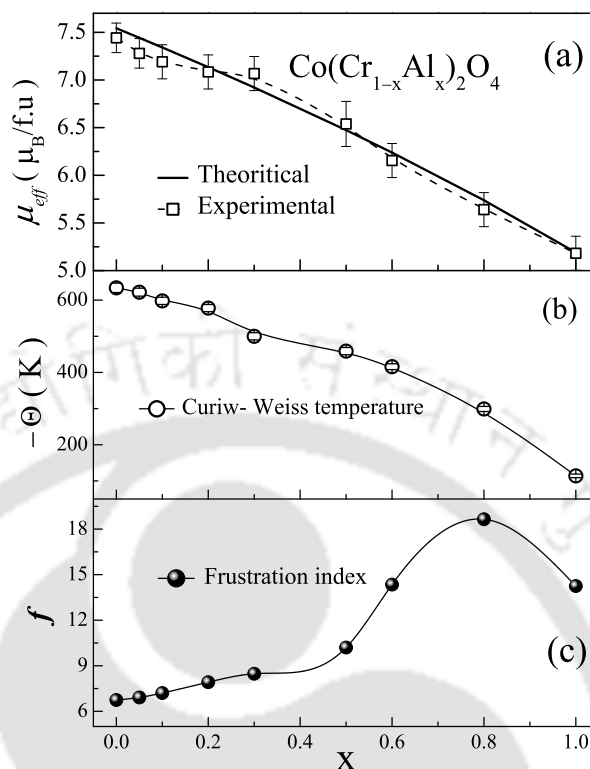


**Figure 5.12:** (a) Variation of experimental and calculated effective magnetic moment as a function of ‘Al’ concentration. (b) Curie-Weiss temperature as a function of Al concentration. (c) is the variation of frustration index  $f \sim |\Theta|/T_C$  with Al concentration  $x$ .

the magnetism in these materials is governed by the negative superexchange interactions. Decrease in the magnitude of the  $\Theta$  with increase in the ‘Al’ concentration represents the decrease in the strength of the superexchange interaction between the intra and inter magnetic moments of the A- and B-sublattices in the spinel structure. It can be seen that with increase in the ‘Al’ concentration, the frustration index  $f \sim |\Theta|/T_C$ , initially increases slightly up to  $x = 0.5$ , but beyond it increases sharply up to  $x = 0.8$  and then decreases. The  $f$  value of  $\text{CoAl}_2\text{O}_4$  is in good agreement with the previous reports [68, 69, 129].

Approximate NN superexchange interactions in these spinel compounds are estimated by employing Lotgering mean-field approach [124, 125]. Values of superex-

## 5. Studies in $\text{Co}(\text{Cr}_{1-x}\text{Al}_x)_2\text{O}_4$ series

**Table 5.1:** Parameters obtained from the analysis of the paramagnetic susceptibility of  $\text{Co}(\text{Cr}_{1-x}\text{Al}_x)_2\text{O}_4$  samples. Here exchange interactions  $J_{AA}$ ,  $J_{BB}$  and  $J_{AB}$  are average values of NN superexchange interactions.

| x    | c<br>( $\frac{\text{emu}}{\text{mole.Oe.K}}$ ) | $\Theta$<br>( K ) | $\xi$<br>( $\frac{\text{mole.Oe}}{\text{K}}$ ) | $\Theta'$<br>( K ) | $J_{AA}$<br>( K ) | $J_{BB}$<br>( K ) | $J_{AB}$<br>( K ) | u           |
|------|--|-------------------|--|--------------------|-------------------|-------------------|-------------------|-------------|
| 0.0  | 6.91(1)  | -634(12)          | 1006(13)                                       | 86.9(3)            | -9.2(2)           | -24.3(2)          | -12.1(3)          | $\sim 2$    |
| 0.05 | 6.63(1)  | -553(10)          | 941(14)  | 84.4(6)            | -8.8(2)           | -22.7(2)          | -11.4(2)          | $\sim 1.88$ |
| 0.1  | 6.47(1)  | -598(10)          | 1143(10)                                       | 78.2(6)            | -7.8(3)           | -22.0(4)          | -10.7(1)          | $\sim 1.85$ |
| 0.2  | 6.27(1)  | -578(8)           | 1590(17)                                       | 64.4(6)            | -6.8(3)           | -20.9(3)          | -10.0(2)          | $\sim 1.74$ |
| 0.3  | 6.25(1)  | -500(10)          | 1128(13)                                       | 64.1(3)            | -5.5(1)           | -18.2(3)          | -8.9(1)           | $\sim 1.41$ |
| 0.5  | 5.34(1)  | -459(5)           | 2681(19)                                       | 28.8(2)            | -3.4(1)           | -17.3(2)          | -7.8(2)           | $\sim 1.10$ |
| 0.6  | 4.72(1)  | -416(8)           | 2947(70)                                       | 27.3(2)            | -2.4(1)           | -14.3(1)          | -7.3(1)           | $\sim 0.78$ |
| 0.8  | 3.89(1)  | -299(2)           | 3158(20)                                       | 6.2(2)             | -1.0(1)           | -9.9(2)           | -6.9(1)           | $\sim 0.28$ |
| 1.0  | 3.36(1)  | -114(2)           | —  | —                  | —                 | —                 | —                 | —           |

change interactions obtained for the fitted  $\Theta$ ,  $C$ ,  $\xi$  and  $\Theta'$  from the paramagnetic susceptibility of  $\text{Co}(\text{Cr}_{1-x}\text{Al}_x)_2\text{O}_4$  samples are listed in the Table.5.1. Here we can see that with increase in the ‘Al’ concentration all the NN superexchange interactions decrease. The values of NN  $J_{ij}$  are in good agreement with the reported isostructural spinel compounds  $\text{MnCr}_2\text{O}_4$ [125] and  $\text{ZnCr}_2\text{O}_4$ [126]. The LKDM  $u$  parameter is calculated by using these  $J_{BB}/J_{AB}$  ratio. The  $u$  value is also found to decrease with increase in the Al concentration[Table.5.1].

### 5.3.2.2 Magnetic relaxation

We noticed that the samples with ‘Al’ concentration  $0.6 \leq x \leq 0.8$  exhibit glassy behaviour in the temperature dependent magnetization [Fig5.6]. To probe this behaviour, time dependent magnetization measurement has been carried out in  $\text{Co}(\text{Cr}_{0.4}\text{Al}_{0.6})_2\text{O}_4$  sample. Sample is cooled from room temperature to 5 K in the applied field of 50 Oe, then the time dependent magnetization is measured for several hours. The sophisticated stable at each point mode is used to carry out this measurement. As shown in

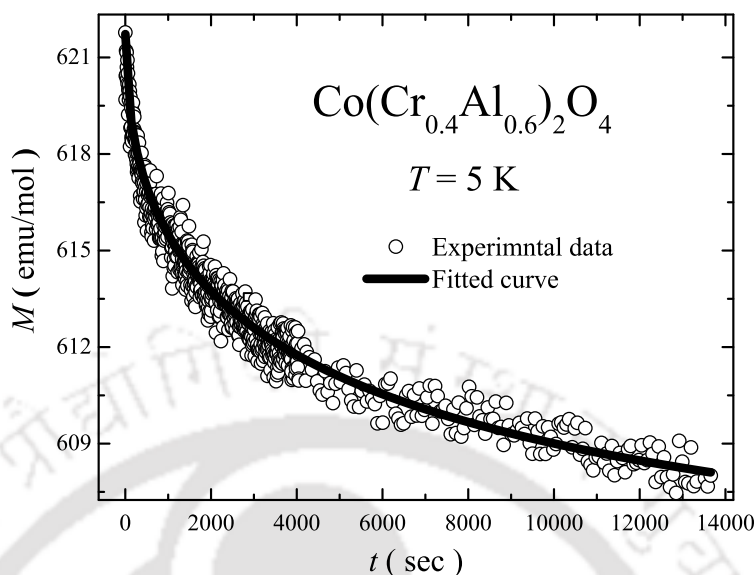


**Figure 5.13:** Variation of the magnetization of  $\text{Co}(\text{Cr}_{0.4}\text{Al}_{0.6})_2\text{O}_4$  sample as a function of time at 5 K.

the Fig.5.13  $\text{Co}(\text{Cr}_{0.4}\text{Al}_{0.6})_2\text{O}_4$  sample exhibits tendency of relaxation in the magnetization as the time elapses. The experimental time dependent magnetization can be well fitted to a stretched exponential Kohlrausch law of the form,

$$M(t) = M_0 - M_g \cdot \exp \left[ - \left( \frac{t}{t_r} \right)^{1-n} \right] \quad (5.3)$$

here  $M_0$  and  $M_g$  are the intrinsic FM moment and the glassy component of the system, respectively.  $t_r$  is the characteristic time component, and  $n$  is the stretched exponential exponent. According to the percolation model, in the glassy state of the magnetic system the exponent  $n$  in Eq.5.3 varies in the range  $0.33 \leq n \leq 1$ . Best fit of the experimental data to eq.5.3 as shown in the Fig.5.13 yields  $M_0 = 602.7 \pm 1$  emu/mol,  $M_g = 18.3 \pm 1$  emu/mol,  $t_r = 6089 \pm 100$  sec and  $n = 0.55 \pm 0.03$ .  $n = 0.55$  may signifies the typical glassy behaviour of the sample.

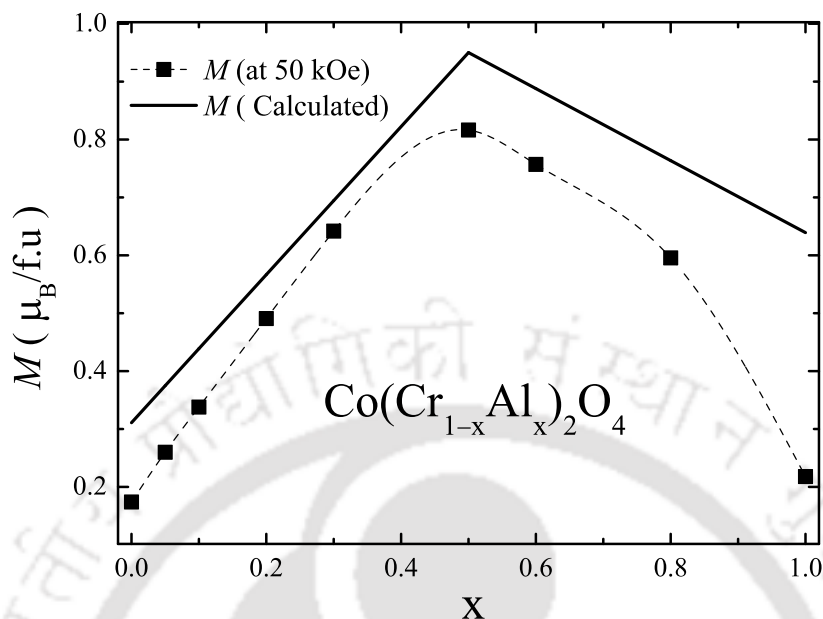


**Figure 5.14:** Calculated and observed value of magnetization of  $\text{Co}(\text{Cr}_{1-x}\text{Al}_x)_2\text{O}_4$  as a function of Al concentration.

## 5.4 Discussion

From the analysis of XRD patterns we observed that the substituted Al ions occupy the B-site. This can be even understood from the linear variation of the cell parameter ‘ $a$ ’ following the Végard law. We know that the A-site moment in  $\text{CoCr}_2\text{O}_4$  is along [001] easy axis and the resultant of the B-site moment is antiparallel to it [28, 29, 71]. But the B-site is further divided into B1 and B2 sub-lattices. B1-site moment is parallel to that of the A-site and B2-site moment is antiparallel. The total magnetization per formula unit can be written as  $M = | \uparrow \mu_A + \uparrow \mu_{B1} - \downarrow \mu_{B2} |$ . Here,  $\uparrow \mu_A$ ,  $\uparrow \mu_{B1}$  and  $\downarrow \mu_{B2}$ , respectively, are the longitudinal components of the magnetic moments of the A-site, B1-site and B2-site ions along the magnetic field direction. Enhancement in the magnetization with increasing in the Al concentration up to  $x = 0.5$  may be due to the occupation of the majority of  $\text{Al}^{3+}$  in the B2-site. The decrease in the magnitude of magnetization beyond  $x = 0.5$  is also clear as there is no B2-

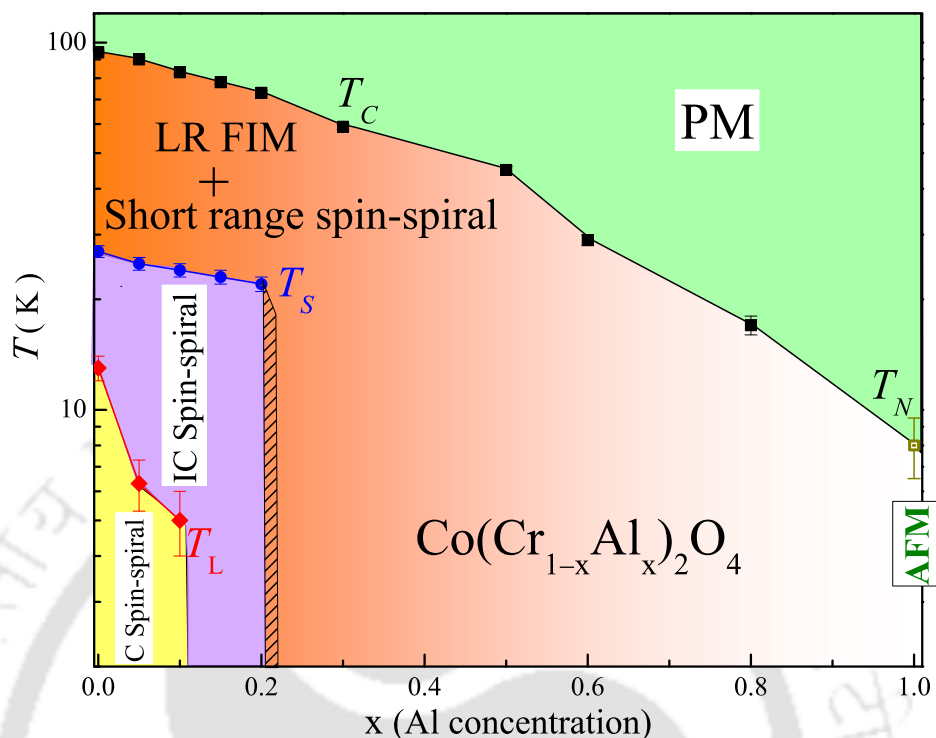


**Figure 5.15:** Magnetic phase diagram of  $\text{Co}(\text{Cr}_{1-x}\text{Al}_x)_2\text{O}_4$ .  $T_C/T_N/T_S/T_L$  represent FIM/AFM/magneto-structural/lock-in transition temperatures. Shading of the orange colour in the combined phase of long range FIM & short range spin-spiral phase indicates that this phase gradually decreases and finally becomes AFM, i.e.,  $T_C$  becomes  $T_N$  as the contribution from B-site vanishes for  $\text{CoAl}_2\text{O}_4$ .

site to accommodate the substituted  $\text{Al}^{3+}$  ions, they occupy the B1-site. To justify this argument, the magnetization of  $\text{Co}(\text{Cr}_{1-x}\text{Al}_x)_2\text{O}_4$  as a function of Al concentration is calculated by considering the magnetic configuration of  $\text{CoCr}_2\text{O}_4$ . As shown in the Fig.5.14 the trend of calculated and experimental values of the net magnetization as a function of Al concentration are comparable. However, beyond  $x = 0.5$  the deviation between the calculated and experimental values becomes more as the long range order vanishes with more diluted B-site. Lacking of the long range order also results in the change of canting angles of the magnetic moments. Moreover the ionic disorder of the substituted Al ions in the available crystallographic sites also gives rise to this discrepancy between the calculated and observed values.

## 5. Studies in $\text{Co}(\text{Cr}_{1-x}\text{Al}_x)_2\text{O}_4$ series

---

Substitution of the non-magnetic  $\text{Al}^{+3}$  for  $\text{Cr}^{+3}$  ions also decreases the NN magnetic exchange interactions [Table.5.1]. This could be the possible reason for the decrease in the magnetic ordering temperature  $T_C$ . For  $x \geq 0.6$  (i.e., B-site possesses only  $\leq 40\%$  of magnetic  $\text{Cr}^{+3}$  ions), the magnetic elements in the B-site, and the exchange interactions of the compound are diluted. We know that for the concentrations less than the percolation threshold concentration the long range magnetic ordering is not possible so the system undergoes short range ordering. Transition from the FIM behaviour to spin-glass-like behaviour probed by the temperature and time dependent magnetization in case of the samples with  $x \geq 0.6$  could be attributed to the lacking of long range ordering of the B-site ions due to the dilution of magnetic  $\text{Cr}^{+3}$  ions. Further, the ionic disorder and the frozen transverse components of the moments also lead to the glassy behaviour in the samples. From transition into the spin-glass state from the AFM is also observed in the spinel system  $\text{Zn}(\text{Cr}_x\text{Ga}_{1-x})_2\text{O}_4$  due to the dilution of the magnetic B-site with the non magnetic  $\text{Ga}^{+3}$  [130]. This series exhibits the glassy behaviour even for the lower concentration of non-magnetic  $\text{Ga}^{+3}$  ions owing to the absence of the magnetic ion in the A-site and hence the the domination of the geometric frustration of the B-site pyrochlore lattice. As the Al concentration increases further, the magnetic contribution from the B-sublattice vanishes and the ordering becomes completely AFM in nature. As the non-magnetic  $\text{Al}^{+3}$  ions replace the  $\text{Cr}^{+3}$  ions in B-site, the  $J_{BB}$  and  $J_{AB}$  value decrease and become zero when  $\text{Al}^{+3}$  occupy the B-site fully. Hence, in case of  $\text{CoAl}_2\text{O}_4$  only possible superexchange interaction among the A-site ions is  $J_{AA}$  along the A–O–Al–O–A, which is AFM in nature. This observation is in agreement with the analysis of the paramagnetic susceptibility.  $\chi(T)$  above  $T_C$  of the samples for  $x \leq 0.8$  follow the Néel two sub-lattice model whereas  $\text{CoAl}_2\text{O}_4$  does not follow. Further this may also indicate that there is no presence of the  $\text{Co}^{+2}$  in the B-site.

We can see that with increasing the Al concentration the LKDM ‘ $u$ ’ parameter

estimated from the superexchange interactions decreases sharply. This could be the possible origin behind the lowering of the spin-spiral transition  $T_S$  and the lock-in transition  $T_L$ . As the  $u$  value decreases, the geometric magnetic frustration is expected to decrease according to the LKDM model, but the experimental measure of frustration, i.e., the frustration index  $f$  sharply increases for  $x \geq 0.5$  and reaches maximum for  $x = 0.8$ , and then decreases. Lacking of long range magnetic order may leads to the frustration in the system. In addition, the the diamond lattice formed in the A-site also gives rise to the frustration as the B-site contribution becomes weak. In deed this is anticipated as the source of frustration in the case of  $\text{CoAl}_2\text{O}_4$  [68, 69, 128, 129].

Fig.5.15 demonstrates the tentative magnetic phase diagram of  $\text{Co}(\text{Cr}_{1-x}\text{Al}_x)_2\text{O}_4$  series extracted from the temperature, field and time dependent magnetic properties. At a glance one can evaluate the different magnetic phases emerge as a function of the Al concentration in the range  $0 \leq x \leq 1$ . Samples for  $x \leq 0.1$  exhibit four phases similar to that of the parent compound. For  $0.1 \leq x \leq 0.2$  the phase boundary between the incommensurate spin-spiral and commensurate spin-spiral marked with the lock-in transition  $T_L$  disappears, and the samples show only three phases. For  $0.2 \leq x \leq 0.8$  samples the spin-spiral phase seems to be vanished and the magnetic ordering becomes simple FIM in nature as the contribution from the B-site magnetic moment is considerable. For  $x = 1.0$  compound ordering becomes simple AFM. Rate of decrease in the FIM ordering temperature is comparatively more above  $x = 0.5$ , this may indicate the of long range magnetic order in the B-site. It can be seen that the intensity of the combined phase of long range FIM and short range spin-spirals observed in case of the parent compound also seems to turn out to be the long range FIM up to  $x = 0.5$ . Samples in the range  $0.6 \leq x \leq 0.8$  show spin-glass-like character as the  $\text{Cr}^{+3}$  ions are diluted with rich  $\text{Al}^{+3}$  concentration.

### 5.5 Summary

To summarize this chapter, we have presented the structural, temperature, field and time dependent magnetic properties of the  $\text{Co}(\text{Cr}_{1-x}\text{Al}_x)_2\text{O}_4$  series for  $x = 0.0-1.0$ . Structural properties obtained from the analysis of XRD patterns show that the substituted  $\text{Al}^{+3}$  ions occupy the octahedral or B-site of the spinel structure and the crystal structure remains unchanged as a function of  $\text{Al}^{+3}$  concentration. Study of temperature dependent magnetization as a function of  $\text{Al}^{+3}$  concentration shows that the  $\text{Al}^{+3}$  substitution lowers the FIM ordering temperature. This observation understood in terms of decrease in the strength of the various magnetic exchange interactions among inter and intra sub-lattices of the spinel structure with the non-magnetic  $\text{Al}^{+3}$  ions. The non-collinear spin-spiral phase exists for  $x \leq 0.2$ , beyond this concentration it vanishes. Samples for  $0.6 \leq x \leq 0.8$  exhibit spin-glass-like character as the long range magnetic order lacks due to the dilution  $\text{Cr}^{+3}$  ions. Further the time dependent magnetization data also supported this glassy behaviour. Variation in the net magnetization of the sample as a function of Al concentration is also understood based on the magnetic configuration of  $\text{CoCr}_2\text{O}_4$ . Magnetic phase diagram constructed as a function of Al concentration offers various magnetic phases as the Al concentration varies gradually from 0.0 to 1.0. With increasing the Al concentration the FIM phase smoothly transforms into AFM phase as the contribution from B-site decreases. However, it may be fruitful to investigate this series with the ac magnetic susceptibility to further support the conclusions drawn from dc magnetization data in this work.

# Chapter 6

## Conclusions

This chapter concludes the dissertation by summarising the overall results obtained from three distinct substitution effects. Detailed investigations on  $\text{Co}(\text{Cr}_{1-x}\text{M}_x)_2\text{O}_4$  ( $\text{M} = \text{Fe}, \text{Co} \ \& \ \text{Al}$ ) by means of structural, magnetic, EB, and thermodynamic properties draw the following conclusions.

Substituted Fe ions for Cr-site initially occupy the octahedral (B) site up to 10%, thereafter they prefer to occupy in both the tetrahedral and octahedral sites. Gradual replacement of Cr by Fe systematically enhances the FIM transition possibly due to the result of strengthening of the superexchange interactions. For lower concentrations of Fe (up to  $\sim 11\%$ ), the magneto-structural transition persists and for concentrations beyond  $x = 0.3$ , it gets suppressed. Presumably this is due to the decrease in the underlying magnetic frustration with occupation of Fe ions having larger magnetic moment in the tetrahedral site, which hinders the formation of the spin-spirals [28, 29]. It is also observed that a few percent of Fe substitution for Cr in  $\text{CoCr}_2\text{O}_4$  results in the magnetization reversal below  $T_{comp}$  under small applied fields. Further, increasing the applied field leads to field induced transitions across  $T_{comp}$ . In the compensated stoichiometry, the coercive field of the loop shows unusual temperature dependence. It exhibits a divergence, followed by a collapse in the vicinity of  $T_{comp}$  upon approaching  $T_{comp}$  either from above or below the compensation temperature. EB field, evaluated

## 6. Conclusions

---

from the asymmetric characteristics of FC  $M$ - $H$  loops, is elucidated to change sign across  $T_{comp}$ . This observation in the present bulk insulating compound is replica of the recent findings in the context of rare-earth intermetallics and core-shell nano particles [17–19]. This signifies that the sign change in the EB field is not only limited to the rare-earth intermetallics and core-shell nano particles but also can be observed in the bulk insulating materials in which magnetization reversal is observed and possess the magnetic configurations similar to the former. We attempted to understand the sign change in EB across  $T_{comp}$  by considering the spin reorientation. Further, the thermodynamic properties and the high field susceptibility also show the fingerprints of this quasi field induced phase transition across  $T_{comp}$ . In addition, the observation of EB effect in the conical spin-spiral phase below  $T_S$  unveils the richness of the  $\text{Co}(\text{Cr}_{1-x}\text{Fe}_x)_2\text{O}_4$  system. Double switching of EB field and its complicated spectrum of  $\text{Co}(\text{Cr}_{1-x}\text{Fe}_x)_2\text{O}_4$  system provides the tunable EB as a function of temperature, cooling field, and Fe concentration and this behaviour, adds the additional degree of freedom to the multifunctionality of the system. These attributes have great potential applications in multiferroic based switching device and field effect device [73–75]. Magnetic phase diagram of  $\text{Co}(\text{Cr}_{1-x}\text{Fe}_x)_2\text{O}_4$  series exhibits various magnetic phases as a function of substituted Fe concentration. It is also explored that metastability influences the field-temperature magnetic phase diagram of the compensated samples.

In  $\text{Co}(\text{Cr}_{1-x}\text{Co}_x)_2\text{O}_4$  ( $x = 0.0$ – $0.1$ ), substituted Co ions are found to reside in the B-site. In contrast to the Fe, Co substitution for Cr increases the magnitude of the magnetization, without any signature of compensation. Due to the non-magnetic nature of substituted Co ions in the octahedral site, the magnitude of magnetic moment of B-sublattice decreases and it results in enhancement of the net magnetization of the compound. In addition, EB effect is observed more significantly only below  $T_L$ , and disappears elsewhere. Again this characteristics indicate the entanglement of EB effect and the lock-in transition. Absence of the EB in the parent compound  $\text{CoCr}_2\text{O}_4$

---

may further indicates that the non-collinear spin-spirals need to be disturbed with the substitution to give rise EB effect. We explained the EB below  $T_L$  in the light of presence of commensurate spin-spiral and the unidirectional magnetic anisotropy driven by the non-collinear spin-spirals as noticed in the temperature dependence of the coercive field.

We extended studies in  $d^0(\text{Al}^{+3})$  ion substituted series, i.e.,  $\text{Co}(\text{Cr}_{1-x}\text{Al}_x)_2\text{O}_4$  to comprehend the non- $d^0$  element substituted series. Substituted  $\text{Al}^{+3}$  ions occupy the octahedral(B)-site. As the  $\text{Al}^{+3}$  ion posses zero magnetic moment, effect of the impact of the Al substitution on the magnetic properties up to 50% of Al is similar to  $\text{Co}^{+3}$  substitution. But different magnetic ordering temperatures are lowered quite fast compared to the case of  $\text{Co}^{+3}$  substitution and it may be due to the absence of d-electrons in  $\text{Al}^{+3}$ , which are necessary to keep the superexchange interactions alive in long ranges. In Al rich concentration samples( $0.6 \leq x \leq 0.8$ ) the short range superexchange interactions among the diluted magnetic  $\text{Cr}^{+3}$  ions gives rise to the observation of spin-glass-like behaviour. Similar to the Fe substituted series,  $\text{Co}(\text{Cr}_{1-x}\text{Al}_x)_2\text{O}_4$  also possesses rich magnetic phase diagram.

## Future scope

The contributions obtained from the different studies in this dissertation lay the foundation for further research in this era. Below listed are the some of remarks/comments which are under way and should be addressed.

- Even though the detailed characterization claim the homogeneity of the materials, we can't rule out the possibility of disorder of randomly substituted ions, the microscopical clustering and grain boundary effects, hence, defectless single crystalline samples are appreciable for the study of EB effect, especially in the compensated samples.
- Further, to probe more deep insight into the underlying magnetic mechanisms

## 6. Conclusions

---

proposed in this dissertation, hi-resolution neutron scattering and/or X-ray magnetic circular dichroism(XMCD) measurements are highly recommended.

- It may be fruitful to investigate  $\text{Co}(\text{Cr}_{1-x}\text{Al}_x)_2\text{O}_4$  series with the ac magnetic susceptibility to further support the conclusions drawn from dc magnetization data in this work.

- It is needful to study the magnetoelectric/dielectric properties to sort out the intricate multiferroic and the strong spin-lattice coupling in these systems which is yet to be understood.

- We noticed rich magnetic phase diagram in case of Fe and Al substituted series, but Co substituted series failed to form in the single phase beyond 10%. It will be appreciable to implement some other method to prepare full series in single phase and to construct the magnetic phase diagram.

- This study can be extended in the Mn, V and Ga substitution for Cr in  $\text{CoCr}_2\text{O}_4$ . Studies on the  $\text{Co}(\text{Cr}_{1-x}\text{Mn}_x)_2\text{O}_4$  are under progress.

# References

- [1] J. Leala, L. Rodriguesa, b. A.T. Sousaa, and P. Freitas, *Journal of Magnetism and Magnetic Materials* **140144**, Part **3**, 2215 (1995), International Conference on Magnetism. ix, 20
- [2] J.-E. Wegrowe, A. Comment, Y. Jaccard, J.-P. Ansermet, N. M. Dempsey, and J.-P. Nozières, *Phys. Rev. B* **61**, 12216 (2000).
- [3] R. H. Koch, G. Grinstein, G. A. Keefe, Y. Lu, P. L. Trouilloud, W. J. Gallagher, and S. S. P. Parkin, *Phys. Rev. Lett.* **84**, 5419 (2000).
- [4] B. Warot, A. K. Petford-Long, and T. C. Anthony, *Journal of Applied Physics* **93** (2003).
- [5] Y. Zheng et al., *Magnetics*, *IEEE Transactions on* **40**, 2248 (2004). 20
- [6] J. C. S. Kools, *Magnetics*, *IEEE Transactions on* **32**, 3165 (1996). 1, 20
- [7] B. Dieny, V. S. Speriosu, S. S. P. Parkin, B. A. Gurney, D. R. Wilhoit, and D. Mauri, *Phys. Rev. B* **43**, 1297 (1991). 1, 20
- [8] J. Nogus and I. K. Schuller, *J. Magn. Magn. Mater.* **192**, 203 (1999). ix, 1, 20, 26, 28
- [9] V. Skumryev, S. Stoyanov, Y. Zhang, G. Hadjipanayis, D. Givord, and J. Nogués, *Nature* **423**, 850 (2003). 20
- [10] J. Nogués, V. Skumryev, J. Sort, S. Stoyanov, and D. Givord, *Phys. Rev. Lett.* **97**, 157203 (2006). ix, 20
- [11] W. H. Meiklejohn and C. P. Bean, *Phys. Rev.* **102**, 1413 (1956). ix, 19, 24
- [12] W. H. Meiklejohn and C. P. Bean, *Phys. Rev.* **105**, 904 (1957). ix, 19, 20, 22, 25, 26, 28, 29
- [13] W. H. Meiklejohn, *Journal of Applied Physics* **33**, 1328 (1962). ix, 20, 22, 25, 26
- [14] D. Niebieskikwiat and M. B. Salamon, *Phys. Rev. B* **72**, 174422 (2005). ix, 22
- [15] Y.-k. Tang, Y. Sun, and Z.-h. Cheng, *Phys. Rev. B* **73**, 174419 (2006). 22

## REFERENCES

---

- [16] P. D. Kulkarni, S. K. Dhar, A. Provino, P. Manfrinetti, and A. K. Grover, *Phys. Rev. B* **82**, 144411 (2010). ix, 23, 26, 56, 73, 77
- [17] P. D. Kulkarni, A. Thamizhavel, V. C. Rakhecha, A. K. Nigam, P. L. Paulose, S. Ramakrishnan, and A. K. Grover, *EPL* **86**, 47003 (2009). ix, xxiv, 25, 26, 27, 73, 76, 84, 128
- [18] S. Venkatesh, U. Vaidya, V. C. Rakhecha, S. Ramakrishnan, and A. K. Grover, *J. of Phys: Condens. Matter* **22**, 496002 (2010). ix, 26, 56, 73, 84
- [19] P. K. Manna, S. M. Yusuf, R. Shukla, and A. K. Tyagi, *Appl. Phys. Lett.* **96**, 242508 (2010). ix, 27, 56, 128
- [20] R. P. Singh, C. V. Tomy, and A. K. Grover, *Appl. Phys. Lett.* **97**, 182505 (2010). ix, 28, 56, 73, 76
- [21] K. Yoshii, *Applied Physics Letters* **99**, 142501 (2011). 76, 86
- [22] F. Hong, Z. Cheng, J. Wang, X. Wang, and S. Dou, *Applied Physics Letters* **101**, 102411 (2012). ix, 28
- [23] Y. Yamasaki, S. Miyasaka, Y. Kaneko, J.-P. He, T. Arima, and Y. Tokura, *Phys. Rev. Lett.* **96**, 207204 (2006). x, xxiii, xxiv, 13, 14, 17, 18, 28, 41, 53, 70, 76, 91, 95
- [24] Y. J. Choi et al., *Phys. Rev. Lett.* **102**, 067601 (2009). x, 11, 14, 17, 18, 76, 85, 91
- [25] K. Singh, A. Maignan, C. Simon, and C. Martin, *Appl. Phys. Lett.* **99**, 172903 (2011). 18
- [26] S. Yang et al., *Journal of Physics D: Applied Physics* **45**, 265001 (2012). x, 18, 19, 28, 41
- [27] H. Katsura, N. Nagaosa, and A. V. Balatsky, *Phys. Rev. Lett.* **95**, 057205 (2005). x, 17, 18
- [28] N. Menyuk, K. Dwight, and A. Wold, *J. Phys. France* **25**, 528 (1964). x, xxiii, 5, 6, 7, 11, 13, 14, 15, 18, 28, 53, 70, 74, 85, 91, 95, 98, 122, 127
- [29] K. Tomiyasu, J. Fukunaga, and H. Suzuki, *Phys. Rev. B* **70**, 214434 (2004). x, 11, 13, 14, 15, 18, 28, 53, 70, 85, 91, 95, 98, 122, 127
- [30] L. J. Chang, D. J. Huang, W.-H. Li, S.-W. Cheong, W. Ratcliff, and J. W. Lynn, *Journal of Physics: Condensed Matter* **21**, 456008 (2009). x, 11, 14, 18, 56, 85, 94
- [31] A. V. Pronin et al., *Phys. Rev. B* **85**, 012101 (2012). x, xxiii, 15, 16, 28, 41, 43, 56, 67, 70, 108, 114
- [32] V. Tsurkan et al., *Phys. Rev. Lett.* **110**, 115502 (2013). x, xxiii, 15, 16, 18, 28, 41, 70
- [33] C. Ederer and M. Komelj, *Phys. Rev. B* **76**, 064409 (2007). x, 28

- [34] B. C. Melot, J. E. Drewes, R. Seshadri, E. M. Stoudenmire, and A. P. Ramirez, *J. of Phys: Condens Matter* **21**, 216007 (2009). x, 7, 43
- [35] H. Bao, S. Yang, and X. Ren, *J. of Phys: Conf. Series* **266**, 012001 (2011).
- [36] I. Kim et al., *Applied Physics Letters* **94**, 042505 (2009). x, 85, 86, 91, 96, 98
- [37] C. Kittel, *Introduction to Solid State Physics*, Wiley, 2004. 1, 34
- [38] V. Wadhawan, *Introduction to Ferroic Materials*, Taylor & Francis, 2000.
- [39] Begun and S. Joseph, New York: Rinehart (1949).
- [40] S. Stringari and R. Wilson, *Rendiconti Lincei* **11**, 115 (2000).
- [41] C. Tsang et al., *Magnetics, IEEE Transactions on* **33**, 2866 (1997). 20
- [42] C. Tsang et al., *Magnetics, IEEE Transactions on* **35**, 689 (1999).
- [43] S. Gangopadhyay et al., *Journal of Applied Physics* **87**, 5407 (2000). 1, 20
- [44] J. Lier, G. J. Koel, W. Gestel, L. Postma, J. Gerkema, F. Gorter, and W. F. Druyvesteyn, *Magnetics, IEEE Transactions on* **12**, 716 (1976). 1
- [45] Weiss, Pierre, *J. Phys. Theor. Appl.* **6**, 661 (1907). 3
- [46] W. Heisenberg, *Zeitschrift fr Physik* **38**, 411 (1926). 3
- [47] L. NÉEL, *Nobel Lectures, Physics 1963-1970* (1970). 5, 97, 116
- [48] J. Goodenough, *Magnetism and the chemical bond*, Interscience monographs on chemistry: Inorganic chemistry section, Interscience Publishers, 1963. 5
- [49] D. H. Lyons, T. A. Kaplan, K. Dwight, and N. Menyuk, *Phys. Rev.* **126**, 540 (1962). 5, 11, 13, 14
- [50] G. A. Sawatzky, F. Van Der Woude, and A. H. Morrish, *Phys. Rev.* **187**, 747 (1969). 6, 45
- [51] A. Tari, J. Popplewell, S. W. Charles, D. S. P. Bunbury, and K. M. B. Alves, *Journal of Applied Physics* **54** (1983). 6
- [52] D. Peddis et al., *Journal of Physics: Condensed Matter* **23**, 426004 (2011). 6
- [53] S. Sachdev, *Nat. Phys.* **4**, 173 (2008). xxiii, 8, 10
- [54] M. Harris, *Nature* **456**, 886 (2008).
- [55] E. A. Goremychkin, R. Osborn, B. D. Rainford, R. T. Macaluso, D. T. Adroja, and M. Koza, *Nature Physics* **4**, 766 (2008).

## REFERENCES

---

- [56] L. Balents, *Nature* **464**, 199 (2010). xxiii, 8, 10
- [57] A. A. Zvyagin, *Low Temperature Physics* **39**, 901 (2013). xxiii, 8, 10
- [58] M. Harris, *Nature* **399**, 311 (1999). 8
- [59] H. Kikuchi et al., *Phys. Rev. Lett.* **94**, 227201 (2005). 8
- [60] J. Kang, C. Lee, R. K. Kremer, and M.-H. Whangbo, *Journal of Physics: Condensed Matter* **21**, 392201 (2009). 8
- [61] D. G. Tomuta, S. Ramakrishnan, G. J. Nieuwenhuys, and J. A. Mydosh, *Journal of Physics: Condensed Matter* **13**, 4543 (2001). 8
- [62] K. Matan et al., *Phys. Rev. Lett.* **96**, 247201 (2006). 8
- [63] C. Ruegg, *Nature Physics* **6**, 837 (2010). 8
- [64] F. H. GAidoudi, D. W. Aldous, R. J. Goff, S. M. Z., J. P. AU Attfield, R. E. Morris, and P. Lightfoot, *Nature Chem* **4**, 801 (2011). 8
- [65] O. Tchernyshyov, R. Moessner, and S. L. Sondhi, *Phys. Rev. Lett.* **88**, 067203 (2002). 10
- [66] S.-H. Lee, C. Broholm, W. Ratcliff, G. Gasparovic, Q. Huang, T. H. Kim, and S.-W. Cheong, *Nature* **418**, 856 (2002). 10, 11, 98
- [67] T. A. Kaplan and N. Menyuk, *Philosophical Magazine* **87**, 3711 (2007). 11, 13, 70
- [68] N. Tristan, J. Hemberger, A. Krimmel, H.-A. Krug von Nidda, V. Tsurkan, and A. Loidl, *Phys. Rev. B* **72**, 174404 (2005). 12, 105, 106, 108, 113, 114, 119, 125
- [69] O. Zaharko, A. Cervellino, V. Tsurkan, N. B. Christensen, and A. Loidl, *Phys. Rev. B* **81**, 064416 (2010). 119, 125
- [70] B. Roy, A. Pandey, Q. Zhang, T. W. Heitmann, D. Vaknin, D. C. Johnston, and Y. Furukawa, *Phys. Rev. B* **88**, 174415 (2013). 12, 105
- [71] D. Kamenskyi et al., *Phys. Rev. B* **87**, 134423 (2013). 14, 15, 70, 74, 122
- [72] D. Khomskii, *Physics* **2**, 20 (2009). 16
- [73] X. He et al., *Nat Mater* **9**, 579 (2010). 29, 128
- [74] V. Skumryev, V. Laukhin, I. Fina, X. Martí, F. Sánchez, M. Gospodinov, and J. Fontcuberta, *Phys. Rev. Lett.* **106**, 057206 (2011).
- [75] S. M. Wu, S. A. Cybart, P. Yu, M. D. Rossell, J. X. Zhang, R. Ramesh, and R. C. Dynes, *Nat Mater* **9**, 756 (2010). 29, 102, 128

- [76] S. M. Wu, S. A. Cybart, D. Yi, J. M. Parker, R. Ramesh, and R. C. Dynes, *Phys. Rev. Lett.* **110**, 067202 (2013). 16, 29
- [77] N. A. Benedek and C. J. Fennie, *The Journal of Physical Chemistry C* **117**, 13339 (2013). 16
- [78] T. Kimura, T. Goto, H. Shintani, K. Ishizaka, T. Arima, and Y. Tokura, *Nature* **426**, 55 (2003). 17
- [79] C. Lu et al., *Sci. Rep.* **3**, 03374 (2013).
- [80] L. C. Chapon, G. R. Blake, M. J. Gutmann, S. Park, N. Hur, P. G. Radaelli, and S.-W. Cheong, *Phys. Rev. Lett.* **93**, 177402 (2004). 17
- [81] M. Mostovoy, *Phys. Rev. Lett.* **96**, 067601 (2006). 17
- [82] R. L. Stamps, *Journal of Physics D: Applied Physics* **33**, R247 (2000). 20
- [83] K. O. Grady, L. Fernandez-Outon, and G. Vallejo-Fernandez, *Journal of Magnetism and Magnetic Materials* **322**, 883 (2010). 20
- [84] D. J. Webb, A. F. Marshall, T. H. Geballe, and R. M. White, *IEEE Trans. Magn.* **24**, 2013 (1988). 24, 26
- [85] J. Nogues, D. Lederman, T. J. Moran, and I. K. Schuller, *Phys. Rev. Lett.* **76**, 4624 (1996). xxiv, 24, 25, 27, 28
- [86] N. C. Koon, *Phys. Rev. Lett.* **78**, 4865 (1997). 25
- [87] S. Demirtas, A. R. Koymen, and H. Zeng, *Journal of Physics: Condensed Matter* **16**, L213 (2004). 25
- [88] C. Wang et al., *Journal of Applied Physics* **104**, (2008).
- [89] W. Wang, F. Takano, M. Takenaka, H. Akinaga, and H. Ofuchi, *Journal of Applied Physics* **103**, (2008). 25
- [90] V. Papaefthymiou et al., *Journal of Applied Physics* **67**, 4487 (1990). 28
- [91] S. Giri, M. Patra, and S. Majumdar, *Journal of Physics: Condensed Matter* **23**, 073201 (2011). 28
- [92] S. Dong et al., *Phys. Rev. Lett.* **103**, 127201 (2009). 29
- [93] Y. F. Tian et al., *Sci. Rep.* **3**, 1 (2013). 29, 86, 102
- [94] X. Xue et al., *The European Physical Journal B* **86**, 1 (2013). 86

## REFERENCES

---

- [95] Z. Li, C. Jing, J. Chen, S. Yuan, S. Cao, and J. Zhang, *Applied Physics Letters* **91**, (2007). 29, 86, 102
- [96] A. West, *Solid State Chemistry and Its Applications*, Wiley, 1987. 31
- [97] H. M. Rietveld, *Journal of Applied Crystallography* **2**, 65 (1969). 34
- [98] J. Rodriguez-Carvajal, *Physica B: Condensed Matter* **192**, 55 (1993). 34
- [99] T. Roisnel and J. Rodriguez-Carvajal, *Proceedings of the Seventh European Powder Diffraction Conference (EPDIC)* **7**, 118 (1997).
- [100] A. Boultif and D. Louër, *Journal of Applied Crystallography* **37**, 724 (2004). 34
- [101] *Review of Scientific Instruments* **30**, 547 (1959). 38
- [102] J. S. Hwang, K. J. Lin, and C. Tien, *Review of Scientific Instruments* **68** (1997). 39
- [103] E. Dachs and A. Benisek, *Cryogenics* **51**, 460 (2011). 39
- [104] G. Lawes, B. Melot, K. Page, C. Ederer, M. A. Hayward, T. Proffen, and R. Seshadri, *Phys. Rev. B* **74**, 024413 (2006). 43, 70, 96, 108
- [105] J. Dormann, S. Bhargava, J. Jov, and D. Fiorani, *Hyperfine Interactions* **50**, 625 (1989). 43
- [106] K. R. Choi, S. B. Kim, and C. S. Kim, *Journal of Applied Physics* **101**, 09M105 (2007). 45
- [107] A. Hauet, J. Teillet, B. Hannyoyer, and M. Lenglet, *physica status solidi (a)* **103**, 257 (1987).
- [108] H. Mohan, I. Shaikh, and R. Kulkarni, *Physica B: Condensed Matter* **217**, 292 (1996). 45
- [109] R. Pradheesh, H. S. Nair, V. Sankaranarayanan, and K. Sethupathi, *Applied Physics Letters* **101**, (2012). 68, 69
- [110] N. Kumar and A. Sundaresan, *Solid State Communications* **150**, 1162 (2010). 70
- [111] X. H. Chen, K. Q. Wang, P. H. Hor, Y. Y. Xue, and C. W. Chu, *Phys. Rev. B* **72**, 054436 (2005). 73, 78
- [112] H. Adachi, H. and Ino, *Nature* **401**, 148 (1999). 73
- [113] J. Mao et al., *Solid State Communications* **151**, 1982 (2011). 76
- [114] D. J. Webb, A. F. Marshall, Z. Sun, T. H. Geballe, and R. M. White, *IEEE Trans. Magn.* **24**, 588 (1988). 76
- [115] D. H. Lyons, T. A. Kaplan, K. Dwight, and N. Menyuk, *Phys. Rev.* **126**, 540 (1962). 77
- [116] C. Ederer and M. Komelj, *Phys. Rev. B* **76**, 064409 (2007). 78, 79

- [117] R. Masrour, M. Hamedoun, A. Hourmatallah, K. Bouslykhane, N. Benzakour, and A. Benyoussef, *Canadian Journal of Physics* **86**, 1287 (2008). 78
- [118] E. L. Jr. et al., *Journal of Magnetism and Magnetic Materials* **320**, 622 (2008). 78
- [119] G. Hu, J. H. Choi, C. B. Eom, V. G. Harris, and Y. Suzuki, *Phys. Rev. B* **62**, R779 (2000). 88
- [120] R. K. Mishra and G. Thomas, *Journal of Applied Physics* **48** (1977). 88
- [121] A. Rautiainen, M. Lindblad, L. B. Backman, and R. L. Puurunen, *Phys. Chem. Chem. Phys.* **4**, 2466 (2002). 89
- [122] G. Beech and R. M. Lintonbon, *Thermochimica Acta* **3**, 97 (1971). 89
- [123] R. Padam, S. Pandya, S. Ravi, A. K. Nigam, S. Ramakrishnan, A. K. Grover, and D. Pal, *Applied Physics Letters* **102**, 112412 (2013). 91
- [124] F. K. Lotgering, *Philips Res. Rep.* **11** (1956). 97, 119
- [125] E. Winkler et al., *Phys. Rev. B* **80**, 104418 (2009). 97, 119, 120
- [126] A. J. García-Adeva and D. L. Huber, *Phys. Rev. Lett.* **85**, 4598 (2000). 97, 98, 120
- [127] T. C. Schulthess and W. H. Butler, *Phys. Rev. Lett.* **81**, 4516 (1998). 102
- [128] B. C. Melot, K. Page, R. Seshadri, E. M. Stoudenmire, L. Balents, D. L. Bergman, and T. Profen, *Phys. Rev. B* **80**, 104420 (2009). 105, 125
- [129] N. Tristan et al., *Phys. Rev. B* **77**, 094412 (2008). 105, 106, 108, 113, 114, 119, 125
- [130] D. Fiorani, J. L. Dormann, J. L. Tholence, and J. L. Soubeyrou, *Journal of Physics C: Solid State Physics* **18**, 3053 (1985). 124

## Vitae

Padam Rajender was born on 12<sup>th</sup> May, 1984 in Andhra Pradesh state, India. He obtained his Bachelors in Physics from Ramakrishna Degree College, Jagtial, Andhra Pradesh and completed Masters in Physics discipline from Kakatiya University, Warngal, Andhra Pradesh. He pursued his doctoral research career with experimental condensed matter physics, at the Department of Physics, IIT Guwahati under the supervision of Dr. Dilip Pal and Prof. Seenipandian Ravi. His current research interests include Multiferroics, Magnetism, Phenomenon of Magnetization reversal and Exchange bias, Magnetic frustration and Strongly correlated electron systems.